Dissertation
submitted to the
Combined Faculties for the Natural Sciences and for Mathematics
of the Ruperto-Carola-University of Heidelberg, Germany
for the degree of
Doctor of Natural Sciences

put forward by
Christian Smorra
born in Lich, Germany

Date of oral examination: July 20, 2012

# High-precision Q-value and mass measurements for neutrino physics with TRIGA-TRAP and commissioning of an on-line ion source for TRIGA-SPEC

Referees: Prof. Dr. Klaus Blaum

Dr. Yuri Litvinov

# Abstract

The observation of neutrinoless double-electron capture would prove the Majorana character of neutrinos. Transitions with an energy degeneracy of the initial and final state show a resonant enhancement of the decay rate and would be important for neutrino physics experiments. In order to identify such transitions, precise $Q$-value measurements with Penning-trap mass spectrometers play a key role. In this thesis, the resonance condition of neutrinoless double-electron capture in $^{106}$Cd, $^{108}$Cd, and $^{184}$Os was investigated by $Q$-value measurements with the Penning-trap mass spectrometer TRIGA-TRAP. In addition, the $Q$ value of the double-beta decay in $^{110}$Pd was measured.

A high-voltage platform and an on-line ion source for the ionization of short-lived neutron-rich fission products for the TRIGA-SPEC experiment located at the research reactor TRIGA Mainz has been commissioned and tested. The aim is to provide a radioactive ion beam for high-precision mass spectrometry and collinear laser spectroscopy. For the extraction from the TRIGA reactor, the fission products are attached to aerosol particles and transported with a gas-jet system to the on-line ion source. This ion source has to cope with a high gas load and has to destroy the bond between fission product and aerosol particle. It was investigated, whether an 2.45 GHz ECR ion source is suited for this task.



# Zusammenfassung

Der Nachweis des neutrinolosen doppelten Elektroneneinfangs kann zum Beweis des Majoranacharakters von Neutrinos verwendet werden. Übergänge mit einer Energieentartung zwischen dem Anfangs- und dem Endzustand weisen eine resonante Verstärkung der Zerfallsrate auf, so dass diese besonders für Experimente in der Neutrinophysik geeignet sind. Um solche resonanten Übergänge zu identifizieren, spielen genaue $Q$-Wert-Messungen mit Penningfallen-Massenspektrometern eine wichtige Rolle. In dieser Arbeit wurde die Resonanzbedingung des neutrinolosen doppelten Elektroneneinfangs in den Nukliden $^{106}$Cd, $^{108}$Cd und $^{184}$Os durch $Q$-Wert-Messungen mit dem Penningfallen-Massenspektrometer TRIGA-TRAP untersucht. Zusätzlich wurde der $Q$-Wert des doppelten Beta-Zerfalls in $^{110}$Pd bestimmt.

Desweiteren wurde eine Hochspannungsplattform und eine on-line Ionenquelle für die Ionisation von kurzlebigen neutronenreichen Spaltprodukten für das TRIGA-SPEC-Experiment am Forschungsreaktor TRIGA Mainz aufgebaut und erfolgreich in Betrieb genommen. Mit diesem Aufbau soll ein radioaktiver Ionenstrahl für hochpräzise Massenmessungen und kollineare Laserspektroskopie zur Verfügung gestellt werden. Die Spaltprodukte werden an Aerosole gebunden, um sie mit Hilfe eines Gasjet-Transportsystems vom Reaktor in die Ionenquelle zu transportieren. Dies stellt besondere Anforderungen an die Ionenquelle dar, da sie unter einer hohen Gaslast arbeiten und die Bindung zwischen Aerosolteilchen und Spaltprodukt aufbrechen muss. Es wurde untersucht, ob eine 2.45 GHz EZR-Ionenquelle für diesen Zweck geeignet ist.

# Contents

# List of Tables

# List of Figures

# Chapter 1

# Introduction

Neutrinos are very elusive particles, electrically neutral, almost massless, and hardly interact at all with matter. Their existence was first postulated by Wolfgang Pauli in 1930 [Pau77], who explained the continuous energy-spectrum of the nuclear beta decay by the emission of an additional particle that escapes detection. Thereby, the law of energy and impulse conservation could be preserved in beta decay. The experimental evidence of Pauli's prediction took more than 20 years, and succeeded finally in 1956. Cowan and Reines observed an inverse beta decay, which was induced by a neutrino [Rei56]. Today, neutrinos are included in the Standard Model as uncharged, massless, spin-1/2 fermions that take part in weak-interaction processes by left-handed currents. However, neutrinos have still several unknown properties, such as the mass of the neutrinos, the mass hierarchy of the neutrino families, and whether neutrinos are Dirac or Majorana particles.

As spin-1/2 fermions, neutrinos can be described as a four-component Dirac field, where the components correspond to the neutrino and the antineutrino, each in both helicity states. Weyl demonstrated that the description of massless fermions can be reduced to a two-component field, which describes the two experimentally observed neutrino types: left-handed neutrinos and right-handed anti-neutrinos.

An alternative description of neutrinos was developed in 1937 by Ettore Majorana, who was not satisfied with the Dirac theory at that time, which considered positrons with negative energies as holes in the Dirac sea of electron states [Bil06]. Majorana developed a symmetrical formulation of particles and antiparticles. As consequence of the application of Majorana's theory to uncharged fermions, neutrinos could be identical with their antiparticle, and only one Majorana neutrino would exist.

Nowadays, it is still not clarified whether neutrinos are Dirac or Majorana particles. Weyl's description of massless neutrinos had to be dismissed due to the observation of neutrino oscillations [Ahm02], i.e. the transition of neutrinos between the three lepton families. This requires a mass difference between the neutrino eigenstates as an explanation. Dirac and Majorana neutrinos could be distinguished in the neutrinoless double-beta decay ($0\nu\beta\beta$) or the neutrinoless double-electron capture ($0\nu\epsilon\epsilon$). The mere observation of either of these processes would reveal physics beyond the Standard Model, since two neutrinos have to annihilate during the process. Thus, these processes require neutrinos to be massive Majorana particles to

take place, and the total lepton number conservation would be violated. This conservation rule of the total lepton number is included in the Standard Model, but rather weak, since it is not based on any fundamental symmetry.

A clear evidence for neutrinoless double-beta transitions is still missing. Only one claim of the detection of the $0\nu\beta\beta$-decay in $^{76}$Ge has been made [Kla04]. The neutrino-accompanied double-beta ($2\nu\beta\beta$) decay, which is allowed within the Standard Model, was observed for several nuclides with half-lives in the order of $10^{19}$ to $10^{21}$ years [Zub04b]. However, in this process Dirac and Majorana neutrinos cannot be distinguished. The half-life of the neutrinoless transitions are expected to be in the order of $10^{25}$ years and beyond and therefore experimentally challenging.

One key ingredient to identify the signal of the $0\nu\beta\beta$ decay is the precise knowledge of the $Q$ value of this process, which is the difference of the atomic masses of the mother and the daughter nuclides in their ground state. The sum energy of the two emitted electrons in this transition corresponds to the $Q$ value and a narrow peak in the energy spectrum at the position of the $Q$ value could be interpreted as signature for this rare decay.

The half-life of the $0\nu\epsilon\epsilon$ process is in general in the order of $10^{30}$ years or longer, which makes the possibility of the experimental detection of this process less promising. However, it was realized that the $0\nu\epsilon\epsilon$ process can be resonantly enhanced, if the initial and the final state of the transition are degenerate in energy [Vol82, Ber83, Kri11]. This requires that the total excitation energy of the final state of the transition composed of the energies of the two-electron hole state in the electron shell and possibly of an excited nuclear state to match the $Q$ value within the width of the final state, typically a few 10 eV. Considering the narrow width of the excited state, a resonantly enhanced transition could be regarded as a fortunate coincidence in nature, if existing at all. In order to search for resonantly enhanced transitions suited for neutrino experiments, precise $Q$-value measurements are required.

The $Q$-value measurements presented in this thesis were performed with the Penning-trap mass spectrometer TRIGA-TRAP [Ket08], which is located at the research reactor TRIGA-Mainz as part of the TRIGA-SPEC experiment. The precision of atomic mass measurements with Penning traps is presently unmatched [Bla06]. The enhanced observation time of confined charged particles in a superposition of a strong magnetic field and a weak electric field in vacuum, and the fact that the mass measurement is converted into a frequency measurement are the main advantages of this method. Atomic masses of stored particles are determined by measuring the cyclotron frequency $\nu_c = qB/(2\pi m)$ of an ion with mass $m$ and charge $q$, and by calibrating the magnetic field strength $B$ with an ion of well-known mass. In case of a $Q$-value measurement, the daughter nuclide can be used as reference mass for the mother nuclide and the $Q$ value can be directly obtained from the cyclotron frequency ratio of the two ion species. In this thesis, the $Q$ values of double-electron capture in three nuclides, $^{106}$Cd, $^{108}$Cd and $^{184}$Os, have been determined with high precision and the resonance conditions for neutrinoless double-electron capture have been investigated. In addition, the $Q$ value of double-beta decay in $^{110}$Pd has been measured as well.

The second part of this thesis concerns the on-line coupling of the TRIGA-

SPEC experiment. The aim of TRIGA-SPEC is to investigate the ground-state properties, like nuclear binding energies, nuclear spins, nuclear radii, as well as magnetic and spectroscopic quadrupole moments of neutron-rich fission products of uranium, plutonium and californium. The nuclear binding energies are determined with TRIGA-TRAP, the other properties by the collinear laser spectroscopy experiment TRIGA-Laser. Experimental measurements of these properties allow to test and improve the predictive power of nuclear models on the neutron-rich side of the nuclear chart, which would improve calculations of the astrophysical rapid-neutron capture process for the nucleosynthesis and the neutron drip line [Ket08, Ket10b].

The nuclides of interest are produced by thermal neutron-induced fission close to the core of the TRIGA reactor. These short-lived fission products have to be extracted from the production location to the experimental area and converted into a radioactive ion beam for the experiments. The transport is carried out by a gas-jet system, which is since long frequently applied in nuclear chemistry experiments [Sil77]. Radionuclides are emitted from the production target due to the recoil energy from the fission process and stopped in a gas-filled recoil chamber. The fission products attach themselves to aerosol particles with a diameter of about 100 nm, which serve as carrier particles for the transport through long (several 10 m), thin (about 1 mm diameter) capillaries. The transport through the capillary to the experimental area is element independent, thus refractory elements can be extracted as well from the target, which is an advantage of this method. Such a gas-jet system has been successfully used in combination with a surface ion source in on-line mass spectrometers [Brü85, Sch87]. However, surface ion sources lack in ionization efficiency of elements with a high ionization potential and a high melting and vaporization temperature. In order to extent the number of elements available from gas-jet coupled ion sources, a different ionization method has to be used.

An electron cyclotron resonance (ECR) ion source has been commissioned as gas-jet coupled ion source for the production of radioactive ion beams within this thesis. ECR ion sources contain a plasma with hot electrons, which can ionize elements with high ionization potential by electron impact ionization. The ionization efficiency and the applicability of ECR ion sources as gas-jet coupled ion sources has been investigated.

The outline of this thesis is as follows: In Chap. 2, neutrinos and neutrinoless double-beta transitions are discussed with respect to the possible Majorana character of neutrinos. The importance of precise $Q$ values of these transitions for neutrino experiments is pointed out. The measurement principle of high-precision $Q$ values with Penning traps is explained in Chap. 3. The radioactive ion beam production at the TRIGA-SPEC experiment is introduced in Chap. 4 with focus on the principle of ECR ion sources. In Chap. 5, the experimental setup for the on-line coupling of TRIGA-SPEC and the Penning-trap mass spectrometer TRIGA-TRAP are described. The next two chapters are dedicated to the results obtained within this thesis. Chap. 6 reports the on-line and off-line tests of a 2.45 GHz ECR ion source as a gas-jet coupled ion source for the on-line commissioning of TRIGA-SPEC. Chap. 7 presents the results of the $Q$-value measurements of four double-beta transitions and measurements of the atomic masses of the involved nuclides performed with the TRIGA-TRAP mass spectrometer. Finally, the conclusions of the experiments and

future perspectives for TRIGA-TRAP and the on-line coupling of TRIGA-SPEC are discussed in Chap. 8.

# Chapter 2

# Neutrino physics and double-beta transitions

Neutrinos were postulated by Wolfgang Pauli in the 1930s [Pau77] to explain the continuous energy spectrum of electrons from beta decay and to save the energy conservation in this process. The first experimental proof of the existence of neutrinos succeeded in 1956, when Cowan and Reines observed an inverse beta decay [Rei56]:

$$\overline{\nu_e} + p \rightarrow e^+ + n. \tag{2.1}$$

Two more generations of neutrinos have been found since then, the muon neutrino $\nu_\mu$ and the tau neutrino $\nu_\tau$, so that six different neutrinos have been included in the Standard Model of particle physics: One of each generation with its antiparticle. They are characterized as uncharged, massless, spin-1/2 particles and take part in the weak interaction only as left-handed neutrinos or right-handed antineutrinos. These properties are in accordance with the today available experimental observations of neutrinos.

Despite the success of the Standard Model, there are still open questions concerning the properties of neutrinos. In particular, there were observations of neutrino flavor oscillations [Ahm02], which require at least one neutrino to have a finite rest mass - in contrary to the Standard Model. Neutrino flavor oscillations are sensitive to the differences of the squared masses of the neutrinos undergoing the oscillation. Although the absolute masses of the neutrinos were not determined yet, there is a lower limit for one of the mass eigenstates from the neutrino oscillation experiments in the range of 10 - 50 meV [Ahm02] and an upper limit from the measurement of the endpoint of electron energy spectrum in the beta decay of tritium of 2.0 eV for the anti-electron neutrino mass at a confidence level of 95% [Ott08]. The value of the absolute masses and the mass hierachy of the neutrino flavors are of high interest.

Another open question is, whether neutrinos - the only uncharged fermions in the Standard Model - are their own antiparticles, i.e. of Majorana type. An experimental proof of the Majorana character would indicate physics beyond the Standard Model, since the conservation of the total lepton number would be violated. One promising method to reveal the possible Majorana character of neutrinos is to observe neutrinoless double-beta transitions. Double-beta transitions are second-order

weak interaction processes, which change the charge number $Z$ of a nuclide by two, whereas the mass number $A$ remains unchanged. The different possible transitions are discussed in Sect. 2.2. As second-order process these transitions have half-lives in the order of $10^{20}$ years and beyond and are challenging to observe due to background signals from the decay of other nuclides and cosmic rays.

In the first section of this chapter an introduction is given how neutrinos are described in the Standard Model and how it could be extended to include massive neutrinos, as Dirac or Majorana particles. The Majorana character can be probed in double-beta transitions, which are discussed in this respect in the second section of this chapter. In particular, it is elaborated how precise $Q$-value measurements, such as presented in Chap. 7, can contribute to neutrino experiments. This chapter is mainly based on the references [Zub98, Zub04b, Zub04a, Bla10].

## 2.1 Neutrinos in the Standard Model and Majorana neutrinos

The Standard Model describes fermions with spin 1/2 and mass $m$ as a Lorentz-covariant 4-spinors $\psi(x)$, which obey the Dirac equation:

$$(i\gamma_\mu \partial^\mu - m)\psi(x) = 0. \tag{2.2}$$

This holds also for neutrinos, which are assumed to be massless $m = 0$ and uncharged $q = 0$. Any spinor $\psi$ which solves the Dirac equation can be written as sum of its left-handed and right-handed chiral components $\psi_L$ and $\psi_R$[1]:

$$\psi = (P_L + P_R)\psi = P_L\psi + P_R\psi = \psi_L + \psi_R, \tag{2.4}$$

using the projection operators

$$P_L = \frac{1}{2}(1 - \gamma_5) \quad \text{and} \quad P_R = \frac{1}{2}(1 + \gamma_5). \tag{2.5}$$

Using these chiral projections, the Dirac equation (2.2) can be expressed by the following two equations:

$$\left(i\frac{\partial}{\partial x^0} - i\sigma_i\right)\psi_R = m\gamma_0\psi_L \tag{2.6}$$

$$\left(i\frac{\partial}{\partial x^0} + i\sigma_i\right)\psi_L = m\gamma_0\psi_R. \tag{2.7}$$

In the case of massless particles these two equations decouple and the 4-component spinors $\psi_L$ and $\psi_R$ can be replaced by two independent 2-component Weyl spinors in the Weyl representation of neutrinos [Sch97].

[1]The $\gamma$ matrices in the equations (2.2) and (2.5) are given by

$$\gamma_0 = \begin{pmatrix} 1 & 0 \\ 0 & -1 \end{pmatrix},\ \gamma_i = \begin{pmatrix} 0 & \sigma_i \\ -\sigma_i & 0 \end{pmatrix}, \gamma_5 = \begin{pmatrix} 0 & 1 \\ 1 & 0 \end{pmatrix}, \tag{2.3}$$

where $\sigma_i$ are the Pauli matrices, and $i = 1, 2, 3$.

It can be shown that $\psi_L$ and $\psi_R$ are eigenspinors of the helicity operator $\mathcal{H} = \sigma \cdot p/|p|$, so that chirality and helicity are identical. $\psi_L$ has the eigenvalues $\mathcal{H} = +1$ for particles (left-handed), and $\mathcal{H} = -1$ for antiparticles (right-handed), and $\psi_R$ vice versa. Neutrinos have been observed in weak interaction processes only as left-handed neutrinos and right-handed antineutrinos. Therefore, neutrinos are described by:

$$\psi_\nu = \frac{1}{2}(1 - \gamma_5)\,\psi = \psi_L. \tag{2.8}$$

In the case of massive particles the equations (2.6) and (2.7) do not decouple anymore and Weyl spinors are not sufficient to describe neutrinos, they have to be described by a four component Dirac spinor. Furthermore, $\psi_L$ and $\psi_R$ are not eigenspinors of the helicity operator anymore. Thus, massive particles always carry both helicity components.

An alternative description of neutrinos was developed by Majorana, where neutrinos are particles, which are identical to their charge conjugated state $\psi^C = \pm\psi$, i.e. their own antiparticles. The charge conjugated state is obtained with the charge conjugation operator $C$, which obeys the relation:

$$C^{-1}\gamma_\mu C = -\gamma_\mu^T, \tag{2.9}$$

and is given by $C = i\gamma_2\gamma_0$, if the $\gamma$ matrices in equation (2.3) are used. A Majorana field $\psi_M$ can be constructed from any spinor $\psi$:

$$\psi_M = \frac{1}{\sqrt{2}}\left(\psi + \eta_C\psi^C\right), \tag{2.10}$$

where $\eta_C = \lambda_C e^{i\phi}$ is called creation phase and $\lambda_C = \pm 1$. $\psi_M$ fulfills the requirement $\psi_M^C = \pm\psi_M$. In the case of massless neutrinos the Majorana representation is identical to the Weyl representation [Zub98].

However, the experimental observation of neutrino oscillations [Ahm02, Egu03] brought evidence that neutrinos have a finite rest mass. A neutrino can change its flavor on the way from a source to a detector, if the flavor eigenstates are different from the mass eigenstates, and the squared mass differences $\Delta m_{i,j}$ of the mass eigenstates are not vanishing. The mixing of the flavor eigenstates $\nu_e$, $\nu_\mu$, and $\nu_\tau$ and the mass eigenstates $m_i$, $i = 1, 2, 3$ is described by a unitary transformation $U$:

$$\nu_\alpha = \sum U_{\alpha i}\nu_i. \tag{2.11}$$

The mixing matrix $U$ is called Pontecorve-Maki-Nakagawa-Sato (PMNS)-matrix. It is analogous to the mixing matrix in the quark sector, which is called Cabbibo-Kobayashi-Maskawa (CKM) matrix. It can be parameterized by three mixing angles $\theta_{i,j}$ and a CP-violating phase $\delta$:

$$U = \begin{pmatrix} c_{12}c_{13} & s_{12}c_{13} & s_{13}e^{i\delta} \\ -s_{12}c_{23} - c_{12}s_{23}s_{13}e^{i\delta} & c_{12}c_{23} - s_{12}s_{23}s_{13}e^{i\delta} & s_{23}c_{13} \\ s_{12}s_{23} - c_{12}s_{23}s_{13}e^{i\delta} & -c_{12}s_{23} - s_{12}c_{23}s_{13}e^{i\delta} & c_{23}c_{13} \end{pmatrix}, \tag{2.12}$$

where $s_{i,j} = \sin(\theta_{i,j})$ and $c_{i,j} = \cos(\theta_{i,j})$. In the case of the mixing of two neutrino flavors the transition probability is given by

$$P(\nu_\alpha \to \nu_\beta) = \sin^2(2\theta_{i,j})\sin^2\left(\pi\frac{L}{L_0}\right), \tag{2.13}$$

where $L$ is the distance between source and detector, $L_0$ the oscillation length

$$L_0 = 4\pi\hbar c\frac{E}{\Delta m^2} = 2.48\frac{E/\mathrm{MeV}}{\Delta m^2/\mathrm{eV}}\mathrm{m}, \tag{2.14}$$

and $E$ the neutrino energy. $\Delta m_{1,2} \approx 8 \cdot 10^{-5}$ eV$^2$ and $\Delta m_{2,3} \approx 2.5 \cdot 10^{-3}$ eV$^2$ were obtained from the so far performed neutrino oscillation experiments [Zub04a, Ahm04, Egu03].

This requires a description of neutrinos as massive particles, either as Dirac or Majorana particles. The Dirac equation (2.2) can be derived from the Lagrangian density $\mathcal{L}$

$$\mathcal{L} = \overline{\psi}\left(i\gamma_\mu\frac{\partial}{\partial x^\mu} - m_D\right)\psi, \tag{2.15}$$

where $m_D$ denotes the Dirac mass, which is identical to $m$ in equation (2.2). It contains already the Dirac mass term $\mathcal{L}_D$,

$$\mathcal{L}_D = \overline{\psi}m_D\psi, \tag{2.16}$$

to describe massive neutrinos that differ from their antiparticles. If the chiral projections are used, the Dirac mass term can be written as

$$\mathcal{L}_D = m_D\left(\overline{\psi}_L\psi_R + \overline{\psi}_R\psi_L\right). \tag{2.17}$$

Thus, it requires left- and right-handed neutrinos to construct this mass term. Therefore, the neutrinos were included as massless particles in the Standard Model due to lack of observation of right-handed currents.

In case of Majorana neutrinos, the charge conjugated fields $\psi^C$ can be used to construct an additional mass term $\mathcal{L}_M$

$$\mathcal{L}_M = \frac{1}{2}m_L\left(\overline{\psi}_L\psi_R^c + \overline{\psi}_R^c\psi_L\right) + \frac{1}{2}m_R\left(\overline{\psi}_R\psi_L^c + \overline{\psi}_L^c\psi_R\right), \tag{2.18}$$

which is called Majorana mass term. $m_L$ and $m_R$ denote the Majorana masses. In the most general form, Dirac and Majorana masses are included via the mass term

$$\mathcal{L}_{M,D} = \frac{1}{2}\left(\overline{\Psi}_L M\Psi_R^c + \overline{\Psi}_R^c M\Psi_L\right), \tag{2.19}$$

where $M$ is a $2 \times 2$ matrix

$$M = \begin{pmatrix} m_L & m_D \\ m_D & m_R \end{pmatrix}, \tag{2.20}$$

and $\Psi_{L,R} = \left(\psi_{L,R}\ \psi_{L,R}^C\right)^T$. Equation (2.19) can be generalized to $n$ neutrino flavors, by extending the mass matrix $M$ to $2n \times 2n$ and $\Psi_{L,R}$ to $2n$ components. In the case of $n = 1$ the mass eigenvalues $m_{1,2}$ of $M$ are given by

$$m_{1,2} = \frac{1}{2}\left[(m_L + m_R) \pm \sqrt{(m_L - m_R)^2 + 4m_D^2}\right], \tag{2.21}$$

and $|m_{1,2}|$ is used as mass for the neutrino fields. Thus, the physics of neutrinos is determined by the mass values $m_L$, $m_R$ and $m_D$. Different scenarios are possible:

- $m_L = m_R = 0$:

  Both Majorana eigenstates are degenerate in mass with $m_{1,2} = m_D$. They can be used to construct a Dirac field, so that an equivalent description is obtained, if only $\mathcal{L}_D$ is used. Therefore, a Dirac neutrino can be seen as a pair of degenerate Majorana neutrinos.

- $m_D \gg m_L, m_R$:

  In this case the neutrinos are called pseudo-Dirac neutrinos. They are almost degenerate in mass with $m_{1,2} \approx m_D$.

- $m_D = 0$:

  This is the case of two pure Majorana neutrinos with $m_1 = m_L$ and $m_2 = m_R$. The corresponding Majorana fields are $\phi_1 = \psi_L + \psi_R^C$ and $\phi_2 = \psi_R + \psi_L^C$.

- $m_L = 0,\ m_D \ll m_R$:

  The two neutrino fields have the mass eigenvalues $m_1 = m_D^2/m_R$ and $m_2 \approx m_R$. This scenario is favored by the so called seesaw model [Gel79, Yan80], which tries to include neutrino masses in Grand Unified Theories (GUT). The mass of all fermions is generated by coupling to the Higgs-boson, therefore the Dirac mass of neutrinos should be similar to those of charged leptons and quarks. Depending on the GUT model, $m_R$ can take values up to $10^{16}$ GeV $c^2$ [Zub98].

A promising way to distinguish Dirac and Majorana neutrinos experimentally, and one way of determining the neutrino mass, are neutrinoless double-beta transitions.

## 2.2 Neutrinoless double-beta transitions

A double-beta transition is a second-order weak-interaction process, which change the charge number $Z$ of a nuclide by two, while conserving the mass number $A$. They are rare since they have to compete with the common beta transitions of first order, which have much higher decay rates. Therefore, the single-beta transitions have to be forbidden or strongly suppressed for the double-beta transitions to occur. The mass differences of the involved nuclides determine whether the reactions are energetically allowed and can take place.

The first model to predict predict the masses or binding energies of all nuclides is the liquid-drop model, which was developed by Bethe and Weizsäcker. They created an empirical model which is based on the assumption that the attractive interaction between two nucleons has a short range, so that a nucleon can only interact with its neighboring nucleons in analogy to atoms or molecules in a liquid. A number of different models have been developed until now with different approaches, however the Bethe-Weizsäcker model matches the measured binding energies despite its lack of shell effects quite well. The binding energy of a nucleus $E_B$ according to Bethe and Weizsäcker consists of five terms [Wei35, Bet36]:

$$E_B = E_V - E_S - E_C - E_A - E_P, \tag{2.22}$$

the volume term $E_V$, the surface term $E_S$, the Coulomb term $E_C$, the asymmetry term $E_A$ and the pairing term $E_P$, which are described in the following.

It is assumed that the binding energy is proportional to the volume of the nucleus and that the nucleus is spherical. The radius of the nucleus $R$ is proportional to $A^{1/3}$, and therefore $E_V \propto A$.

The nucleons at the surface of the nucleus are interacting with less neighbors than the nucleons in the center, as a consequence their binding energy is reduced. This effect is taken into account by the surface term $E_S$, which scales with the magnitude of the surface $E_V \propto A^{2/3}$.

Since the protons in the nucleus are also interacting with the repulsive Coulomb interaction, the binding energy of the nucleus is further reduced by the Coulomb term $E_C$, which is proportional to $Z^2/A^{1/3}$. This term can be derived from electrostatics [Bet08].

The asymmetry term $E_A$ takes into account that the heavy nuclides require more neutrons in order to be stable. This term can be derived from a Fermi gas model of the nucleus and scales with $(N-Z)^2/A$.

The last term $E_P$, called pairing term, is in particular important for the thermal-neutron induced fission. It considers the fact that nuclides with an even number of protons and neutrons are bound stronger than nuclides which have "unpaired" nucleons, i.e. an odd number of protons or neutrons or both. The pairing term $E_P$ is

$$E_P = \delta A^{1/2}, \tag{2.23}$$

where the proportionality constant $\delta$ is 11.2 MeV/$c^2$ for even-even nuclides, 0 for even-odd nuclides and -11.2 MeV/$c^2$ for odd-odd nuclides.

For a constant mass number $A$ a parabola for the masses in $Z$ is obtained for the sum of the first four terms of the liquid drop model (see Eq. 2.22). For nuclides with odd $A$ the pairing term (see Eq. 2.23) is zero. Therefore, all nuclides with odd $A$ can decay towards the nuclide with charge number $Z_{min}$ at the minimum of the mass parabola, which is stable against beta decay. If $Z < Z_{min}$ the nuclides decay via $\beta^-$ transitions, otherwise for $Z > Z_{min}$ via $\beta^+$ decay or electron capture $\epsilon$.

If $A$ is even, there are two mass parabolas, one for odd-odd nuclides and one for even-even nuclides, that are separated by the pairing term. This is shown in Fig. 2.1, where the mass excesses

$$ME(Z,A) = M(Z,A) - A \text{ u} \tag{2.24}$$

of the nuclides with mass number $A = 124$ are shown. The nuclides $Z < 50$ and $Z = 51$ decay via $\beta^-$ decay, as discussed above. However, the $\beta^-$ decay of the even-even nuclide $^{124}$Sn ($Z = 50$) into the odd-odd nuclide $^{124}$Sb ($Z = 51$) is not allowed, since the energy release in the reaction, i.e. the reaction $Q$ value

$$Q_{\beta^-}(Z,A) = (M(Z,A) - M(Z+1,A))c^2 \tag{2.25}$$

is negative. This is caused by the larger mass of the daughter nuclide due to the pairing term. But, $^{124}$Sn can decay into the beta-stable $^{124}$Te ($Z = 52$) via the neutrino-accompanied ($2\nu\beta^-\beta^-$) or the neutrinoless ($0\nu\beta^-\beta^-$) double-$\beta^-$ decay:

$$(Z,A) \rightarrow (Z+2,A) + 2e^- \ (+\ 2\overline{\nu_e}), \tag{2.26}$$

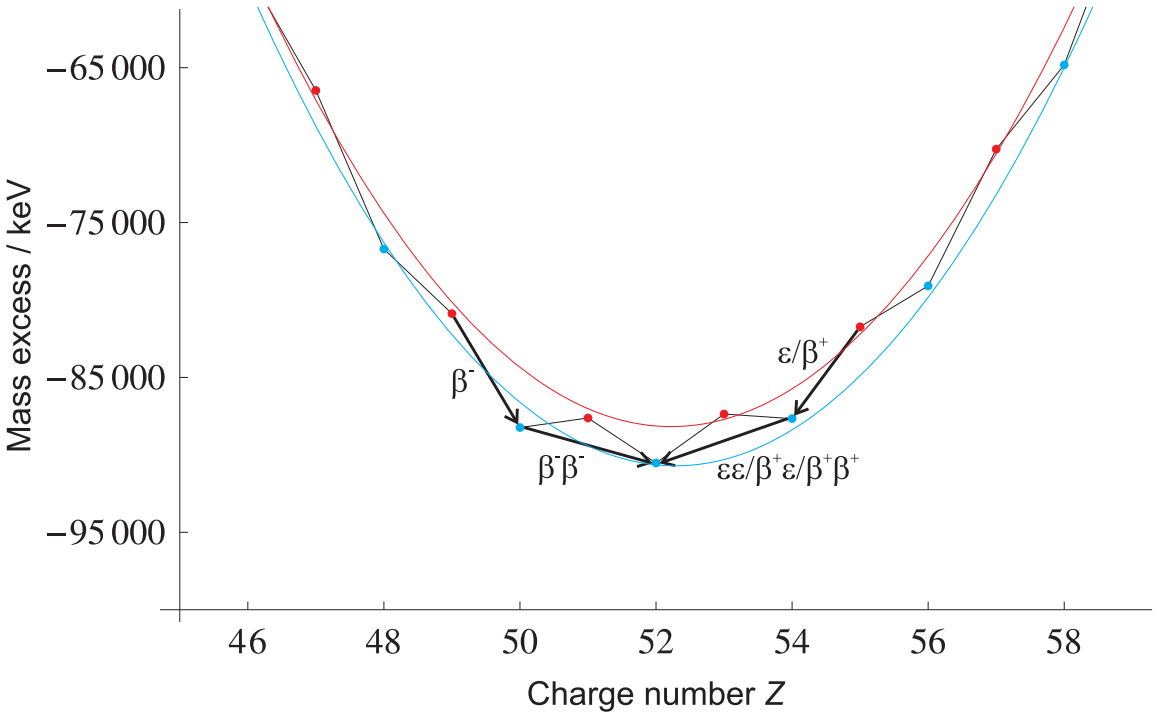


Figure 2.1: The mass excess of nuclides with $A$=124 [Aud03] as function of the charge number $Z$ is shown as light-blue points for even-even nuclides and as red points for odd-odd nuclides. The red and the blue line are fits of a second-order polynom to the odd-odd and even-even nuclides, respectively. The thick lines indicate the decay processes of the nuclides. Details are found in the text.

where two or no antineutrinos are emitted, respectively. In Fig. 2.2 (a) and (b) the decay schemas of the $2\nu\beta^-\beta^-$ and the $0\nu\beta^-\beta^-$ processes are shown. The process can be seen as the subsequent decay of two neutrons in the nucleus. The latter process requires the right-handed antineutrino emitted in the decay of the first neutron to be absorbed as left-handed neutrino in the decay of the second neutron. Therefore, the neutrinoless process requires the neutrino to be its own antiparticle and to have both helicity state components. Thus, the $0\nu\beta^-\beta^-$ process is not consistent with the Standard Model, and only allowed, if neutrinos are massive Majorana particles.

The reaction $Q$ value of the double-beta decay is given by

$$Q_{\beta^-\beta^-}(Z,A) = (M(Z,A) - M(Z+2,A))c^2, \tag{2.27}$$

and, in the case of $^{124}$Sn, it is positive (see Fig. 2.1), so that both decay modes are energetically allowed. Therefore, the conditions for a nuclide $(Z,A)$ to decay (primarily) via double-$\beta^-$ decay are:

$$M(Z,A) > M(Z+2,A), \tag{2.28}$$

and for practical reasons

$$M(Z,A) < M(Z+1,A), \tag{2.29}$$

since the decay of the nuclide is otherwise dominated by $\beta^-$ decay. Thus, only even-even nuclides are suitable to study the neutrinoless double-$\beta^-$ decay. In total, there

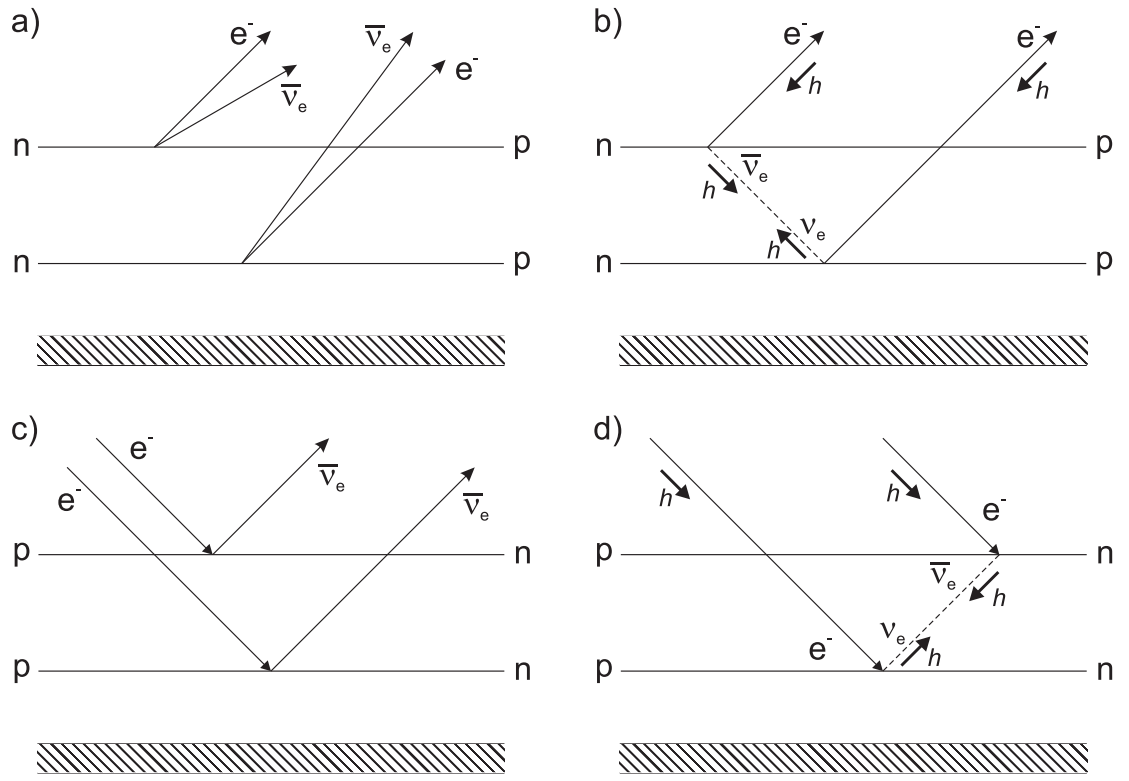


Figure 2.2: Decay schemes of the (a) $2\nu\beta^-\beta^-$, (b) the $0\nu\beta^-\beta^-$, (c) the $2\nu\epsilon\epsilon$, and (d) the $0\nu\epsilon\epsilon$ process. The dashed band symbolizes the remaining nucleons in the nucleus.

are 36 nuclides, which fulfill these conditions. A list of these nuclides can be found in Ref. [Böh92]. So far, only the neutrino-accompanied double-beta decay ($2\nu\beta^-\beta^-$) has been observed for several nuclides [Zub98], whereas there is only one questionable claim for the detection of the neutrinoless process ($0\nu\beta^-\beta^-$) [Kla04], but no clear evidence. $^{110}$Pd is one of the promising candidates for neutrino experiments due to its high $Q$ value. The $Q$ value of this nuclide was studied with TRIGA-TRAP within this thesis (see Chap. 7).

The nuclides on the neutron-deficient side of the mass parabola in Fig. 2.1 with $Z > 54$ and $Z = 53$ decay via $\epsilon$ or $\beta^+$ decay. It is important to mention, that the $Q$ value of the $\beta^+$ decay

$$Q_{\beta^+}(Z,A) = (M(Z,A) - M(Z-1,A) - 2m_e)c^2 = Q_\epsilon(Z,A) - 2m_e c^2 \qquad (2.30)$$

is reduced by 2 $m_e c^2$ compared to the electron-capture $Q$ value $Q_\epsilon(Z,A)$. Therefore, electron capture can take place also for mass differences between the mother and daughter nuclides smaller than 2 $m_e$, whereas the $\beta^+$ decay is not allowed.

For $^{124}$Xe ($Z = 54$) neither electron capture nor $\beta^+$ decay are allowed, since the daughter nuclide has a heavier mass than the mother nuclide, similar to the situation of $^{124}$Sn. A decay via a double-beta transition into the beta-stable $^{124}$Te is energetically possible. In this case six different decay modes are possible:

- Neutrino-accompanied ($2\nu\epsilon\epsilon$) and neutrinoless double-electron capture ($0\nu\epsilon\epsilon$):

$$(Z,A) + 2e^- \rightarrow (Z-2,A)\ (+\ 2\nu_e), \qquad (2.31)$$

with a $Q$ value given by:

$$Q_{\epsilon\epsilon}(Z,A) = (M(Z,A) - M(Z-2,A))c^2. \tag{2.32}$$

Decay schemes of these processes are shown in Fig. 2.2 (c) for the $(2\nu\epsilon\epsilon)$ in Fig. 2.2 (d) for the $(0\nu\epsilon\epsilon)$ process.

- A combination of electron capture and $\beta^+$ decay in the neutrino-accompanied $(2\nu\beta^+\epsilon)$ and neutrinoless $(0\nu\beta^+\epsilon)$ transition:

$$(Z,A) + e^- \rightarrow (Z-2,A) + e^+ \ (+\ 2\nu_e), \tag{2.33}$$

with a $Q$ value given by:

$$Q_{\beta^+\epsilon}(Z,A) = Q_{\epsilon\epsilon} - 2m_e c^2. \tag{2.34}$$

- Neutrino-accompanied $(2\nu\beta^+\beta^+)$ and neutrinoless double-$\beta^+$ decay $(0\nu\beta\beta)$:

$$(Z,A) \rightarrow (Z-2,A) + 2e^+ \ (+\ 2\nu_e), \tag{2.35}$$

with a $Q$ value given by:

$$Q_{\beta^+\beta^+}(Z,A) = Q_{\epsilon\epsilon} - 4m_e c^2. \tag{2.36}$$

The difference of the atomic masses of the mother and daughter nuclides $M(Z,A) - M(Z-2,A) = Q_{\epsilon\epsilon}(Z,A)/c^2$ determine which processes can take place. The double-$\beta^+$ decay requires a mass difference larger than $4m_e$, which is only the case for six nuclides, among them is the example $^{124}$Xe from Fig. 2.1 with $Q_{\epsilon\epsilon}(54,124) = 2864.4(2.4)$ keV. The double-$\beta^+$ decay is always accompanied by the $\beta^+\epsilon$ and the $\epsilon\epsilon$ mode, which require only a mass difference larger than $2m_e$ or zero, respectively. Since the requirements for these processes are less restrictive, there is a larger number of nuclides undergoing these decay processes.

As in the case of double-$\beta^-$ decay the neutrinoless processes are also not included in the Standard Model and require neutrinos to be massive Majorana particles. The decay rates of the $0\nu\beta^+\beta^+$ and the $0\nu\beta^+\epsilon$ transitions are lower compared to the $0\nu\beta^-\beta^-$ decay rate due to the smaller kinetic energy release and the Coulomb suppression of the positrons. Therefore, the detection of these processes is more challenging, since the half-lives of these processes are longer. However, the $0\nu\beta^+\epsilon$ process may be of interest to probe whether the neutrinoless transitions, if they occur at all, are dominated by Majorana masses or by right-handed currents [Hir94].

The $0\nu\epsilon\epsilon$ transition is in general not allowed, since energy and angular momentum conservation require the emission of additional particles [Doi93]. One of the proposed decay modes includes the emission of an additional photon:

$$(Z,A) + 2e^- \rightarrow (Z-2,A) + \gamma, \tag{2.37}$$

which also reduces the decay rate compared to the $0\nu\beta^-\beta^-$ decay, since it is a higher-order process. In particular, for $0^+ \rightarrow 0^+$ transitions with a $KK$-electron capture

this decay mode is also forbidden due to angular momentum conservation ($\Delta L = 1$).

Most neutrino experiments have so far been focused on the detection of the $0\nu\beta^-\beta^-$ decay, since the experimental conditions are more favorable, i.e. the expected decay rate is higher and the signature of the decay can be easily detected for neutrino experiments. However, the situation is different for the $0\nu\epsilon\epsilon$ process in the case of an energy degeneracy of the initial and final state of the transition, where the emission of an additional photon is not required. In this case, the transition is resonantly enhanced and the half-life can compete with the $0\nu\beta^-\beta^-$ decay. The opportunity to observe the $0\nu\epsilon\epsilon$ decay in resonantly enhanced transitions offers a different approach to probe the Majorana character of neutrinos. As discussed below, for neutrino experiments it is essential to know the $Q$ value precisely for these transitions to differentiate nuclides with resonant enhancement. In Chap. 7 the $Q$-value measurements of three double-electron capture nuclides $^{106}$Cd, $^{108}$Cd, and $^{184}$Os are presented. In the latter case, the $Q$ value was used to make a new estimate of the half-life. In this respect, the decay rates of the $2\nu\beta^-\beta^-$, $0\nu\beta^-\beta^-$, and $0\nu\epsilon\epsilon$ transitions are discussed in the following.

## Decay rates of double-beta transitions

The decay rate of double-beta transitions can be calculated by using Fermi's golden rule:

$$\frac{dW}{dt} = \frac{2\pi}{\hbar} M_{if}^2 \, \delta\left(E_f - E_i\right), \tag{2.38}$$

where $M_{if}$ is the matrix element of the $2\nu\beta^-\beta^-$ decay, and due to the discrete energy spectrum, the $\delta$ function containing the energy difference between the initial and final state $E_f - E_i$ is used. $M_{if}$ is in the case of $2\nu\beta^-\beta^-$ decay of second order:

$$M_{if} = \sum_m \frac{\langle f \left| H_{if} \right| m \rangle \langle m \left| H_{if} \right| i \rangle}{E_i - E_m}, \tag{2.39}$$

where $H_{if}$ is the weak interaction Hamiltonian operator. The transitions take place between the ground states of two even-even nuclides, which are $0^+ \rightarrow 0^+$ transitions. Therefore, they can be seen as two subsequent Gamow-Teller transitions via an intermediate state $|m\rangle$ with $J^P = 1^+$. Fermi transitions are strongly suppressed by isospin selection rules [Hax84]. An exact calculation of the decay rate $\lambda_{2\nu} = (T_{1/2}^{2\nu})^{-1} \cdot \ln(2)$ can be found in [Doi85, Böh92]. It can be expressed as

$$\left(T_{1/2}^{2\nu}\right)^{-1} = G^{2\nu}\left(Q, Z\right) \left| M_{GT}^{2\nu} + \frac{g_V^2}{g_A^2} M_F^{2\nu} \right|^2, \tag{2.40}$$

where $G^{2\nu}\left(Q, Z\right)$ is the phase space factor, $M_{GT}^{2\nu}$ and $M_F^{2\nu}$ the Gamow-Teller and Fermi nuclear matrix elements (NMEs), and $g_V$ and $g_A$ the vector and the axial-vector coupling constant. The decay rate depends strongly on the $Q$ value. In total, a polynom of eleventh order in $Q$ is obtained. Thus, the $Q$ value determines strongly the magnitude of the decay rate, since $(T_{1/2}^{2\nu})^{-1} \propto Q^{11}$.

In the neutrinoless case, the decay rate is obtained in a similar way. In addition to the $2\nu\beta^-\beta^-$ decay an additional propagator for the exchange of the virtual neutrino

has to be considered, so that Fermi transitions can also occur [Mut88]. The decay rate $(T^{0\nu}_{1/2})^{-1}$can be written as:

$$\left(T^{0\nu}_{1/2}\right)^{-1} = G^{0\nu}\left(Q,Z\right)\left|M^{0\nu}_{GT} - M^{0\nu}_{F}\right|^2 \left(\frac{\langle m_{\nu_e}\rangle}{m_e}\right)^2, \tag{2.41}$$

where $G^{0\nu}\left(Q,Z\right)$ is the phase space factor, which scales in this case with $Q^5$, $M^{0\nu}_{GT}$ and $M^{0\nu}_{F}$ are the Gamow-Teller and Fermi NMEs, and

$$\langle m_{\nu_e}\rangle = \left|\sum_i U^2_{ei} m_i\right| \tag{2.42}$$

the effective electron neutrino mass. Thus, if the $0\nu\beta^-\beta^-$ decay rate can be experimentally determined, it could be used to derive the electron neutrino mass.

In both cases, the decay rates depend strongly on the $Q$ value, scaling with $Q^{11}$ and $Q^5$, respectively. Therefore, nuclides with larger $Q$ values ($Q > 2$ MeV) are favored in neutrino experiments. There are 11 nuclides in total, which fulfill this condition [Böh92]. One of these nuclides is $^{110}$Pd for which a $Q$-value measurement has been performed in this thesis. A precise $Q$ value can be used for the prediction of the half-life, and in case of a successful measurement of the $0\nu\beta^-\beta^-$ decay rate for a precise determination of $\langle m_{\nu_e}\rangle$.

The transition rates of double-electron capture can also be derived by second-order perturbation theory [Ber83, Suj04] or it can be obtained by treating the two states that are degenerate in energy as oscillating system, where the atom oscillates between the ground-state of the mother nuclide and an excited state in the daughter nuclide [Kri11]. Both methods obtain the same result for the decay rate:

$$\left(T^{0\nu}_{1/2}\right)^{-1} = \frac{1}{\ln(2)} \frac{V^2 \Gamma_{2h}}{((M_i - M_f)c^2)^2 + \frac{1}{4}\Gamma^2_{2h}}, \tag{2.43}$$

where $V$ denotes the transition potential, $M_i$ and $M_f$ the masses of the initial and final nuclear states and $\Gamma_{2h}$ the width of the final state in the daughter nucleus, which can be approximated by the width of the two electron hole state, since the width of the nuclear excited state is at least one order of magnitude smaller in most of the cases. The mass difference, which is also often expressed as the excess energy $\Delta$, can be written as:

$$\Delta = \left(M_i - M_f\right) c^2 = Q_{\epsilon\epsilon} - B_{2h} - E_\gamma, \tag{2.44}$$

by using the double-electron capture $Q$ value $Q_{\epsilon\epsilon}$, the energy of the two hole electron state in the daughter nuclide $B_{2h}$, and the nuclear excitation energy of the daughter nuclide $E_\gamma$. The transition rate has a maximum, if the initial and final state are degenerate in energy, which means $\Delta = 0$. In this case the transition has the highest decay rate

$$\left(T^{0\nu}_{1/2}\right)^{-1}_{min} = \frac{4V^2}{\ln(2)\Gamma_{2h}}, \tag{2.45}$$

and the transition is resonantly enhanced up to a factor in the range of $10^4$ to $10^6$ compared to the non-resonant case. A less restrictive requirement for resonant enhancement is the condition

$$\Delta < \Gamma_{2h}, \tag{2.46}$$

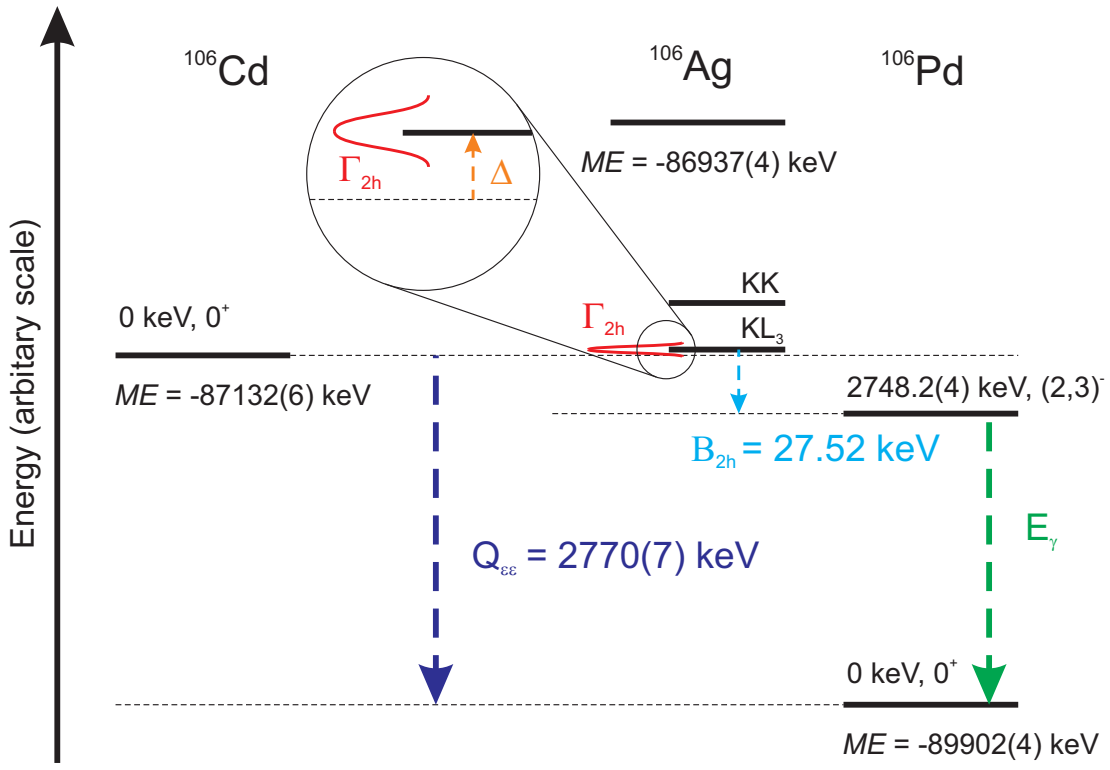


Figure 2.3: Level scheme for the double-electron capture in $^{106}$Cd. The energies in equation (2.44) for the resonance condition are shown, i.e. the double-electron capture $Q$ value $Q_{\epsilon\epsilon}$ = 2770(7) keV, the nuclear excitation energy $E_\gamma$ = 2748.2(4) keV, and the atomic excitation energy of the two-electron hole state $B_{2h}$ = 27.52 keV, as well as the sum of the widths of two-electron hole state and the excited nuclear state $\Gamma_{2h}$ = 8 eV and the excess energy $\Delta$ = -0.33(41) keV. The mass excess values were taken from Ref. [Aud03], all other values from Ref. [Gon11].

which still requires a precise determination of $\Delta$ with an uncertainty as low as a few 10 eV, which is a typical value for $\Gamma_{2h}$. The resonance condition is illustrated in Fig. 2.3 with a level scheme of the nuclide $^{106}$Cd as example, which was one of the nuclides investigated in this thesis. The uncertainty of $\Delta$ is often limited by the precision of $Q_{\epsilon\epsilon}$, which is known with an uncertainty of a few keV typically. The nuclear and atomic excitation energies are usually known with higher precision. Therefore, precise measurements of $Q_{\epsilon\epsilon}$ improve the uncertainty of $\Delta$ and can contribute to the identification of resonantly enhanced transitions.

Several transitions have already been investigated by other experiments, such as $^{74}$Se $\rightarrow$ $^{74}$Ge [Mou10], $^{136}$Ce $\rightarrow$ $^{136}$Ba [Kol11], $^{152}$Gd $\rightarrow$ $^{152}$Sm [Eli11b], and $^{156}$Dy $\rightarrow$ $^{156}$Gd [Eli11a]. The results of the $Q_{\epsilon\epsilon}$ measurements of the transitions $^{106}$Cd $\rightarrow$$^{106}$Pd, $^{108}$Cd $\rightarrow$$^{108}$Pd, and $^{184}$Os $\rightarrow$$^{184}$W, obtained at the TRIGA-TRAP mass spectrometer (see Chap. 5) are presented in this thesis (see Chap. 7). The aim of these measurements was to investigate the resonance condition in equation (2.46) by reducing the uncertainty of $\Delta$ with a direct measurement of the mass difference $M(A,Z) - M(A,Z-2)$.

The transition potential $V$ in equation (2.43) is required to calculate the half-life

of the transition, which is given by:

$$V_{\alpha\beta}\left(J_f^\pi\right) = \frac{1}{4\pi} G_F^2 \cos(\theta_C)^2 \left\langle m_{\nu_e} \right\rangle \frac{g_A^2}{R} \sqrt{2J_f + 1} A_{\alpha\beta} M^{0\nu}\left(J_f^\pi\right), \tag{2.47}$$

where $G_F$ denotes the Fermi coupling constant, $\theta_C$ the Cabbibo angle, $R$ the nuclear charge radius, and $M^{0\nu}(J_f^\pi)$ the NME of the transition. $\alpha$ and $\beta$ summarize the quantum numbers $(n_\alpha j_\alpha l_\alpha m_\alpha)$ and $(n_\beta j_\beta l_\beta m_\beta)$ of the captured electrons, and $A_{\alpha\beta}$ are the lepton factors averaged over the nuclear volume. $V$ is also proportional to the effective neutrino mass $\langle m_{\nu_e} \rangle$ given in equation (2.42). Thus, the neutrino mass can be also derived from a measurement of the $0\nu\epsilon\epsilon$ decay rate.

The NME has to be calculated by theory in order to estimate the half-life, and it is the most uncertain part in equation (2.47). Two approaches have been recently applied for the calculation of double-beta transition NMEs. The calculation with the proton-neutron Quasiparticle Random Phase Approximation (QRPA) [Rod03a, Sim08] and the energy density functional (EDF) method [Rod10a, Rod11]. The main difference between the methods is that QRPA assumes a spherical symmetry, whereas the EDF method includes quadrupole deformation. On the contrary, the EDF method does not include quasiparticle excitations and certain symmetry breaking effects [Rod10a]. The EDF method has been used to calculate the NME for the transition $^{184}$Os $\rightarrow$ $^{184}$W, in order to reevaluate the half-life of this process (see Chap. 7 and [Smo12b]).

## Double-beta experiments

The detection of the double-beta decay is challenging due to its long half-life. Several approaches have been followed to determine the half-life experimentally. Direct counting experiments are a promising method, since they can distinguish between the $2\nu\beta^-\beta^-$ and the $0\nu\beta^-\beta^-$ decay. A large source and a low background is essential for such an experiment. The best result for the lower limit of the half-life of the $0\nu\beta^-\beta^-$ decay has been obtained in direct counting experiments with $^{76}$Ge by the Heidelberg-Moscow experiment [Kla01], which was running from 1990-2003. The advantage is that germanium as semiconductor can be used as source and detector with a high energy resolution at the same time. In this case 11 kg germanium enriched in $^{76}$Ge were used. The two simultaneously emitted electrons are detected and the sum of their kinetic energies is recorded as shown in the energy spectrum in Fig. 2.4 (a). The $2\nu\beta^-\beta^-$ process has a continuous energy distribution, since the two emitted neutrinos are not detected. The half-life has been determined with more than 50000 events to be $T_{1/2}^{2\nu} = 1.55 \pm 0.01^{+0.91}_{-0.15} \times 10^{21}$ years [Kla01].

In the neutrinoless transition $0\nu\beta^-\beta^-$ the sum energy of the two electrons would be identical to the $Q$ value of this reaction. Thus, the $0\nu\beta^-\beta^-$ process would be identified in the energy spectrum by a mono-energetic line at the position of the $Q$ value. Therefore, a precise determination of the $Q$ value with an uncertainty in the order of 1 keV helps to identify the $0\nu\beta^-\beta^-$ signal. In the first evaluation of the data, no $0\nu\beta^-\beta^-$ signal was obtained in the peak region and the lower limit for the half-life is $T_{1/2}^{0\nu} > 1.9 \times 10^{25}$ years, which corresponds to an upper limit of $\langle m_{\nu_e} \rangle < 0.35$ eV / $c^2$. A subgroup of the experiment has reevaluated the data and claims to

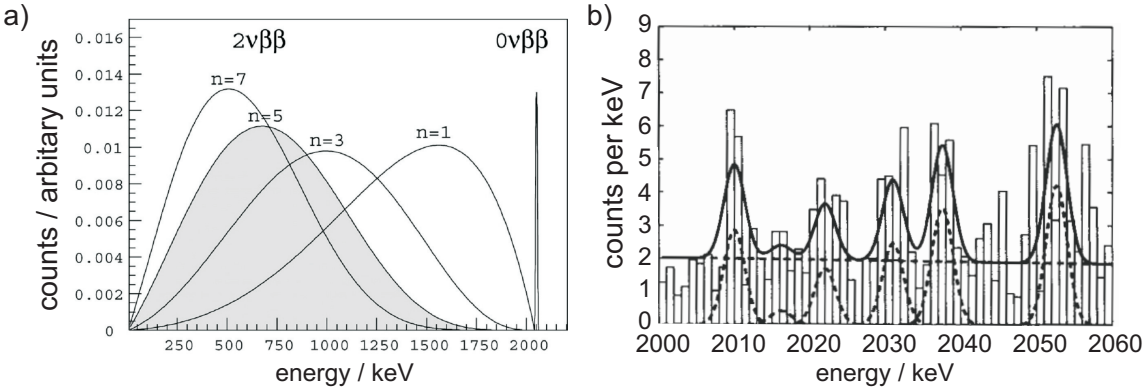


Figure 2.4: (a) Theoretical double-beta decay energy spectrum for $^{76}$Ge [Zub04a]. The counts are shown as function of sum energy of the two emitted electrons. The gray filled curve ($n = 5$) shows the continuous energy spectrum of the $2\nu\beta\beta$ decay. The mono-energetic line at 2039 keV is the signal of the $0\nu\beta\beta$ decay. The other curves belong to other decay modes discussed in [Zub04a]. (b) Experimentally measured energy spectrum by the Heidelberg-Moscow experiment for the double-beta decay of $^{76}$Ge in the region where the $0\nu\beta\beta$ signal is expected [Kla04].

have found a signal with $T^{0\nu}_{1/2} = 0.6$ - $7.3 \times 10^{25}$ years, which would imply a neutrino mass of $\langle m_{\nu_e} \rangle = 0.2$ - 0.6 eV / $c^2$ [Kla04]. Fig. 2.4 (b) shows the reevaluated energy spectrum of the Heidelberg-Moscow experiment in the region, where the $0\nu\beta^-\beta^-$ signal is expected ($Q_{\beta^-\beta^-} = 2039.061(7)$ keV [Mou10]). However, there is no unambiguous result, and therefore a new counting experiment with $^{76}$Ge, called GERDA [Sch05], has been started to clarify this matter.

Other methods for the detection of the double-beta decay are geochemical or radiochemical experiments. The former method measures the isotropic anormally of double-beta decay daughter nuclides in old ores, which have been accumulated for a long time. This method is used only for selenium and tellurium ores, which decay into noble gases, so that the expected small anormally can be detected in a mass spectrometer [Kir86]. The latter method takes advantage of the radioactive decay of the daughter nuclide to detect the double-beta transition. There are two suitable transitions, $^{232}\text{Th} \rightarrow {}^{232}\text{U}$ and $^{238}\text{U} \rightarrow {}^{232}\text{Pu}$, where the $\alpha$ particle of the daughter nuclide is being detected. The $2\nu\beta^-\beta^-$ half-life of $^{238}$U was determined with this method [Tur91]. However, these methods are not suited to distinguish the neutrinoless from the neutrino-accompanied decay. Therefore, the Majorana character of neutrinos can only be revealed in direct counting experiments.

In summary, the double-$\beta^-$ decay has been investigated and the $2\nu\beta^-\beta^-$ process has been observed for several nuclides, whereas for the $0\nu\beta^-\beta^-$ signal there is no unambiguous result [Zde02]. Compared to this, few attempts have been made to search for the double-electron capture, since the half-life is expected to be longer and the detection of this process is more challenging. Double-electron capture has not been experimentally observed yet. One nuclide which has been investigated in several experiments is $^{106}$Cd [Zub01, Ruk11, Bel11]. The following experimental signatures can be used to detect the double-electron capture: X-rays (21 keV in the

case of $^{106}$Cd) or Auger electrons from the deexcitation of the electron shell in the daughter nucleus, photons carrying away the excess energy $\Delta$, and in case of $\beta^+\beta^+$ or $\beta^+\epsilon$ transitions, photons from the positron annihilation. The limits obtained for the double-electron transitions are $T^{2\nu}_{1/2} > 3.6 \times 10^{20}$y for the $2\nu\epsilon\epsilon$ transition to the nuclear ground state in $^{106}$Pd, and $T^{0\nu}_{1/2} > 1.1 \times 10^{20}$y for the $0\nu\epsilon\epsilon$ transition to the excited state with 2741.0 keV excitation energy, which was expected to be the state with the smallest $\Delta$. The experiments on $^{106}$Cd yield the best experimental value for the restriction of the half-life of double-electron capture processes. The $Q$ value of double-electron capture in $^{106}$Cd has been studied in this thesis, and the resonant enhancement in this nuclide is discussed in detail in Chap. 7, but a resonant enhancement to this state is excluded due to the measurement presented here and in other recent $Q$-value measurements [Gon11].

In case the transition goes to an excited state a coincident detection of $\gamma$-rays from the deexcitation of the daughter nucleus can be used as well to detect the $0\nu\epsilon\epsilon$ process [Kri11]. Due to the small phase space for the two neutrinos in the $2\nu\epsilon\epsilon$ transition, the neutrino-accompanied transition to the excited state is strongly suppressed if $\Delta$ is smaller than 1 keV. The phase space factor in the $2\nu\epsilon\epsilon$ process scales also with the fifth power of the excess energy $\Delta^5$.

Precise measurements of double-beta transition $Q$ values can contribute to neutrino experiments in the following ways:

- The peak position in the two-electron energy spectrum of the $0\nu\beta^-\beta^-$ transition can be independently determined.
- Accurate predictions of double-beta transition half-lives are possible. In particular, resonantly-enhanced double-electron capture transitions can be identified.
- The electron neutrino mass $\langle m_{\nu_e} \rangle$ can be determined from a measurement of the decay rate, if the $Q$ value is well known (see equations (2.41), (2.43) and (2.44)). The uncertainty of $\langle m_{\nu_e} \rangle$ is limited by the nuclear matrix elements, which have to be calculated by theory, and also require the $Q$ value as input parameter.

# Chapter 3

# Mass and $Q$-value measurements with Penning traps

Mass spectrometry is a technique which is used to separate particles of different masses on an atomic or molecular scale and to determine the masses of these particles. Thus, the quality of a mass spectrometer can be characterized by two parameters: the mass resolving power $R = m/\Delta m$ and the relative uncertainty of the mass measurement $\delta m/m$. $\Delta m$ denotes the lowest mass difference which can be resolved and $\delta m$ the uncertainty of the measurement.

The first mass measurement was performed in the year 1897, when J.J. Thompson determined the mass-to-charge ratio of the electron [Tho97a], which marks the beginning of mass spectrometry in physics. Since that time many efforts have been made to develop new mass spectrometers with higher mass resolving power and lower uncertainty. Nowadays, the type of mass spectrometer which is leading in both of these physical quantities is the Penning trap, which can store charged particles in a superposition of a strong homogeneous magnetic and a weak quadrupolar electric field. The Penning makes advantage of the particle confinement, which enhances the observation time, and the fact that the mass measurement is converted into a frequency measurement. Frequency is a quantity that can be determined with highest precision. Compared to other mass spectrometers such as sector-field or time-of-flight mass spectrometers the mass measurement in a Penning trap is completely decoupled from the initial ion motion. Therefore, high-precision measurements are possible [Bla06]. Mass resolving powers of up to $R = 10^7$ [Bla04] and relative uncertainties $\delta m/m$ of $10^{-11}$ and below [Rai04, Red09] can be reached. Therefore, the Penning trap is the tool of choice for high-precision mass measurements with a variety of applications in atomic, nuclear, nuclearastro and particle and physics[1].

In the context of this thesis atomic masses and $Q$ values, i.e. differences of atomic masses given by the equations (2.27) and (2.32), were determined by measuring the

[1] A second method, which has been also successfully applied to determine mass values with high precision, is mass spectrometry in storage rings, where the mass measurement is based on measuring the revolution frequency []. Two different approaches can be used: the Schottky mode, where the velocity spread of the ions is cooled to zero, and Isochronous mode, where the revolution frequency becomes independent of the particle velocity. The latter one allows to study nuclides with half-lives below 1 ms.

cyclotron frequency

$$\nu_c = \frac{1}{2\pi}\frac{qB}{m} \tag{3.1}$$

of trapped ions with the Penning-trap mass spectrometer TRIGA-TRAP. In particular, the time-of-flight ion-cyclotron-resonance method (TOF-ICR) was used to determine the cyclotron frequency. The intention of this chapter is to introduce the measurement procedure for the results presented in Chap. 7. Therefore, the basic principles of a Penning trap, as well as the TOF-ICR method are described. A detailed discussion of Penning traps and their application in mass spectrometry is found for example in the references [Bro86, Bla06].

## 3.1 Basic principles of a Penning trap

The confinement of a charged particle in a Penning trap is achieved in a superposition of a strong homogeneous magnetic field $\vec{B} = B\hat{e_z}$, which defines the main axis of the trap, and a weak quadrupolar electrostatic field. The magnetic field provides the radial and the electric field the axial confinement. The electric field is ideally created by hyperbolically-shaped trap electrodes: two endcaps and a ring electrode. A sketch of a Penning trap is shown in Fig. 3.1. The electric potential in the trap is given by

$$V(x,y,z) = V_0\frac{2z^2 - x^2 - y^2}{d^2}, \tag{3.2}$$

where $V_0$ is the potential difference between the ring and the endcaps and $d$ the geometry parameter of the trap. For a trap with hyperbolic electrodes, as shown in Fig. 3.1(a), $d$ is given by

$$d^2 = z_0^2 + \frac{1}{2}r_0^2, \tag{3.3}$$

where $z_0$ and $r_0$ are the minimal axial and radial distances from the trap center to the electrode. Cylindrical traps, as shown in Fig. 3.1(b), provide a quadrupolar field in a region around the trap center. $d$ can be determined for cylindrical traps numerically calculating the trap potential for a given electrode configuration.

The equations of motion of a charged particle in a Penning trap can be obtained by solving the Euler-Lagrange equations of the Lagrange function for a time-independent electric and magnetic field [Kre92a]. The generalized potential for the Lagrangian is

$$\Phi(\vec{x},\dot{\vec{x}}) = qV(\vec{x}) - \frac{qB}{2}\dot{\vec{x}}\cdot\vec{\rho}\times\hat{e_z}, \tag{3.4}$$

where $V(\vec{x})$ is given by equation (3.2), and $\vec{\rho}$ is the radial vector $(x,y,0)$. The Lagrange function is given by

$$L(\vec{x},\dot{\vec{x}}) = \frac{1}{2}m\dot{\vec{x}}^2 - \frac{qV_0}{4d^2}\left(2z^2 - (x^2+y^2)\right) - \frac{m\omega_c}{2}\left(\dot{x}y - x\dot{y}\right). \tag{3.5}$$

The solution of the Euler-Lagrange equations can be found in [Bro86, Kre92a]. It can be described by a superposition of three harmonic eigenmotions, one axial motion with the eigenfrequency $\nu_z$, and two radial motions: the modified cyclotron motion

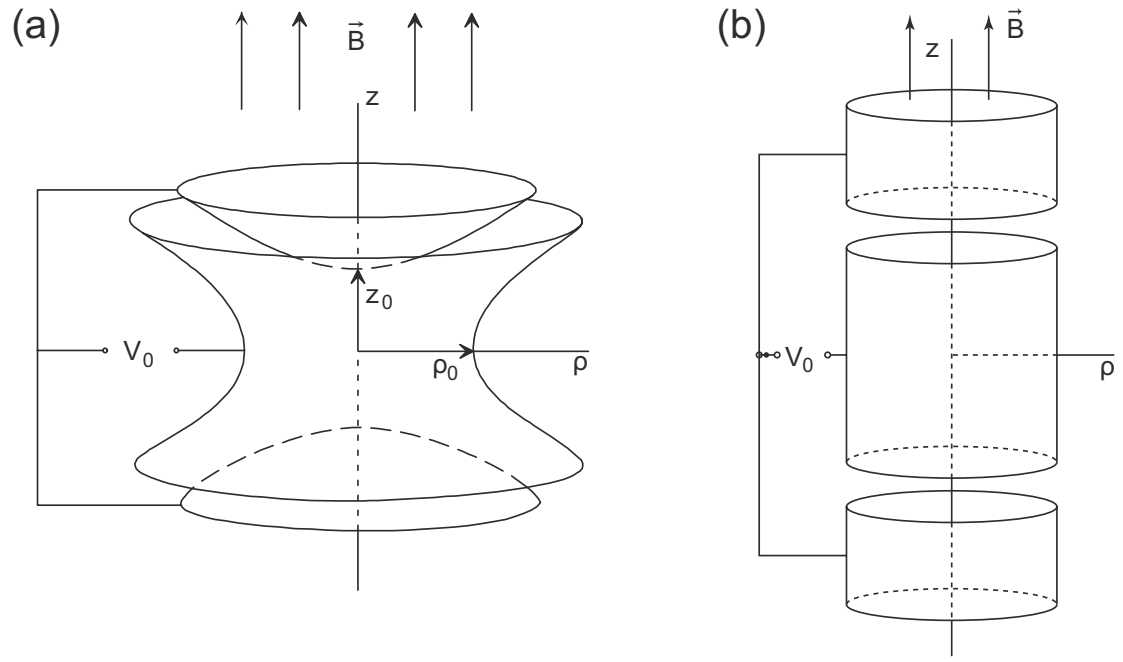


Figure 3.1: Electrode configurations of Penning traps are shown for a hyperbolic trap (a) and a cylindrical trap (b). The electrode configuration consists in both cases of a ring electrode in the center and an endcap electrode at the top and at the bottom.

with eigenfrequency $\nu_+$, which is a modification of the cyclotron motion caused by the presence of the electric field, and the magnetron motion with the eigenfrequency $\nu_-$, which is a slow ($\vec{E}\times\vec{B}$)-drift motion around the trap center. The eigenfrequencies of the three eigenmotions are given by the following equations:

$$\nu_z = \frac{1}{2\pi}\sqrt{\frac{qU_0}{md^2}}, \tag{3.6}$$

$$\nu_+ = \left(\frac{\nu_c}{2} + \sqrt{\frac{\nu_c^2}{4} - \frac{\nu_z^2}{2}}\right) \approx \nu_c - \frac{V_0}{4\pi d^2 B}, \tag{3.7}$$

$$\nu_- = \left(\frac{\nu_c}{2} - \sqrt{\frac{\nu_c^2}{4} - \frac{\nu_z^2}{2}}\right) \approx \frac{V_0}{4\pi d^2 B}. \tag{3.8}$$

An ion motion in a Penning trap is shown in Fig. 3.2.

A closed orbit is only obtained if the radicands in equations (3.6)-(3.8) are positive. Thus, the polarity of the electric field has to be chosen such that the $z$-component of the electric force points towards the trap center ($qV_0 > 0$) and the magnetic field strength $B$ has to be large enough to compensate the electric field in the radial direction, which would otherwise drive the particle out from the trap center. The constraint on $B$ is

$$B > \sqrt{\frac{2mV_0}{qd^2}}. \tag{3.9}$$

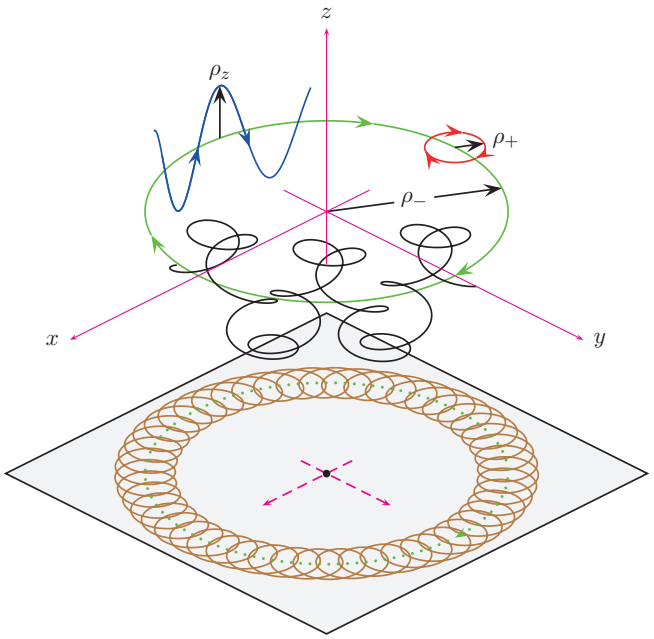


Figure 3.2: The three eigenmotions of a charged particle in a Penning trap are shown individually: The modified cyclotron motion is shown in red, the magnetron motion in green, and a superposition of the axial and magnetron motion in blue. $\rho_+$, $\rho_z$ and $\rho_-$ are the respective motional amplitudes. The ratios of the eigenfrequencies $\nu_+ : \nu_z : \nu_-$ is 50 : 10 : 1. The superposition of all three eigenmotions is shown in black. The projection in the (x,y)-plane shows the superposition of the two radial motions in brown and the magnetron motion as dotted green line [Ket09b].

The following relations hold for an ideal trap and are important in respect to mass spectrometry:

$$\nu_c = \nu_+ + \nu_-, \tag{3.10}$$

$$\nu_c^2 = \nu_+^2 + \nu_-^2 + \nu_z^2, \tag{3.11}$$

$$2\nu_+\nu_- = \nu_z^2. \tag{3.12}$$

Furthermore, the magnitudes of the eigenfrequencies follow the order

$$\nu_c \approx \nu_+ > \nu_z > \nu_-, \tag{3.13}$$

as becomes obvious from Fig. 3.3, where typically eigenfrequencies for TRIGA-TRAP as function of the atomic mass number $A$ for singly-charged ions and $B$ = 7 T and $V_0$ = 7 V are shown. For the measurement techniques described in Sect. 3.2 it is of particular importance that the reduced cyclotron frequency $\nu_+$ is at least two orders of magnitude larger than the magnetron frequency $\nu_-$. $\nu_-$ is in general almost mass-independent, as shown in the approximation in equation (3.8).

Since only the cyclotron frequency $\nu_c$ scales directly with the mass $m$ of the ion of interest, $\nu_c$ needs to be determined in the Penning trap. However, the cyclotron motion is not an eigenmotion of the particle and the cyclotron frequency cannot be observed directly. The equations (3.10) and (3.11) hold the relations between the eigenfrequencies of the charged particle and the cyclotron frequency that are used

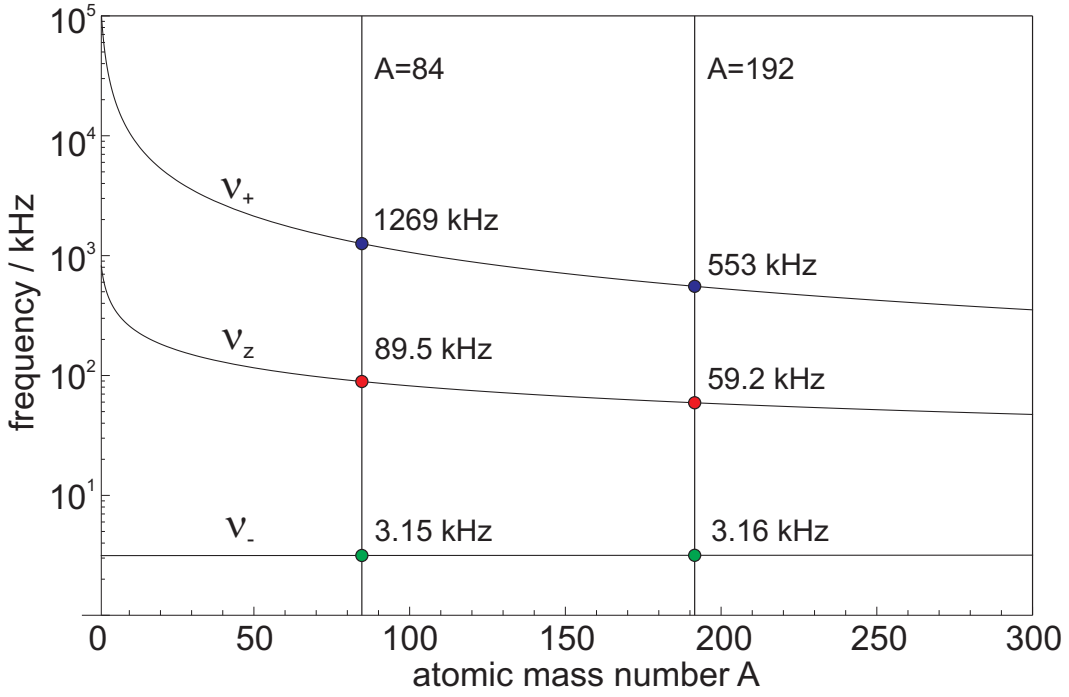


Figure 3.3: Eigenfrequencies in a Penning trap as function of the atomic mass number $A$ are shown on a logarithmic scale for the TRIGA-TRAP precision trap (see Chap. 5) with the parameters $B = 7$ T, $V_0 = 7$ V, $d = 5.03$ mm. The frequency values for the lightest ($A = 84$) and heaviest ($A = 192$) mass investigated in this thesis are given.

to derive $\nu_c$ from a measurement. Equation (3.11) is also true for a non-ideal trap and is therefore referred to as invariance theorem [Gab09], with $\nu_c^2 = \hat{\nu}_+^2 + \hat{\nu}_-^2 + \hat{\nu}_z^2$, where $\hat{\nu}_+$, $\hat{\nu}_-$, and $\hat{\nu}_z$ are the perturbed eigenfrequencies.

Another important fact about the magnetron motion is its energy contribution to the total energy. This can be seen from the Hamiltonian for the ion motion of a spinless particle, which can be derived from equation (3.5). By using the canonical momenta one obtains [Kre92a]:

$$H = \frac{1}{2m}\left(p_x^2 + p_y^2 + p_z^2\right) - \frac{\omega_c}{2}\left(xp_y - p_x y\right) + \frac{m\omega_1^2}{8}\left(x^2 + y^2\right) + \frac{m\omega_z^2}{2}z^2, \qquad (3.14)$$

where $\omega_1^2 = 1/2\sqrt{\omega_c^2 - 2\omega_z^2}$. The Cartesian coordinates and momenta can be replaced by the following expressions:

$$q_{+/-} = -\frac{1}{\sqrt{2}}\left(-\sqrt{\frac{m\omega_1}{2}}x \pm \sqrt{\frac{2}{m\omega_1}}p_y\right), \qquad (3.15)$$

$$p_{+/-} = \frac{1}{\sqrt{2}}\left(\pm\sqrt{\frac{m\omega_1}{2}}y + \sqrt{\frac{2}{m\omega_1}}p_x\right), \qquad (3.16)$$

for the radial motions, and by $q_3 = \sqrt{m\omega_z}z$ and $p_3 = 1/\sqrt{m\omega_z}p_z$ for the axial motion. Thereby the Hamiltonian becomes:

$$H = \frac{\omega_+}{2}\left(q_+^2 + p_+^2\right) - \frac{\omega_-}{2}\left(q_-^2 + p_-^2\right) + \frac{\omega_z}{2}\left(q_3^2 + p_3^2\right). \qquad (3.17)$$

Here, it becomes obvious that the contribution of the magnetron motion to the total energy is negative. Therefore, a charged particle in a Penning trap is a metastable system, since the energy can be decreased by increasing the magnetron radius. This is in particular important for the buffer-gas cooling technique described in Sect. 3.2.

The Hamiltonian (3.17) can also be used to develop a quantum mechanical description of the motion by introducing creation and annihilation operators for the three eigenmotions. A description of the Penning trap as a quantum mechanical system can be found in [Bro86, Kre92a, Geo05, Ket10b].

In order to derive a mass value from a cyclotron frequency measurement, it is necessary to determine the magnetic field strength $B$ with the same precision as the cyclotron frequency. This is done by calibrating the magnetic field with a cyclotron frequency measurement under identical conditions with an ion species with a well-known reference mass $m_{ref}$. In case of singly-charged ions, the mass $m_{ion}$ of the ion of interest is obtained by using:

$$m_{ion} = (m_{ref} - m_e)\,\frac{\nu_{c,ref}}{\nu_{c,ion}} + m_e, \tag{3.18}$$

where $m_e$ denotes the electron mass, and $\nu_c$(ref) and $\nu_c$(ion) the cyclotron frequencies of the reference ion and the ion of interest. $Q$ values of double-beta transitions (see equation (2.27) and (2.32)) can either be determined by two individual mass measurements of the mother and daughter nuclides, respectively, or by measuring the ratio of the cyclotron frequency of the mother nuclide $\nu_c$(M) and daughter nuclide $\nu_c$(D), and the $Q$ value is obtained via

$$Q/c^2 = (m_{\mathrm{M}} - m_e)\left(1 - \frac{\nu_c(\mathrm{M})}{\nu_c(\mathrm{D})}\right), \tag{3.19}$$

where $m_{\mathrm{M}}$ denotes the atomic mass of the mother nuclide. This method has the advantage that only one frequency ratio needs to be determined for the $Q$-value measurement. The uncertainty of the $Q$ value is mainly determined by the uncertainty of the frequency ratio, since $(1 - \nu_c(\mathrm{M})/\nu_c(\mathrm{D}))$ is a small value due to the similar cyclotron frequencies of the isobaric mother and daughter nuclides. Therefore, the uncertainty contribution of $M_{\mathrm{M}}$ is small compared to the one of the cyclotron frequency ratio. Note, that this measurement reveals only the mass difference of the two nuclides and not the absolute masses.

## 3.2 Imperfections of a real Penning trap

In a real Penning trap distortions that affect the frequency measurement due to imperfections are inevitable. Distortions of the electric and magnic fields have been neglected in the last chapter. In a real Penning trap, the ideal hyperbolic shape of the trap electrodes cannot be realized, since the electrodes have a finite size, a hole in each endcap electrode for injection and ejection of the ions, and slits for the the segmentation of the trap electrodes, which are necessary for the ion excitation as discussed below. Further distortions of the electric field may arise from surface potentials and from the manufacturing and assembling precision. The

magnetic field for the Penning trap is created by a superconducting magnet, which has only a limited region with a high field homogeneity. In addition, the magnetic susceptibilities of the materials in the trap tube, such as the vacuum tube and the trap electrodes, perturb the magnetic field. These field distortions manifest themselves in shifts of the eigenfrequencies that depend on the motion amplitudes [Bro86, Bol90]. Furthermore, frequency shifts are caused by a misalignment of the trap axis with respect to the magnetic field, by an elliptic distortion of the electric field [Bro86, Gab09], by relativistic effects [Ber02], and by Coulomb interaction with other ions in the trap [Bol92, Kön95].

The TOF-ICR method, which was used for the cyclotron frequency measurements in this thesis, obtains the cyclotron frequency via equation (3.10), which is in principle only valid in an ideal Penning trap. The sum frequency $\nu_+ + \nu_-$ is sensitive to frequency shifts, thus the measured frequency may differ from the true cyclotron frequency $\nu_c$. The invariance theorem (3.11) is also valid for small misalignments of the trap axis and elliptic field distortions in a real Penning trap, and therefore, it should hold up to a higher level of precision [Gab09]. In the following, most relevant origins of frequency shifts are discussed. Furthermore, it is discussed how the validity of equation (3.10) can be experimentally verified.

## Electric field imperfections

The perturbations of the electric field can be expressed by expanding the potential in Legendre polynoms:

$$V(r,\theta) = \sum_l \frac{V_0}{2z_0^l} r^l C_l P_l(\cos\theta), \tag{3.20}$$

where $C_l$ is the dimensionless multipole coefficient. The ideal potential has $C_2 = 1$ and $C_l = 0$ for $l \neq 2$. For the expansion of the potential, axial symmetry and mirror symmetry about the $z = 0$ plane was assumed. Therefore, only Legendre polynoms with $m = 0$ and only even orders of $l$ contribute. The lowest orders of imperfection are the octupole and the dodecapole term. The shifts of the sum frequency are

$$\Delta(\nu_+ + \nu_-)_{4,V} \approx \frac{3}{4}\frac{C_4}{z_0^2}\nu_- \left(\rho_+^2 - \rho_-^2\right) \approx -47.4 \text{ Hz } C_4 \tag{3.21}$$

for the octupole term and

$$\Delta(\nu_+ + \nu_-)_{6,V} \approx \frac{15}{8}\frac{C_6}{z_0^4}\nu_- \left[3z^2\left(\rho_-^2 - \rho_+^2\right) + \left(\rho_+^4 - \rho_-^4\right)\right] \approx 3.48 \text{ Hz } C_6 \tag{3.22}$$

for the dodecapole term. Here, $\rho_+$, $z$, and $\rho_-$ denote the motional amplitudes, and the numerical value for the frequency shift was calculated using the difference of the motional amplitudes between the upper limits at the beginning ($\rho_+ = 0$ mm, $z = 1$ mm, $\rho_- = 0.5$ mm) and the end ($\rho_+ = 0.5$ mm, $z = 1$ mm, $\rho_- = 0$ mm) of the measurement procedure, $z_0 = 5$ mm, and $\nu_- = 3.16$ kHz. The frequency shifts are mass-independent, because they are proportional to the magnetron amplitude and affect the frequency ratio which is used to derive the mass (see equation (3.18)).

Thus, contributions of the higher multipole terms to the electric field have to be minimized. In real Penning traps correction electrodes are added to the trap structure (see Sect. 5.5), which can compensate the higher-order terms in the trap center. This is especially important for cylindrical Penning traps to obtain an as harmonic electric field as possible.

## Inhomogeneities of the magnetic field

The magnetic field inhomogeneities also cause shifts of the ion's eigenfrequencies. The distortions of the magnetic field can also be expressed by a multipole expansion. The frequency obtained in a measurement is the average cyclotron frequency over one turn. Therefore, the dipole term $B_1$ cancels out. The lowest-order imperfection is the quadrupole term [Bol90]:

$$B\left(r,z\right)=B_0\left[1+\beta_2\left(z^2-\frac{r^2}{2}\right)\right], \tag{3.23}$$

where $\beta_2$ is the quadrupole coefficient. The shift of the sum frequency can be expressed as

$$\Delta\left(\nu_+ + \nu_-\right)_{2,B} \approx \beta_2\nu_c\left(z^2-\rho_-^2\right) \approx 3.8\times10^{-9}\nu_c, \tag{3.24}$$

where the same parameters for the amplitudes have been used as in the equations (3.21) and (3.22) and $\beta_2 = 3.8\times10^{-9}$ mm$^{-2}$ [Rep08]. In this case the frequency shift scales with the cyclotron frequency $\nu_c$, so that for identical motional amplitudes the frequency shifts would cancel out in the frequency ratio. However, this can only be guaranteed within certain limits in the experiment, therefore the magnetic field needs to be as homogeneous as possible. TRIGA-TRAP uses a 7-T superconducting magnet to create the magnetic field for the traps (see Sect. 5.5). The magnet has correction coils that are used to create a field homogeneity of $\Delta B/B < 10^{-6}$ in the region of about 1 cm$^3$ around the trap center, so that the relative shift of the cyclotron frequency is in the order of $10^{-9}$ [Rep08]. The magnetic field of the superconducting magnet is also subject to temporal changes. The current in the superconducting magnet decreases due to the flux creep effect [And62]. Active compensation coils are used to increase the temporal stability of the magnetic field. The decay of the magnetic field can be approximated by a linear function, which yields a positive slope in the case of TRIGA-TRAP due to overcompensation by the compensation coils [Ket10a]:

$$\frac{\Delta B}{B}\frac{1}{\Delta t} = 1.31(35)\times10^{-9}\ /\ \text{h}. \tag{3.25}$$

Furthermore, temperature changes and pressure changes in the liquid helium dewar cause non-linear fluctuations of the magnetic field. Therefore, a temperature and pressure stabilization of the magnet is necessary. The systematic uncertainties of these effects are discussed in detail in Chap. 7.

## Misalignment of the trap axis and ellipticity of the trap potential

If the main axis of the Penning trap is misaligned to the magnetic field lines, the magnetic field $\vec{B} = B\hat{e_z}$ is modified to:

$$\vec{B} = B\left(\sin\theta\cos\phi, \sin\theta\sin\phi, \cos\theta\right)^T, \tag{3.26}$$

where $\theta$ and $\phi$ are the tilt angles. Additionally, the electric potential may have elliptical distortions, which causes the equipotential lines in a $z$-plane to be elliptical instead of circular. The modified trap potential is given by:

$$V(x,y,z) = \frac{1}{2}m\omega_z^2\left[z^2 - \frac{1}{2}\left(x^2+y^2\right) - \frac{1}{2}\epsilon\left(x^2-y^2\right)\right], \tag{3.27}$$

where $\epsilon$ is the ellipticity of the trap potential, which is for small values the fractional difference of the two principal axes of these ellipses. Elliptical traps have been investigated in detail in [Kre08, Bre08]. The shift caused by these effects is given by [Gab09]

$$\Delta\left(\nu_+ + \nu_-\right)_{\theta,\epsilon} = \hat{\nu}_-\left(\frac{9}{4}\theta^2 - \frac{1}{2}\epsilon^2\right), \tag{3.28}$$

where $\hat{\nu}_-$ denotes the perturbed magnetron frequency. The total contribution of this systematic error in a frequency ratio is given by

$$\Delta r = \left(\frac{9}{4}\theta^2 - \frac{1}{2}\epsilon^2\right)\left(\frac{\nu_{c,ref}}{\nu_{c,ion}} - 1\right)\frac{\hat{\nu}_{-,ion}}{\hat{\nu}_{+,ref}}, \tag{3.29}$$

where $\hat{\nu}_{+,ref}$ is the perturbed reduced cyclotron frequency of the reference ion. The magnitude of $\Delta r$ can be as low as $10^{-9}$, for a well-aligned trap and if reference ions with similar cyclotron frequencies to the ion of interest are used [Gab09]. The invariance theorem (3.11) is not sensitive to these perturbations, since the shift of the radial frequencies is compensated by the axial frequency [Bro86]. Therefore, the precision of a measurement is not limited by equation (3.29) if the cyclotron frequency is obtained via the invariance theorem.

## Ion-ion interaction

Frequency shifts can occur if more than one ion is stored in the trap due to ion-ion interaction. So far, only experimental studies were made concerning the frequency shifts as function of the number of ions. The following experimental observations were made [Bol92]: If multiple ions of the same ion species are stored in the trap the cyclotron frequency of the center-of-mass is determined, so that no change in the cyclotron frequency is observed. If two different ion species are stored in the trap, $n_1$ ions with mass $m_1$ and $n_2$ ions with mass $m_2$, the cyclotron frequencies are shifted. The magnitude and the sign of the shifts depend on the resolving power $R$ and the number of ions $n_1$ and $n_2$. In case the mass difference $m_1 - m_2$ is so small that it cannot be resolved, one peak is observed at the center of mass of all ions. The width of the resonance is smaller than expected from the overlap of the two

individual resonances. If the masses can be resolved, both frequencies are shifted to lower values, and the magnitude of the frequency shift of ion species 1 depends on $n_2$ and vice versa.

Systematic uncertainties due to ion-ion interaction are avoided by using in the ideal case only one ion in the trap for the cyclotron frequency measurement. In a real measurement multiple ion events are also recorded, but in the data analysis procedure frequency shifts due to ion-ion interaction are taken care of by dividing the data into classes depending on the number of detected ions. Thereby, the cyclotron frequency is obtained as function of the number of ions, and the value which corresponds to one ion in the trap is used to determine the mass [Kel03].

## 3.3 Cyclotron frequency measurement methods

In the following the methods used for the cyclotron frequency measurement including ion preparation are discussed. A measurement cycle at TRIGA-TRAP consists of the following steps:

- A bunch of ions either from the on-line or from one of the off-line ion sources (see Chap. 5) is injected into the first of two Penning traps, called purification trap. The ion bunch may consist of several ion species including the ions of interest.

- A mono-isotopic bunch of ions is prepared in the purification trap by the so-called buffer-gas cooling technique [Sav91], which centers one ion species in the center of the trap with low motional amplitudes. Unwanted ion species are located on a larger radius and lost after ejection at an aperture between the two Penning traps (see Chap. 5).

- The mono-isotopic ion bunch is transferred into the second Penning trap, called precision trap (see Chap. 5), where the actual measurement of the cyclotron frequency takes place. Two measurement methods are intended at TRIGA-TRAP for this purpose: the destructive time-of-flight ion-cyclotron-resonance (TOF-ICR) and the non-destructive Fourier-transformation ion-cyclotron-resonance (FT-ICR) technique.

All these methods require that the motional amplitudes of the stored ions can be externally manipulated. Therefore, the ion manipulation is discussed first, before the individual detection techniques are discussed.

### Ion manipulation

As discussed in Sect. 3.1 the motion in the Penning trap can be treated as three independent harmonic oscillators. Therefore, the motional amplitudes can be manipulated by adding an external force to the system, similar to a classical harmonic oscillator with external force. In a Penning trap the force is introduced by irradiating radiofrequency signals, which can change the amplitudes of the individual

motions. A detailed mathematical treatment of the excitation can be found in [Kön95, Kre92b, Geo05].

An increase of the amplitude of one eigenmotion is achieved with a dipolar excitation with a frequency corresponding to the eigenfrequency of the motion. The radial motions can be excited by a field of the form

$$\vec{E} = \frac{U_d}{a} \cos\left(2\pi\nu_{rf} - \phi_{rf}\right) \hat{x}, \tag{3.30}$$

where $\nu_{rf}$ is the excitation frequency, and $U_d$ the amplitude at radius $a$ of the excitation signal. The excitation frequency $\nu_{rf}$ can be either the $\nu_+$ to address the modified cyclotron motion or $\nu_-$ to address the magnetron motion. In order to apply a signal as described in equation (3.30) the ring electrode of the trap needs to be segmented, as shown in Fig. 3.4, so that on two opposing segments the signal with 180° phase shift can be applied. The ring electrode is usually segmented into at least four parts, so that quadrupolar excitation can also be applied. The axial motion can be addressed as well by applying a radiofrequency with $\nu_z$ and 180° phase shift between the two endcaps.

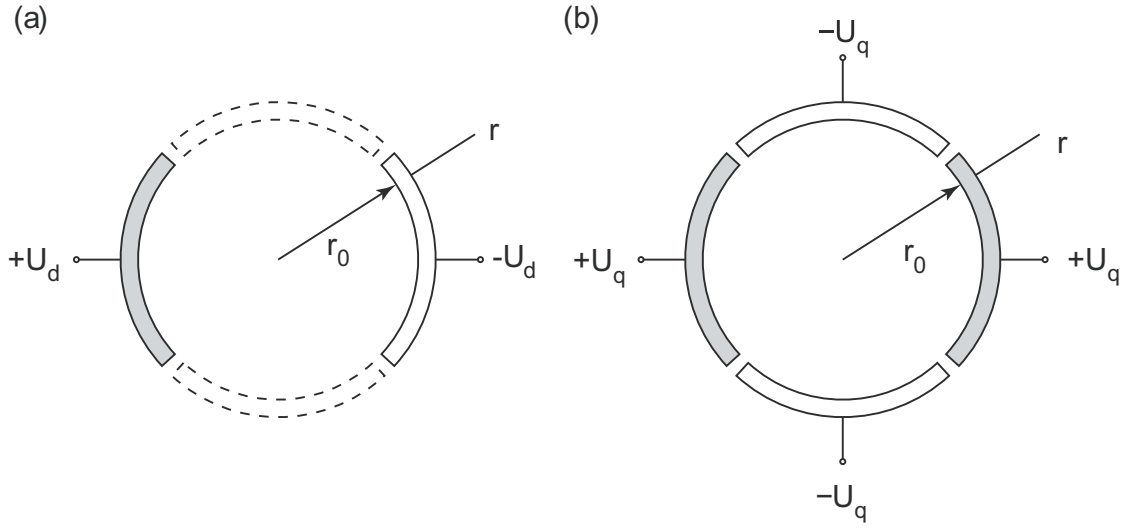


Figure 3.4: A four-fold segmented ring electrode is shown with the excitation scheme for the rf-signal for the dipolar excitation in (a) and for the quadrupolar excitation in (b) [Bla06].

The relative phase of the ion motion and the excitation signal $\phi_{rf}$ can be of importance for the magnetron excitation [Bla03a]. If the ions have an initial magnetron radius $\rho_-$ and $\phi_{rf} = 90°$, the magnetron radius is monotonically increasing, whereas for $\phi_{rf} = 270°$ $\rho_-$ is first decreased to zero before it starts to increase continuously.

Since the magnetron frequency is almost mass-independent, a magnetron excitation can be used to drive out all ion species simultaneously from the center of the trap. Excitation at the reduced cyclotron frequency can be used to selectively increase the motional amplitude of one ion species. This can be used to remove unwanted ions species from the trap.

A quadrupolar excitation signal can transfer the motional amplitude of one eigenmotion into another by coupling the two eigenmotions with an excitation at the sum

of their eigenfrequencies. This kind of excitation signal is in particular important for the cleaning and cyclotron detection methods described below. The electric field of the excitation signal for the conversion of the radial eigenmotions has the form:

$$\vec{E} = \frac{2U_q}{a^2} \cos\left(2\pi\nu_{rf} - \phi_{rf}\right) \begin{pmatrix} -y \\ x \\ 0 \end{pmatrix}, \tag{3.31}$$

where $U_q$ is the amplitude of the excitation signal at the radius $a$. A full conversion of the two radial motions can be achieved if the excitation frequency $\nu_{rf}$ is equal to the sum frequency $\nu_+ + \nu_-$, which is identical to the cyclotron frequency $\nu_c$ (see equation 3.10). In case of a resonant excitation a periodic conversion between the magnetron and modified cyclotron motions takes place [Kön95]. A full conversion is obtained in the time $T_{conv}$ given by:

$$T_{conv} = \frac{4\pi a^2 B}{U_q}. \tag{3.32}$$

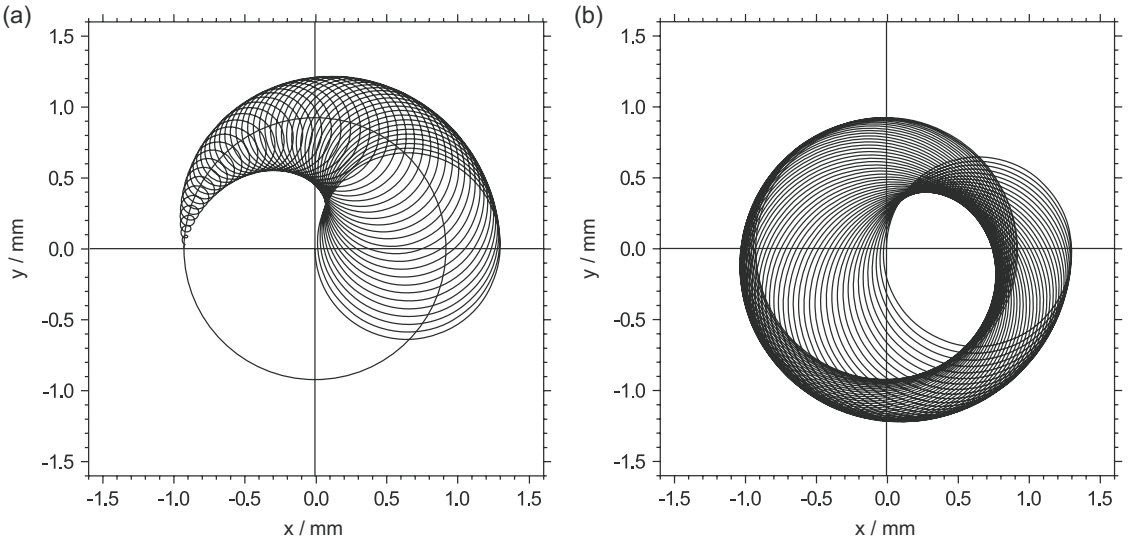


Figure 3.5: The trajectory for an ion which undergoes a full conversion of the magnetron into the modified cyclotron motion by quadrupolar excitation is shown. In (a) the conversion is shown for $t = 0$ to $t = T_{conv}$ / 2 and in (b) for $t = T_{conv}$ / 2 to $t = T_{conv}$ [Bla06]. For details see text.

Fig. 3.5 shows the trajectory from $t = 0$ to $t = T_{conv}$ of an ion with initially pure magnetron motion. At $T_{conv}$ the magnetron radius has decreased to zero, whereas the amplitude of the modified cyclotron has the magnitude of the initial magnetron radius [Bol90]. If the irradiation of excitation signal is further continued the motion is converted back into the magnetron motion, which is the time inverted process of the one shown in Fig. 3.5. The radial energy of the ions is given by:

$$E_r(t) = \frac{1}{2} m\omega_+^2 \rho_+(t)^2 - \frac{1}{2} m\omega_-^2 \rho_-(t)^2 \approx \frac{1}{2} m\omega_+^2 \rho_+(t)^2. \tag{3.33}$$

For the approximation, the relation from equation (3.13) has been used. Thus, the radial energy at $t = 0$ is close to zero, and has its maximum value at $t = T_{conv}$. For a non-resonant excitation $\nu_{rf} \neq \nu_c$, the full conversion is not achieved, and the amplitude of the modified cyclotron motion does not reach the initial magnetron radius [Kön95]. Since the full conversion takes place at the sum frequency $\nu_+ + \nu_- = \nu_c$ the detection of the cyclotron frequency can be based on detecting the degree conversion of the two radial motions, as it is the case for the TOF-ICR technique.

## Mass-selective buffer gas cooling

The simultaneous presence of ion species with different masses causes a shift of the detected cyclotron frequency, as discussed in Sect. 3.2. Ion sources deliver in general several ion species simultaneously. Therefore, it is essential to clean unwanted ion species from the trap. The buffer-gas cooling technique [Sav91] can be used to remove all unwanted ion species, and to center the desired ion species in the trap by reducing all motional amplitudes. This technique is performed in the purification trap of TRIGA-TRAP (see Chap. 5). After applying this technique, the ions are transferred into the precision trap, where a cold bunch of mono-isotopic ions remains in the trap center, which can be used for the cyclotron frequency measurement. The fact that the ions are cooled increases the measurement precision, because the ions are confined in a small volume at the trap center, so that they experience less field inhomogeneities during the measurement process.

For the buffer-gas cooling a small amount of helium is leaked into the purification trap. Thereby, the ions experience a damping force due to collisions with the buffer-gas atoms:

$$\vec{F} = -\delta m \vec{v}, \tag{3.34}$$

where $m\vec{v}$ is the momentum of the ion, and $\delta$ is the damping constant, which is given by:

$$\delta = \frac{q}{m} \frac{1}{K_{ion}} \frac{p/p_N}{T/T_N}. \tag{3.35}$$

$K_{ion}$ denotes the mobility of the ions in the buffer gas, and $p$ and $T$ are the pressure and the temperature in units of the normal pressure $p_N$ and and temperature $T_N$. The energy of the ion decreases due to the damping force. Thus, the motional amplitudes of the modified cyclotron and the axial motion decreases, but due to the negative energy contribution of the magnetron motion (see equation (3.17), the magnetron radius increases with time. The damping force is proportional to the momentum of the eigenmotions, therefore, eigenmotions with higher frequencies are cooled faster. Thus, according to (3.13) the amplitudes of the modified cyclotron motion and the axial motion decrease much faster than the magnetron amplitude can increase. The calculated trajectory in the radial plane of an ion in buffer-gas is shown in Fig. 3.6. The modified cyclotron motion is rapidly cooled, and the magnetron radius increases slowly.

The mass-selective buffer-gas cooling technique uses the damping of the eigenmotions to select one ion species in the trap. The procedure consists of the following steps:

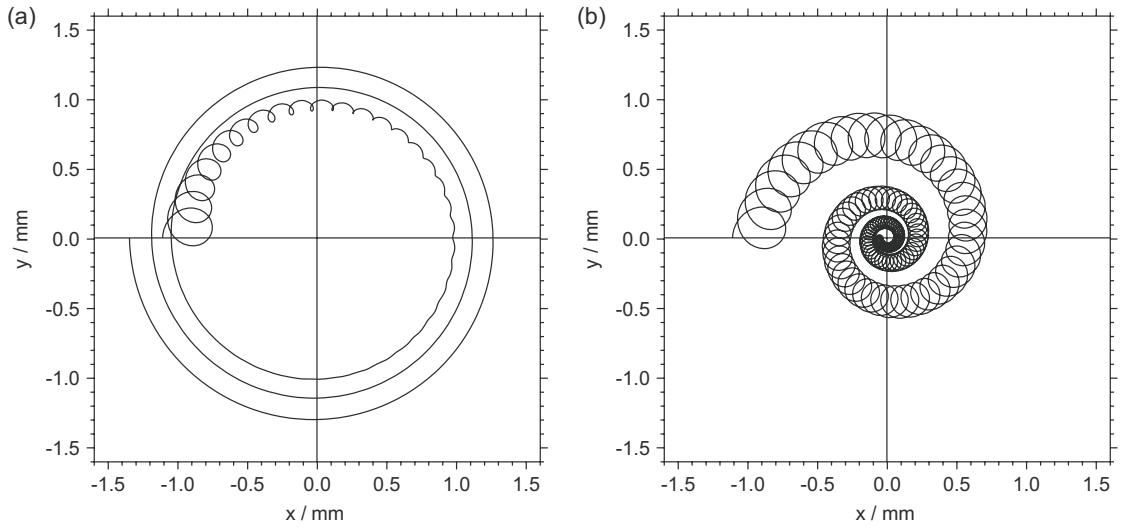


Figure 3.6: Simulations of the orbit for an ion in buffer gas without external excitation is shown in (a). The projection of the motion in the radial plane for an ion with a finite magnetron and modified cyclotron amplitude is illustrated. In (b) the trajectory of an ion with identical starting condition as in (a) is shown, but a quadrupolar excitation at the cyclotron frequency $\nu_c$ is applied. The magnetron motion is continuously transferred into the modified cyclotron motion, which is rapidly cooled. Therefore, both amplitudes decrease with time [Bla06]. For details see text.

- A cloud of ions is injected in the trap by lowering the potential of the endcap on the injection side for a short time. The cloud consists of several ion species. After a short waiting time the modified cyclotron and axial amplitudes are cooled, and the ions have only a finite magnetron radius.

- A dipolar excitation with the magnetron frequency is applied to drive all ions further out from the center. After the excitation the ions are located on a well-defined radius, which is larger than the aperture placed between the purification and the precision trap.

- In the next step the ions of interest are selectively centered in the trap. This is achieved by a quadrupolar excitation at the respective cyclotron frequency of the ions of interest. Thereby, the magnetron motion is converted into the modified cyclotron motion. Instead of a periodic conversion, a decrease in both motion amplitudes is obtained, since the fraction of the magnetron motion, which is converted into the modified cyclotron motion, is rapidly cooled by the buffer gas. Hence, the ions of interest are centered in the trap after the quadrupole excitation. Since the cyclotron frequency is mass-dependent, only one ion species is addressed with a certain resolving power depending on the quadrupolar excitation time $R \propto 1/T_{rf}$.

- Finally, the ions are ejected from the trap and are transferred into the precision trap. All unwanted ions that are located on a large radius are lost at the aperture, and only the ions of interest are captured in the precision trap.

The mass resolution obtained for ions with $A \approx 120$ is in range of $10^4$ - $10^5$, depending on the excitation time and on the strength of the damping force [Geo11]. Ions with different mass number $A$ are well separated, but isobaric contaminants with a small mass difference are not resolved by buffer-gas cooling and may cause frequency shifts during the measurement procedure. If the contaminant ion species are known, the ion species can be removed by a narrow-band dipolar excitation at the reduced cyclotron frequency.

This method is in principle also suited to derive the mass of the ions, since the ions are only centered in the trap if the frequency of the quadrupolar excitation $\nu_{rf}$ is resonant to the cyclotron frequency $\nu_c$ of the ions. If the number of ions coming from the trap is measured as function of $\nu_{rf}$, the highest number is obtained for a resonant excitation. The precision of this detection method is limited due to the presence of the other ions and the buffer gas in the trap, and the fact that the ions probe field inhomogeneities in a large region during the buffer-gas cooling procedure. A much higher precision is achieved in the precision trap by using the ion-cyclotron-resonance method described below. This has the advantages that generally only one ion species is present, the vacuum conditions are good, and the measurement can take place in the homogeneous region of the trap.

The cyclotron frequency detection technique which is used at TRIGA-TRAP have been introduced. In the future the non-destructive FT-ICR detection will be used at TRIGA-TRAP complementary to the TOF-ICR technique. This is discussed in Chap. 8. In the next chapter the physical processes required for the production of a radioactive ion beam is described.

## Time-of-flight ion-cyclotron-resonance method

The time-of-flight ion-cyclotron-resonance (TOF-ICR) method is a destructive detection method, which has been applied for mass measurements on stable nuclides [Ber02] and short-lived radioactive nuclides [Bol96]. It was first used to determine the proton to the electron mass ratio [Grä80]. This method is applied as well at TRIGA-TRAP in the precision trap to determine the cyclotron frequency of the stored ions. The method is destructive because the ions are ejected from the trap and destructively detected with an electron multiplier. The ions' time of flight is measured for different excitation frequencies $\nu_{rf}$. Thus, for each time-of-flight measurement step ions have to be loaded into the trap. The measurement procedure consists of the following steps:

- A bunch of cooled mono-isotopic ions from the purification trap is captured in the precision trap. In the ideal case only one ion is captured.
- A dipolar excitation is applied to excite the ions on a well-defined magnetron radius.
- An external quadrupolar radiofrequency with the frequency $\nu_{rf}$ close to the sum frequency $\nu_+ + \nu_-$ is applied to convert the magnetron motion to the modified cyclotron motion. In case of a resonant excitation with the duration $T_{conv}$ (see equation (3.32)), the magnetron motion is completely converted into

the modified cyclotron motion, as shown in Fig. 3.5, and the maximum possible radial energy is obtained according to equation (3.33).

- The ions are ejected from the trap and their time of flight to an ion detector (usually an MCP or channeltron detector) is measured. During their flight to the detector the ions leave the bore of the superconducting magnet and pass through the field gradient. The decreasing magnetic field causes the radial energy to be converted into axial energy due to the conservation of the magnetic moment of the ions' motion. This effect is discussed as magnetic mirror effect in Sect. 4.4 (see equation (4.23)). Therefore, the ions which gained the highest radial energy in the trap have the shortest time of flight to the ion detector and vice versa.

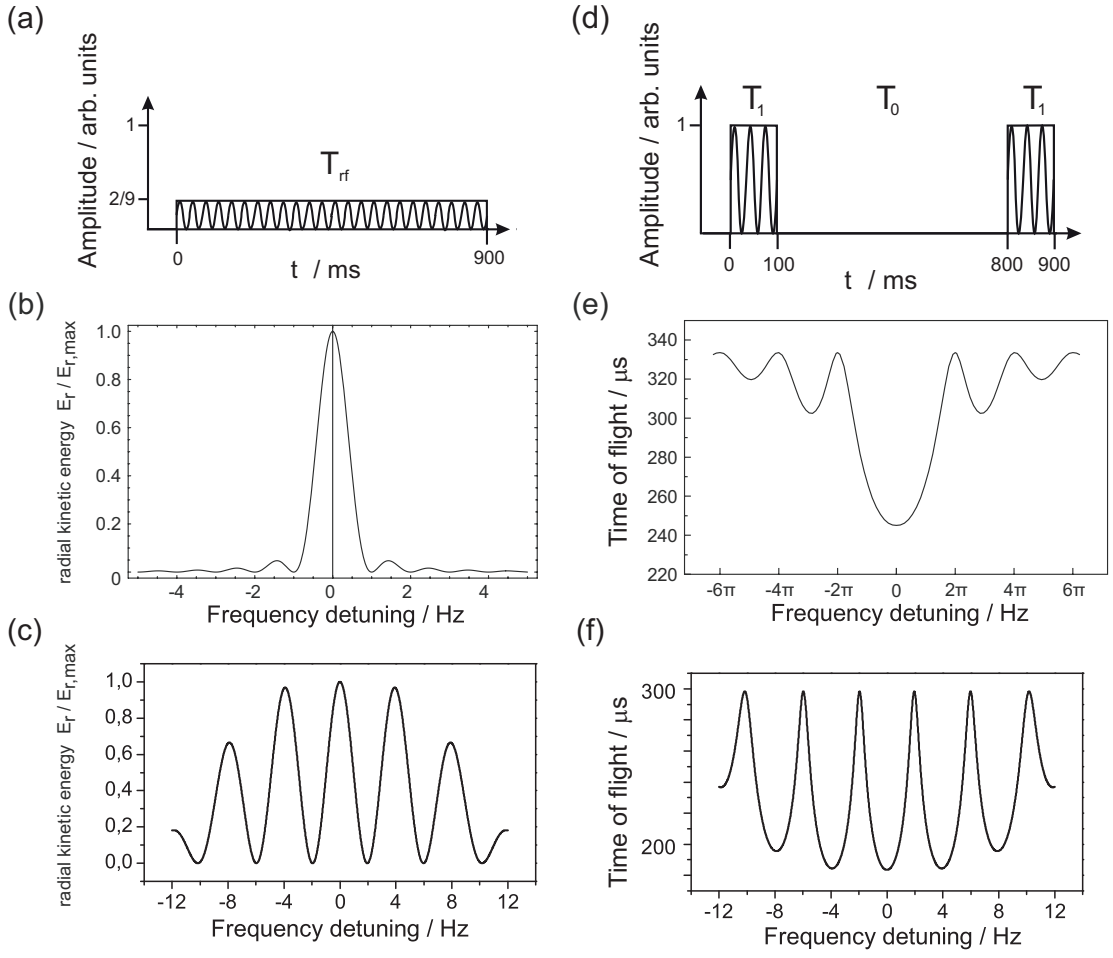


Figure 3.7: The relative radial energy $E_r/E_{r,max}$ as function of the frequency detuning $\Delta\nu$ in units of $T_{conv}^{-1}$ is shown in (a). The corresponding time of flight obtained for the TOF-ICR detection is shown in (b) [Bla06]. An excitation scheme of a two pulse Ramsey excitation is shown in (a) with the same scale as in Fig. 3.7(a) for continuous excitation [Geo07a]. The radial kinetic energy and the time of flight for the Ramsey excitation scheme as function of the frequency detuning are shown in (b) and (c), respectively [Geo05].

Due to the finite length of the quadrupolar excitation pulse $T_{rf}$, the frequency spectrum of the excitation signal contains also a finite amplitude at $\nu_+ + \nu_-$ for excitation frequencies with a small detuning $\Delta\nu$ from the resonance frequency. The excitation signal for a continuous excitation pulse with constant amplitude is shown in Fig. 3.7(a), the radial energy as function of $\Delta\nu$ in units of $T_{rf}^{-1}$ in Fig. 3.7(b). The measurement cycle described above is repeated for several excitation frequencies $\nu_{rf}$ to obtain a time-of-flight spectrum similar to the one shown in Fig. 3.7 (c). The time of flight for a certain detuning $\Delta\nu$ can be calculated by

$$T\left(\nu_{rf}\right) = \int_0^{z_1} \sqrt{\frac{m}{E_z - qV(z) - \mu\left(\nu_{rf}\right) B\left(z\right)}} dz, \tag{3.36}$$

where $z = 0$ is the position of the trap center, $z_1$ the position of the detector, $E_z$ the initial axial energy in the trap, $V\left(z\right)$ and $B\left(z\right)$ the electric and magnetic potential on the axis from the trap to the detector, and $\mu\left(\nu_{rf}\right)$ the magnetic moment of the ion motion. Equation (3.36) is evaluated by approximating the electric and magnetic field gradients in several intervals [Geo05], and the line shape of the resonance for a mass spectrometer with a given $V(z)$ and $B(z)$ can be calculated. The cyclotron frequency of the ions is obtained by extracting the position of the time-of-flight minimum from the time-of-flight spectrum by fitting the well-understood line shape [Kön95] to the data. At this point it is assumed that the sum frequency $\nu_+ + \nu_-$ is equal to the cyclotron frequency of the ions (see (3.10)). Thus, the systematic uncertainty given in equation (3.29) has to be considered for this measurement method.

The statistical uncertainty of the cyclotron frequency measurement with the TOF-ICR method is given by [Kel03]

$$s\left(\nu_c\right) = C\frac{1}{\sqrt{N_{ion}}}\frac{1}{T_{rf}}, \tag{3.37}$$

where $C$ is a constant and $N_{ion}$ is the total number of ions. Thus, a smaller uncertainty is reached, if a longer excitation pulse is applied. For this purpose the excitation amplitude has to be decreased according to equation (3.32), so that $T_{rf} = T_{conv}$. The maximum excitation time is limited by the pressure conditions in the precision trap. If the excitation pulse is too long, damping of the modified cyclotron motion due to collisions with residual gas occurs. Thereby, the difference between the maximum and minimum of the time of flight decreases and the uncertainty of the measurement increases. The maximum number of ions is limited due to the systematic uncertainty caused by non-linear magnetic field fluctuations which increase with the measurement time (see Chap. 7).

One method of increasing the precision for identical statistics and a fixed excitation time is to use a Ramsey excitation scheme, which consists of several phase-coherent separated excitation pulses. In Fig. 3.7 (d) the Ramsey excitation signal with two pulses of length $T_1$ separated by a waiting time $T_0$ is shown, so that the total time is equal to the excitation time of the continuous excitation signal shown in Fig. 3.7 (a). The integral of the rf-amplitude over time has to stay identical in order to achieve a full conversion. Therefore, the amplitude has to be increased compared to the continuous excitation. The radial energy and the time of flight as function

of the frequency detuning are shown in Fig. 3.7(e) and (f).Due to a decrease in the width of the fringes and strongly pronounced sidebands, the cyclotron frequency can be obtained with a factor of two to three higher precision with identical statistics [Kre07, Geo07a, Geo07b]. The measurements reported in Chap. 7 were exclusively performed with a two-pulse Ramsey excitation.

In equation (3.18) it was shown that it is necessary to calibrate the magnetic field by performing a cyclotron frequency measurement with a reference ion species. Mass-independent frequency shifts cause systematic errors of the obtained mass depending on the mass difference of the ion of interest and the reference ion. The deviation of the obtained mass is given by [Smo08a]:

$$\Delta m_{ion} = \frac{\Delta\nu_c}{\Delta\nu_c + \nu_{c,ion}} \left(m_{ref} - m_{ion}\right), \tag{3.38}$$

where $\Delta\nu_c$ is a mass-independent frequency shift of the cyclotron frequency, which can be created by higher multipole components of the electric field (see the equations (3.21) and (3.22)). Due to this fact, it is advantageous to use reference masses with a small mass difference to the ion of interest. Carbon cluster ions are an ideal choice, since they provide each 12 mass units a reference mass, which is an integer multiple of the unified atomic mass unit. The use of carbon cluster ions is in particular important for heavy ions, since the heaviest ion which is known with high precision is $^{133}$Cs [Aud03]. Therefore, a carbon cluster ion source has been developed [Smo08a] and commissioned at TRIGA-TRAP within this thesis.

Systematic uncertainties of the frequency ratios $\Delta r$ (3.29) can be determined experimentally by using carbon cluster ions. Since carbon is used to define the atomic mass, masses of carbon clusters are integer multiples of the atomic mass unit, except for their binding energies. Thus, carbon cluster ions provide a comb of reference masses, and systematic uncertainties in the frequency ratio measurements can be revealed by measuring the well-known frequency ratios of two carbon cluster ions. This study has been performed on a large mass range for TRIGA-TRAP [Ket10a], and the results are briefly discussed in Chap. 7. Another method to study systematic uncertainties with respect to the invariance theorem is to compare cyclotron frequencies obtain via the invariance theorem and equation (3.10) [Böh09].

The TOF-ICR method is an established method for mass measurements of short-lived radionuclides with on-line mass spectrometers. The method has been exploited up to the borders of applicability concerning precision ($^1$H, $1.8{\cdot}10^{-10}$ [Sol08]), half-life ($^{11}$Li, $T_{1/2}$ = 8.8 ms [Smi08]) and production rate ($^{252}$No, 0.4 s$^{-1}$ [Dwo10]). The latter limitation can be overcome by using a non-destructive detection method, which can use an ion which is captured once in several measurement cycles. Thus, a non-destructive detection method may ultimately require only one ion for a mass measurement. This is an advantage compared to the TOF-ICR method where the ions are lost in the destructive detection. In addition, each frequency step of the measurement requires a certain number of ions to obtain a cyclotron resonance with a decent uncertainty. This illustrates the demand for a non-destructive detection method if nuclides with lower production rates are to be investigated. In the future the non-destructive Fourier-transformation ion-cyclotron resonance (FT-ICR) method will be implemented at TRIGA-TRAP [Eib13], but was not part of this

thesis. The present status and the applications of this method are mentioned in Chap. 8.

# Chapter 4

# Radioactive ion-beam production at TRIGA-SPEC

Until now about 3300 different nuclides have been discovered [Aud03]. Only a small fraction of 300 of them can be found in nature. These nuclides are either stable or have sufficiently long half-lives, so that they still remain since their synthesis. Radioactive nuclides with a shorter half-life can be also found in nature. They are either decay products of long-lived nuclides, such as nuclides of the decay chains of uranium or thorium, or they are constantly created by cosmic rays, like for example $^{14}$C. All other nuclides have to be artificially created by nuclear reactions in particle accelerators or nuclear reactors.

The investigation of the properties of these exotic nuclides have revealed new phenomena in nuclear physics which are not present in stable nuclei, such as halo nuclei [Tan85, Nör09], change of magic numbers [Oza00], the island of inversion [Thi75], etc. Many radioactive ion beam facilities worldwide are dedicated to this subject [Kug00, Mün79, Ärj86] and various methods have been developed to access nuclides far away from the valley of stability. In the following, three different methods for radioactive ion beam production are briefly introduced, which cover a large fraction of the available methods. They are distinguished by the target type, thick or thin target, and whether an in-flight or a reacceleration technique is used [Tan08].

ISOL (Isotope Separation On-Line) facilities, such as ISOLDE at CERN, Geneva [Kug00] and TRIUMF, Vancouver [Dom00], use thick targets and a reaccelerated beam of secondary ions. In case of ISOLDE, a pulsed $\mu$A beam of 1.4 GeV protons impinches typically on a thick uranium carbide target and mainly neutron-deficient radionuclides are created by spallation and fragmentation reactions, and proton-induced fission. In this case, the primary beam and the radionuclides, which have recoil energies due to the nuclear reactions up to 100 MeV, are completely stopped in the target and subsequently released by diffusion from the heated target. After the release from the target they are ionized and accelerated up to 60 keV for further mass spearation.

Another method, which uses a thin target and a reaccelerated ion beam, is the ion-guide isotope separator on-line (IGISOL) technique, which was developed at JYFL in Jyväskylä [Ärj86]. A thin target, which is placed in a gas-filled target or recoil chamber, is bombarded by a cyclotron-accelerated beam of protons or light

ions up to $^{4}$He to produce radioactive ions. The reaction products are recoiling out of the target with a high charge-state and thermalize with the helium gas in the target chamber, so that their charge state decreases. In most cases the radionuclides can be directly obtained as singly charged ions after the thermalization, so that no further ion source is required [Ärj86]. However, reionization of neutralized radionuclides by laser ionization can increase the selectivity and the yield [Moo10]. Subsequently, the radionuclides are extracted from the target chamber by a radio-frequency ion guide into a region of low vacuum, where the ions are reaccelerated.

In-flight methods always use thin targets for the radioactive ion beam production. One facility making use of this technique is the velocity filter SHIP at GSI, Darmstadt [Mün79]. Heavy ions are accelerated by a linear accelerator up to an energy of several MeV per nucleon and pass through the thin target foil. Radionuclides are produced in transfer reactions, projectile fragmentations, fission in flight or fusion evaporation reactions. The later type offers the opportunity to create super-heavy elements [Hof07]. The primary beam and the reaction products can be separated due to their different kinematics in the velocity filter SHIP behind the production target. For low energy experiments such as the Penning trap mass spectrometer SHIPTRAP [Dil00, Blo05], which is located behind the velocity filter SHIP, the secondary beam of radionuclides has to be stopped. For this purpose, the secondary beam is injected through a thin metal foil window into a gas-cell, where the ions are stopped and thermalized by collisions with helium gas. The ions are extracted by electric fields from the gas-cell and transported to the Penning-trap experiment SHIPTRAP , which is the mother experiment of TRIGA-TRAP (see section 5.5).

TRIGA-SPEC makes use of a different approach to produce a radioactive ion beam. The high flux of thermal neutrons of the research reactor TRIGA-Mainz is used to produce radionuclides by thermal-neutron-induced fission of a thin actinoid target, e.g. U-235 or Cf-249, in a recoil chamber, which can be placed close to the reactor core (see Sect. 5.1). Thereby, short-lived neutron-rich are produced, which can be used to provide a radioactive ion beam for further investigation. As a part of this thesis the first steps have been made to provide an ion beam of exotic radionuclides for the TRIGA-SPEC experiment in order to determine ground-state properties of short-lived nuclides with half-lives down to about one second [Ket08]. One challenge is to extract short-lived nuclides fast enough to provide them to the experimental installations before their decay. Usually, this is achieved by ionization of the radionuclides and a fast extraction by acceleration with electric fields as in case of the ISOL or IGISOL technique. However, the use of a gas-jet transport system is required at the TRIGA reactor to extract the radionuclides from the interior through the concrete shield. Subsequently, ions of the fission products have to be produced in an ion source. After the ionization the radionuclides are extracted as radioactive ion beam, which is mass-separated and delivered to the experiments with a kinetic energy of 20-60 keV. TRIGA-SPEC is the only experiment of its kind located at a nuclear reactor. The only comparable experiment is the CARIBU project, which uses a strong source of $^{252}$Cf inside a gas cell to produce radioactive ions [Sav08]. $^{252}$Cf undergoes spontaneous fission, so that no incident particles are required. The yields obtained from this source are similar to those available at TRIGA-SPEC.

The following chapter gives an overview into different methods that are used to

produce radioactive ion beams at the TRIGA-SPEC experiment. The first section 4.1 describes the neutron-induced fission, and Sect. 4.2 the transport mechanism with the gas-jet system. Ionization methods, which are used at TRIGA-SPEC to create ions, are described in Sect. 4.3, including the off-line ionization of stable nuclides, as well as on-line ionization of short-lived radionuclides. The last section 4.4 concerns ECR ion sources, since an ECR ion source has been commissioned and used for the first on-line experiments presented in Chap. 6.

## 4.1 Thermal-neutron-induced fission

The process in use to produce radionuclides at the TRIGA-SPEC experiment is thermal-neutron-induced fission [Bet08, Pov09]. In this process a thermalized slow neutron reacts with a fissionable nucleus $(Z_0, A_0)$:

$$(Z_0, A_0) + n \rightarrow (Z_0, A_0 + 1)^* \rightarrow (Z_1, A_1)^* + (Z_2, A_2)^* + k\ n + \Delta E, \tag{4.1}$$

where $(Z, A+1)^*$ denotes the excited compound nucleus after the neutron has been captured. Subsequently, the excited compound nucleus decays into two excited fission fragments $(Z_1, A_1)^*$ and $(Z_2, A_2)^*$, which deexcite by emission of gamma radiation and neutron emission. In case the fission fragments are unstable against beta decay, they undergo a chain of beta decays until a stable nuclide is reached. $k$ is the average number of emitted neutrons during this process, which includes prompt neutrons from the decay of the compound nucleus, and delayed neutrons from the deexcitation of the fission fragments. $\Delta E$ is the excess energy, which is released due to the difference of the binding energies of the involved nuclides. Since the two fission fragments around $A \approx 100$ are stronger bound than the much heavier mother nuclide (e.g. $^{235}$U), typically energies in the order of 100 MeV per fission are released, mainly as kinetic energy of the reaction products.

As a model to describe the fission process, an elliptically deformable nucleus with constant volume is used. The liquid drop model (see Eq. 2.22) is used to describe the binding energy of an elliptically deformed nucleus by replacing the radius $R$ with the expression:

$$R = R_0 \left(1 + \sum_i \alpha_i P_i(cos\theta)\right), \tag{4.2}$$

where $R_0$ is the radius of the spherical nucleus, $P_i$ the Legendre polynom of the order $i$, and $\alpha_i$ the deformation coefficient. It is sufficient to consider only quadrupolar deformations ($i = 2$) for small deformations.

The nucleus changes its shape from a spherical to an elliptical shape in the beginning of the fission process, as the nucleus starts to seperate into two fragments. This shape transition stabilizes the nucleus against fission, since the surface of the nucleus increases, and thus, the contribution of the surface term $E_S$. However, the Coulomb term $E_C$ favors the elliptical deformation of the nucleus, since the average distance between the protons increases. The energy change of these two terms under deformation is found by replacing the nuclear radius $R$ in equation (2.22) by equation (4.2). The result is:

$$\Delta E_S = \frac{2}{5}\alpha_2^2 E_S^0 \tag{4.3}$$

$$\Delta E_C = -\frac{1}{5}\alpha_2^2 E_S^0, \tag{4.4}$$

where $E_S^0$ and $E_C^0$ are the surface and Coulomb terms of the undistorted nucleus, respectively [Boh39]. A nucleus becomes unstable against fission if $|\Delta E_C| \geq \Delta E_S$. In this case the energy gain through separating the protons is larger than the energy needed for the surface deformation, and the nucleus can undergo fission. If this criteria is used, nuclei with $Z^2/A > 48$ are fissionable. This is the case for nuclides with $Z > 114$ and $A > 270$. Nuclides with a smaller $Z^2/A$ value have a fission barrier. The binding energy has a local maximum as function of the quadrupolar deformation parameter $\alpha_2$ (see Fig. 4.1). However, the shell structure of the nucleus is not considered in the liquid-drop model. If the shell corrections [Str67] are considered, multiple potential wells and fission barriers can exist [Nix72], as shown in Fig. 4.1.

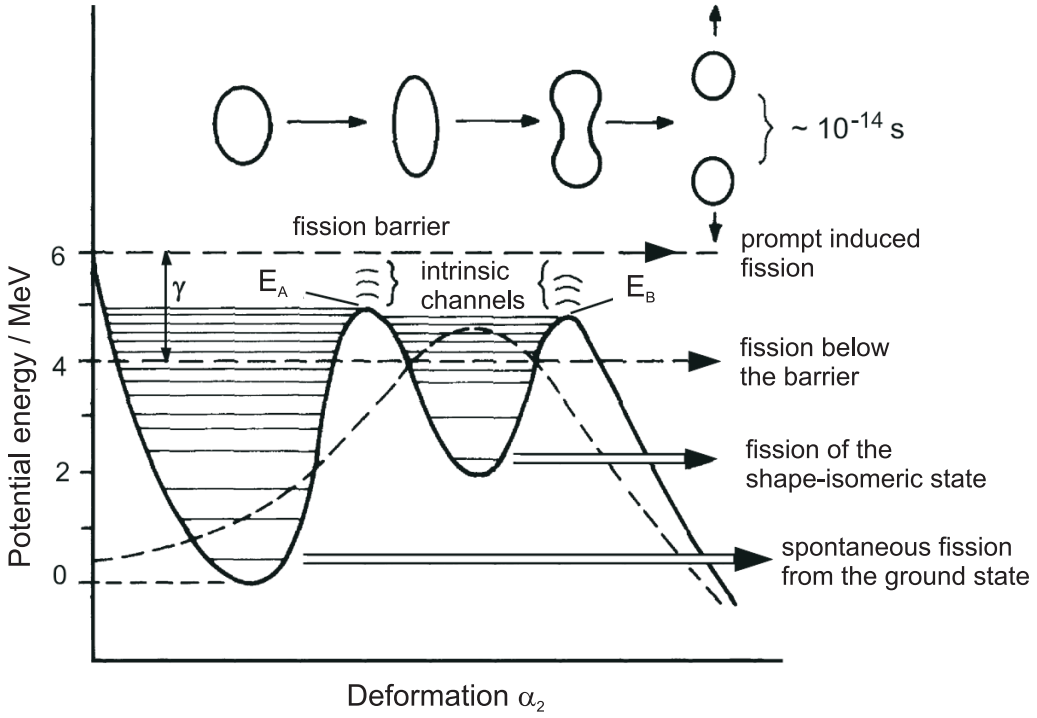


Figure 4.1: Potential energy of a nucleus as function of the deformation [Bet08]. The dashed line shows the energy dependence of the liquid-drop model as function of the deformation (see equations (4.3) and (4.4)). The solid line shows the potential energy as function of the deformation parameter $\beta$ including the shell structure of the nucleus. Two potential wells are shown, one for the ground state and one for a shape-isomeric state. Fission can occur from both states or any of the excited nuclear states with a low probability due to the tunnel effect. If the excitation energy of the nucleus is above the fission barrier, prompt induced fission takes place.

For nuclides with $Z > 90$ the fission barrier is typically only 6 MeV and it can be overcome by exciting the nucleus, e.g. by capture of a thermal neutrons. The pairing term $E_P$ makes a crucial difference, whether a nucleus can be fissioned by thermal neutrons. If a thermal neutron is captured by a nucleus with an odd number of neutrons, e.g. $^{235}$U, the compound nucleus $^{236}$U$^*$ has an excitation energy (6.4 MeV)

larger than the fission barrier (5.5 MeV) due to the release of the pairing energy. A nucleus with an even number of neutrons, e.g. $^{238}$U, has only 4.9 MeV excitation energy after the capture of a thermal neutron [Pov09], so that the fission barrier cannot be overcome unless additional kinetic energy is available. The neutron-capture cross section is proportional to $1/v$, where $v$ is the neutron velocity, so that fission induced by fast neutron is less efficient. Therefore, actinides with an odd neutron number, such as $^{235}$U, $^{239}$Pu, or $^{249}$Cf, are used as fissionable material. Targets of this species are available at TRIGA-SPEC for the production of radionuclides (see Chap. 5.1).

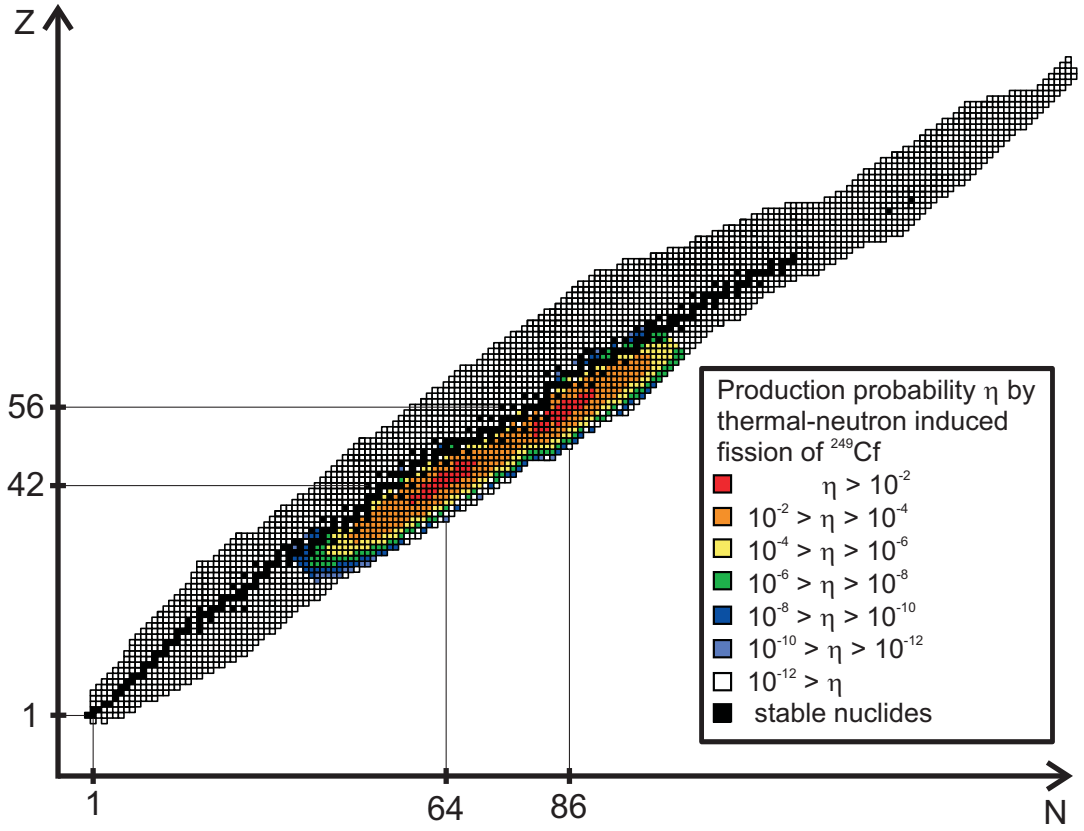


Figure 4.2: Nuclide chart with the individual fission probabilities $\eta$ of $^{249}$Cf [Eng94]. The fission probabilities in the range from $10^{-1}$ to $10^{-12}$ are shown in the color code as explained above. Nuclides which are colored in white have a probabilities of less than $10^{-12}$ to be created. Stable nuclides are shown in black. The numbers indicate the two maxima of the fission probability.

The yields of fission products $\Gamma(Z, A)$ obtained from a target are given by

$$\Gamma(Z, A) = \sigma_f \ \Phi_n \ N_{target} \ \eta_i(Z, A), \tag{4.5}$$

where $\sigma_f$ is the neutron capture cross-section, $\Phi_n$ is the neutron flux, $N_{target}$ is the number of target atoms and $\eta_i(Z, A)$ is the individual fission probability of the nuclide $(Z, A)$ from [Eng94]. Fig. 4.2 shows the individual fission rates $\eta$ for a $^{249}$Cf target. $\eta$ is the probability per fission that a certain nuclide is created. Neutron-rich nuclides are obtained to a large extent. The distribution of the fission products is

asymmetric, which means that fission of a nucleus into a nuclide with $A \approx 100$ and a heavier nuclide with $A \approx 140$ is favored compared to the decay into two nuclides with similar mass numbers $A \approx 120$. The position of the maximum of the light fission branch depends on the target material as shown in Fig. 4.3. It shifts to heavier masses for a heavier target material, whereas the maximum of the heavy branch does not change. The nuclides obtained from the thermal-neutron-induced fission are subject of investigation at TRIGA-SPEC.

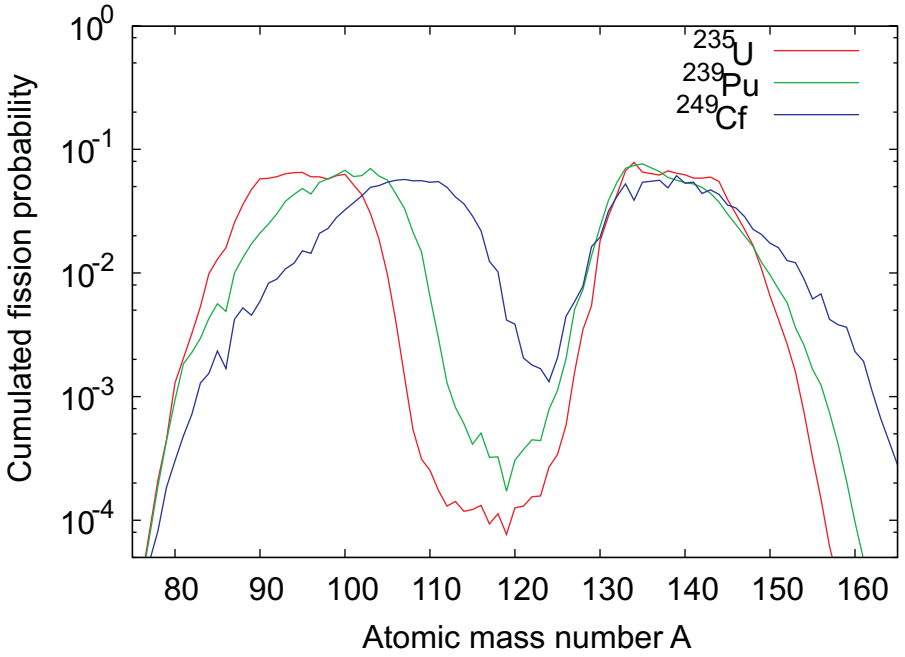


Figure 4.3: Accumulated fission probabilities from [Eng94] in dependence of the atomic mass number $A$. Three curves are shown for the thermal-neutron-induced fission of $^{235}$U (red curve), $^{239}$Pu (green curve), and $^{249}$Cf (blue curve). The maximum of the light branch of the fission products shifts to heavier masses for a heavier fissionable material.

## 4.2 Gas-jet transport systems for radionuclides

In order to provide a low energy ion beam of exotic nuclides for the precision mass- or laser-spectroscopy measurements the radionuclides have to be extracted from the interior of the reactor, where the fission takes place, to an ion source, which is placed in an accessible low-radiation background area to form an ion beam of radionuclides. For this purpose a gas-jet transport system has been used, which can transport radionuclides in an aerosol through a thin capillary with a typical inner diameter of one millimeter over distances up to several 100 meters in a short time [Gäg91]. This method was developed in the 1960s and is frequently applied in nuclear chemistry [Mac69] to transport radionuclides for experiments to an area with low-radiation background. It was also demonstrated that the gas-jet can be coupled to a surface ion source (see Sect. 4.3.1) in order to produce a radioactive ion beam [Ich02, Sch87, Brü85].

Radionuclides are isotropically emitted from the target with high kinetic energies due to the energy release of the fission process in the order of 100 MeV. It is necessary to stop the radionuclides before they implant into the walls of the target chamber and are lost. The energy loss $(-dE/dx)$ of a charged particle with charge $z \cdot e$ in a medium can be calculated with the Bethe-Bloch formula [Bet33]:

$$-\frac{dE}{dx} = \frac{z^2 e^4 n_e}{4\pi\epsilon_0^2 c^2 m_e \beta^2}(\ln\frac{2m_e c^2\beta^2}{I(1-\beta^2} - \beta^2), \tag{4.6}$$

where $n_e$ denotes the average electron density of the medium, and $I$ its average ionization potential. In case of a gas the electron density $n_e$ is given by:

$$n_e = \frac{Z}{A}\frac{pN_A M_{gas}}{k_B T} \tag{4.7}$$

with the pressure in the target chamber $p$, the Avogadro constant $N_A$, the mass of the gas atoms or molecules $M_{gas}$, the Boltzmann constant $k_B$ and the gas temperature $T$. Thus, the range until the emitted particles are thermalized can be decreased by either increasing the pressure $p$, or by using a heavier gas with a higher atomic or molecular mass $M_{gas}$. Another possibility is to cover the target with a thin layer (several micrometer) of aluminum to decrease the range of the fission products. This can be also used to selectively suppress radionuclides with a large atomic mass number $A$ by stopping them inside the aluminum layer, since they have a shorter stopping range [Brü83, Fin51].

In initial experiments of radionuclide extraction from a recoil chamber with a gas-jet it was observed that the extraction efficiency of the radionuclides with pure helium gas decreased rapidly with the transport distance, so that an efficient extraction with distances larger than one meter was not possible [Äst73]. This is due to diffusion of the particles to the walls of the transport capillary, where non-volatile particles attach themselves to the wall and are lost for the transport process. The transport mechanism of particles in a capillary is in detail described in [Wol76]. It is essential that the flow in the capillary is laminar, since turbulences can cause that particles in the carrier gas touch the wall. Therefore, the velocity of the gas-jet has to be subsonic in the capillary, since otherwise shockwaves that disturb the laminar flow are formed. For a fast extraction helium is preferred as carrier gas due to its high sonic speed (1000 m/s).

Three effects have to be considered for a particle moving in a tube with a small diameter: diffusion, sedimentation, and Bernoulli's principle. As mentioned above particles entering at the center of the capillary move due to diffusion closer to the walls with increasing transport time $t$. As soon as the root mean square (rms) distance

$$x_{rms} = \sqrt{2Dt} \tag{4.8}$$

is as large as the radius of the capillary particles get lost. $D$ denotes the diffusion coefficient, which depends on the mass of the particles $m_p$ [Kul11, Dem08]:

$$D = \frac{1}{n\sigma}\sqrt{\frac{8k_B T}{9\pi m_p}}. \tag{4.9}$$

Here, $n$ denotes the particle density, $\sigma$ the interaction cross-section with the carrier gas. In total, $x_{rms}$ is proportional to $m_p^{-1/4}$. Thus, light particles are getting lost by diffusion after a short time, whereas heavier particles remain longer at the center of the capillary. However, sedimentation causes the heavier particles to attach themselves to the walls due to gravity. The distance the particles pass due to sedimentation $x_{sed}$ is given by [Kul11]:

$$x_{sed} = v_{sed}t = \frac{gC_c}{\eta}(\frac{\rho_p}{162\pi^2}m_p^2)^{1/3}, \tag{4.10}$$

with the sedimentation velocity $v_{sed}$, which is determined by the equilibrium of the gravitational force and the drag force according to Stoke's law. $g$ denotes the gravitational acceleration, $C_c$ the slip correction factor, $\eta$ the viscosity of the gas, and $\rho_p$ the particle density. These two effects cause the particle to move away from the center with increasing transport time $t$. The third effect is a force $K_B$ due to Bernoulli's law

$$K_B \propto m_p^{4/3} v_0^2 r \rho_g, \tag{4.11}$$

which depends on the particle's mass $m_p$, the velocity difference on the surface of the particle $v_0$, the distance to the capillary axis $r$ and the density of the carrier gas $\rho_g$. According to Newton's friction model the velocity profile in the capillary the velocity of the particles increases with the square of the distance to the wall. Thus, velocity on the surface of the particle facing the wall of the capillary is always smaller than on the surface which is facing the center. Therefore, the force $K_B$ is always driving the particle back to the center. This increases in particular the transmission for heavy particles due to the $m_p^{4/3}$ dependence.

In conclusion, a long tube acts as a band-pass filter in the particle mass with the highest transmission in the range of $10^9$ to $10^{10}$ u. Therefore, the fission products with a maximum mass of about 160 u are much too light to be transported efficiently over large distances. Aerosol particles with a diameter of about 200 nm have the most suitable mass for the transport in a capillary and thus the highest transmission [Wol76]. It was demonstrated, that fission products can be transported over more than 100 meters, if they attach themselves to aerosol particles in the recoil chamber [Gäg91]. For this purpose, the target chamber is continuously flushed with an aerosol, which contains carrier particles of suitable size. The fission products of all non-volatile elements attach themselves to the surface of the aerosol particles after thermalizing in the target chamber. Radionuclides of noble gases and halogenes are transported by the gas flow without carrier particles.

The attachment of the fission products to the aerosol particles in the recoil chamber is due to diffusion after thermalization of the fission products in the carrier gas [Gün93]. Direct implantation during the recoil has only a low probability ($\approx 10^{-4}$) due to the low aerosol density in the recoil chamber ($\approx 10^6$ / cm$^3$). The attachment rates of the fission products via diffusion are derived in [Bau67] and depend on their charge state, their thermal velocity, diffusion coefficient, and the charge and diameter of the aerosol particles. The attachment of the radionuclide to the aerosol particle is either due to van-der-Waals interaction, Coulomb interaction or chemiesorption. Thus, the properties of the surface and the aerosol material influence the attachment of the radionuclides.

Table 4.1: Extraction efficiencies for different aerosols and the used carrier gases are listed. Extraction efficiency is the ratio of radionuclides produced in the recoil chamber to the number of radionuclides obtained at the end of the capillary. The recoil chamber, the capillary length and diameter are not identical in all measurements listed here. In case of multiple references, the minimum and maximum of the highest measured efficiency is given.

| Aerosol material | Carrier gas | Transport efficiency | Reference |
|---|---|---|---|
| KCl | He | 35 - 83% | [Brü79, Brü83, Maz80, Gün93] |
| KCl | $N_2$/Ar | 43% | [Brü79] |
| KCl | $N_2$/Ar | 43% | [Brü79] |
| C | He | 51 - 72% | [Eib09, Eib10] |
| $PbCl_2$ | He | 55% | [Kar82, Brü83] |
| $PbI_2$ | He | 55 - 65% | [Brü83, Ich02] |
| $MgCl_2$ | He | 52% | [Brü83] |
| $ZnBr_2$ | He | 55% | [Brü83] |
| $CdBr_2$ | He | 56% | [Brü83] |
| $C_2H_4$ | $C_2H_4$ | 75% | [Aum79] |
| $CO_2$ | $CO_2$ | 25 - 60% | [Aum79, Sil77] |

Tab. 4.1 lists which kind of aerosol material were used at the research reactor TRIGA-Mainz or other facilities for the transport of radionuclides. An extraction efficiency in the range of 25% to 80% have been achieved, which is in most of the cases equivalent for all elements except for halogenes and noble gases, which do not attach to the aerosol particles.

Due to the fact that the radionuclides are extracted from the recoil chamber with the gas-jet method at TRIGA-SPEC, it is necessary to release the fission products from the aerosol particles and reionize them in an ion source. In order to obtain high yields for all elements, it is necessary to have an ion source with an element independent ionization efficiency of the same order of magnitude. In addition to that, the ion source has to be capable of dealing with the high gas load from the carrier gas. In the next section 4.3 several types of ionization mechanisms are discussed.

## 4.3 Ionization methods

Ion sources play an important role in many physics experiments, since the creation of an ion beam of the desired species is a mandatory step to perform the experiment. The ion source has to fulfill two tasks: First, the ionization of the desired particles by removing (at least) one electron from the atoms or molecules[1]. Thus, an ion source contains usually a plasma of electrons, ions, and the neutral species. The reaction energy necessary for the ionization process is therefore at least the first ionization energy $E_i = e\phi_i$ of the atoms or molecules, where $\phi_i$ is the ionization potential and $e$ the elementary charge. Second, the extraction of the ions from the

[1]This chapter is restricted to the creation of singly-charged positive ions.

ion source plasma and the formation of an ion beam, which matches the requirements in intensity, energy and emittance of the following accelerator or experiment.

Due to the difference in the ionization potential and the physical and chemical properties of the elements of interest many kinds of ion sources have been developed, most of the optimized for a specific task [Wol95]. In this section the different ionization processes of the ion sources used at the TRIGA-SPEC experiment are discussed. A more detailed view of electron cyclotron resonance (ECR) ion sources and laser ablation ion sources is given, both of them cover a large part of this thesis. The detailed description of the experimental setup of the different ion sources is found in section 5.2. The following information are based on [Wol95, Zha99, Bro04, Gel96].

### 4.3.1 Surface ionization

Ions may be created on hot metal surfaces by the so called contact or surface ionization [Tay33]. Neutral atoms of the desired species are deposited on the hot surface and are evaporated again. If the work function $W_A$ of the surface material is higher than the ionization potential $\phi_i$ of the atom, there is a probability that the atom leaves an electron on the metal surface, which is transmitted by quantum tunneling into the Fermi band of the metal. This probability is expressed by the Langmuir-Saha-Equation [Lan25]:

$$\frac{n_i}{n_a} = \frac{g_i}{g_a} \exp\left(-\frac{(e\phi_i - W_A)}{kT}\right), \tag{4.12}$$

where $n_i$ and $n_a$ are the rate of ions and atoms released from the surface, and $g_i$ and $g_a$ are the corresponding atomic weighting factors, given by $(2J + 1)$ with the total angular momentum $J$.

The ionization probability depends on the ionization potential $\phi_i$ and the work function $W_A$ and decreases exponentially if the ionization potential is higher than the work function of the surface (see Fig. 4.4(a)). Therefore, materials with a high work function such as tungsten ($W_A = 4.54$ eV), iridium ($W_A = 5.4$ eV) or platinum ($W_A = 5.32$ eV) are good choices as contact ionizer [Alt93]. Ionization efficiencies close to 100% are reached for alkali elements. Since the highest work function is less than 6 eV, there is no possibility to get high ionization efficiencies for other elements with a high ionization potential, even at high temperatures (see Fig. 4.4(b)).

The evaporation of the material from the surface needs to be considered in addition to the ionization efficiency. If more than a mono-layer of atoms condenses on the surface, the work function of the surface is reduced and a lower ionization probability is obtained. However, if the evaporation rate of the surface is too high, the atoms cannot get in thermal equilibrium with the surface, which also reduces the ionization probability. The sticking time to the surface is optimal in the range of $10^{-5}$ to $10^{-3}$ seconds, so that the ionizing surface is partially covered with a mono-layer of the atoms of interest. A measurement of the ionization rate as function of the temperature for sodium can be found in [Kaw90] as example for the typical behaviour of the temperature dependence. The highest yield for alkali ions is obtained in the range of 1000 to 1500 K [Zha99].

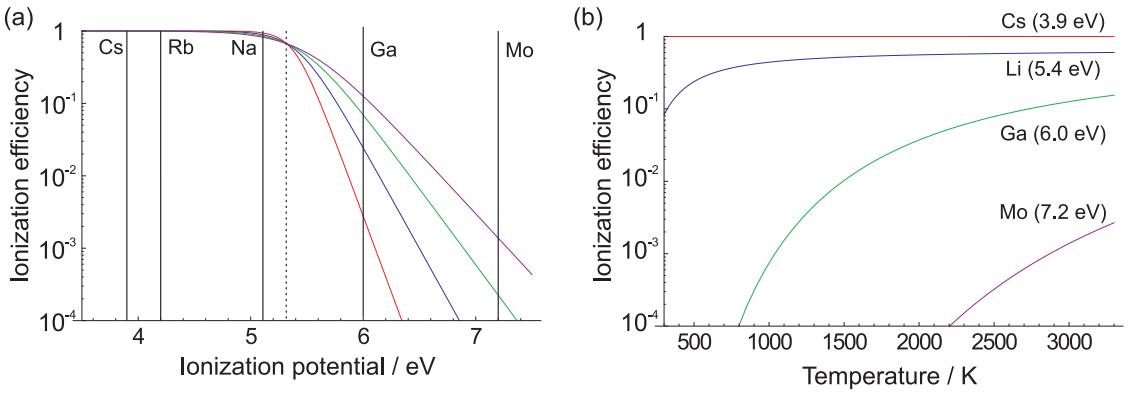


Figure 4.4: (a) Surface ionization efficiency on a platinum surface ($W_A = 5.32$ eV) according to the Langmuir-Saha equation (4.12) as function of ionization potential for different surface temperatures: 1200 K (red), 1800 K (blue), 2400 K (green) and 3000 K (purple). The work function of platinum is marked with a dashed line. (b) Surface ionization efficiency on a platinum surface as function of the temperature for four different elements: Cs (red), Li (blue), Ga (green), and Mo (purple). The ionization potentials of these element are given in brackets. Work functions and ionization potentials were taken from [Wol95, Alt86, Alt93].

For some elements with high melting points, in particular refractory elements such as molybdenum, tantalum, and tungsten, the temperature to evaporate the material from the surface cannot be reached. Therefore, surface ionization is only suited to create positive singly-charged ions of alkali elements with high efficiency. Earth-alkali, rare earth, and transuranium elements can be obtained with moderate ionization efficiencies [Alt93].

Surface ion sources are used at TRIGA-SPEC to provide beams of stable ions, mainly $^{133}$Cs, for transport optimization, off-line tests, and mass calibration for mass measurements. The construction of these ion sources is described in 5.2.

### 4.3.2 Electron impact ionization

Electron impact ionization is the process of moving bound electrons from an atom or molecule into the continuum by bombardment with energetic electrons. The minimum kinetic energy $E_e$ of the incident electron has to be larger than the first ionization energy of the atom or molecule $E_e > E_i = e\phi_i$ to obtain ionization. The reaction can be expressed by the following reaction equation:

$$A + e^- \rightarrow A^+ + 2e^-, \tag{4.13}$$

where $A$ denotes an atom or molecule and $A^+$ its ion. The ionization rate per electron $\nu_i$ is calculated by the following equation:

$$\nu_i = \frac{1}{\lambda} v_e = n \left\langle \sigma_i(v_e) v_e \right\rangle , \tag{4.14}$$

where $\lambda$ denotes the mean free path of the electrons, $n$ the density of the atoms, $\sigma(v_e)$ is the velocity dependent ionization cross-section, and $v_e$ the electron velocity.

The cross section for the electron impact ionization $\sigma_i$ as a function of the electron velocity $v_e$ or electron energy $E_e$ is calculated by the semi-empirical formulas of Müller and Salzborn [Mül80] or Lotz [Lot67]. Fig. 4.5 shows the ionization cross section as function of the electron energy $E_e$.

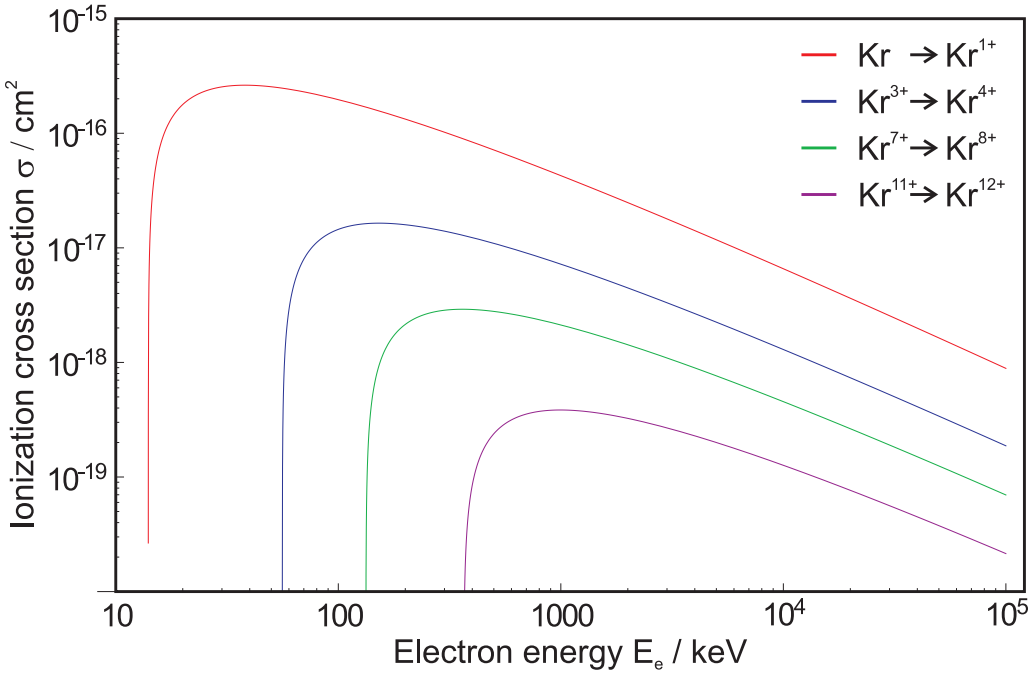


Figure 4.5: Cross section of the electron impact ionization as function of the electron energy for krypton according to [Mül80]. The lines represent the ionization cross-sections for different charge states. The ionization energies were taken from [Car70].

The cross section is zero for $E_e < e\phi_i$. The ionization cross-section for atoms can be approximated close to the ionization threshold by,

$$\sigma_i = \alpha(E_e - e\phi_i)^n, \tag{4.15}$$

where $\alpha$ is a constant and $n = 1.1269$. The ionization cross section has a maximum at about three to four times the ionization energy, since the velocities of the bound and the incident electrons are equal in this range. At higher kinetic energies the cross section decreases due to shorter interaction times between the incident and the bound electron.

Electrons may be produced from a hot filament and accelerated with electric fields to the kinetic energy with the highest ionization cross section. This method is used in electron impact ion sources to ionize gas in an ionization region, where the electron energy is well defined by the electric potential. The optimum cross section can be reached in principle for all elements by adapting the electron energy in a controlled way to ionize even elements with a high ionization potential such as noble gases. Therefore, this method has an advantage compared to the surface ionization method. This method is well suited to ionize gases by increasing the partial pressure of the desired gas in the interaction region.

Electron impact ionization takes also place in high temperature plasmas, which is found for example in an ECR ion source (see Sect. 4.4). In this case the electrons have an energy distribution, which is defined by the plasma conditions, so that only a fraction of the electrons has suitable energies for a high ionization cross section. If the energy distribution is known, the average ionization probability can be calculated by the following term:

$$\langle P_i \rangle = \langle v_e n_e(v_e) \sigma_i(v_e) \rangle \,. \tag{4.16}$$

If the electron temperature $kT_e$ is in the order of one electron volt, the high energy tail of the energy distribution in the plasma is responsible for the ionization.

Electron impact ionization is also used to produce highly-charged ions by removing electrons in subsequent steps from an atom. Ions sources using an electron beam for the ionization are called electron beam ion trap (EBIT) or electron beam ion source (EBIS). Highly charged ions may also be produced in ECR plasmas, if the ions are confined in the plasma, so that the step-wise ionization can occur.

### 4.3.3 Laser ionization

Atoms may also be ionized by interacting with photons. The most monochromatic light source with the highest intensity is the laser, which is the tool of choice to produce ions with photons. Two fundamentally different approaches exist for the ion production, which have to be distinguished: the resonant laser ionization, which is based on exciting and ionizing an atom by resonant absorption of photons, and the laser ablation ionization, which creates ions from a plasma formed by heating a solid sample with high intensity laser pulses. Both methods are introduced in this section. The resonant laser ionization is of interest for the development of a new on-line ion source (see Chap. 8) and the laser ablation method is used in an off-line ion source at TRIGA-TRAP [Smo08a, Smo09], which is described in Sect. 5.2.

Ions may be created by irradiating photons with energies that are resonant to electronic transitions in the atom. Thereby, an electron is excited and subsequently removed leaving an ion behind. This process is called resonant laser ionization. The energy of a single photon in the visible or ultraviolet spectral range ($E_{ph} \approx$ 3 eV) is for all elements smaller than the ionization energy $e\phi_i$, so that a bound electron cannot be removed directly by absorption of one photon. Therefore, it is necessary to populate an excited state first before the electron can be transferred into the continuum by absorbing a second photon from the same or another laser. An advantage of this method is that the excitation energies of the excited states are unique fingerprints of each element. Therefore, if narrow-band lasers are used for the excitation, a highly selective ionization can be achieved. The ionization cross-section is much larger for an excitation via a resonant transition than a non-resonant excitation with a two-photon excitation. Several excitation schemes are possible for a selective ionization [Mau04]. Excitation with one or two resonant transitions is possible, where the latter one has the higher selectivity. Each transition requires its own laser with a matching wavelength. In addition, an autoionizing state above the ionization energy can be addressed to increase the ionization cross section. Another possibility for a selective ionization is to populate a Rydberg state in the atoms by

a resonant (selective) excitation, and ionize the Rydberg atoms by field ionization [Let87].

The resonant laser ionization requires that atoms of the desired element are provided. This method has been applied, e.g. to samples heated by a filament or in a hot cavity [Wen00], or to laser ablated atoms [Mau04] in off-line measurements. On-line resonant laser ion sources for short-lived nuclides have been used with two approaches, with hot cavities, e.g. at ISODLE (RILIS [Fed08]) or with gas cells, e.g. at LISOL [Huy92] in Leuville-la-Neuve, Belgium, where radioactive ions are stopped and neutralized in a recoil chamber and ionized either in the gas cell or in the sextupole ion guide (SPIG) [Kud09]. Resonant laser ionization is especially useful at on-line facilities, since several orders of magnitude in the suppression of isobaric contaminants can be gained, and the number of accessible elements can be increased [Fed08]. A recent new developement in that context is the Laser Ion Source Trap (LIST) technique where the combination of radiofrequency quadrupole trap and laser ionization is used to increase the selectivity of the conventional RILIS method [Bla03b, Sch10].

The laser ablation is a method which uses short ($\approx 10^{-13}$-$10^{-8}$ s) laser pulses with high power densities ($\approx 10^{9}$-$10^{14}$ W cm$^{-2}$) to remove macroscopic amounts of material from the surface of a solid sample. The phenomenology of laser ablation is quite broad, since several orders of magnitude in pulse duration and power are involved, and the nature of this process depends fundamentally on these two parameters [Rus02, Lor06].

At low laser pulse energies below the ablation threshold, only single atoms, electrons or ions may be released from the surface, whereas above the ablation threshold substantial fraction of the solid is removed and expands into the vacuum in a plume of vapor. As the laser intensity is further increased the plume is partially ionized during the laser pulse [Cal95], since electrons are released and accelerated by photons from the incoming light wave by inverse bremsstrahlung in ion-electron collisions. Thereby, a plasma is formed which contains ions of the material of the solid sample. Due to the high laser power densities ($10^{8}$-$10^{16}$ W / cm$^{2}$) sufficiently high temperatures in the order of $10^{4}$ K are reached [Lor06] to even evaporate and ionize materials with a high meting point, such as tungsten (see Sect. 7). The plasma can partially shield the surface from the incoming light wave (see Sect. 4.4). This reduces the ablation efficiency, since the effective energy which is deposited in the surface is decreased. A large increase in the ablated mass is observed, if the threshold for explosive boiling is reached. A phase transition into the metastable two-phase region takes place and large bubbles of liquid and gas are released on a microsecond timescale. At even higher intensities, the electron density above the surface increases rapidly in the beginning of the laser pulse by thermionic and photoelectric emission before material is released from the surface.

Laser ablation has been studied for laser intensity in the region slightly above the laser ablation threshold to reveal the exact ablation process [Kel99, Lor03, Lor06]. In the following the processes for different pulse durations are discussed. For pulses shorter than the time scales of collective motions of the atoms and of heat conduction, which is on the order of $10^{-11}$ s, the energy is transferred rapidly to the electrons of the solid, which form a hot, dense, overcritical electron gas. Subse-

quently, the hot electrons attempt to thermalize with the phonons in the solid, so that ultimately the material starts to melt, and the incoming photons interact with the growing liquid phase by inverse bremsstrahlung [Lor06]. The liquid phase can neither expand or cool on this time scale. Two different processes are responsible for the material release depending on the laser energy. Either by a transition into the gas-liquid two-phase region takes place, which results in a phase explosion, or a the liquid phase undergoes a fragmentation process into a heterogeneous, clustered fluid as it expands into the vacuum [Per02].

For picosecond pulses with pulse durations $> 10^{-11}$ s, the solid surface material becomes liquid by homogeneous and heterogeneous melting. The liquid phase can expand and is cooled via heat conduction during the irradiation process. A transition into the two-phase region does not take place, and phase explosion does not occur. The liquid expands relatively slowly into the vacuum and forms a heterogeneous, fragmented fluid through a so called "trivial" fragmentation [Per03].

The ablation process for nanosecond pulses is not fully understood yet. The solid-liquid transition is expected to take place at the equilibrium melting temperature [Fab86]. For the material release, a subsequent transition into the metastable phase, where explosive boiling or phase explosion can occur, has been proposed [Kel99], contrary to a second-order phase transition at the critical point [Lor03].

Laser ablation is used in mass spectrometry to produce ions from solid samples [Bla02, Cha07, Smo09]. In particular, it is suited to produce carbon cluster ions as mass reference in a large range (12 u $< m <$ 288 u) [Bla02, Smo09], as well as ions of rare-earth metals for mass measurements [Ket11]. It is applicable for samples containing at least $10^{15}$ atoms of nuclides with a half-life larger than one year. For short-lived nuclides with low yields, this method is not suitable, since a large fraction of the material is evaporated as gas or as clusters, so that the ionization efficiency is comparably low. Furthermore, the time that ions remain on the surface until they are released may prevent the extraction of nuclides with half-lives less than one second, even with simultaneous laser bombardment. Therefore, this ionization method was used to provide ions for off-line measurements, such as the $Q$-value and mass measurements reported in Chap. 7.

## 4.4 Electron-cyclotron-resonance ion source

The electron-cyclotron-resonance (ECR) ion sources use electron impact ionization for the ion beam formation. ECR ion sources are in use at many accelerator facilities for beam injection, since they can provide high intensity beams of highly charged ions. Whereas other electron impact ionization ion sources use a filament and a DC acceleration field to generate energetic electrons, the ECR ion source is a filament free ion source which uses a microwave discharge to create a plasma and resonant heating of electrons in a magnetic field by microwave radiation. Thereby, hot electrons are created which have sufficiently high energies to ionize any element and even create highly-charged ions. The feasibility of using an ECR ion source as an on-line ion source at TRIGA-SPEC has been investigated within this thesis. In particular, the injection of the gas-jet with fission products attached to the aerosol particles

into the ECR ion source has been studied. Since the ECR ion source offers the possibility to ionize all elements created in the neutron-induced fission process and a low maintenance due to the operation without any filament, the ionization efficiency of the fission products has been investigated. Therefore, the physics of the ECR ion source are described in this section in more detail. The following discussion is based mainly on the textbooks [Gel96] and [Bro04].

An ECR ion source with its basic components is shown in Fig. 4.6. The ion source consists of a magnetic field configuration, which confines the charged particles of the plasma by the magnetic mirror effect and provides the so-called resonance surface, where the conditions for the cyclotron heating of the electrons by the microwave is matched. The magnetic field is provided by coils, or permanent magnets, or a combination of both. The ion source chamber acts as a multi-mode cavity for the microwave, which is injected into the ion source by a connected wave guide. A second connection to the ion source chamber provides the possibility to inject samples for ionization into the source. Gaseous samples are naturally the best choice for the ionization in an ECR ion source. The atoms or molecules of the sample are reflected from the walls of the plasma chamber and pass multiple times through the plasma, so that in principle high ionization efficiencies above 90% can be reached [Jar02]. Other samples are evaporated by an oven or injected by other methods discussed below. An electric potential between the ion source chamber and the extraction electrode extracts ions from the plasma and forms the ion beam. In the following some basic plasma properties are introduced first.

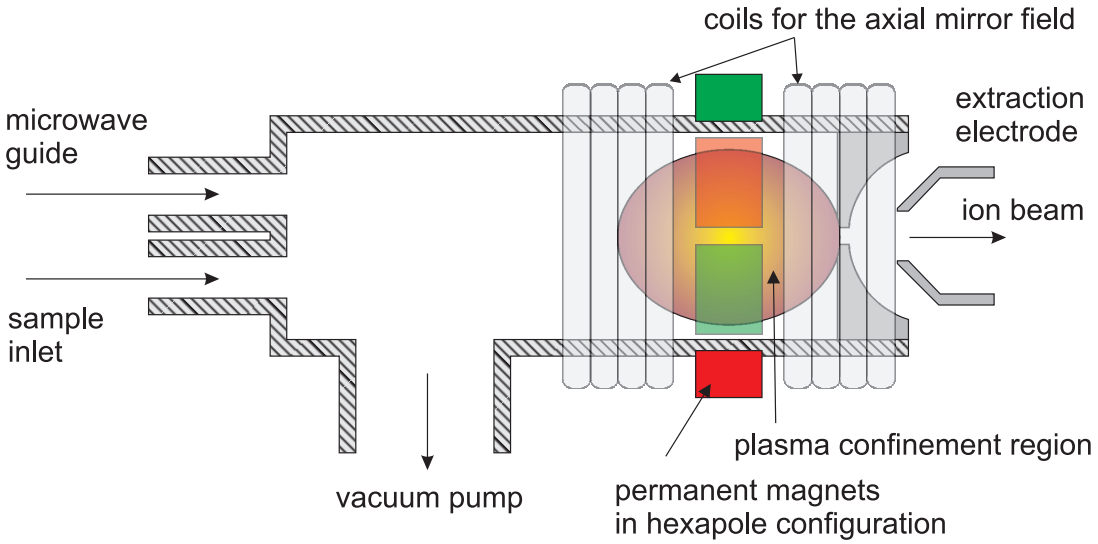


Figure 4.6: Schematic drawing of an ECR ion source with its basic components. For details see text.

If a gas is heated up, the thermal energy becomes high enough to release electrons from the atoms and the gas becomes a plasma. The interaction of the particles in the plasma is not only by collisions as in the gaseous phase but the charged particles also experience the electromagnetic interaction. The plasma is characterized by the density of electrons $n_e$, ions $n_i$, and neutrals $n_n$. The electron density $n_e$ is often also called "plasma density".

The plasma conserves charge neutrality. If there was a region with a space charge in the plasma, electrostatic forces would occur, which attract particles of the opposite charge until charge neutrality is reached. Therefore, the ion density is identical to the electron density $n_i$=$n_e$, or in case that also multiply-charged ions are present,

$$\sum_s Q_s n_s = 0, \tag{4.17}$$

where $s$ is an index parameter of all particles species in the plasma, $Q_s$ the charge of the particle, and $n_s$ the particle density.

However, on a small scale there can be violations of the charge neutrality due to the thermal motion of the charged particles. Suppose a charged particle is displaced from its position where charge neutrality is conserved, it experiences a repelling force. For small amplitudes this force is assumed to be harmonic. This causes an oscillation in the plasma for particles with charge $Q_s$ and mass $m_s$ the plasma oscillation frequency $\omega_{p,s}$ is:

$$\omega_{p,s} = \sqrt{\frac{n_s Q_s}{m_s \epsilon_0}}. \tag{4.18}$$

This is the natural collective oscillation due to charge displacement by thermal motion of charged particles in the plasma. The electron plasma oscillation frequency $\omega_{p,e}$, also often just called 'plasma frequency', is the highest oscillation frequency in an ECR plasma and is of importance for the interaction between the plasma and external fields.

The distance scale in which space-charge fluctuations in the plasma cancel out is called Debye length $\lambda_D$, also called screening length, since this is also the distance over which the field of a test particle extends in the plasma. It is given by:

$$\lambda_D^2 = \frac{\epsilon_0 k T_e}{e^2 n_e}, \tag{4.19}$$

where $\epsilon_0$ is the permeability of the vacuum, $k$ the Boltzmann constant, and $T_e$ the electron temperature.

At the boundary of the plasma, such as the ion source vacuum chamber, the properties of the plasma change. Due to a higher mobility of the electrons in the plasma more electrons are lost to the wall than ions. Due to this effect, the charge neutrality is not preserved at the plasma boundaries and the plasma is on a positive potential compared to the walls of the vacuum chamber. This potential difference is called plasma potential $V_p$, which is typically of the magnitude of three to four times $kT_e$. The plasma boundary region is also of the scale of the Debye length.

External static electric fields are screened similar to as a conductor shields itself from the penetration of external fields. The plasma boundary region, which is also called plasma sheath, increases compared to the situation without an external field. The thickness of the plasma sheath $d_{sheath}$ is approximately given by:

$$d_{sheath} \approx \lambda_D \sqrt{\frac{eV}{kT_e}}, \tag{4.20}$$

where $V$ is the applied potential difference. This fact is important for the ion extraction, since there is usually a high voltage applied between the ion source

chamber and the extraction electrode. The ions that are extracted from the plasma are only those inside the plasma sheath, all other charged particles are unaffected by the extraction field.

A plasma inside a magnetic field is also called magnetoplasma, since it has different properties compared to a field-free plasma. The presence of the magnetic field forces the charged particles on a helical orbit due to the Lorentz force:

$$\vec{F} = q(\vec{v} \times \vec{B} + \vec{E}). \tag{4.21}$$

The charged particles move in case of a collision-free motion around a magnetic field line with the cyclotron frequency $\nu_{c,s}$:

$$\nu_{c,s} = \frac{1}{2\pi}\frac{Q_s B}{m_s}. \tag{4.22}$$

If the collision frequency of the particles $\nu_{coll,s}$ is small compared to the cyclotron frequency $\nu_{coll,s} \ll \nu_{c,s}$ the plasma is called magnetized. Otherwise the path of the particle motion is mainly determined by scattering and not by the cyclotron motion.

The interaction of the plasma with external magnetic fields allows to provide a confining structure for the plasma due to the magnetic mirror effect. A long confinement time of the plasma increases the interaction time between ions and electrons, which increases the ionization efficiency especially for higher charge states. Therefore, it is favorable to have long confinement times of charged particles in the plasma.

Due to their helical motion the charged particles have a magnetic moment $\mu$, which is adiabatic constant during the motion. The magnetic moment $\mu$ is given by

$$\mu = \frac{m v_r^2}{2B}, \tag{4.23}$$

where $v_r$ is the velocity of the radial motion perpendicular to the magnetic field lines. Thus, the radial velocity increases if the charged particle moves into a higher magnetic field region. This leads to a decrease of the axial velocity component $v_a$ due to the energy conservation. In case the axial energy is not high enough to pass the maximum of the magnetic field strength, the charged particle is reflected into the direction of lower magnetic field strength. This effect is called the magnetic mirror effect, which is used to confine the plasma in ECR ion sources in a "minimum B-field" configuration[2]. The magnetic confinement is not perfect, since not all charged particles with all velocities are confined. If the angle between the velocity and the magnetic field lines $\theta$ is too small the charged particles can pass the magnetic field maximum. The loss cone with opening angle $\theta$ in the velocity space is defined by:

$$\sin\theta = \frac{v_r}{v_a} = \sqrt{\frac{B_{min}}{B_{max}}} = \sqrt{\frac{1}{R_m}}, \tag{4.24}$$

where $B_{min}$ and $B_{max}$ are the minimum and maximum of the magnetic field strengths, respectively, and $R_m$ is the so-called mirror ratio of a magnetic mirror field. This

[2]The same effect is also important for the TOF-ICR method for the cyclotron frequency detection in the Penning trap, which makes use of the increasing axial energy if the ions moves to a lower magnetic field region (see Sect. 3.3).

Table 4.2: Magnetic field ratios to the resonant magnetic field strength $B_{res}$ for an ECR ion source [Bro04]. In the last column the magnetic field strength values for a 2.45 GHz ECR ion source are given.

| Position | $B$ / $B_{res}$ | $B$ / mT (2.45 GHz) |
|---|---|---|
| Maximum on injection side on center axis | $\approx 4$ | 350 mT |
| Maximum on ejection side on center axis | $\approx 2$ | 175 mT |
| Minimum field strength | $\approx 0.8$ | 70 mT |
| Maximum in radial direction | $> 2$ | $> 175$ mT |

type of confinement is quite convenient for ECR ion sources, since the ionization is done by electrons, which were heated selectively in their cyclotron motion and therefore have a large radial velocity component. Thus, hot electrons are well confined and pass several times through the ECR plasma. The power dissipation of the ion source is therefore lower compared to an electron beam ion source (EBIS), where the electrons pass only once through the ionization region.

The magnetic mirror field in an ECR ion source is either made by permanent magnets or by two coils as illustrated in Fig. 4.6. They provide two magnetic field maxima on the center axis of the ion source and a minimum between the two coils. In order to enhance the radial confinement time a magnetic hexapole field is added around the center region so that the magnetic field increases also in the radial direction. Thereby, the diffusion of particles to the wall in the radial direction is suppressed. The electron cyclotron heating is discussed below, but at this point it is important to mention that the absolute field strength of the magnetic field depends on the microwave frequency $\nu_{rf}$ of the ion source, since the resonance condition for the electron cyclotron heating needs to be matched:

$$B_{res} = 2\pi\frac{m_e}{e}\nu_{rf} = 35.9 \text{ mT/GHz} \times \nu_{rf}, \tag{4.25}$$

where $B_{res}$ is the resonant magnetic field strength, where the cyclotron frequency of the electrons match the microwave frequency. In between the magnetic field minimum and maximum there is a closed surface with the resonance field strength $B_{res}$. This is the natural parameter to define the magnetic field configuration of an ECR ion source. Tab. 4.2 lists the relative field strength to the resonance field strength $B_{res}$ and the minimum field strength $B_{min}$ at the most important positions for highly efficient ECR ion sources [Bro04]. The mirror ratio on the extraction side is usually chosen lower than on the injection side to favor the loss of particles from the plasma on the extraction side, where they are extracted as an useful ion beam. The magnetic field configuration of the ECR ion source used in this thesis is made of permanent magnets only for a microwave operating at 2.45 GHz (see Sect. 5.2).

The interaction of the electric fields with the plasma is rather well understood, whereas the calculation of heating rates for the cyclotron heating is complex. Therefore, only the principle of microwave absorption in the plasma is discussed below based on [Eld72, Gel96]. More detailed calculations of the electron cyclotron heating can be found in literature [Eld72, Gir04].

Static electric fields cannot penetrate the plasma further than the depth of the plasma sheath $d_{sheath}$ as discussed above. Electromagnetic waves can penetrate the

plasma, if the frequency of the external wave $\nu_{rf}$ is larger than the plasma frequency $\nu_{p,e}$, since the electrons in the plasma can react to external perturbations with lower frequencies. Thus, the plasma acts like a high-pass filter for electromagnetic waves. Therefore, it is necessary to use microwave radiation to penetrate the plasma and reach the resonance zone in the center.

At this point it is important to mention that the plasma frequency $\nu_{p,e}$ increases with the electron density. Therefore, a microwave with the fixed frequency $\nu_{rf}$ plasma can penetrate the plasma only up to the critical electron density $n_{crit}$:

$$n_{crit} = \frac{4\pi^2 \epsilon_0 m_e}{e^2} \nu_{rf}^2. \tag{4.26}$$

This limit is of importance for the ionization probability of a particle, such as an aerosol particle, moving through the plasma. The electron density is fundamentally limited in an ECR ion source by its operating microwave frequency. It is possible to generate also over-dense plasmas with a higher electron density than the critical density $n_{crit}$. It is assumed that the microwave is in this case absorbed in non-linear processes and a turbulent plasma is generated [Sti92, Gel96]. The properties of over-dense plasmas are much lower electron temperatures than below the critical density and therefore also a lower charge-state distribution of the ions. Therefore, under-dense plasmas are generally favored. However, over-dense plasmas with low-energy electrons are still useful for the creation of singly-charged ions at high ambient pressures. Usually, 2.45 GHz ion sources are used for this purpose. Therefore, this is the realistic scenario for the plasma properties in a gas-jet coupled ECR ion source. In over-dense plasmas plasma internal waves need to be considered for the heating [Gel96], which leads to a more complicated heating procedure, which is beyond the scope of this work. In the following, the interaction of external waves with under-dense plasmas and the power absorption at the resonance zone are introduced.

The plasma affects the propagation of electromagnetic waves. In magnetoplasmas, as in an ECR ion source, the anisotropy of the conductivity affects the wave propagation in particular. This expresses itself in the permittivity tensor of the plasma, which is deduced for a cold collisionless plasma to be [Suc98, Sti92]:

$$\epsilon = \begin{pmatrix} \epsilon_1 & i\epsilon_2 & 0 \\ -i\epsilon_2 & \epsilon_1 & 0 \\ 0 & 0 & \epsilon_3 \end{pmatrix}, \tag{4.27}$$

where the magnetic field is in $z$-direction and the matrix entries $\epsilon_i$ are functions of $\nu_{p,e}$, $\nu_{c,e}$ and $\nu_{rf}$ only. From this permittivity tensor it is deduced that only four different kinds of waves can propagate through the plasma. For waves propagating along the magnetic field lines with $\vec{k} \parallel \vec{B}$ there are left-hand and right-hand circularly polarized waves, called L- and R-waves, respectively, and for waves propagating perpendicular to the magnetic field $\vec{k} \perp \vec{B}$ there is the ordinary wave (O-wave), which is linearly polarized and parallel to the magnetic field, and the extraordinary wave (X-wave), which has an oscillating electric field vector in the plane perpendicular to the magnetic field lines. In the following the resonances of these waves in the plasma are discussed. For this purpose the dispersion relation $n(\nu_{rf})$ for these polarization components is given and the wave cut-offs and resonances occur at singularities of the refractive index.

- **R-wave,** $\vec{k} \parallel \vec{B}$
  The R-wave is the most important polarization component for the cyclotron heating. The electric field vector oscillates in the same direction as the cyclotron motion of the electrons in the plasma. Therefore, it is intuitively clear that R waves are responsible for the cyclotron heating.

  In the cold plasma approximation the dispersion relation for R waves is:

$$n^2 = \frac{k^2c^2}{\omega^2} = 1 - \frac{\nu_{p,e}^2}{\nu_{rf}(\nu_{rf} - \nu_{c,e})}, \tag{4.28}$$

  which has a singularity at the electron cyclotron frequency $\nu_{rf} = \nu_{c,e}$, which indicates that the radiofrequency is absorbed at the electron cyclotron frequency. A more well-defined result is obtained if a finite electron temperature is included. The refractive index becomes [Eld72]:

$$n^2 = 1 - \frac{A(\nu_{rf} - \nu_{c,e})}{k^2v^2} + i\frac{B\sqrt{\nu_r f}}{kv} \exp\left[-\frac{(\nu_{rf} - \nu_{c,e})^2}{8\pi^2k^2v^2}\right], \tag{4.29}$$

  where $A$ and $B$ are constants, and $v^2$ is the average squared radial velocity of the electrons. The imaginary part of the refractive index corresponds to the absorption of the wave by the plasma. Its absolute value is only different from zero close the $\nu_{rf} = \nu_{c,e}$, which leads to the same result as the cold plasma approximation. At finite temperatures electrons absorb the wave also outside of the resonance surface due to the Doppler shift caused by their thermal motion [Gir04].

- **L-wave,** $\vec{k} \parallel \vec{B}$
  The electric field of the L-wave oscillates in the opposite direction of the electron cyclotron motion. The dispersion relation for L-waves is given by:

$$n^2 = 1 - \frac{\nu_{p,e}^2}{\nu_{rf}(\nu_{rf} + \nu_{c,e})}, \tag{4.30}$$

  which has its only singularity at $\nu_{rf} = 0$, which means there is no absorption of the L-waves in the plasma.

- **O-wave,** $\vec{k} \perp \vec{B}$**,** $\vec{E} \parallel \vec{B}$
  The O-wave is a linearly polarized wave, which has an electric field parallel to the magnetic field lines. Therefore, it does not contribute to the cyclotron heating. In the cold plasma calculation the dispersion relation is given by:

$$n^2 = 1 - \frac{\nu_{p,e}^2}{\nu_{rf}^2}, \tag{4.31}$$

  with a singularity at $\nu_{rf} = 0$. Thus, the O-waves are also not absorbed in the plasma. However, at high temperatures the O-wave increases the axial energy of the electrons and scatters hot electrons into the loss cone [Eld72]. The average electric field of the O-wave is zero for electrons with a low cyclotron radius, but if the cyclotron radius of the electron is a quarter of the wavelength of the microwave, the relative phase between the O-wave and the electron stays constant. In this case the motion parallel to the magnetic field lines is heated.

- **X-wave, $\vec{k} \perp \vec{B}$, $\vec{E} \perp \vec{B}$**
  The X-wave also contribute to the cyclotron heating [Yad04], since the electric field vector rotates in either direction in the plane perpendicular to the magnetic field. It is partially a longitudinal wave. Its dispersion relation is given by:

$$n^2 = 1 - \frac{\nu_{p,e}}{\nu_{rf}} \frac{\nu_{rf}^2 - \nu_{p,e}}{\nu_{rf}^2 - \nu_{UH}}, \tag{4.32}$$

  with a resonance at the upper hybrid frequency $\nu_{UH} = \sqrt{\nu_{p,e}^2 - \nu_{c,e}^2}$.

Thus, only R-waves and X-waves contribute to the cyclotron heating. If the microwave is injected axially into the ion source, it is favorable to use a right-hand circularly polarized microwave for efficient cyclotron heating. The microwave can be converted in the waveguide or by using a proper antenna. The latter method is applied in the ECR ion source, which was tested for the on-line coupling of TRIGA-SPEC.

The average electron energy or temperature depends on the microwave power and frequency. 2.45 GHz ECR ion sources have electron temperatures in the order of 10 eV, so that singly-charged ions can be produced. Higher-frequency ECR ion sources reach higher charge states and have electron temperatures up to a few 10 keV.

ECR ion sources are often used to produce an ion beam for the injection into an accelerator [Nak10]. Depending on the application, beams of hydrogen, helium, or highly-charged heavy ions can be produced. These ion sources are operated with high power and high frequencies and are optimized on high current to provide the highest yields for the experiments. However, for the efficient ionization of radionuclides with a limited yield the ionization efficiency of the injected material is of higher importance.

One application, which is particular of interest for the development of an efficient on-line ion source for TRIGA-SPEC, is the development of highly-efficient ECR ion sources for singly-charged ions at GANIL [Jar02, Jar10]. The aim of this development is to build a radiation-hard ion source, which contains a target for the production of radionuclides. Therefore, an efficient conversion of the injected material into an ion beam is desired. Ionization efficiencies of more than 90% are obtained (except for helium), and even ions of non-volatile elements that are produced from gaseous molecules, such as sulfur from $SO_2$ or $SF_6$, are extracted with a total yield of more than 90 %. Thus, this ion source provides an excellent ion confinement, so that almost all ions leave the plasma through the extractor as part of the ion beam.

These properties are also desired for a gas-jet coupled ion source. However, the fundamental difference, which needs to be considered for aerosol particles or in general non-volatile atoms or molecules, is that gaseous particles are reflected from the ion source chamber and pass several times through the plasma until they are ionized. Non-volatile particles most likely pass once through the plasma and remain on the cold walls of the ion source chamber and are lost for the ionization process. While gases are directly injected into source, the production of ion beams from non-volatile elements requires additional effort. One possibility is, as mentioned above, to use a gaseous compound of a metallic element and evaporate it into the

ion source. The molecules are broken apart in the ECR plasma and metallic ions can be extracted. For elements with moderate boiling points, it is possible to use an oven to evaporate the material. However, the condensation of the vapor on the walls of the ion source chamber needs to be considered. Although a fraction of the deposited metallic atoms may be released from the wall by sputtering from plasma electrons and ions, the time that the atoms remain on the surface, which is in the order of hours or days, is too long to recover short-lived radionuclides. Metals with high boiling points, such as the refractory elements, are preferably ionized with the insertion technique [Jac88]. A solid sample is placed inside the ECR plasma, so that the sample is bombarded with hot electrons and ions. Thereby, the sample absorbs a fraction of the microwave power and temperatures with sufficiently high vapor pressures of refractory elements are reached. The drawback of this method is that the sample disturbs the plasma confinement, depending on the size and position. Therefore, the evaporation with an oven is generally preferred, if possible, since it yields higher ionization efficiencies.

The ECR ion source used in this thesis was developed for ion-ion collision studies [Lie92] and has been adapted for the on-line coupling at TRIGA-SPEC. Its technical details are described in Chap. 5.2. The ion source has been used in off-line tests, as well as in the first on-line coupling tests, which are described in Chap. 6. The final aim of the on-line coupling is to provide a radioactive beam for the Penning-trap mass spectrometer TRIGA-TRAP and the collinear laser spectroscopy experiment TRIGA-LASER (see Chap. 5).

# Chapter 5

# The TRIGA-SPEC experimental setup

The TRIGA-SPEC project has been started in 2008 at the research reactor TRIGA-Mainz. The aim of the project is to determine ground-state properties of short-lived neutron-rich fission products produced by the TRIGA research reactor and of long-lived isotopes of transuranium elements. For this purpose, the Penning-trap mass spectrometer TRIGA-TRAP and the collinear laser-spectroscopy (CLS) experiment TRIGA-LASER have been installed [Ket08]. An overview of the present status of the TRIGA-SPEC facility is shown in Fig. 5.1. A picture of the setup is shown in Fig. 5.2. The commissioning of the setup for the extraction, ionization and beam preparation of short-lived nuclides from the TRIGA reactor has been started within this thesis and are described in the sections 5.1-5.4. The TRIGA-TRAP setup, which was used within this tesis to determine atomic masses, is discussed in detail in Sect. 5.5.

The CLS experiment TRIGA-Laser was not a part of this thesis and is only described briefly here. CLS can used to determine the nuclear spin, the nuclear magnetic moment, the spectroscopic quadrupole moment, and changes in the nuclear charge radii along isotopic chains. These results are obtained via a measurement of the hyperfine structures and the isotope shifts by overlapping a laser and an ion beam in collinear or anti-collinear geometry and detecting the fluorescence signal. The laser is operated at a fixed frequency and the ionic transitions are tuned in resonance with the laser via the Doppler shift. For this purpose, the velocity of the ions is changed by an electric potential, which is applied to the detection region. In case ionic transitions are not favorable for the laser frequency, it is possible to neutralize the ions after the velocity tuning in a charge exchange cell, which is filled with alkali vapor. The CLS benefits from the reduction of the relative velocity spread of the accelerated ions, which allows to determine the transition frequencies with high precision. More details about CLS are found in [Bro89, Klu03] and about TRIGA-LASER in [Krä10].

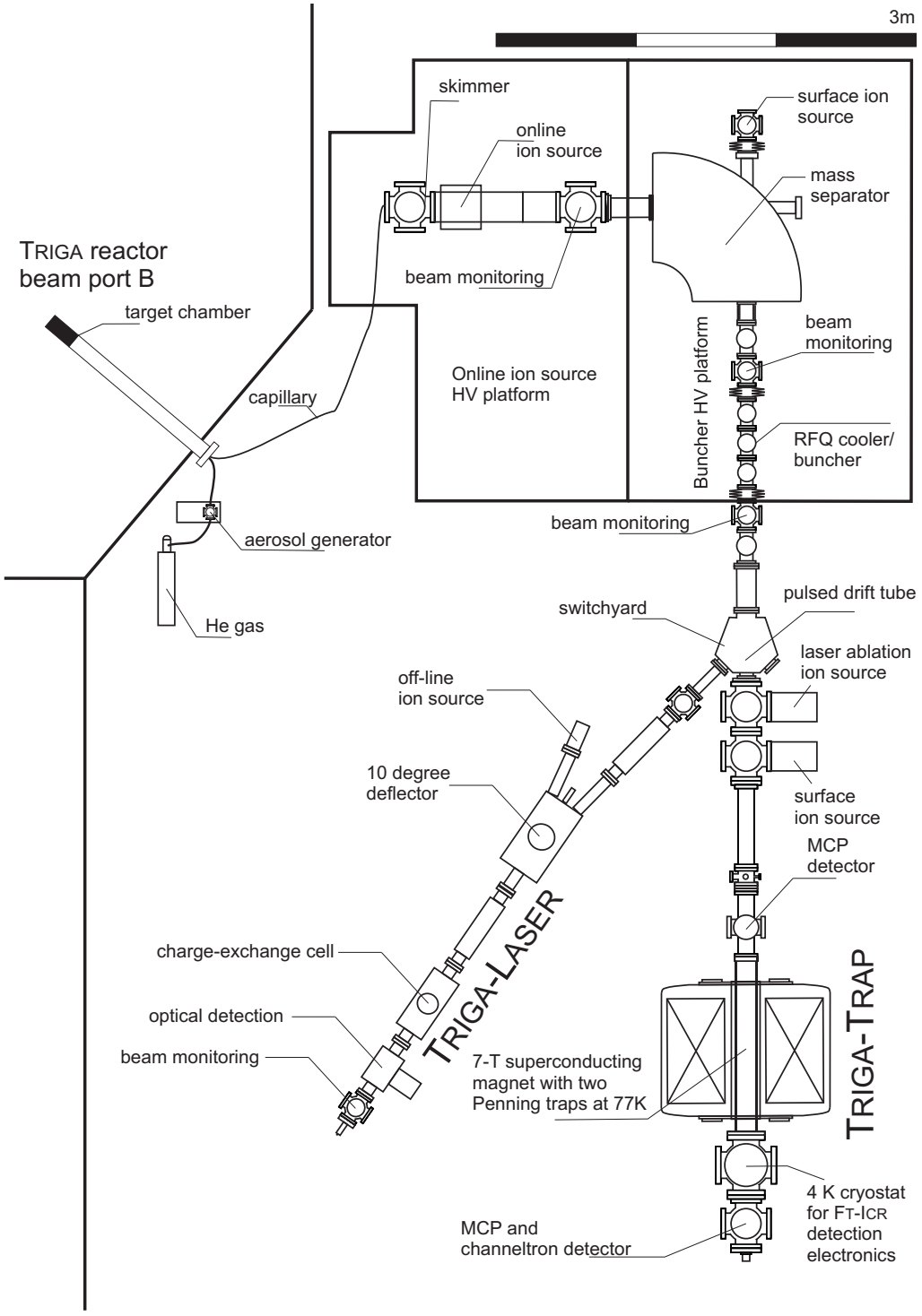


Figure 5.1: Overview of the TRIGA-SPEC experimental setup. The double-Penning trap mass spectrometer TRIGA-TRAP and the collinear laser spectroscopy experiment TRIGA-LASER are coupled to the research reactor TRIGA Mainz, which provides short-lived radionuclides via a common beam line, including an on-line ion source, a mass separator and a RFQ cooler and buncher. For details see text.

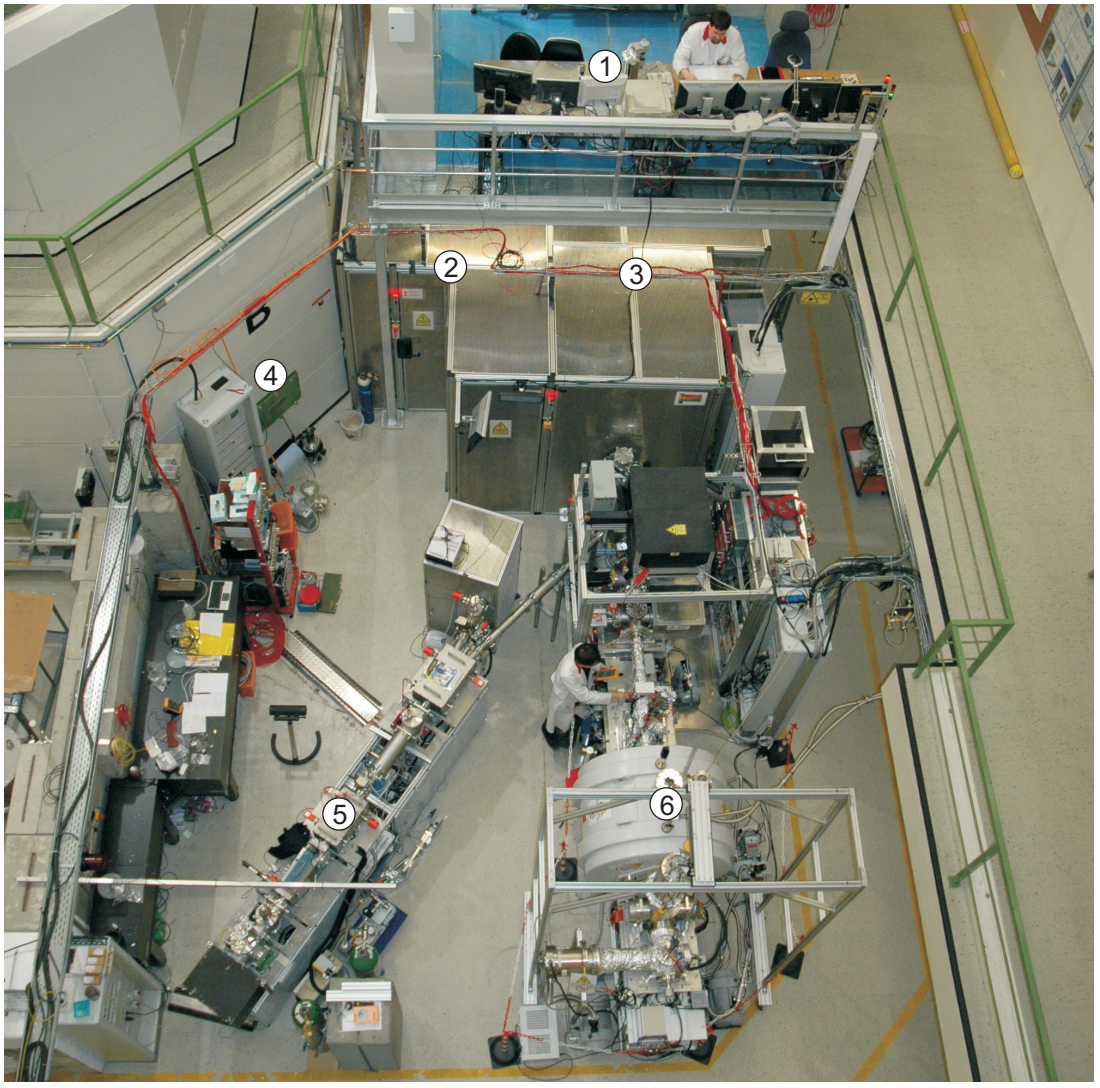


Figure 5.2: A picture of the TRIGA-SPEC experimental setup. The TRIGA-SPEC control platform (1), the HV cages for the on-line ion source (2) and the RFQ buncher (3), beam port B (4), which contains the target chamber with the fissionable target, TRIGA-LASER (5), and TRIGA-TRAP (6) are shown.

## 5.1 The on-line coupling of TRIGA-SPEC

The research reactor TRIGA-Mainz is a TRIGA Mark II reactor, which was constructed by General Atomics and became operational in 1965 [Ebe00, Ham06]. The reactor consists of a cylindrical light-water filled aluminum tank with 6 m in height and 2.5 m in diameter surrounded by a thick concrete radiation shield. The fuel-moderator elements are located at the bottom of the tank. They are made of an uranium-zirconium-hydride (UZrH) alloy with an enrichment of 20% in $^{235}$U. Most of the neutron moderation takes place by collisions with hydrogen atoms inside the fuel-moderator elements. This guarantees the inherent safety of the reactor due to the prompt negative temperature coefficient of the fuel elements. If the reactor is operated in an overcritical state, the fuel elements start to heat up and the tem-

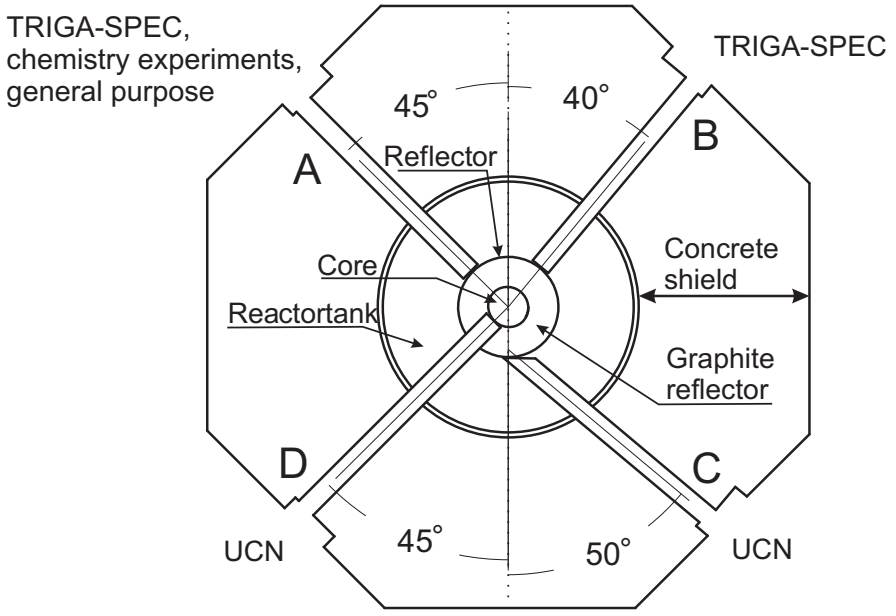


Figure 5.3: Sketch of the reseach reactor TRIGA-Mainz [Eib09]. The four horizontal beam ports provide access to a high neutron flux close to the reactor core. TRIGA-SPEC makes use of beam port A for test purposes and beam port B for the on-line operation. Beam port A is also used for general purpose and chemistry experiments. Beam port C and D are used for the production of ultra-cold neutrons (UCN).

perature of the neutrons increases. The hot neutrons cause less fission in the fuel elements and the reactor reduces its power within a few milliseconds. This allows two operation modes of the reactor: In the steady-state mode the thermal power of the reactor is kept constant and can be adjusted in the range from 100 mW to 100 kW according to experimental requirements. The operation in an overcritical state for a short time is called pulsed mode. A peak power of 250 MW can be reached with a pulse width of about 30 ms.

The research reactor allows to irradiate samples with thermal neutrons at different positions. TRIGA-SPEC makes use of the horizontal beam ports which penetrate the concrete shield of the reactor, as shown in Fig. 5.3. A fission target for the production of the radionuclides is placed inside a target chamber as close as possible to the reactor core. The targets consist of electrodeposited $^{235}$U, $^{239}$Pu, or $^{249}$Cf on a titanium or aluminum backing, with a target thickness ranging from 50 $\mu$g/cm$^2$ for $^{249}$Cf to a few mg/cm$^2$ for $^{235}$U. The thermal neutron flux at the target position is $9.8 \times 10^{10}$/(cm$^2$ s) in beam port A and $1.8 \times 10^{11}$/(cm$^2$ s) in beam port B in the steady-state mode with 100 kW thermal power. In the pulsed mode neutron fluxes of the order of $10^{15}$/(cm$^2$ s) can be reached [Ham06].

The tests in this thesis were performed with a 310 $\mu$g $^{235}$U target covered with a 13 $\mu$m aluminum foil in beam port A. The corresponding fission yields calculated from this target are shown in Fig. 5.4(a). The mass-dependent transmission factor of the aluminum foil, which suppresses the heavy fission branch, is not included in this figure. The transmission factor was empirically determined in [Fin51]. The highest number of fissions per second is achieved by using a $^{249}$Cf target in beam

port B, since neutron flux is a factor of two higher, and the cross section for thermal-neutron induced fission of $^{249}$Cf is a factor of three higher compared to $^{235}$U. This combination will ultimately be used for the radionuclide production at TRIGA-SPEC. The corresponding calculated yields are shown in Fig. 5.4(b).

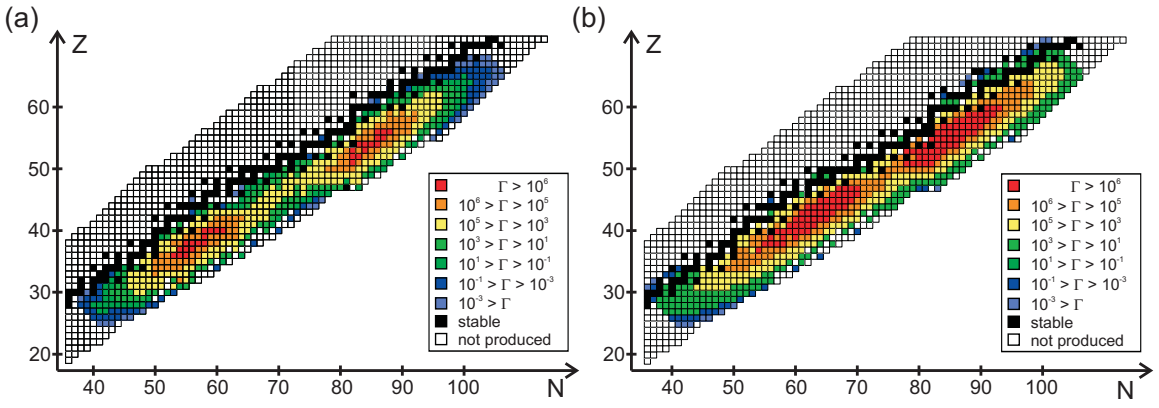


Figure 5.4: The fission yields Γ in $s^{-1}$ are shown for the 310 $\mu$g $^{235}$U target in beam port A with a neutron flux of $9.8\times10^{10}/(cm^2\ s)$ in (a), and for a 300$\mu$g $^{249}$Cf target in beam port B with a neutron flux of $1.8\times10^{11}/(cm^2\ s)$ in (b).

The target chamber which contains the fissionable target is shown in Fig. 5.5. The target chamber has three connections for the aerosol inlet, the aerosol outlet, and one for pressure monitoring. The shape of the target chamber has been optimized to provide best conditions for the fission product extraction. The wall contacts of aerosol particles, which cause a loss of efficiency and clogging of the outlet, have been minimized by the conical-shaped outlet. The stopping volume of the target chamber is 348 ml [Brü83], in which the fission products have to thermalize. The pressure has to be adjusted so that the fission products thermalize before they are implanted into the walls of the target chamber. The stopping ranges as function of the pressure were studied in detail in [Zud86]. In case of the covered uranium target, an absolute pressure of 2.7 bar is necessary for helium, and for nitrogen, argon, or $CO_2$ an absolute pressure of 2 bar [Eib09]. Only the light fission branch can be obtained with this target, since the fission products of the heavy branch are already stopped in the foil. It is inevitable to use an uncovered target if nuclides of the heavy fission branch are to be investigated. Helium does not provide sufficient stopping power in that case. Thus, it is necessary to use a heavier gas.

The pressure in the target chamber is defined by the flow resistance and the gas flow, which is regulated by a mass flow controller in the range of 0 to 5 l/min. The length and diameter of the capillary between the target chamber and the experiment define the flow resistance. A capillary of 0.86 mm diameter and 7 m length has been used to connect the target chamber to the direct catch setup, where fission products were collected on a filter and investigated by $\gamma$-spectroscopy. A capillary with 1 mm diameter and 10 m length served as further connection from the direct catch setup to the on-line ion source. Depending on the transport gas a flow in the range of 350 ml/min for $CO_2$ up to 1500 ml/min for helium has been used. For a fast extraction a direct connection from the target chamber to the on-line ion source is planned.

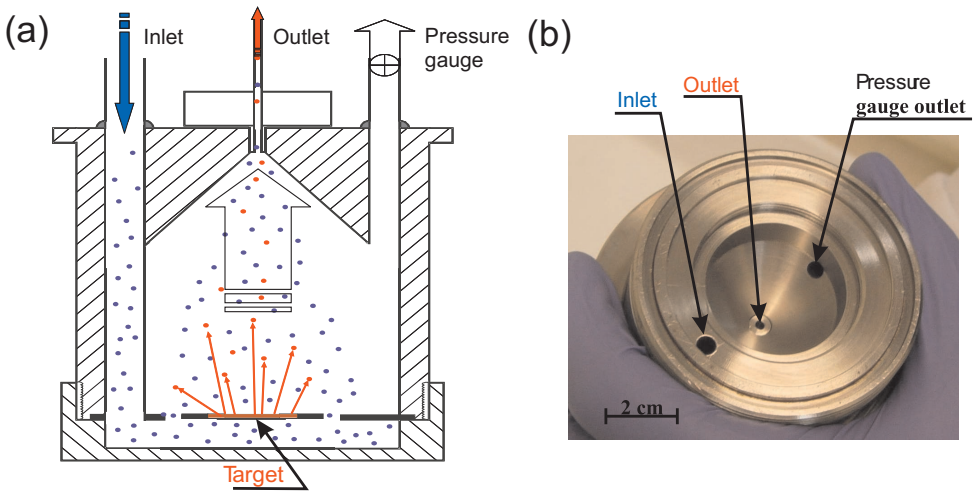


Figure 5.5: A sketch and a picture of the target chamber are shown in (a) and (b), respectively (figure taken from [Eib09]). An aerosol consisting of a carrier gas (e.g. He) and aerosol particles (e.g. KCl) is flushed through the target chamber. Fission products thermalize and attach themselves to the aerosol particles and are transported to the experiments through the outlet. In order to control the recoil range of the fission products a pressure gauge is connected to the target chamber to monitor the pressure.

The minimum capillary length is about 7 m.

Different aerosol particles have been used to investigate the transport of the fission products. The use of potassium-chloride (KCl) aerosol particles is a reliable method in chemistry applications for the extraction of radionuclides [Gün97]. They are produced with a furnace (Heraeus ROK 3/30), which is heated to about 660°C, which is about 100°C below the melting point of KCl. A ceramic sagger filled with KCl is put into a quartz tube, which is place inside the heated stainless-steel tube of the furnace, as shown in Fig. 5.6(a). The transport gas is guided through the quartz tube, and sublimating KCl-particles are carried away with the gas flow through the temperature gradient at the end of the furnace. Thereby, the gas is cooled down and aerosol particles are created by forming condensation nuclei, and through condensation and coagulation of the created particles. The size distribution of the created aerosol particles is a log-normal distribution with a mean diameter of about 200 nm [Gün93]. The furnace can be also used to create aerosol particles of other anorganic salts with melting points below 1000°C. The optimum temperature for the aerosol production of several materials has been carried out in [Maz81]. A high transport efficiency with KCl (35 - 83%) and other salts ($\approx$ 50%) has been demonstrated with this kind of aerosol generator (see Tab. 4.1).

Carbon aerosol particles have been used for the first extraction of fission products for TRIGA-SPEC [Eib09, Eib10]. A sketch of the carbon aerosol generator is shown in Fig. 5.6(b). The aerosol particles are generated in a discharge between two graphite electrodes. The capacitor connected between the two graphite electrodes is charged by a high voltage power supply until the breakdown voltage is reached and electrode material is released in a discharge and carried away by the gas flow. The

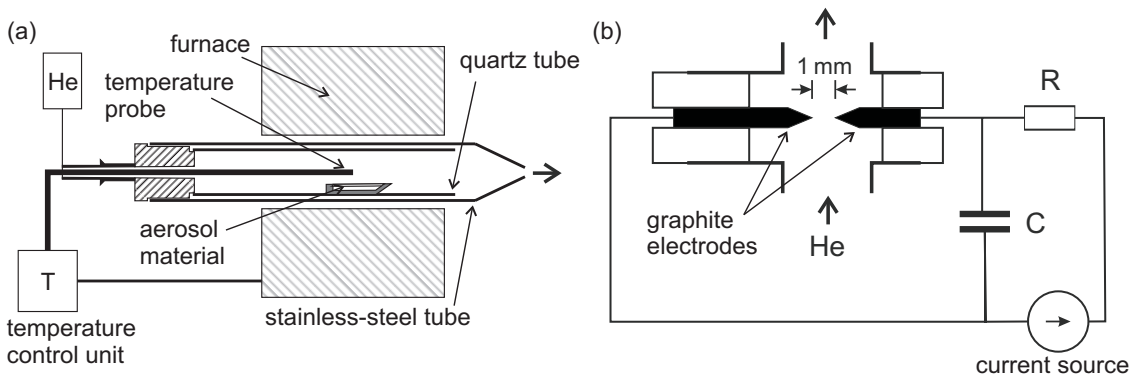


Figure 5.6: A sketch of the furnace used to produce aerosol particles of anorganic salts is shown in (a). A sample of the aerosol material is placed inside the furnace, which is temperature regulated to the optimum temperature for aerosol formation. The principle of the carbon aerosol generator is shown in (b). A capacitor between two graphite electrodes is charged until the breakdown voltage is reached and carbon particles are released in a discharge. Details of the aerosol formation are discussed in the text and in [Eib09, Eib10].

aerosol particles are also formed by condensation and coagulation and a log-normal distribution with a maximum of a few 100 nm can be obtained [Eib09], similar to the size distribution of KCl particles. The amount of produced aerosol particles is controlled by changing the discharge frequency through the charging current of the power supply. It is necessary to control the amount of produced aerosols, since it was observed that the exit of the target chamber gets clogged within a few hours for high densities of carbon aerosol particles, which results in a decrease of the transport efficiency [Eib09]. Carbon aerosol particles have been used to determine the transport time by collecting aerosol particles on a filter in front of a $\gamma$-detector during a pulse of the reactor. The transport time, i.e. the time difference between the $\gamma$ radiation from the reactor pulse and the arrival time of the activity (50% of the maximum value) caused by the incoming fission products, has been determined to be 390 $\pm$ 90 ms. The transport time marks the limit for the shortest half-life that can be studied with a gas-jet transport system, since the ion transport, ion preparation, and the measurement can be performed in a shorter time.

Pure gases can be also used to form fission product carrying particles. For this purpose, the gas has to partially condensate as it is expanding from the supply tank with high pressure into the transport system with lower pressure. The formation of the aerosol particles and the transport efficiency depend on various parameters [Aum79]. It has been demonstrated, that the temperature of the pressure reducing valve has to be smaller than the one of the supply tank to obtain a high transport yield, and that it is favorable to operate the supply tank close to the critical temperature of the gas. Gases which have critical temperatures much lower than the temperature of the supply tank (e.g. $CH_4$, $T_c$ = -82.1 °C, $CF_4$, $T_c$ = -45.5 °C) are not suitable to transport fission products with aerosol particles [Aum79]. Aerosol particles formed by the expansion of pure gases have a limited life-time because the condensed droplet of liquid gas evaporates since heat is transfered from the hotter

gas to the particle [Aum79]. This effect decreases the transport efficiency in addition to the effects discussed in Sect. 4.2.

These three methods have been used to produce aerosol particles for the transport of fission products from the target chamber through the concrete radiation shield of the reactor. The capillary is either connected to a filter system (see Chap. 6), where the activity transported by the aerosol particles is collected and analyzed by $\gamma$-spectroscopy, or to the on-line ion source to prepare the ion beam for the experiments.

## 5.2 The ECR on-line ion source

The ECR ion source which was tested as an on-line ion source in this thesis was originally constructed at the University of Giessen in order to study ion-ion collisions [Lie92]. The ion source was donated to the TRIGA-SPEC experiment, in order to test whether ECR ion sources can be used as gas-jet coupled ion sources. The setup of the ion source has been adapted in this thesis to allow on-line injection of the gas-jet into the ion source. The final setup of the ECR ion source which has been used for the on-line tests in Chap. 6 is shown in Fig. 5.7.

Due to the high gas load of the gas-jet in the order of 1 l/min the gas-jet is injected into the ion source through a skimmer, which separates the carrier gas and the aerosol particles. The aerosol particles and the carrier gas move through the capillary at the same velocity because the aerosol particles are accelerated by collisions. Thus, the aerosol particles expand into the vacuum on a cone with smaller diameter than the carrier gas due to momentum conservation. Therefore, a skimmer with proper dimensions can suppress the carrier gas by a large amount, whereas the transmission for the aerosol particles is still high. The exit of the capillary is placed within a distance of 6 mm to 10 mm in front of the hole in the skimmer plate. Here, the gas-jet expands into the vacuum. In the center of the expanding gas-jet the particles are accelerated to supersonic speed and an interaction-free region, the so-called zone of silence, is formed [Sco88]. The gas-jet is expanding undisturbed by any boundary conditions in this region because the supersonic flow is propagating faster than any information transported by sonic waves in the medium. The zone of silence is limited in flow direction by the so-called Mach disk, where shock waves occur and the flow continuous with subsonic speed. The distance of the Mach disk to the capillary exit is given by $x_M = 0.67 \times d\ P_0/P_b$ [Sco88], where $d$ is the capillary diameter, $P_0$ the pressure in the capillary and $P_b$ the background pressure in the skimmer chamber. Using typical values for the present setup ($d = 1$ mm, $P_0 = 2$ bar, $P_b = 10^{-2}$ mbar) the Mach disk is located at about 300 mm behind the end of the capillary. The skimmer is placed in front of the Mach disk in order to extract the aerosol particles from the undisturbed flow.

The skimmer disturbs the zone of silence because particles which are reflected from the skimmer back into the zone of silence can scatter with particles of the supersonic flow and reduce the transmission of the skimmer. Therefore, the shape of the skimmer has an important influence for atomic and molecular beams [Cam84]. A conical shaped skimmer avoids reflection of atoms and molecules into the zone of

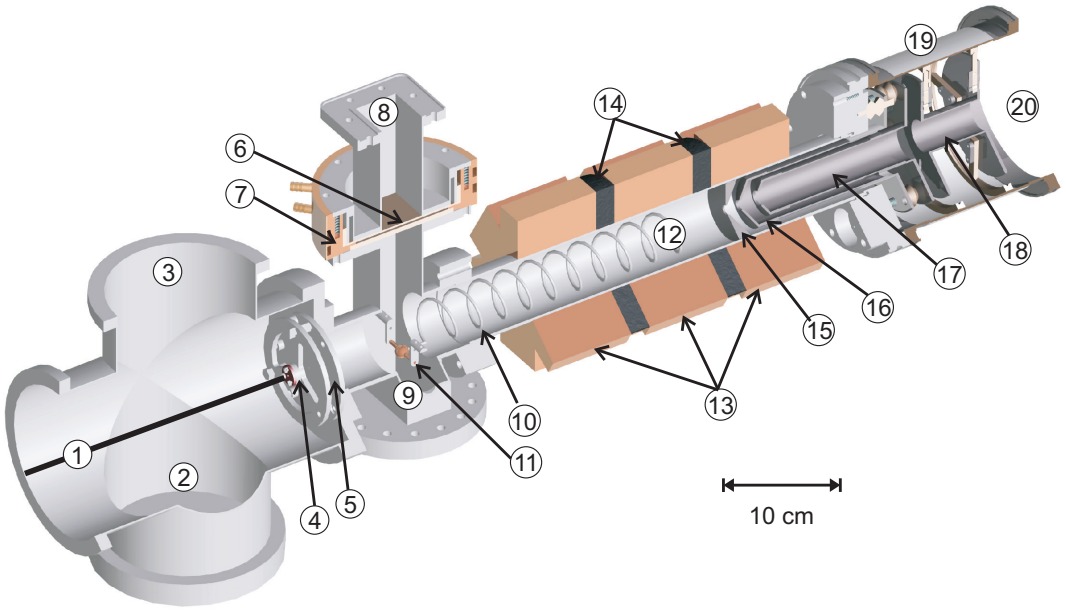


Figure 5.7: A 3D model of the ECR on-line ion source. The capillary (1) from the target chamber enters the skimmer chamber (2), which is pumped by a rootspump via port (3). The capillary holder (4) is used to position the capillary in front of the skimmer plate (5). The microwave is injected into the vacuum through a Teflon disk (6), which is surrounded by a water-cooled copper ring (7). The magnetron is connected to the waveguide via flange (8). A mesh on a linear feedthrough, which acts as a short circuit for the microwave and a turbo-molecular pump are connected to flange (9). The helical antenna (10) couples the microwave from the waveguide into the ion source via the U-shaped antenna holder (11). The ECR plasma (12) is confined by the magnetic field generated by 3 rings, each made of 6 permanent magnets (13) and two iron plates (14). An aperture (15) limits the plasma region on the extraction side. The three extraction electrodes (16), (17) and (18) accelerate the ion beam. A ceramic insulator (19) separates the ion-source high-voltage platform from ground. Additional ion optics connected behind flange (20) guide the ions to the mass separator (see Fig. 5.1).

silence. However, in case of a gas-jet with heavy aerosol particles ($m \approx 10^7 - 10^9$ u) and a light carrier gas ($m \approx 4 - 44$ u) it is even desired to reflect the carrier gas back into the zone of silence [Sch76]. Scattering between the carrier gas and an aerosol particle does not significantly change the transmission of the aerosol particles through the skimmer due to the small impact of the scattering on the momentum of the aerosol particle. However, the transmission of the carrier gas is reduced by scattering with reflected carrier gas particles. Therefore, a flat skimmer is more suited in case of a gas-jet with aerosol particles [Sch76]. Thereby, up to 97.5% of the carrier gas can be suppressed. Additionally, a second gas-jet expanding parallel to the skimmer surface can be used to further suppress carrier gas particles behind the skimmer by scattering. This so-called side-jet technique can achieve a suppression of 99.85% of the carrier gas [Sch76].

The ECR on-line ion source uses a flat skimmer plate with a 1 mm aperture with-

out side-jet. The carrier gas is pumped away by a rootspump (Edwards EH2600C) with a pumping speed of 1900 $m^3/h$. The waveguide behind the skimmer is pumped by a turbo-molecular pump (Leybold, TURBOMAG W300P) with 300 l/s and another turbo-molecular pump (Ebara, ET300W) with 300 l/s is connected to the beamline behind the ion source. A pressure of $3 \times 10^{-2}$ mbar was achieved in the skimmer chamber and $5 \times 10^{-4}$ mbar behind the skimmer with this configuration for on-line operation with a gas flow of 1 l/min. The distance between the capillary end and the skimmer was 6 mm in this case. Without any gas load and by closing a valve between the rootspump and the ECR ion source a pressure in the range of $10^{-7}$ to $10^{-8}$ mbar was typically achieved.

The positioning of the capillary in front of the skimmer is crucial because a slight tilt of the axis or of a slight shift of the position can drastically decrease the transmission. Three space holders are used to fix the capillary holder in front of the skimmer to ensure the alignment of the capillary axis and position with tolerances of 0.2° and 0.1 mm, respectively. A reproducible transmission of 25% of the skimmer has been achieved with this configuration (see Chap. 6), which is comparable to literature [Brü83]. The transmitted aerosol particles move on into the ECR plasma inside the ion source.

The ECR ion source is designed for a microwave with 2.45 GHz, which is resonant to the electron cyclotron frequency at 87.5 mT. The magnetic field for the plasma confinement is provided by 3 rings each of 6 permanent magnets made of NdFeB. The permanent magnets of the left ring and the right ring (see Fig. 5.1) are facing the center with the south pole and north pole, respectively, and provide the axial magnetic mirror field. Two iron plates between the magnet rings increase the axial field strength so that a mirror ratio of 4:1 is reached. The minimum and maximum field strength on axis are 60 mT and 240 mT, respectively. The magnets of the center ring are facing alternately with the north and the south pole to the center to provide the hexapole field for the radial confinement. A closed surface with the resonant field strength is obtained within the center ring.

The microwave for the ECR heating is provided by a magnetron (Muegge, MW-1511-300-01) with 300 W power. It is located at the top of the microwave waveguide connected to flange (8) in Fig. 5.1. In this waveguide a microwave circulator (Philips, PDR 26), a directional coupler (IBF electronic, DC 113) and a three-stub tuner (IBF electronic, R 26) is placed between the magnetron and the ion source. The circulator prevents the destruction of the magnetron by the reflected microwave. The reflected microwave is absorbed into a water-cooled solid-state load. The directional coupler couples out a fraction of $10^{-4}$ of the microwave power, which is detected by a powermeter (Marconi Instruments, 6960B). Thereby, the injected and reflected microwave power can be monitored. The three-stub tuner changes the impedance of the microwave guide in order to match the impedance of the plasma and minimize the reflected power. All these devices are operated at atmospheric pressure in the wave guide. The transfer into the vacuum is done via a 5 mm thick teflon disk, which separates the atmospheric and the vacuum part of the waveguide. The teflon disk is almost transparent for the microwave, only a small fraction of power is absorbed. However, in continuous operation at high power it is necessary to cool the teflon disk. For this purpose, a water-cooled copper ring is used. A chiller (Termotek AG,

E 900) with 900 W cooling power provides the cooling water for all devices on the high voltage platform.

The diameter of the plasma tube is only 60 mm so that the microwave of 2.45 GHz is below cut-off frequency of the plasma tube. Therefore, a microwave antenna is required to couple the microwave from the waveguide into the plasma tube so that the microwaves still reach the resonance zone. The antenna and the antenna holder were modified for the on-line application at TRIGA-SPEC. The previous geometry did not allow to inject the gas-jet on the center axis into the source. Several shapes of the antenna and its holder have been tested. The antenna with the best coupling of the microwave into the plasma is shown in Fig. 5.1. The holder is made of stainless steel and has a U-shape, to allow the gas-jet to pass through on the center axis. The holder has a sphere of 6 mm diameter in the center in horizontal direction, which is displaced vertically by 19 mm from the center axis. The antenna is connected via a thread in this sphere. The magnetic field of the microwave induces an alternating current in the metal sphere, and propagates along the antenna, which is a helical antenna made of a stainless tube with 3 mm outer diameter. A tube was chosen instead of a wire to decrease the weight of the antenna. It has 10 turns with 41 mm diameter and 27 mm pitch. The length of one turn matches the wavelength of the microwave ($\lambda$ = 12.2 cm), so that the microwave is transferred as right-hand circular polarized wave into the resonance region. As discussed in Sect. 4.4, this mode is well-suited for the ECR heating. In order to achieve a good coupling of the microwave to the antenna it is necessary that the field strength of the microwave has a maximum at the position of the sphere of the antenna holder. For this purpose a mesh is installed on a linear feedthrough in the waveguide on the opposing side of the magnetron. This mesh acts as a short-circuit and is placed a quarter wavelength below the sphere in order to achieve the desired situation. The helical antenna provides a good and reliable coupling of the microwave power into the plasma, and the reflected power could be reduced to less than 10 % of the incoming power (see Chap. 6). Antennas of other shapes that were tested, such as cylindrical and conical antennas, performed worse, since the fraction of the microwave which was coupled to the plasma was too small to ignite the plasma and to operate the ion source in a reliable way.

On the extraction side of the ECR ion source an aperture with 10 mm diameter is placed in order to limit the diameter of the extracted ion beam. The extraction electrodes used for ion beam acceleration are shown in Fig. 5.8. A two-step acceleration system shown in Fig. 5.8 (a) has been used in several tests. It consists of a single extraction electrode on an intermediate potential between the ion source platform and ground potential. The ions were first accelerated up to 2.8 keV into the extraction electrode and to 20 keV by the subsequent ion optics on ground potential behind the ceramic insulator (see Fig. 5.7). The three-step acceleration system shown in Fig. 5.8 (b) has the advantage compared to the two-step acceleration system that the diameter of the ion beam at the end of electrode 2 can be controlled by changing the voltage ratio between electrode 1 and 2 (see Fig. 5.8 (c)). Thereby, a parallel beam of smaller diameter can be obtained. Electrode 3 has been added to prevent a flow of secondary electrons to the high voltage platform and to have a well-defined potential for the ion beam between the extraction electrode and the

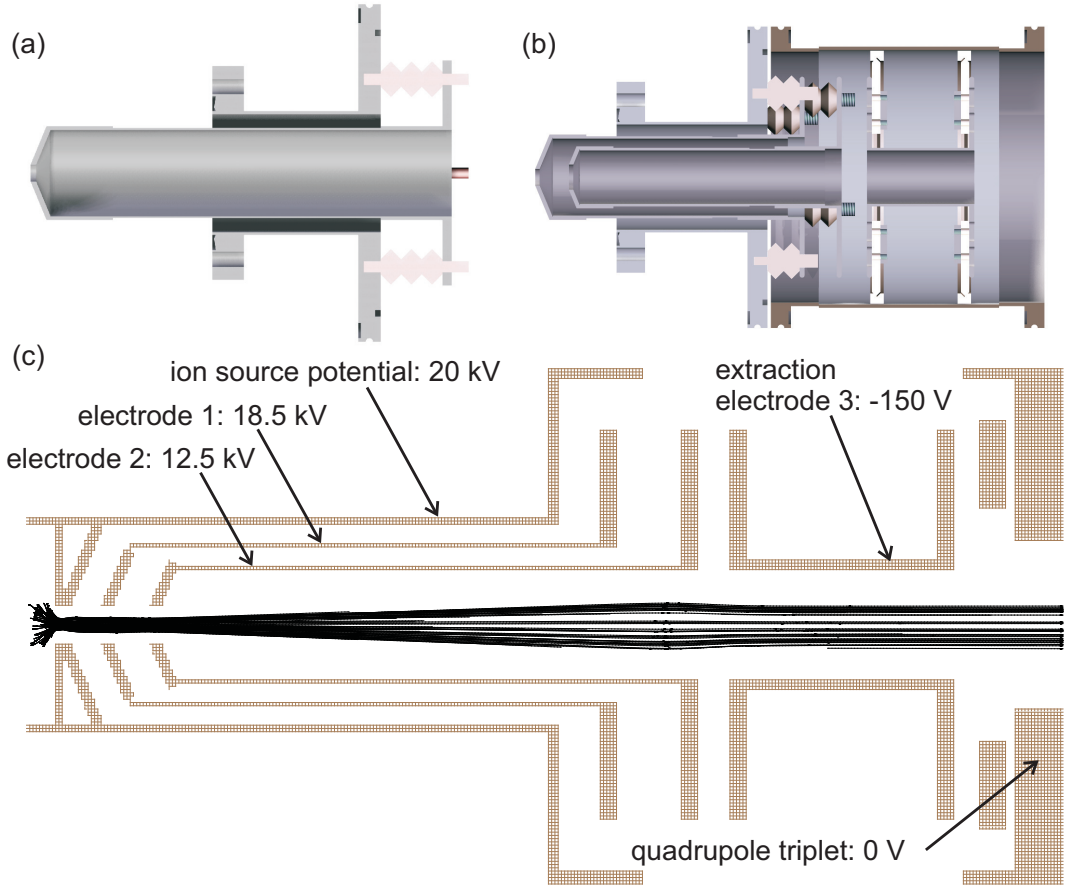


Figure 5.8: Ion beam extraction from the ECR on-line ion source. The one-electrode and the three electrode extraction system are shown in (a) and (b), respectively. A SIMION simulation with 100 ions extracted from the ECR ion source is shown in (c). For details see text.

quadrupole triplet. An ion optics simulation with SIMION [Dah00] using 100 ions is shown in 5.8 (c). The voltages applied to the electrodes are also shown in the figure. After the extraction from the ECR ion source and acceleration of the ion beam up the 30 keV, the ion beam is prepared for the experiments in the following beamline.

The ECR ion source is placed on a high-voltage platform inside a high-voltage cage designed for 30 kV, which defines the maximum energy of the ion beam coming from the on-line ion source. The vacuum chamber of the ECR ion source is separated with a ceramic insulator from the vacuum chamber for the beam transport at ground-potential. All devices required on the high-voltage platform to operate the ion source (microwave power supply, pressure gauges, gas-inlet system, etc.) are placed in a high-voltage rack with ceramic feet. The rootspump and its forepump (Edwards E2M275) are also placed on a support with ceramic feet to be operated at high voltage. Two transformers are used to provide power for the devices on the high-voltage platform. One transformer (Tauscher, maximum load 25 kVA, insulation voltage 30 kV) is dedicated to provide power for the rootspump and its forepump with a total power consumption of 18 kW. The other transformer (Tauscher, maxi-

mum load 15 kVA, insulation voltage 80 kV) provides power for the devices necessary to operate the ion source. The ion source and the rootspump can be galvanically separated in order to reduce noise or ripple from the rootspump, which may affect the stability of the ion beam energy. It was also tested whether the rootspump can be operated on ground potential by using a spark arrester between ion source and rootspump [Sch87]. However, the reduction in pumping speed of the rootspump was too large if the spark arrestor was installed. Without spark arrestor and roots pump at ground potential a discharge in the gas in the insulator between ion source and rootspump prevented the high-voltage operation.

## 5.3 Ion preparation and transport

The on-line ion source produces a continuous ion beam of a large variety of ion species. In the experiments it is desired to have only the ion species of interest present. Furthermore, it is advantageous to convert the continuous beam into a pulsed beam. Thereby, a more efficient injection into the Penning trap, or a noise reduction by several orders of magnitude for collinear laser spectroscopy can be achieved [Nie02]. It is also possible to accumulate the continuous beam for a certain time to create an ion pulse containing a certain amount of the ions of interest. This is especially useful for ion species with low production rates. A dipole magnet, which serves as mass separator, and the radio-frequency quadrupole (RFQ) cooler COLETTE, which was inherited from the MISTRAL experiment at CERN [Lun09], are installed between the ion source and the experiments in order to fulfill this purpose.

The dipole magnet is a 90° magnet with a magnetic homogeneity of $\Delta B/B = 10^{-3}$. The bending radius $r$ of the magnet is 500 mm, and the transmitted ion species are selected by adjusting the magnetic field strength $B$ up to 1.12 T. The mass-to-charge ratio of the transmitted ion species is given by:

$$\frac{m}{q} = B^2 \frac{r^2}{2V_i}, \tag{5.1}$$

where $V_i$ denotes the electric potential of the ion source. The mass resolving power of the dipole magnet depends on the ion beam properties. The dipole magnet is a double-focusing magnet [Hin08], which uses the inhomogeneous field at the entrance and exit of the magnet to focus the beam with a focal length of 500 mm. Therefore, the highest mass resolving power is obtained for a low emittance beam with a focal point 500 mm in front of the magnet. The image of the ion beam in the focal plane behind the magnet has in this case the same diameter as the focal point in front of the magnet. Thereby, a mass resolving power of $m/\Delta m$ up to 1000 can be achieved using a narrow slit in the focal plane behind the magnet. If the ion beam has a larger emittance or the focal point is at a different position, the mass resolving power decreases due to larger beam diameters of the individual masses in the focal plane. The focusing in front of the magnet is done with a harmonic quadrupole triplet [Hin08] (total length 324 mm, electrode radius 30 mm, aperture 52.9 mm). Due to space limitations it is not possible to place it at the proper position, so that

a focal point 500 mm in front of the magnet cannot be achieved. With the current configuration it was possible to achieve a mass resolution larger than $m/\Delta m \approx 130$, which was demonstrated by separating the two xenon isotopes $^{131}$Xe and $^{132}$Xe, despite the expected large emittance of the ECR ion source of about 30 $\pi$ mm mrad [Zel04]. Thereby, the selection of isobars in the mass region of the heavy fission branch has been demonstrated (see Chap. 6).

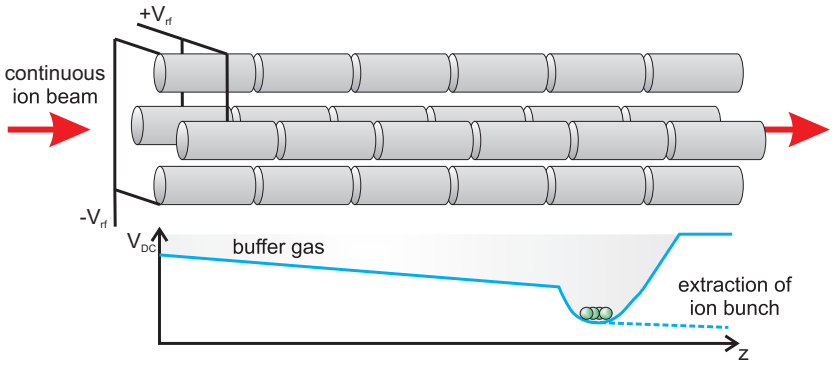


Figure 5.9: Principle of a RFQ cooler and buncher (figure taken from [Ket10b]). A continuous beam of ions is injected into a linear Paul trap. The ions lose energy due to collisions with the buffer gas and accumulate in the well of the axial DC potential. A bunch of ions is extracted by pulsing down the DC potential of the last segment.

After isobaric selection, the ion beam is injected into the RFQ cooler COLETTE [Lun09]. The RFQ cooler and buncher is a linear Paul trap, which confines ions with a certain mass-to-charge ratio $m/q$ in radial direction depending on the amplitude of the quadrupolar rf-field and the quadrupolar electrostatic potential [Maj04]. The principle of an RFQ buncher is shown in Fig. 5.9. The buncher is filled with helium as buffer gas in order to reduce the emittance of the ion beam by collisions. COLETTE has been operated in a continuous beam mode and a reduction of the emittance from 38 $\pi$ mm mrad to 8 $\pi$ mm mrad at 20 keV was achieved [Lun09]. At TRIGA-SPEC it is planned to operate the buncher in pulsed mode [Bey13]. For this purpose the four-electrode structure is segmented in axial direction in order to apply different DC potentials to the segments. The ions lose kinetic energy by collisions with the buffer gas and accumulate in the last segments which create a potential well. An ion pulse is extracted by pulsing down the DC potential of the last segment [Her01]. RFQ systems of this kind are already installed at other Penning-trap mass spectrometers [Her01, Nie01, Rod03b].

A surface ion source is installed behind the dipole magnet for off-line test purposes (see Fig. 5.6). The ion source uses a commercially available pellet (Heat Wave Labs, Model 101139), which produces cesium ions. The ion source is operated with 30 kV acceleration voltage in order to have similar ion beam conditions to the on-line ion source. The pellet which contains the cesium sample is electrically heated with a power of up to 14 W. Thereby, a cesium ion beam with a current up to 1 nA is produced. The magnetic field of the dipole magnet is switched off in order to transport the ion beam from the surface ion source through the magnet. Thereby, the RFQ buncher and the ion transport to the experiments can be tested independently from the on-line ion source [Nie12].

The last element in the beamline before the ion beam reaches the experiments is a switchyard, which distributes the ion beam to the experiments. A 3D model of the switchyard is shown in Fig. 5.10. A horizontal deflector in front of the switchyard can be used to deflect the ions to the entrance of one of the curved electrostatic benders, which guide the ions to the left port, which is reserved for future experiments, or the right port, where TRIGA-LASER is connected. TRIGA-TRAP is connected to the center port of the switchyard. In order to capture the ions efficiently in the Penning traps, it is inevitable to reduce the kinetic energy of the ions to less than 100 eV, since the traps are operated at ground potential. For this purpose a pulsed drift tube (PDT) is used. The design of the PDT was done within this thesis and it is described in the following section.

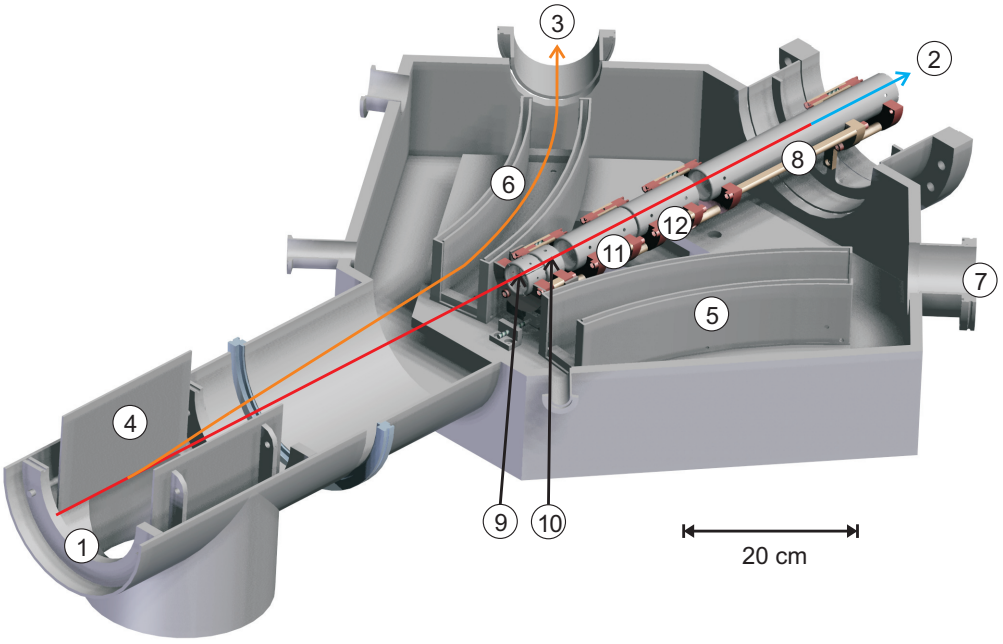


Figure 5.10: A sketch of the switchyard and the pulsed drift tube assembly. Ion trajectories coming from the RFQ buncher (1) for an ion pulse going to TRIGA-TRAP (2) (red, 30 keV energy, and blue, 1.1 keV energy) and TRIGA-LASER (3) (orange, 30 keV energy) are shown. A horizontal deflector (4) can bend the trajectory into the direction of one of the curved deflectors (5, 6), so that the ions leave the switchyard through the left (3) or the right port (7). A PDT (8) is used to decelerate the ions going to TRIGA-TRAP. The PDT is preceeded by a deflector (9) and a drift tube (10) at ground potential and the deceleration lenses 1 (11) and 2 (12). For details see text.

## 5.4 The pulsed drift tube

A PDT decelerates the ions by applying a high voltage $V_h$ while the ion bunch enters the PDT, and pulsing the voltage down to $V_l$ close to ground potential while the ions are inside the tube. In this way the high-voltage pulse does not affect the motion of

the ions inside the tube but their potential energy is reduced by $\Delta E = q(V_h - V_l)$. PDTs are used at other Penning-trap experiments as well, e.g. ISOLTRAP [Her01], to adapt the ion energy for trap loading. The following properties for the ion beam and the high-voltage pulse were considered for the design of the PDT:

- **Ion masses**

  The lightest ion species has the highest velocity for identical kinetic energies and the flight time through the PDT is shortest. Therefore, the design of the pulsed drift tube was carried out using ions with $A = 80$, which matches the lightest fission products that can be obtained from the on-line ion source.

- **Beam emittance**

  A beam emittance of 30 $\pi$ mm mrad is assumed for the 30 keV ion beam from the ECR ion source [Zel04]. If the ions are decelerated from a kinetic energy $E_1$ to $E_2$, the emittance increases by a factor of $\sqrt{E_1/E_2}$, which results in an emittance of about 160 $\pi$ mm mrad for a 1 keV ion beam. This emittance is by far too large to be accepted by the ion optics system for injection into the trap. This demonstrates the importance of cooling the ions with an RFQ buncher for the trap injection. With a buncher typically transversal emittances of 2 $\pi$ mm mrad can be reached at 60 keV, corresponding to 15.5 $\pi$ mm mrad at 1 keV, and longitudinal emittances of 10 eV $\mu$s [Her01]. It was assumed that an emittance of 2 - 4 $\pi$ mm mrad can be reached at TRIGA-SPEC using the RFQ buncher in pulsed mode. Considering a longitudinal emittance of 10 eV $\mu$s of the buncher, the pulsed drift tube has to be long enough to efficiently decelerate a 1 $\mu$s ion bunch with 10 eV energy spread.

- **Switching time**

  A high-voltage switch (Behlke HTS 301-03-GSM) switches the high voltage of the PDT. In order to get the desired ion energy from a 30 keV incoming ion beam, the PDT is put on $V_h = 28.9$ kV for the deceleration and pulsed down to $V_l$ = -1.0 kV. The transport section between the PDT and the Penning traps is also on -1.0 kV, in order to transport the ions with 1.1 keV to the traps and stop them with the endcap at 100 V. The high-voltage switch requires a certain time to switch the high voltage, depending on the capacitance of the PDT. The time constant for the switching is specified to be $\tau \approx 230$ ns with a load of $C = 1$ nF. The effect of the fall time $\tau$ of the switch on the efficiency was also investigated.

A high transmission through the PDT is desired so that the availability of rarely produced nuclei is not limited by the ion deceleration. The ion beam has to have a small energy spread, which is smaller than the trap potential of the Penning trap so that the ions can be efficiently captured. This requires that the energy spread is below 10 eV for a 1.1 keV beam. Furthermore, it is of advantage to be able to control the opening angle, and thus the focal length of the ion beam on the low energy side independently from the deceleration voltage of the drift tube. The system is then flexible enough to adapt to the following ion optics. Furthermore, the design of the

PDT assembly has to fit inside the switchyard with a total length of 430 mm and a maximum diameter of 56 mm due to space limitations. In the following the results of the design studies are presented.

## Electrode layout and beam transport simulations

SIMION simulations were preformed to study the electrode layout as proposed by Mikhail Yavor [Yav09]. The electrode configuration shown in Fig. 5.10 fulfill the requirements discussed above and has been adapted to the experimental requirements.

The ions are ejected from the buncher and a parallel ion beam is prepared with the buncher's extraction optics. Since the buncher and the PDT are not placed on the same holding structure, small misalignments between these parts have to be considered. Therefore, a deflector at ground potential is added behind the buncher, followed by a drift space of about 500 mm from the buncher into the switchyard chamber. The PDT assembly starts also with a deflector, followed by a short drift tube at ground potential, two deceleration lens segments, and the PDT itself (see Fig. 5.10). After deceleration a lens and a deflector for a 1.1 keV ion beam is installed to bridge the space between the PDT and the existing TRIGA-TRAP setup.

Concerning the timing of the pulse, the length of the PDT was chosen to be 22 cm, so that ions with $m = 80$ u require 4 $\mu$s to pass through the tube at 1.1 keV. The potential is pulsed down when the ion bunch is in the most homogeneous region of the electric field at the center of the PDT, to avoid an increase of the energy spread due to the fringe fields caused by the neighboring electrodes during the pulse. Therefore, the duration of the ion pulse has to be considerably shorter than 4 $\mu$s for an efficient deceleration.

In Fig. 5.11(a) and Fig. 5.11(b) the potential and the kinetic energy for an ion on the beam axis obtained from the SIMION simulation are shown. Fig. 5.11(c) shows the enclosing lines for a 2 and a 4 $\pi$ mm mrad ion bunch, respectively, with $m = 80$ u. In order to minimize aberration effects and to obtain a parallel propagating ion pulse in the PDT, the deceleration is carried out in three potential steps. The deflector and the drift tube are on ground potential. The two lens segments act as retarding lenses. Their strength increases in function of the energy ratio $r_i = (E_{i-1}/E_i)$ [Hin08], where $E_{i-1}$ is the ion energy in the preceding electrode, and $E_i$ the energy inside the lens segment (see Fig. 5.11(a)). Aberration effects of lenses scale also with $r_i$. Therefore, the beam diameter in the region of the strongest focusing electric field should be minimized, in order to avoid aberration effects. Thus, in the ideal case the first lens segment focuses the ions at the position between the first and the second lens segment, where the strongest focusing field should be. The voltage on the second lens segment defines the opening angle of the ions in the drift tube. Here, a parallel propagating pulse is desired to avoid ion losses to the walls. To achieve this, the following conditions for the energy ratios $r_i$ should be fulfilled: $r_2 > r_1$ to minimize aberrations, and $r_1 = r_3$ in order to obtain a parallel propagation. In this case, it was not possible to fulfill the first condition due to space limitations. It is not possible to have deceleration lenses of sufficient length, so that the first lens can be made weaker than the second lens. The voltages applied to the electrodes are 24 kV on the first lens, 24.5 kV on the second lens and 28.9 kV on the PDT. This

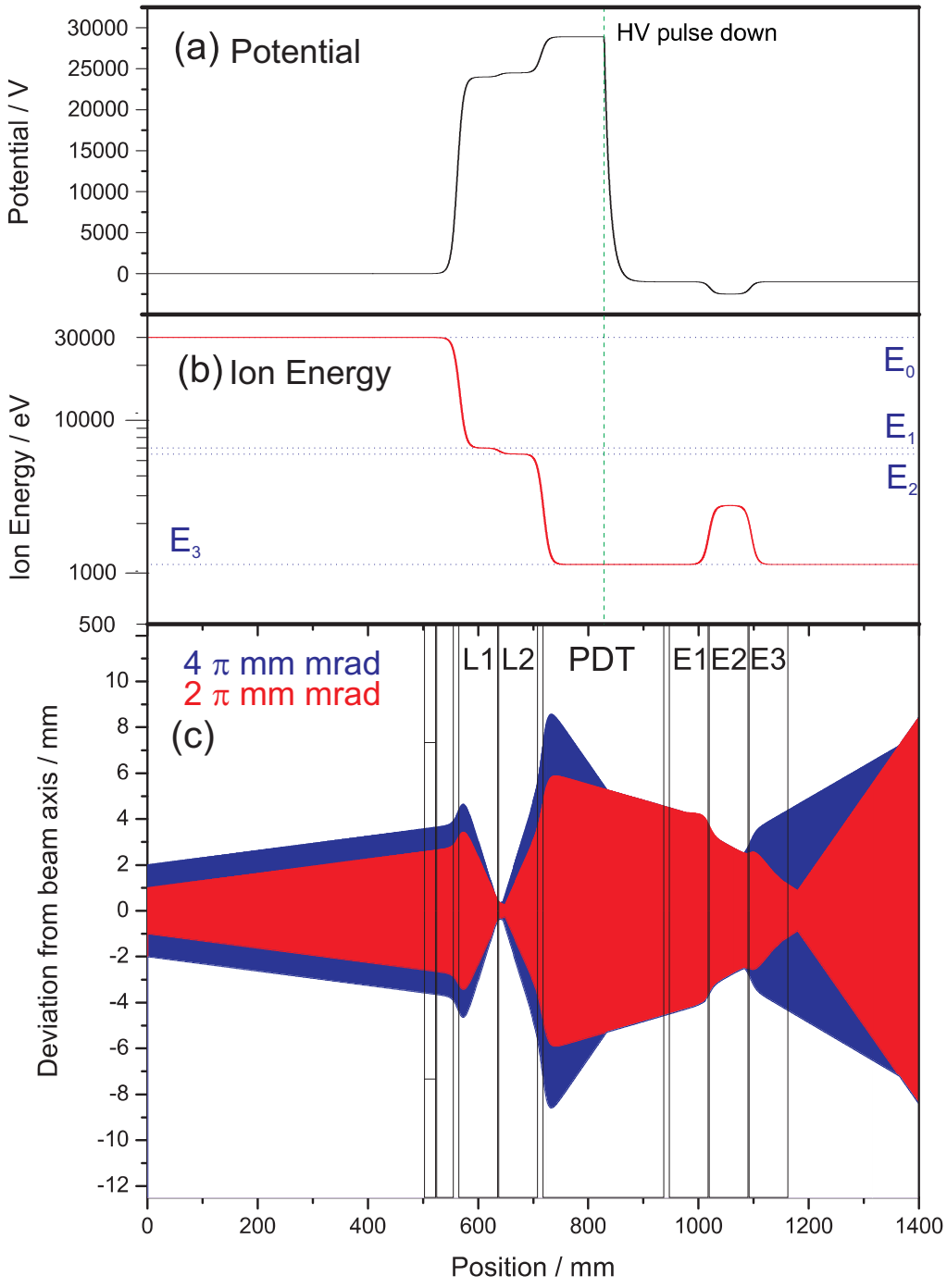


Figure 5.11: Simulation results of the beam transport through the PDT section. In (a) the potential and in (b) the kinetic energy of an ion on axis is shown. The ion is decelerated in three potential steps by two retarding lenses from $E_0 = 30$ keV to $E_3 = 1.1$ keV. While the ions are inside the PDT, the voltage applied to it is switched down to -1.0 kV. Behind the pulsed drift tube an einzel lens is used to focus the beam. In (c) the enclosing lines of a 2 $\pi$ mm mrad (in red) and a 4 $\pi$ mm mrad ion beam (in blue) are shown. For details see text.

corresponds to three retarding lenses with the ratios $r_1 = 5$, $r_2 = 1.1$ and $r_3 = 5$. Nevertheless, the efficiency has proven to be sufficiently high in the simulation, so that the aberration effects can be accepted. Comparing the two enclosing lines in Fig. 5.11(c), the aberration effects can be observed. The focal length of the ions depends on the distance to the beam axis due to spherical aberration, which limits the acceptance of the PDT to about 5 $\pi$ mm mrad for 30 keV ion energy.

For the correction of misalignments, i.e. small shifts and tilts of the center axis of the PDT assembly against the center axis of the buncher, two deflectors are placed in the structure (see Fig. 5.10). One directly behind the buncher and one in front of the deceleration stage. As worst case for the misalignments a tilt of 0.5° and a shift of 2 mm were assumed. These misalignments could be corrected for a 4 $\pi$ mm mrad ion beam and a similar transport efficiency through the PDT was obtained. The deflector voltages required for the correction were below 1 kV.

## Efficiency Studies

The length of the ion bunch $\Delta t$ and the fall time of the high-voltage switch $\tau$ affect the deceleration efficiency, which has been investigated by simulating the trajectories of a bunch of $10^4$ ions moving through the PDT with an emittance of 4 $\pi$ mm mrad. The number of accepted ions has been determined in the simulation. Ions have to fulfill two conditions to be accepted by the TRIGA-TRAP setup: First, the TRIGA-TRAP ion optics are optimized for an ion energy of 1.1 keV. Ions with a different energy can be lost due to chromatic aberration or since they cannot be trapped by the Penning traps. Ions are considered to be accepted in case the deviation from the ideal energy is smaller than 10 eV. Second, the ion should not be lost to the walls before entering the TRIGA-TRAP setup. Ions with a deviation from the beam axis at the trap position smaller than 10 mm are considered to be accepted by the purification trap.

The simulation results for the efficiency of the PDT as function of the ion pulse length $\Delta t$ is shown in Tab. 5.1 for a switch time $\tau$ of 200 ns. For an ion bunch with infinitesimal length an efficiency close to 100% is obtained. The efficiency decreases with increasing pulse length because the electric field inhomogeneties in the PDT become more significant with an increasing ion pulse length $\Delta t$. Most of the ions are not counted as accepted because the energy condition is not matched. For an efficient deceleration $\Delta t$ needs to be shorter than 2 $\mu$s.

The impact of the fall time $\tau$ of the PDT potential on the efficiency has also been investigated in the simulation. The results are shown in Tab. 5.2. The efficiency was determined with a 4 $\pi$ mm mrad ion bunch with 1 $\mu$s width after deceleration. The ion energy on the reference trajectory is shown for different fall times of the PDT potential. In case of less than 500 ns, the reference ion has an energy in the accepted energy range and an efficiency of 85% is achieved for the specified fall time of the high-voltage switch of 230 ns for a load of $C = 1$ nF. For a fall time of 500 ns or longer, the reference ion is not completely decelerated, since it has already passed through the PDT before the voltage has dropped to the low voltage level. In those cases, 40%-90% of the ions still reach the TRIGA-TRAP setup, but they cannot be captured in the purification trap, since the energy condition is not matched.

Table 5.1: Simulation results for the efficiency of the PDT in dependence of the ion pulse width $\Delta t$. The simulation was performed with a pulse of 10000 ions with an emittance of 4 $\pi$ mm mrad and a switching time $\tau$ of 200 ns.

| $\Delta t$ / $\mu$s | Efficiency / % |
|---|---|
| 0 | 99.8±1.0 |
| 1 | 90.5±1.0 |
| 2 | 70.1±0.8 |
| 3 | 54.5±0.7 |
| 5 | 35.9±0.6 |
| 7 | 26.6±0.5 |

Therefore, an efficiency of 0% is given in Tab. 5.2.

Table 5.2: Efficiency of the PDT and kinetic energy of the reference ion as function of the high-voltage fall time $\tau$.

| $\tau$ / ns | Efficiency / % | $E_{ref}$ / eV |
|---|---|---|
| 50 | 98.0±1.0 | 1105 |
| 230 | 86.5±0.9 | 1103 |
| 300 | 67.6±0.8 | 1103 |
| 500 | 0 | 1131 |
| 1000 | 0 | 2047 |
| 2000 | 0 | 6612 |

An experimental test of the PDT has not been performed so far, but the electrodes have been manufactured and installed in the switchyard (see Fig. 5.12). The capacity of the PDT connected to a high-voltage ceramic feedthrough with a blank copper wire has been determined to be $C_{PDT} = 41$ pF. Therefore, the load of the switch is more than an order of magnitude lower than the value specified for $\tau =$ 230 ns, so that a limitation due to $\tau$ for the deceleration efficiency can be excluded.

## 5.5 The TRIGA-TRAP setup

TRIGA-TRAP is a mass spectrometer which uses a double Penning-trap system for mass measurements on short-lived nuclides similar to other on-line Penning-trap experiments [Bol96, Dil00, Koh04]. A 3D model of the TRIGA-TRAP setup is shown in Fig. 5.13.

### 5.5.1 The double Penning-trap system

The heart of TRIGA-TRAP is the double Penning-trap system, which was designed in [Web04]. The first Penning trap is called purification trap, and is used to prepare mono-isotopic ion bunches using the mass-selective buffer-gas cleaning technique (see Sect. 3.3 and [Sav91]). It is also planned to use a broad-band FT-ICR detection system to monitor the trap content [Rep08, Knu09]. The second trap is the

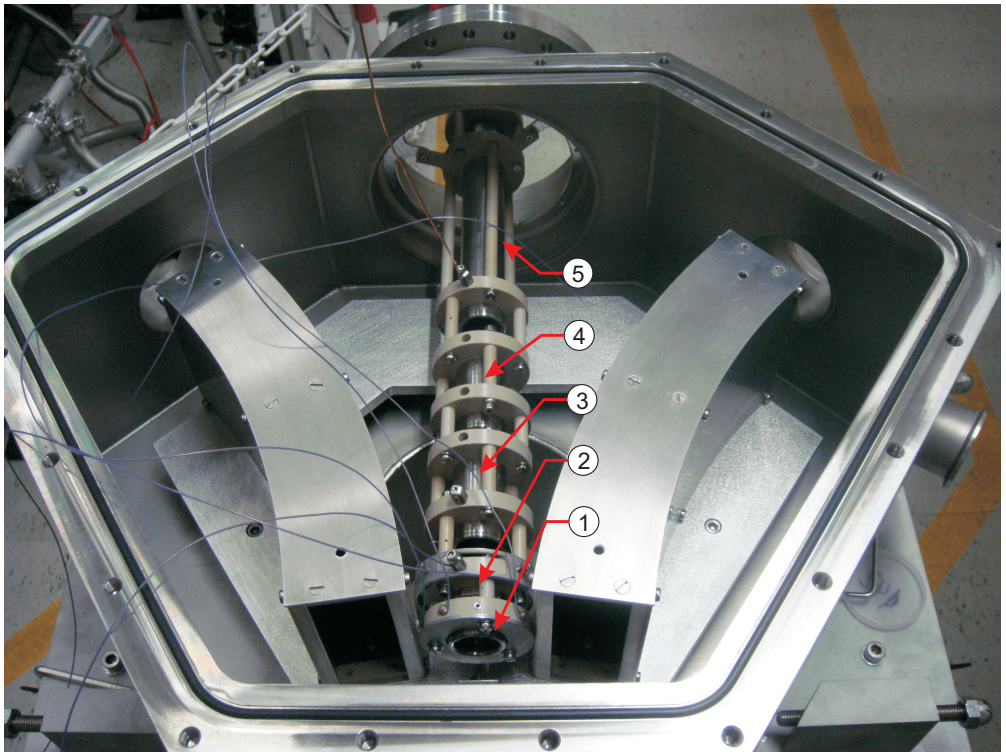


Figure 5.12: A picture of the PDT and its preceding ion optical elements installed in the switchyard. The deflector (1), a drift tube at ground potential (2), the decelerating lens electrodes 1 (3) and 2 (4), and the PDT (5) are shown.

precision trap, where the mass measurement either with the destructive TOF-ICR or the non-destructive narrow-band FT-ICR technique takes place. Both Penning traps are placed within the same superconducting magnet, which was manufactured by Magnex Scientific Ltd. and is the same type of magnet which is also used at SHIPTRAP [Dil00], JYFLTRAP [Koh04] and MLL-TRAP [Koh08]. The magnet has two homogeneous regions in a 10 cm distance from the geometrical center of the trap. The field inhomogeneities at the positions of the traps have been determined with an NMR probe to be $B_2 = 1.05(6) \times 10^{-5}$ T/cm$^2$ for the purification and $B_2 = 5.3(2.0) \times 10^{-6}$ T/cm$^2$ for the precision trap at a field strength of 7 T. The approximately linear decay of the magnetic field is compensated by active compensation coils, which increase the temporal stability of the magnetic field strength to $\Delta B/B \times 1/\Delta t = 1.31(35) \times 10^{-9}$/h [Ket10a]. The trap tube placed in the bore of the superconducting magnet contains the two Penning traps and is designed for a cryogenic operation at 77 K. To this end, the trap vacuum in the center of the tube is surrounded by a liquid nitrogen reservoir, which is thermally decoupled from the outer wall of the tube by an isolation vacuum.

The two Penning traps are shown in Fig. 5.14. The purification trap is a cylindrical Penning trap with 32 mm inner diameter and 212.5 mm total length. It consists of seven electrodes: two endcap, two endcap-correction, two ring-correction and one ring electrode. The correction electrodes are tuned to minimize the higher-order multipole terms of the electric potential. The ring electrode is segmented into two

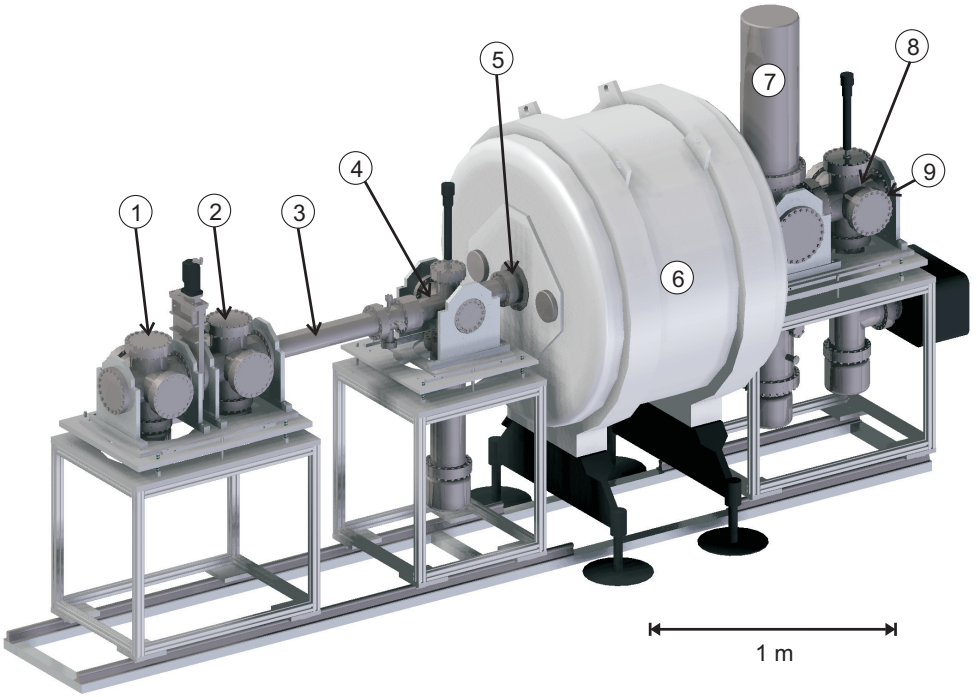


Figure 5.13: A 3D model of the TRIGA-TRAP setup. A laser-ablation ion source (1) and a surface ion source (2) are used for off-line ion production. The ions are guided through the transport section (3), where an MCP detector (4) can be inserted for beam monitoring. The trap tube (5) containing the two Penning traps is located inside the bore of the superconducting magnet (6). A cryostat (7) is used to cool the detection circuit for the image current detection to liquid helium and the Penning traps to liquid nitrogen temperature. An MCP or channeltron detector and a position-sensitive detector for the destructive TOF-ICR technique are located at (8) and (9), respectively.

40° segments and two 140° segments. Two opposing segments cover the same angle. The 40° segments are used for dipolar and quadrupolar excitation, and the two 140° segments for the image current detection. The two endcap-correction electrodes are also split into two segments to allow quadrupolar excitation of the axial motion. One of the endcap electrodes has a connection for a thin capillary, which is used to leak a small amount of helium into the trap for the buffer-gas cooling. Ions of one species are centered in the trap and the whole ion ensemble is ejected towards the precision trap. The two traps are separated by a pumping barrier, which has a small channel with 1.5 mm diameter in the center, so that only the ions that are centered before the ejection can pass into the precision trap. Furthermore, the pumping barrier reduces the buffer-gas pressure by a factor of 100, in order to achieve good pressure conditions in the precision trap for the mass measurement procedure [Nei08].

The precision trap is a seven-pole hyperbolic trap, with a similar electrode structure as the purification trap. The precision trap has been especially designed for the narrow-band image-current detection for singly-charged ions. Therefore, the trap has small dimensions $r_0 = 6.38$ mm and $z_0 = 5.5$ mm and a hyperbolic geometry has been chosen in order to minimize the higher-order terms of the electric potential.

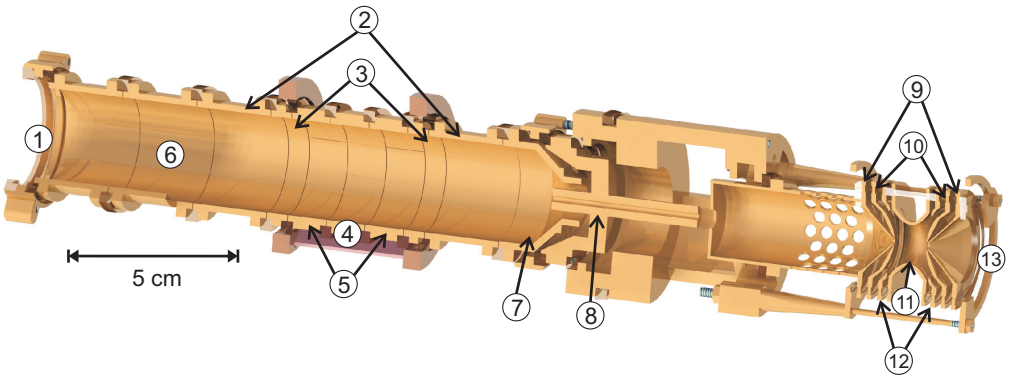


Figure 5.14: A 3D model of the Penning trap electrode stack. Ions are injected from the left (1) into the seven-pole purification trap, which consists of two endcap (2), two endcap-correction (3), one ring (4), and two ring-correction electrodes (5). The trap potential of the purification trap is 70 V. The electrode (6) and the funnel (7) provide an additional confinement with an anharmonic trap potential up to 200 V to increase the accepted energy range of the trap. Unwanted ion species are lost on the funnel (7) or the pumping barrier (8) after buffer-gas cooling and ejection from the purification trap. The pumping barrier suppresses the helium pressure on the side of the precision trap, which is also a seven-pole trap but with hyperbolical electrodes: two endcap-correction (9), two endcap (10), one ring (11), and two ring-correction electrodes (12). For the destructive TOF-ICR detection, the ions are ejected into the time-of-flight section (13). For details see text.

Thereby, an orthogonal trap with eigenfrequencies independent from the motional amplitudes as large as 0.8 $r_0$ is created. This is of importance for the non-destructive ion detection technique discussed in Chap. 8. The ring electrode is also segmented into two 40° segments to apply the excitation signal and two 140° segments for the narrow-band image current detection. The ions are injected and ejected through holes with 1.8 mm diameter in the endcap and endcap-correction electrodes, respectively. The Penning traps and its surrounding electrodes are made of oxygen-free copper because of its low magnetic susceptibility. The electrodes are coated with a thin layer of silver and gold to prevent the oxidation of the surface and to minimize surface patch potentials.

### 5.5.2 Ion transport

The ion optics at the injection side of the superconducting magnet are shown in Fig. 5.15(a). The two off-line ion sources are attached perpendicular to the center beamline. This arrangement allows the injection of the beam from the on-line ion source on the main axis, and prevents neutral particles from the off-line ion sources to reach the Penning traps. Electrostatic 90° benders are used to guide ions from the off-line ion sources to the traps along the main axis. Each ion source has a deflector to correct misalignments, and an einzel lens to focus the beam at the center of the bender. The einzel lenses and deflectors on the transport section are used to prepare a parallel beam on axis. The last einzel lens, consisting of the electrodes lens 3.1,

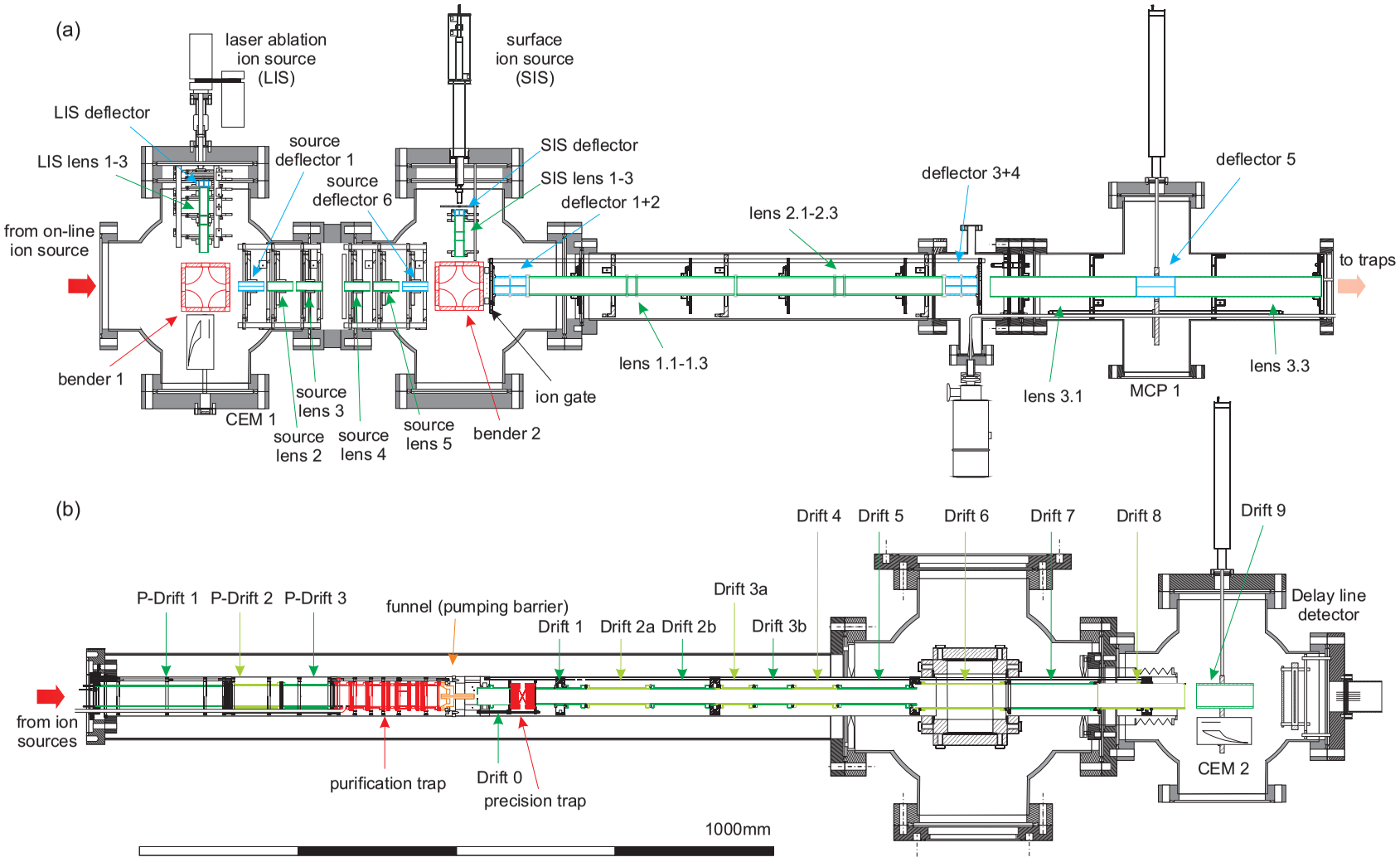


Figure 5.15: Overview of the ion optics in the TRIGA-TRAP setup (figure taken from [Smo08a, Ket10b]). The ion source region is shown in (a). Lens elements are coloured in green, deflectors in blue and the 90°-benders in red. The trap tube is displayed in (b), where the drift tubes are coloured in green, the Penning traps in red, the funnel and the pumping barrier in orange.


88

deflector 5 and lens 3.3 (see labeling in Fig. 5.15), focuses the ions into the magnetic field in order to obtain a beam with small diameter and small cyclotron amplitudes inside the superconducting magnet, where the ions are tied to the center magnetic field line of their cyclotron orbit. Simulations of the ion optics with SIMION have demonstrated that an efficient transport ($> 95\%$) from the off-line ion sources to the purification trap is possible [Smo08a]. For an efficient transport of ions through the pumping barrier into the precision trap it is necessary to apply the buffer-gas cooling in the purification trap.

If the TOF-ICR method is applied, the ions are ejected from the precision trap and are guided through the time-of-flight section, which is shown with the Penning traps in Fig. 5.15(b). The drift tubes 1, 2, 3a, and 3b are used to let the ions slowly drift through the magnetic field gradient, so that the adiabatic conversion of the radial into axial motion can take place. The remaining elements of the drift section are used to focus the beam to the MCP or channeltron detector.

### 5.5.3 The TRIGA-TRAP surface ion source

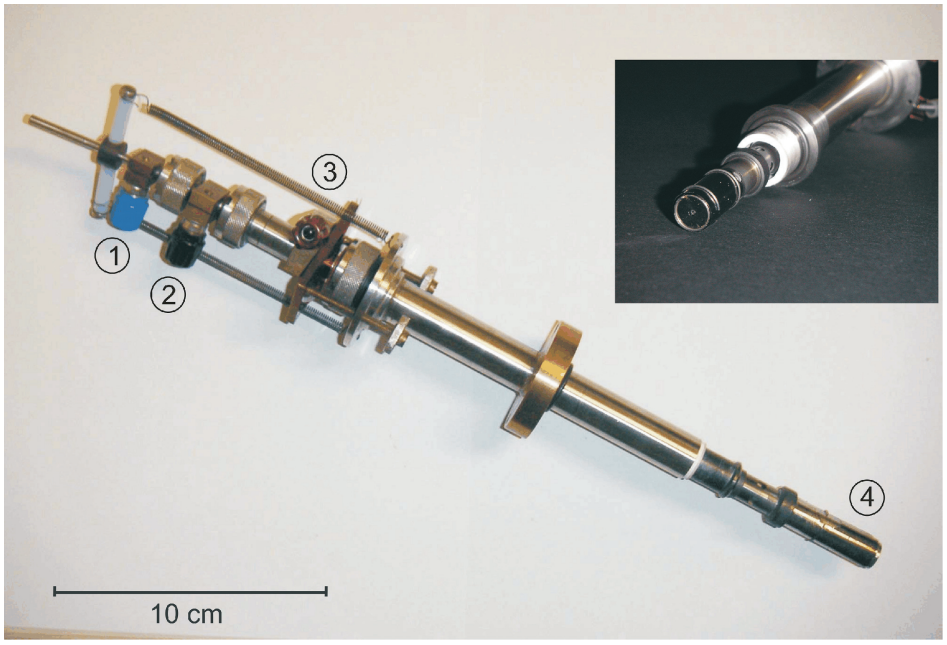


Figure 5.16: A picture of the TRIGA-TRAP surface ion source. The heating current for the electron bombardment is applied to the filament using the connectors (1) and (2), and the acceleration potential is applied via connector (3) to the hot cavity (4), which is shown in detail on the inset. For further details see text.

The surface ion source used at TRIGA-TRAP is a hot cavity ion source built by R. Kirchner at GSI [Kir90]. A picture of the ion source is shown in Fig. 5.16. The hot cavity is formed by a tungsten cup with a small aperture ($d = 0.5$) which is heated via electron bombardment from a hot filament. The advantage of this kind of ion sources is that the atoms collide several times with a hot surface, so that the ionization efficiency is higher compared to a single plain surface. The

cavity contains rubidium zeolite ($Rb_{12}$ $[(AlO_2)_{12}(SiO_2)_{12}]$) and cesium zeolite ($Cs_{12}$ $[(AlO_2)_{12}(SiO_2)_{12}]$) as continuous emitter of rubidium and cesium atoms.

The ion source produces a continuous beam of $^{85}$Rb, $^{87}$Rb, and $^{133}$Cs with high intensity for off-line tests like optimization of the transport voltages or to optimize the trap potential. These nuclides are also used as reference masses because of their well-known mass values [Aud03]. Ion pulses are extracted from the source by switching the potential on the extraction electrode. The hot cavity is biased with a voltage of 102 V, and the extraction electrode is on 200 V in the closed state and on -660 V in the open state. The remaining beam line is biased with a voltage of -1 kV. Hence, the ions have 1.1 keV kinetic energy in the transport section. The number of ions per pulse is regulated via the pulse length, since it is faster and more flexible than waiting for the thermalization of the hot cavity after changing the heating current. The purification trap can efficiently capture ion pulses with a duration of up to 10 $\mu$s and containing several hundred ions.

### 5.5.4 The TRIGA-TRAP laser ablation ion source

The laser ablation ion source has been used to produce ions for the mass and $Q$-value measurements reported in this thesis. Originally, the ion source was designed to produce carbon cluster ions for calibration purposes [Smo08a]. However, the ion source has been also used to produce ions for mass measurements of several elements from solid samples. A detailed description of the laser ablation ion source is found in [Smo08a].

A picture of the laser ablation ion source is shown in Fig. 5.17. A pulsed frequency-doubled Nd:YAG laser (Continuum Minilite) with 532 nm wavelength and 5 ns pulse duration is used in the ablation process. The maximum pulse energy is 50 mJ. It can be regulated by a motorized polarizing beam splitter (Thorlabs, Model PRM1Z8), which turns the direction of the transmitted polarization component against the incoming linearly polarized laser light. This allows to tune the laser pulse energy in a reproducible way. A second beam splitter guides a fraction of 11% for monitoring purposes to a pyroelectric sensor (Thorlabs, Model ES111C), whereas the component with the high intensity is guided to the ablation target. The laser pulse enters the CF-160 vacuum cross from the opposing side of the target through a vacuum window. In order to achieve a high power density on the target a lens with a focal length of $f = 450$ mm is placed in front of the vacuum chamber on a motorized linear stage (Thorlabs, Model MTS50-Z8E) to adjust the position of the focal point on the target. A maximum power density of $1.9 \times 10^{10}$ W/cm$^2$ is reached with this configuration. The ions produced by the laser pulse are extracted by an extraction electrode in Pierce geometry [Pie54]. A deflector and einzel lens are used center and guide the ions through the aperture of the bender, which deflects the ions by 90° in the direction of the traps.

The laser ablation ion source has been used so far for the ion production of the elements listed Tab. 5.3 Different methods have been used for the target preparation as listed in Tab. 5.3. Carbon cluster ions $C_n^+$ with $5 \leq n \leq 26$ [Ket10b] are produced from a Sigradur[1] plate, which is a glassy solid-state configuration of carbon with a

[1]Sigradur is a tradename of the HTW Hochtemperatur Werkstoffe GmbH.

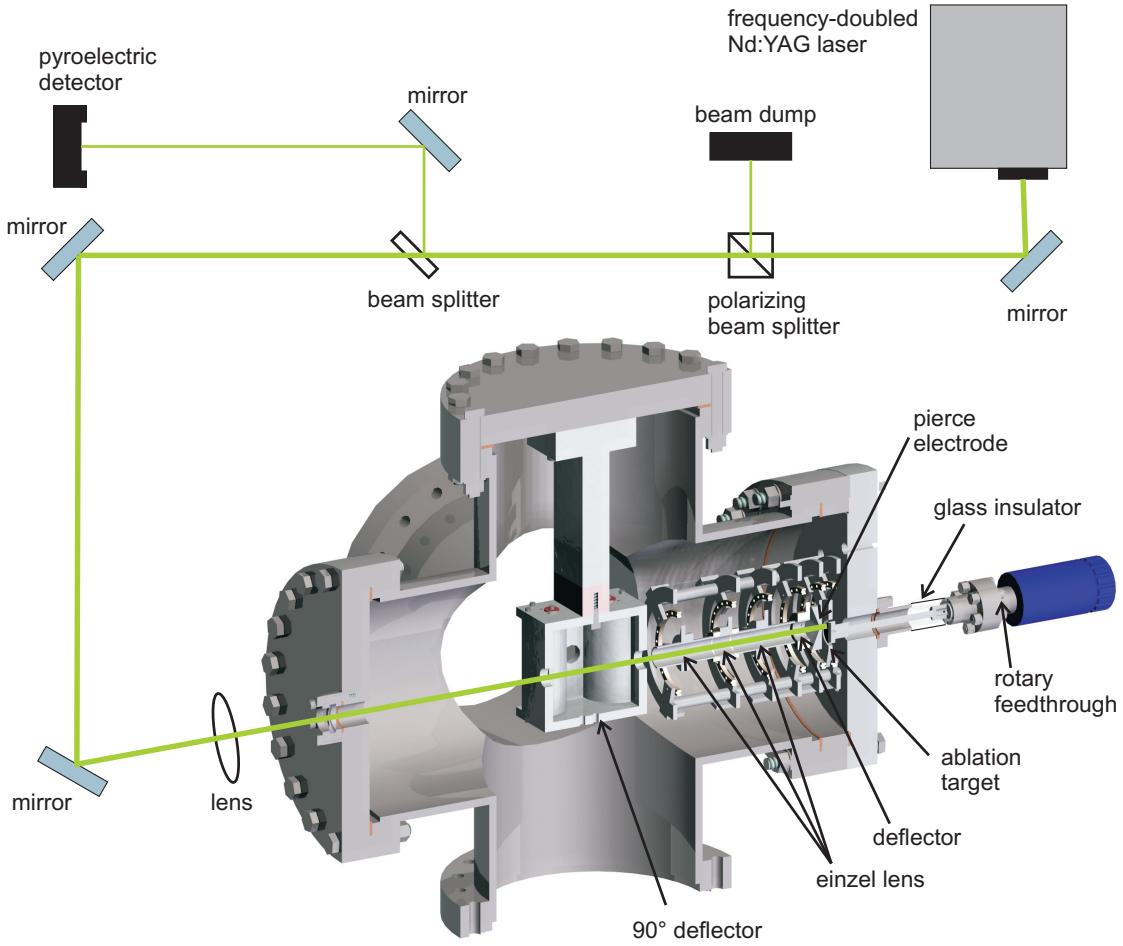


Figure 5.17: A 3D model of the laser ablation ion source. The path of a laser pulse of the frequency-doubled Nd:YAG laser with $\lambda = 532$ nm is shown in green. The laser is focused on an ablation target inside a vacuum chamber. The target is placed 5 mm off-axis on a rotary feedthrough, so that the position of the laser on the target can be changed during operation. The ion optics between the target and the 90° deflector are shown as well.

fullerene-like microstructure. In case heavier carbon cluster ions are needed a pellet produced from $C_{60}$ powder can be used. The $C_{60}$ powder is mixed with a small amount of isopropanol and pressed with a pressure of 130 kg/mm$^2$ to a pellet. In this case carbon cluster ions $C_n^+$ with $1 \leq n \leq 60$ have been produced [Smo08a]. A disadvantage of the $C_{60}$ pellet is that the ion energy is not well defined because the pellet is not conducting. Therefore, Sigradur plates are used for the carbon cluster ion production. A laser pulse energy in the range of 4 mJ to 6 mJ is used in this case.

Metal foils of several elements (Pd, Cd, Sm, Gd, W, Au) have been also used as target material. They are reliable sources for elementary ions of these elements. The production of oxide ions ($SmO^+$ and $GdO^+$) from the samarium and gadolinium foil has been observed as well due to oxidation of the foil in contact with air.

In case only small amounts of a sample are available other methods have to be used to prepare the target. An efficient use of the target material is important in case

Table 5.3: Target types used in the laser ablation ion source for different elements. Target types that were successfully used for mass measurements are marked with X, whereas targets that were no reliable ion production was obtained are marked with -. For details see text.

| Element | Foil / Solid target | Dried Solution | Pressed target | Super-hydrophobic target |
|---|---|---|---|---|
| C | X | | X | |
| Pd | X | | | |
| Cd | X | | | |
| Sm | X | X | | |
| Eu | | X | | |
| Gd | X | X | | X |
| Lu | | X | | |
| Hf | | X | | |
| W | X | - | X | |
| Os | | - | X | |
| Au | X | | | |
| Am | | X | | |

enriched samples or radioactive samples are used. In the latter case, the number of available material can be only a few 10 $\mu$g in case of transuranium elements, and the amount of activity inserted into the ion source should be kept as low as possible. Gadolinium has been used as chemical homologue for the production of transuranium elements. Targets have been prepared by using a solution of $Gd(NO_3)_3$ in 0.1 molar nitric acid with $10^{11}$ to $10^{17}$ atoms per $\mu$l. The simplest method is to deposit a drop of 10 $\mu$l on a Sigradur backing, which is preferred as backing material since it can be simultaneously used to produce carbon cluster reference ions. After evaporation of the liquid the solved material remains on the surface and ions can be produced by low intensity laser pulses from the deposited material (0.1 - 0.5 mJ / mm$^2$). This method has been used for the mass measurements on Gd, Eu, Lu, and Hf with a layer of $10^{15}$ to $10^{17}$ atoms [Ket11]. The lower limit of atoms for the ion production is in the range of $2 \times 10^{12}$ to $10^{15}$ atoms. This was tested by using an americium target, where the number of atoms was determined by measuring the activity of the deposited sample with an $\alpha$-detector. Ions from a sample with $2 \times 10^{12}$ - $5 \times 10^{13}$ were observed with a channeltron detector at the opposing flange of the target in the laser ablation ion source vacuum cross [Smo08b]. In order to determine the cyclotron frequency of the ions with the TOF-ICR method it turned out that layers of $10^{15}$ atoms or more are required due to the present total efficiency of the setup of about 1%.

An alternative approach is to deposit the material by molecular plating, which has been also tested with gadolinium [Ket10b, Ren09]. The gadolinium solution is solved in a few ml of an organic solvent and a voltage up to 2000 V is applied between the backing material, which is used as cathode, and a metal rod, which is placed in the solution as anode. The dissolved molecules migrate towards the cathode and deposit on the backing material. Thereby, much more homogeneous

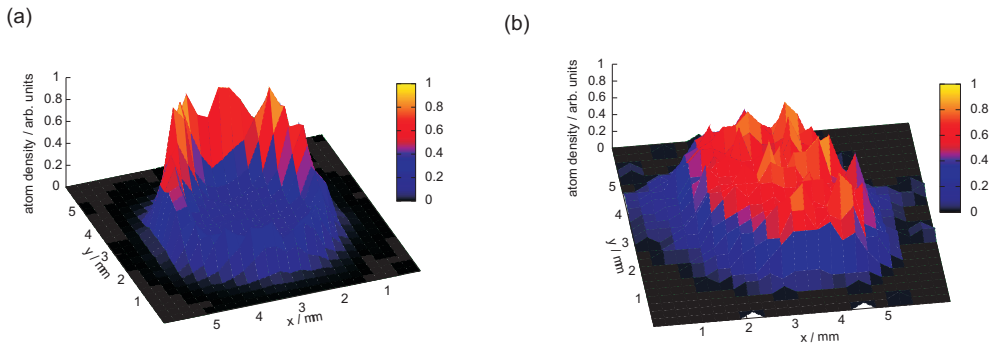


Figure 5.18: Comparison of the material deposition on a dried target shown in (a) and an electroplated target shown in (b) [Ket10b]. For details see text.

targets are obtained compared to the evaporation method, where most of the target material is deposited at the edge of the spot and the enclosed area has only a low density of target atoms. This is due to the fact, that the contact line of the drop is tied to irregularities and defects on the surface, so that an outwards flow occurs when the drop is evaporated [Ren12]. Fig. 5.18 shows a comparison between a target produced by evaporation and molecular plating. The images were obtained by radiography using a position-sensitive imager (Fujifilm FLA 7000) and a gadolinium sample, which was activated by irradiation with neutrons from the TRIGA reactor. Thereby, $^{153}$Gd is produced in the reaction $^{152}\mathrm{Gd} + \mathrm{n} \rightarrow {}^{153}\mathrm{Gd} + \gamma$. The beta decay of $^{153}$Gd produces the signal for the radiography.

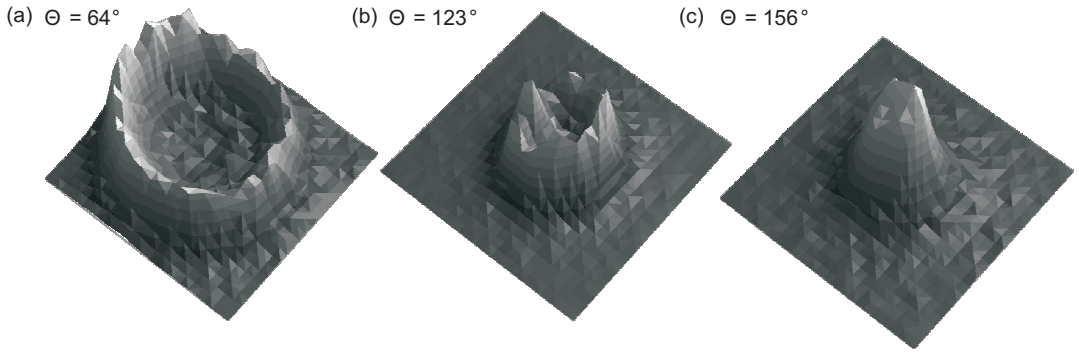


Figure 5.19: Comparison of the material deposition of dried targets on three different surfaces is shown [Ren12]. A hydrophilic surface is shown in (a), a hydrophobic surface in (b), and a super-hydrophobic surface in (c). The contact angles $\theta$ are given in the figure. For details see text and [Ren12].

A more elegant way to produce homogeneous targets is to evaporated the solution on a super-hydrophobic surface [Ren12], where the contact angle between the drop and the backing is larger than 150°. The deposition of the gadolinium solution with $10^{16}$ atoms on such a super-hydrophobic surface resulted in narrow spot with a much more homogeneous layer of gadolinium compared to the hydrophobic surface, as shown in the radiography images of deposited gadolinium on Ti backings with different surface properties in Fig. 5.19. Several targets of this type have been tested

in a MALDI-TOF system under similar conditions as in the TRIGA-TRAP laser ablation ion source, and a factor of four higher amount of ions per laser pulse was obtained compared to the untreated backings [Ren12]. This method will be applied for the preparation of targets from transuranium elements to reduce the amount of required target material for a mass measurement.

For osmium and tungsten a different method had to be used for the target preparation of enriched samples (100 mg of osmium enriched to 1.5 % in $^{184}$Os, and 10 mg of tungsten enriched to $> 90\%$ in $^{180}$W). The evaporation method was not suited in this case because the laser intensity required for the ion production was too high, so that the deposited layer was removed within a few laser shots. Targets were obtained by pressing pellets from the enriched material mixed with silver powder in a ratio of 1:1 and 1:10 for osmium and tungsten, respectively. The addition of silver as adhesive material was necessary to obtain mechanically robust targets. A pressure of 35 kg/mm$^2$ has been used to press the targets.

### 5.5.5 Ion detection

For the TOF-ICR method and for beam monitoring single ions are detected at TRIGA-TRAP with electron multipliers [Ket09a]. Three different types of detectors are used at TRIGA-TRAP.

An MCP (micro-channel plate) detector in Chevron configuration consists of two plates with a micro-channel structure with high resistance. The two plates are stacked on top of each other and a voltage difference of about 1 kV is applied between the front and the back of each plate. Incident particles cause an electron avalanche in a channel and total gain of $10^7$ to $10^8$ and a detection efficiency of 30-50% is obtained for ions with 2 keV kinetic energy. The MCPs used at TRIGA-TRAP have a large active diameter up to 40 mm, so that the acceptance of the MCP detectors is large. One detector of this type has been used at the entrance of the superconducting magnet for beam monitoring and a second one at the exit to detect ions that are ejected from the precision trap.

The second type of electron multiplier is a channeltron electron multiplier (CEM) from DeTech (Model 402 A-H). The advantage of this detector is that it makes use of a conversion dynode, where incoming ions release electrons that are further amplified in an off-axis placed horn-shaped electron-multiplier. Thereby, a detection efficiency $> 90\%$ is reached independent from the kinetic energy of the incoming ions and the detection of neutral particles is avoided due to the detector geometry. However, the acceptance of the CEM is smaller than for the MCP detector, and the ion beam needs to be well focused and guided through the aperture ($d = 11.2$ mm) on the conversion dynode.

TRIGA-TRAP makes also use of a commercial position-sensitive delay-line detector (RoentDek, Model DLD40). The ion signal is also amplified by an MCP detector in Chevron configuration, but the signal read-out allows to determine the position of the incoming particle. Two delay-line wire grids with axes perpendicular to each other are used as anode. The incoming particle creates an electron avalanche in the MCPs, which impacts at a certain position on two wire grids. The position of the particle is determined by the time difference of the signal detected at the

two ends of each wire. This delay-line detector allows to detect particles with a spatial resolution of 70 $\mu$m. The position information of the delay-line detector can be used to distinguish ions with different motion amplitudes in the Penning trap by the image of the trap content of the position-sensitive detector [Eit09]. This allows to detect contaminant ions in the trap if the TOF-ICR excitation scheme is applied being in resonance with one of the ion species.

# Chapter 6

# Results of the on-line commissioning of TRIGA-SPEC

In this chapter the results of the commissioning of the ECR ion source (see Sect. 5.2) for the on-line coupling of TRIGA-SPEC are presented. A sketch of the setup, which has been used for these measurments is shown in Fig. 6.1. Results from the off-line operation of the ECR ion source are discussed in the first part of this chapter. In the second part the results of the on-line tests using a 310 $\mu$g $^{235}$U target covered with a 13 $\mu$m aluminum foil in beam-port A of the reactor are presented.

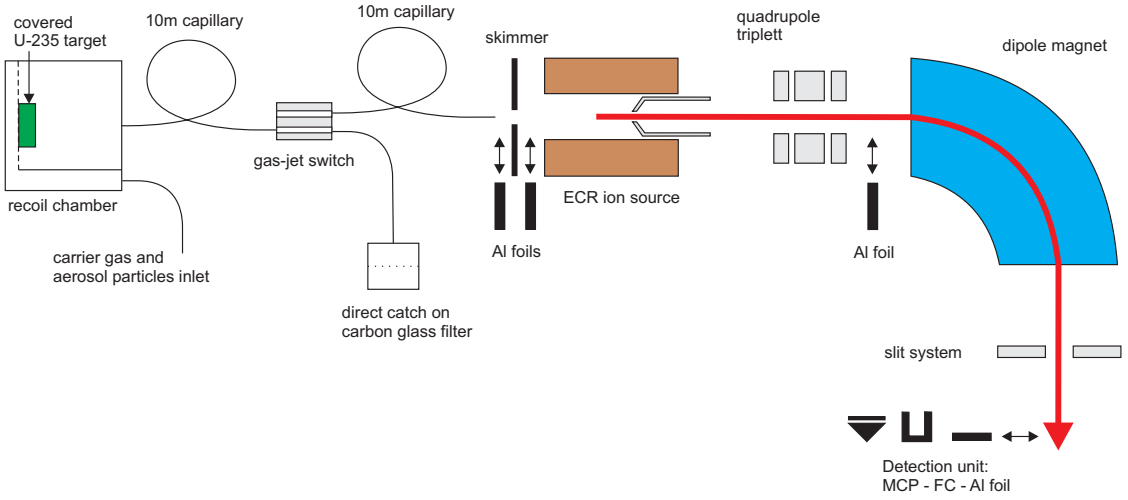


Figure 6.1: A sketch of the setup for the off-line and on-line tests of the ECR ion source. For the off-line operation the ion source is operated only with support gas without gas-jet, or the gas-jet is injected into the ion source without fission products. The mass-separated current of the ECR ion source was detected with a Faraday cup or an MCP detector behind the dipole magnet in order to analyze the composition of the ion beam. During on-line operation the activity transported from the target chamber can be detected also by collecting the fission products on a foil or a filter, and identifying the fission products by $\gamma$-spectroscopy. For this purpose the activity can be collected on a carbon-glass filter in the so called direct-catch (DC) setup before entering the ion source, or on an aluminum foil in front and behind the dipole magnet. Further details are discussed in the text.

## 6.1 Characterization of the ECR ion source in off-line operation

The ECR ion source has been operated off-line to produce an ion beam of gaseous species by leaking a controlled amount of gas into the plasma tube. The leak rate was controlled either by a regulating valve (Pfeiffer Vacuum, EVR 116) or by two mass flow controllers (Analyt-MTC, Model 35823 and Model 35826) with a regulation range of 0 to 50 and 0 to 5 sccm[1], respectively. In addition, a calibrated leak with xenon (VIC, Model 922-719) with a leak rate of $3.6(4)\times10^{12}$ atoms per second has been used to measure the efficiency of the ion source.

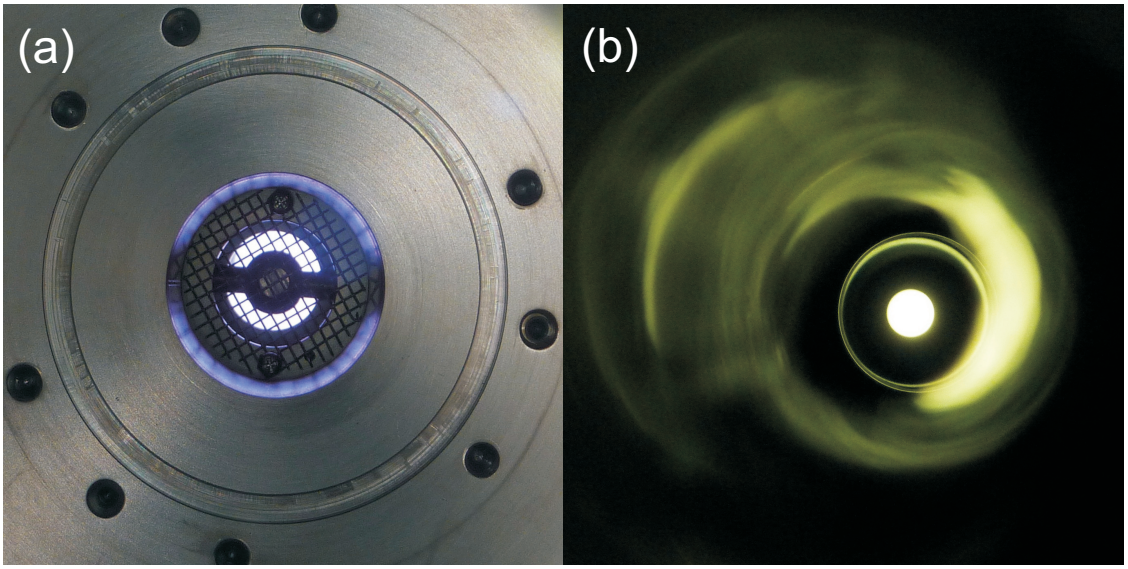


Figure 6.2: A picture of the ECR plasma that was taken from the back of the source with capillary and skimmer removed shown in (a). Argon was used as support gas to ignite the plasma. A picture of the extraction side of the ECR ion source with a plasma using oxygen as support gas is shown in (b).

The ECR ion source has been operated off-line with the original antenna setup [Lie92] and with a new antenna described in Sect. 5.2, which allowed to inject the gas-jet on axis into the plasma tube. For the off-line operation a small amount of support gas (0.1 - 1 sccm) is injected into the source to feed the plasma. Oxygen or argon have been used for this purpose because the ECR plasma could be easily ignited. Pictures of the ECR plasma are shown in Fig. 6.2. A picture of the ion source plasma taken through the skimmer chamber and the waveguide is shown in Fig. 6.2(a) with the skimmer removed. In this case the original antenna was installed with the sphere for the microwave coupling in the center of the plasma tube. Argon was used as support gas. Photons emitted from the recombination processes in the ECR plasma can be observed. Fig. 6.2(b) shows a picture from the extraction side

[1]Sccm is the abbreviation for standard cubic centimeter per minute. Standard conditions for pressure and temperature are $p = 1.01325$ bar and $T = 273.15$ K.

through the aperture of the extraction electrode. In this case, oxygen was used as support gas.

The absorption of the microwave in the plasma depends on the microwave power and the pressure in the source. The most efficient absorption was obtained with both antenna types for a pressure below $7\times10^{-4}$ mbar and a microwave power below 120 W. In this case it was possible to decrease the reflected power below 10%. At higher microwave amplitudes the reflected power increases, which may be caused by reflection of the microwave in an overdense plasma (see Chap. 4.4). If the magnetron was operated at full power it was possible to absorb 280 W power in the plasma with 15% reflection of the incoming wave.

One important point for the on-line operation is the maximum pressure at which the ion source can be operated. It was observed that the fraction of the reflected microwave power increased with higher pressure in the source. This may be caused by a decrease of the number of free electrons due to a higher recombination rate. The power absorbed by the plasma decreased up to a pressure of $8\times10^{-3}$ mbar, which was measured in the waveguide behind the skimmer. Above this limit the ECR plasma extinguished. Thus, the pressure needs to be below this threshold during on-line operation. This sets a limitation for the maximum gas flow of the gas-jet. In order to achieve these pressure conditions, a turbo molecular pump (Leybold TURBOMAG 300, 300 l/s) had to be attached to the waveguide. This allowed to operate the ECR ion source at a pressure of $5\times10^{-4}$ mbar with a gas flow of 1 l argon per minute through the capillary.

Fig. 6.3 shows a typical mass spectrum for the ion source in off-line operation using 0.5 sccm argon as support gas. The magnetic field strength of the dipole magnet has been scanned in the mass range of 0.4 to 45 u. $^{40}Ar^{+}$ is the most abundant ion species in the beam with a current of 53 $\mu$A. If the magnetic field was kept constant at 257.3 mT, a current up to 110 $\mu$A of $^{40}Ar^{+}$ could be detected. Other detected ion species originate from residual gas and from the vacuum chamber in front of the skimmer, which was at a pressure of $8\times10^{-3}$ mbar, due to the end pressure of the rootspump. Therefore, ions and compound ions of $N_2$, $O_2$, and $H_2O$ were observed in the mass spectrum. Doubly-charged ions of nitrogen, oxygen and argon were also detected. Higher charge states up to 4+ could be also produced at good pressure conditions. Therefore, the skimmer had to be removed and the rootspump disconnected, so that the skimmer chamber was also pumped by the turbo pumps, and a lower amount of support gas (0.1 sccm) had to be used. These results are in agreement with a mass spectrum of this ion source observed at the University of Giessen in 1992 [Lie92].

A measure for the ionization efficiency of the ECR ion source can be obtained by injecting a well-known rate of atoms and measuring the ion current using the Faraday cup behind the dipole magnet. This method contains also the transport efficiency to the detector. For these measurements a calibrated leak, with a specified leak rate of $3.6(4)\times10^{12}$ xenon atoms per second has been used. It was verified that about 88% of the gas is pumped away by the turbo molecular pump below the waveguide by comparing the ion current with and without running this turbo molecular pump. Only the remaining fraction of 12% reaches the region of the ECR plasma. This value is a lower limit, since the pressure in the ion source increases, which may lower

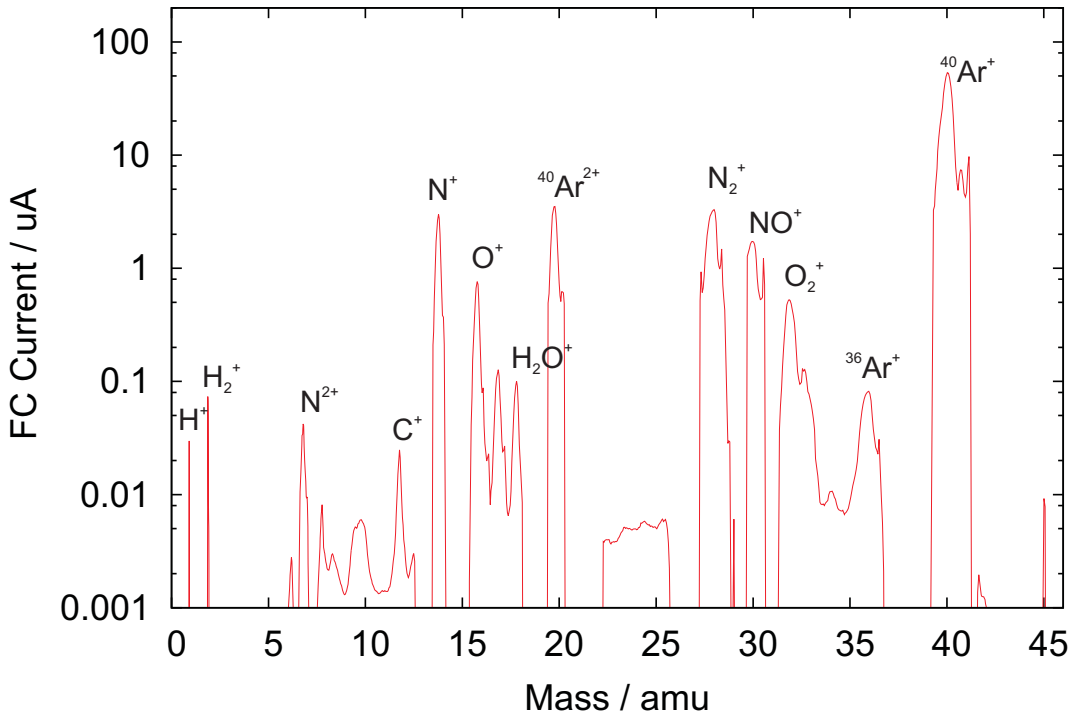


Figure 6.3: A mass spectrum of the 20-keV ion beam from the ECR ion source in off-line operation is shown. The ion beam current detected by a Faraday cup connected to a Keithley 6517A picoamperemeter behind the mass separator is plotted on a logarithmic scale as function of the mass-to-charge ratio. The ECR ion source was operated with 0.5 sccm argon as support gas.

the ionization efficiency. Assuming that 12% of the xenon atoms from the calibrated leak reach the ECR plasma, a total current of 69.6 nA of xenon ions can be expected for 100% ionization and transport efficiency. After mass separation, the current is distributed in seven different mass peaks according to the natural abundance of the xenon isotopes[2].

The efficiency and the mass resolution of the two-step and the three-step acceleration systems presented in Sect. 5.2 has been compared. For the two-step acceleration system the mass resolution of the dipole magnet was about $\Delta m/m \approx 50$ due to the large beam diameter. Closing the slit behind the dipole magnet down to 1 mm improved the mass resolution up to about 100, but the transmission decreased by a factor of 40. For the efficiency measurement the slit was not closed in order to have full transmission through the slit. Hence, the beam components of different masses were overlapping and the intensities of the individual isotopes could not be measured separately. The maximum current at $B = 469$ mT has been taken as a measure for the efficiency. This signal contains a mixture ions from the isotopes $^{128}$Xe to $^{132}$Xe. The contribution of the individual isotopes to the maximum current could not be extracted from the data. Therefore, the efficiency may be underesti-

[2]There are nine stable or lang-lived isotopes of xenon. $^{124}$Xe and $^{126}$Xe are considered as negligible in this context due to their low natural abundances of 0.1% and 0.09%, respectively. The natural abundances of the remaining isotopes are 1.91% for $^{128}$Xe, 26.4% for $^{129}$Xe, 4.1% for $^{130}$Xe, 21.29% for $^{131}$Xe, 26.9% for $^{132}$Xe, 10.4% for $^{134}$Xe, and 8.9% for $^{136}$Xe.

mated by a factor of 2. In addition, the ion current from multiply-charged xenon ions has not been considered for the given efficiency values. However, it is expected by comparing the ratio of singly to doubly-charged ions in other measurements (see Fig. 6.3) that the contribution is below 1% and therefore negligible. In the experiment, multiply-charged xenon ions could not be identified. For singly-charged ions the maximum current measured was 0.8 nA and 2.2 nA for an absorbed microwave power of 92 W to 278 W, respectively. The corresponding values for the efficiency are 1-2% and 3-6%.

The three-step acceleration system performed better in the simulation, because a smaller beam diameter could be obtained at the end of the plasma tube (see Sect. 5.2). In the experiment it was difficult to operate the extraction electrodes at the desired voltages due to discharges between electrode 1 and 2 and the plasma tube of the ion source. This problem occurred in particular during the ion source operation with gas-jet due to the high gas load and the small pumping cross-section between the two extraction electrodes. With operation of the extraction electrodes in the range where no discharges occurred, an efficiency of 2-4% at full microwave power was obtained. The best voltage settings for the ion transport were 17.9 kV on electrode 1 and 14.7 kV on electrode 2. The mass resolution of the dipole magnet of the three-step acceleration system was sufficiently high to separate the xenon isotopes $^{131}$Xe and $^{132}$Xe, as shown in Fig. 6.4. The mass resolving power is better than $R = 132$ with the slit aperture of 1 mm used in this measurement.

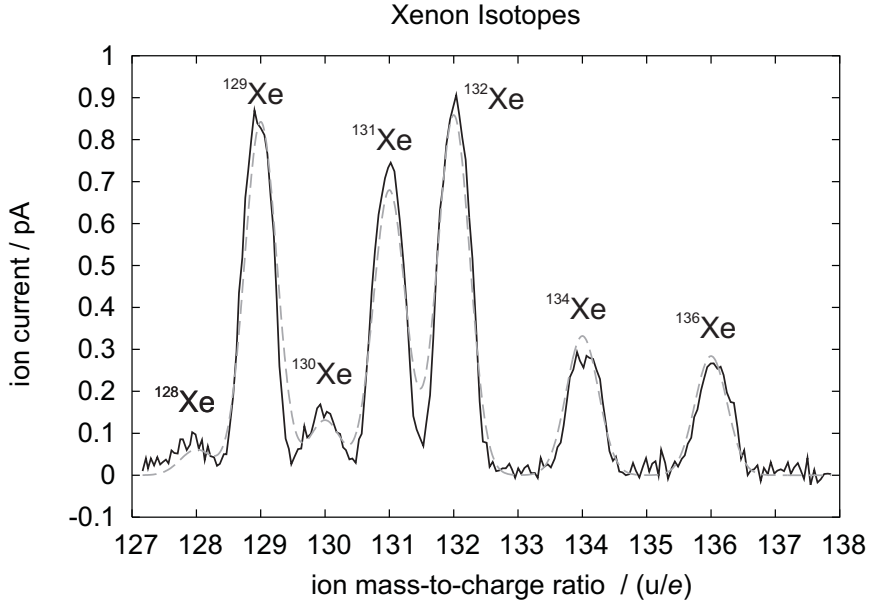


Figure 6.4: Xenon isotopes from residual gas in the ECR ion source are resolved on the Faraday cup behind the dipole magnet. The solid curve shows the measured Faraday cup current as function of the ions' mass-to-charge ratio, and the dashed curve was calculated by superpositioning of the current of all xenon isotopes with their natural abundance. The mass resolution $R$ was better than 132, since the xenon isotopes $^{131}$Xe and $^{132}$Xe could be clearly separated.

The efficiency values given above include the transport efficiency of the ion source

to the Faraday cup behind the magnet. The ion transport efficiency is not optimal because the beam diameter cannot be controlled at the end of the plasma tube for any of the two extraction systems. In case of the two-step acceleration, this possibility is not included in the design, and in the three-step acceleration it is not possible due to the voltage limitation caused by discharges. Therefore, a fraction of the ions is lost in the extraction electrodes.

The diameter of the ion beam has been determined by moving the plates of the slit behind the magnet in and out of the beam and measuring the current as function of the plate position. The beam diameter can be calculated identically to the knife-edge method for laser beams [Wri92]. The beam diameter at the position of the slits is 17±5 mm, which is larger than the detection area of the Faraday cup being 13 mm in diameter. Assuming a beam with circular cross-section and a Gaussian intensity distribution, which has not been cut off at the edges before, and that the beam propagates parallel from the slit to the Faraday cup, only 86% of the intensity can be detected at best.

In order to obtain ionized fission products with the ECR ion source, it is necessary to release them from the surface of the aerosol particles and ionize them. Therefore, the bond of the fission product to the aerosol particle, which is either due to van-der-Waals interaction, Coulomb interaction or chemiesorption, has to be broken by energetic electrons from the plasma. The fission products could be ionized during this process or subsequently in the ECR plasma. The gas jet has been injected into the ECR ion source in off-line operation in order to search for ions of the atoms forming the aerosol particles, because it was not a priori clear how aerosol particles interact with the ECR plasma. The massive aerosol particles, which have about $10^7$ atoms, may have enough momentum to pass quickly through the plasma without releasing the fission products. Therefore, it was investigated, whether ions of the aerosol material can be detected in the mass spectrum of the ion beam behind the dipole magnet. This would indicate that atoms can be released from the aerosol particles and subsequently ionized. The results of these measurements are shown in Fig. 6.5, where the ionization of KCl and $CO_2$ aerosol particles has been investigated.

Fig. 6.5(a) shows the part of the mass spectrum where potassium ions are to be expected. During these tests helium with a flow of 550 ml/min was flushed through the furnace for aerosol particle production (see Sect. 5.1). First, a mass spectrum was recorded with the furnace at room temperature, where no aerosol particles are formed. The second spectrum was recorded after the furnace was heated to the optimum temperature for aerosol production of 660°C (933 K) [Maz81]. No signal of $^{39}K^+$ ions was observed with the Faraday cup[3]. Therefore, the ion current of the aerosol material has to be less than the detection threshold of 1 pA in this measurement. The detection of $^{39}K^+$ with the MCP detector was not possible due to the strong intensity of the neighboring $^{40}Ar^+$ peak. The aerosol particle flow in a helium KCl gas-jet is $1.5\times10^6$ $s^{-1}$ for the given helium flow [Brü83]. Assuming

[3]Chlorine ions may also be released from the aerosol particles, but chlorine may also form negative ions due to its high electron affinity which are not extracted from the source. Therefore, the following discussion focused only on the most abundant potassium isotope $^{39}K$ (93.2% natural abundance), which should form positive ions in the ECR plasma and be a clear evidence for release and ionization of material from the aerosol particles.

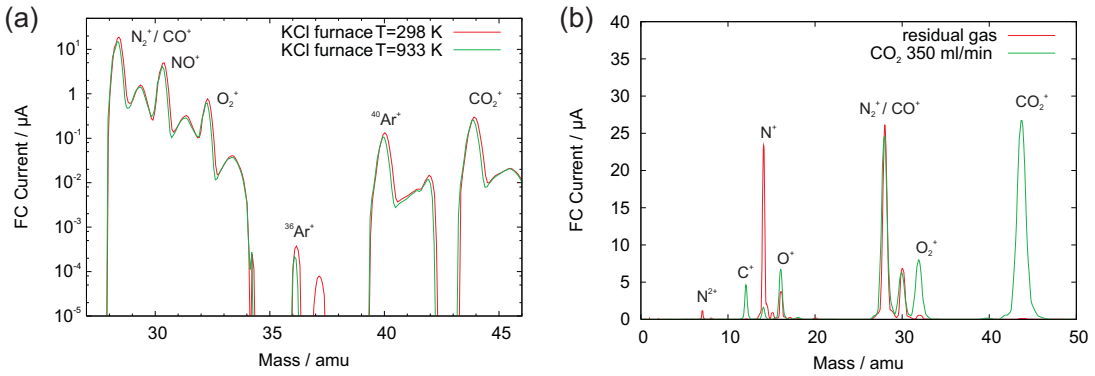


Figure 6.5: Mass spectra of the ion beam with gas-jet in off-line operation. The detected current on the Faraday cup is shown on a logarithmic scale as function of the mass. A comparison between the helium gas-jet without KCl aerosol particles (furnace temperature $T$=298 K), and with aerosol particles ($T$ = 933 K) is shown in (a). A helium flow of 550 ml/min has been used. In (b) a comparison of a mass spectrum with residual gas to a mass spectrum using a the gas-jet with $CO_2$ aerosols at a flow of 350 ml/min is shown. For details see text.

that aerosol particles are massive spheres, this corresponds to a flow of potassium atoms of about $2\times10^{13}$ s$^{-1}$. Considering a skimmer efficiency of 20%, the maximum current of potassium ions obtained from the source is 0.7 $\mu$A for 100% ionization efficieny. Therefore, one can conclude that the conversion efficiency of KCl aerosol particles into ions is less than $10^{-6}$.

A second test was performed with $PbCl_2$ as aerosol material by replacing the salt in the furnace. The temperature used for the aerosol production was in the range of 390°C to 420°C. The background in the mass range of the $Pb^+$ ions ($A$ = 204 to $A$ = 208) is much lower, since no residual or carrier gas ions are expected in this region. For this measurement the MCP detector with single ion sensitivity could be used. A background due to secondary particles created by the ion beam of $10^3$ to $10^4$ counts in the mass range of $m$ = 198 u to 315 u per second was observed, which could not be further reduced. No significant change was observed in the count rate of the MCP detector in the given mass range if the gas-jet was injected. Thus, the ionization of aerosol particles of $PbCl_2$ was also not successful. Therefore, one can expect similar results for other anorganic salts.

In Fig. 6.5(b) a comparison of two mass spectra is shown: one with residual gas in the ECR ion source and one with $CO_2$ gas-jet operation with a flow of 350 ml/min. An increase by more than two orders of magnitude of the $CO_2^+$ current, and an increase of ions of fragments of the $CO_2$ molecule $C^+$, $O^+$, $CO^+$, and $O_2^+$ was observed. A value for the ionization efficiency of $CO_2$ can be estimated by calculating the number of atoms that are injected into the source. The gas flow in the capillary corresponds to $1.5\times10^{20}$ atoms per second. Considering the suppression factor of the skimmer for gases (99.75% [Sch87]), and the fraction of the gas, which is pumped away by the turbo molecular pump behind the skimmer (88%), about $4\times10^{17}$ s$^{-1}$ are injected into the ECR plasma. With these assumptions, the ionization efficiency of $CO_2$ can be estimated to be 0.4% using only the $CO_2^+$ current of 26.7 $\mu$A, and 0.8%

taking the sum of the current of $C^+$, $CO^+$, and $CO_2^+$ of 55.8 $\mu$A. This estimate is within the same order of magnitude as the efficiency measured for xenon. However, it is not clear from these measurements, whether the ionized $CO_2$ molecules are entirely from gaseous $CO_2$, or whether a fraction of the current is contributed by ions from aerosol particles.

In conclusion, the ionization of atoms from the aerosol particles could not be clearly identified in the off-line tests. For KCl aerosol particles, it was observed that a fraction of less than $10^{-6}$ of the aerosol particles' atoms are released as ions. For $CO_2$ it was not possible to distinguish ions from the carrier gas and from the aerosol particles. Based on the results of the measurement with the helium KCl gas-jet, it is likely that the aerosol particles pass only once through the plasma without being stopped or destroyed in the plasma. The fission product would have to be released during the single path of the aerosol particle through the plasma. The mean-free path $\lambda$ for collisions of an electron and an aerosol particle in the ECR plasma is given by $\lambda = v/\nu_{coll}$, where $v$ is the velocity of the aerosol particles and $\nu_{coll}$ the collision frequency, which can be calculated by Eq. (3.17). For the calculation of $\nu_{coll}$ the geometrical cross-section of an aerosol particle with 100 nm diameter, and a Maxwell-Boltzmann distribution of the electron velocity with a thermal energy of $kT$ =10 eV has been used to characterize the electrons in the ECR plasma[4]. In the best case a plasma density of $7.4\times10^{10}$ cm$^{-3}$, which is the critical density for a 2.45 GHz ion source, on a length of about 10 cm can be assumed. The aerosol particles are accelerated inside the capillary by collisions to the flow velocity of carrier gas. Therefore, the sonic speed of helium (970 m/s) is used as estimate for the velocity of the aerosol particle. With these assumptions, $\lambda = 0.8$ $\mu$m is obtained for collisions with electrons with an energy above the ionization threshold of potassium. The mean-free path for the ionization of a single potassium atom in the plasma is about 3 cm if the Müller-Salzborn formula [Mül80] is used for the ionization cross-section.

Thus, it is likely that electrons are removed from an aerosol particle, and that an atom once released from the aerosol particle would be ionized as well. But it is not clear, whether there is a process that could release atoms or ions from an aerosol particle. Scattering of the aerosol particle with electrons or ions can be excluded due to the small energy transfer during the process. The energy transfer on an atom of the aerosol particle is in the order of $10^{-4}$ to $10^{-5}$ eV and 0.1 eV for scattering with electrons at a temperature of $kT_e = 10$ eV and ions with $kT_i = 0.1$ eV, respectively. These are typical values for electron and ion temperatures in a plasma of a 2.45 GHz ECR ion source [Pop91, Kog02].

The aerosol particles could be destroyed in the ECR plasma by Coulomb explosion, if they reach a critical charge state by subsequent ionization [Iak85]. But it is questionable whether this is possible in the ECR plasma, due to charge exchange processes.

The process responsible for the ionization of fission products injected by a gas-jet into a surface ion source is fundamentally different. Aerosol particles are collected on the hot surface, where they can be completely evaporated during the thermal-

[4]It is known that the electrons in the ECR plasma have a non-thermal velocity distribution, but an exact description of the velocity distribution as not been developed [Gel96]. The Maxwell-Boltzmann distribution is used as an approximation.

ization process. Thus, fission products get in contact with the hot surface and can be released as ions from the hot surface. This was successfully demonstrated in [Maz81, Sch87]. In the surface ion source, the aerosol particles can interact with a macroscopic amount of matter, whereas the matter density in an ECR plasma is rather low ($n_{crit} = 7.4{\times}10^{10}$ cm$^{-3}$), and the aerosol particles pass quickly through the plasma, which may be too short for thermalization. In order to conclude, whether it is possible to ionize fission products with the ECR ion source, on-line experiments were performed, which are discussed in the following.

## 6.2 Results of the on-line operation of the gas-jet transport system

For the on-line experiments fission products were produced in beam port A of the reactor with the covered uranium target with fission yields as shown in Fig. 5.4(a). The 13 $\mu$m thick aluminum foil, which covers the target, prevents fission products of the heavy fission branch from leaving the target. Thereby, contamination of the setup with long-lived fission products can be avoided. A fraction of the fission products from the light branch is transmitted through the foil. An empirical value for the foil transmission factor is in the range of 3% to 6%, depending on the mass of the radionuclide [Fin51]. The yield of this target is sufficiently high to determine the efficiency for the on-line coupling of TRIGA-SPEC. For on-line experiments that require a higher rate of radionuclides an uncovered target can be used.

The rate of emitted fission products from the covered target was determined experimentally by $\gamma$-spectroscopy as measure for the maximum yield, which serves as a reference for the efficiency measurements. For this purpose, a 5 mm thick Teflon disk was attached to the target in order to collect all fission products that passed through the aluminum foil. The reactor was operated at a thermal power of 10 kW and fission products were collected during that time in the Teflon disk. Subsequently, the Teflon foil was removed from the target chamber and after 20 minutes waiting time a $\gamma$-spectrum was recorded for 30 minutes with a Ge-detector (ORTEC, Model 50195) and the $\gamma$-spectrum shown in Fig. 6.6(a) was obtained. The most significant lines which could be unambiguously assigned to fission products have been labeled. Due to the waiting time not all nuclides emitted from the target can be observed. The nuclides with half-lives shorter than $T_{1/2} = 2$ min have decayed to more than 99% via $\beta$ decay. Thus, for most of the $\beta$-decay chains only one nuclide with a suitable half-life of several 10 minutes is left in the Teflon disk, and only $\gamma$-lines from the decay of these nuclides can be observed. Table 6.1 lists the nuclides with the most significant peaks in the $\gamma$-spectrum that were used for the efficiency measurements of the on-line coupling.

The efficiency measurements were carried out by comparing the collection rates $r$ of the fission products calculated from the detected activity of the $\gamma$-lines from the reference measurement in the target chamber to the ones from samples collected at one of the following positions: (1) at the direct catch setup, (2) in front of the skimmer, and (3) behind the skimmer. For the determination of the efficiency of the ECR ion source samples were also collected on the aluminum foil in front, and

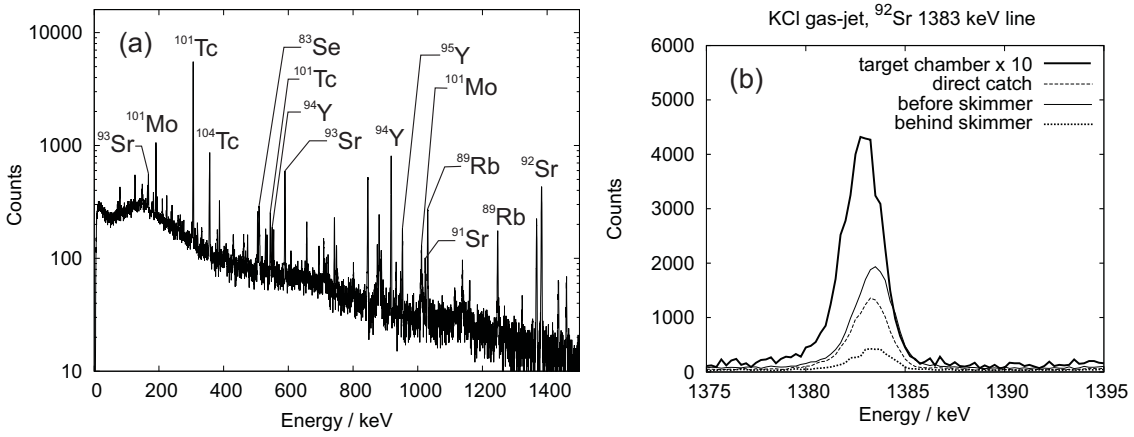


Figure 6.6: In (a) a $\gamma$-spectrum of fission products collected on a Teflon disk attached to a covered target is shown. The most significant $\gamma$-lines of fission products which could be identified are labeled. As a comparison of the detected activity between different collection positions, the detected events as function of the $\gamma$-energy are shown in (b) in the region of the 1383.93(5) keV line of $^{92}$Sr. For details see text.

| Isotope | Energy / keV | $T_{1/2}$/min | $I_\gamma$ | $\epsilon_{D,1}$/% | $\epsilon_{D,2}$/% | $T_{1/2,\mathrm{M}}$/s |
|---|---|---|---|---|---|---|
| $^{101}$Tc | 306.83(3) | 14.2 | 88.7(4.4) | 3.8 | 2.9 | 876 |
| $^{94}$Y | 918.74(5) | 18.7 | 56(3) | 1.6 | 1.3 | 74 |
| $^{92}$Sr | 1383.93(5) | 162.7 | 90(5) | 1.1 | 0.9 | 4.5 |
| $^{101}$Mo | 191.92(2) | 14.6 | 18.21(21) | 5.3 | 3.9 | 7.1 |
| $^{104}$Tc | 358.0(1) | 18.2 | 89(3) | 3.4 | 2.6 | 60 |
| $^{93}$Sr | 590.238(23) | 7.45 | 68(3) | 2.3 | 1.8 | 5.8 |

Table 6.1: The nuclides and the energies of the $\gamma$-lines used for efficiency measurements are listed. The half-lives $T_{1/2}$, the intensities of the $\gamma$-lines $I_\gamma$, the detection efficiencies of the two Ge-detectors (ORTEC, Model 50195) $\epsilon_{D,1}$ and $\epsilon_{D,2}$, and the half-lives of the mother nuclide $T_{1/2,M}$ are given as well. The energy-dependent detection efficiency of the Ge-detectors was determined by using a calibrated sample with a radioisotope mixture (GE Healthcare Limited, QCY 48) directly after the measurements. The values listed here were interpolated with a fifth-order polynom to the corresponding energy value. For further details see text.

behind the dipole magnet (see Fig. 6.1). As an example, the counts of detected $\gamma$-quanta of the 1383.93(5) keV line from the decay of $^{92}$Sr for samples collected at different positions is shown in Fig. 6.6(b).

The collection rate $r$ of the fission products was calculated by using the radioactive decay law. The counts $N_{det}$ observed from the sample is the integrated activity during the measurement time:

$$N_{det} = \epsilon I_\gamma \int_0^{T_m} \lambda N_M e^{-\lambda t} dt, \tag{6.1}$$

where $\epsilon$ is the detection efficiency, $I_\gamma$ the intensity of the $\gamma$-line listed in Tab. 6.1, $T_m$ the measurement duration, $\lambda$ is the decay constant, and $N_M$ is the number of atoms on the sample at the beginning of the measurement time. $N_M$ is given by the

number of atoms accumulated during the collection time considering the decay losses during the collection and waiting time. During the collection time, the number of atoms $N(t)$ obey the differential equation

$$\frac{dN}{dt} = -\lambda N(t) + r, \tag{6.2}$$

with $N(0)$=0. During the waiting time the standard equation for radioactive decay is $dN/dt = -\lambda N(t)$ with $N(T_c)$=$N_c$, where $T_c$ and $N_c$ denote the collection time and the number of atoms on the sample after the collection, respectively. Using these equations, $N_M$ can be obtained:

$$N_M = e^{-\lambda T_w} \frac{r}{\lambda} \left(1 - e^{-\lambda T_c}\right), \tag{6.3}$$

where $T_w$ denotes the waiting time. The collection rate $r$ can be calculated via equations (6.1) and (6.3) by measuring $N_{det}$:

$$r = \frac{1}{\epsilon} \frac{e^{\lambda T_w}}{(e^{-\lambda T_m} - 1)} \frac{\lambda N_{det}}{(1 - e^{-\lambda T_c})}. \tag{6.4}$$

The six different nuclides listed in Tab. 6.1 have been used to determine the transport efficiencies to different collection positions. The decay of the mother nuclides can be neglected due to the sufficiently short half-life of all nuclides considered, except $^{101}$Tc. The individual production rate of $^{101}$Tc is only 73.4 s$^{-1}$ compared to 8.4×10$^4$ s$^{-1}$ of $^{101}$Mo. Thus, $^{101}$Tc is mainly produced by the decay of $^{101}$Mo and the collection rate of $^{101}$Mo can be calculated from the number of detected decays of $^{101}$Tc, if the mother-daughter decay of these two nuclides is considered.

Tab. 6.2 shows the calculated collection rates $r$ and the corresponding transport efficiencies $\epsilon$ for the three nuclides $^{93}$Sr, $^{94}$Y, and $^{101}$Mo. The collection in the target chamber was carried out with a factor ten reduced neutron flux in order to limit the radiation dose while removing the Teflon disk from the target chamber. The reactor was operated at 10 kW$_{th}$ for this measurement, whereas 100 kW$_{th}$ was used for all other measurements. Hence, the collection rate of this measurement given in Tab. 6.2 was scaled up by a factor of 10 to compensate the factor of ten lower neutron flux, in order to be comparable to the other measurements.

The first set of measurements was performed using KCl aerosol particles and helium as carrier gas. The helium flow was adjusted to obtain 2.7 bar pressure in the target chamber in order to have sufficient stopping power for the fission products. A 10 m long capillary of 0.86 mm inner diameter between the target chamber and the first gas-jet switch was installed (see Fig. 6.1), where the gas-jet was either guided to the direct-catch setup (capillary with 0.1 m length, 0.86 mm inner diameter) or to the skimmer chamber (capillary with 10 m length, 1 mm inner diameter). The helium flow was adjusted between 1050 ml/min for the collection in the skimmer chamber and 1500 ml/min for the direct catch measurements. The skimmer efficiency for the helium-KCl gas-jet $\epsilon_{\mathrm{Sk,KCl}}$ was determined by calculating the ratio of $r$ in front and behind the skimmer. The results are shown in Table 6.3. A direct catch measurement was performed directly after each collection at the skimmer, to avoid systematic errors due to fluctuations of the gas-jet efficiency $\epsilon_{\mathrm{G,KCl}}$. An average value for $\epsilon_{\mathrm{G,KCl}}$

Table 6.2: Collection rates $r$ and transport efficiencies $\epsilon$ of the gas-jet transport system determined with $\gamma$-spectroscopy are listed. The collection positions given are in the target chamber (I), in front of the skimmer (II), behind the skimmer (III), and at the direct catch setup (IV). The collection rates $r$ and the transport efficiencies $\epsilon$ for $^{93}$Sr, $^{94}$Y, and $^{101}$Mo, have been measured and are given with their statistical uncertainties. The values determined for the other nuclides given in Tab. 6.1 are not shown here, since they have similar characteristics. The measurement in the target chamber is used as calibration measurement for the efficiency. The collection rates of the calibration measurement at position (I) are scaled up by factor of 10 to compensate the lower neutron flux compared to the other measurements. The different waiting times $T_w$ between the collection and the measurement have been respected in the calculations. For further details see text.

| Pos. | Aerosol | $T_w$ | $r(^{93}\mathrm{Sr})/(10^3\ \mathrm{s}^{-1})$ | $\epsilon(^{93}\mathrm{Sr})$ | $r(^{94}\mathrm{Y})/(10^3\ \mathrm{s}^{-1})$ | $\epsilon(^{94}\mathrm{Y})$ | $r(^{101}\mathrm{Mo})/(10^3\ \mathrm{s}^{-1})$ | $\epsilon(^{101}\mathrm{Mo})$ |
|---|---|---|---|---|---|---|---|---|
| I | - | 20 | 31.6±0.05 | 100.00% | 25.3±0.03 | 100.00% | 18.9±0.03 | 100.00% |
| II | He / KCl | 29 | 23.2±0.15 | 73.5±0.5 % | 16.3±0.09 | 64.6±0.3 % | 11.9±0.08 | 62.8±0.4% |
| IV | He / KCl | 20 | 18.0±0.14 | 56.8±0.4 % | 12.3±0.08 | 48.4±0.3 % | 9.02±0.07 | 47.7±0.4% |
| III | He / KCl | 22.5 | 6.24±0.11 | 19.8±0.3 % | 3.80±0.05 | 15.0±0.2 % | 2.67±0.04 | 14.1±0.2% |
| IV | He / KCl | 22.5 | 16.4±0.12 | 51.9±0.4 % | 11.3±0.07 | 44.8±0.3 % | 8.87±0.06 | 46.9±0.3% |
| II | He / $PbCl_2$ | 22 | 1.18±0.03 | 3.7±0.1 % | 0.852±0.020 | 3.6±0.1 % | 0.577±0.017 | 3.1±0.1 % |
| IV | He / $PbCl_2$ | 22 | 13.9±0.13 | 43.8±0.4 % | 9.02±0.07 | 44.3±0.3 % | 8.11±0.07 | 42.9±0.4 % |
| III | He / $PbCl_2$ | 25 | 5.90±0.09 | 18.7±0.3 % | 3.82±0.04 | 17.0±0.2 % | 2.55±0.04 | 13.5±0.2 % |
| IV | He / $PbCl_2$ | 25 | 13.3±0.15 | 42.0±0.5 % | 8.00±0.07 | 44.4±0.3 % | 7.02±0.07 | 37.1±0.4 % |
| IV | $CO_2$ | 20 | 2.98±0.05 | 9.4±0.2 % | 2.07±0.03 | 8.2±0.1 % | 1.67±0.03 | 8.9±0.1 % |
| II | $CO_2$ | 26 | 0.845±0.034 | 2.7±0.1 % | 0.474±0.016 | 1.9±0.1 % | 0.200±0.011 | 1.1±0.1 % |
| IV | $CO_2$ | 26 | 1.13±0.05 | 3.6±0.1 % | 0.629±0.020 | 2.5±0.1 % | 0.558±0.021 | 2.9±0.1 % |
| III | $CO_2$ | 28 | 0 | 0 | 0 | 0 | 0 | 0 |
| IV | $CO_2$ | 20 | 0.778±0.025 | 2.5±0.1 % | 0.550±0.015 | 2.2±0.1 % | 0.419±0.014 | 2.2±0.1 % |

is given in Tab. 6.4 calculated by the average of the two direct catch measurements. Similar values for the average skimmer efficiency (22.0±1.7 %) and the average gas-jet efficiency (48.1±4.8%) were obtained as in previous experiments (see [Brü79, Brü83, Maz80, Gün93], and Tab. 4.1, respectively). The absolute efficiency from the target chamber through the skimmer is 14.4±2.0%.

| Nuclide | $\epsilon_{Sk,KCl}$/% | $\epsilon_{Sk,PbCl_2}$/% | $\epsilon_{Sk,CO_2}$/% |
|---|---|---|---|
| $^{101}$Tc | 21.2±0.1 | 21.2±0.3 | 3.2±0.3 |
| $^{94}$Y | 23.2±0.3 | 22.3±0.6 | 0 |
| $^{92}$Sr | 15.1±0.3 | 21.5±0.8 | 0 |
| $^{101}$Mo | 22.5±0.4 | 22.6±0.7 | 0 |
| $^{104}$Tc | 23.0±0.3 | 20.6±0.6 | 0 |
| $^{93}$Sr | 26.9±0.5 | 20.0±0.6 | 0 |
| Weighted mean | 22.0±1.7 | 21.4±0.4 | |

Table 6.3: Skimmer efficiencies obtained by comparing the collection rates $r$ of the given nuclides collected in front and behind the skimmer. The skimmer efficiencies for KCl $\epsilon_{Sk,KCl}$, $PbCl_2$ $\epsilon_{Sk,PbCl_2}$, and $CO_2$ aerosol particles $\epsilon_{Sk,CO_2}$ are given. In case of the $CO_2$ gas jet, only one line had sufficient statistics to derive an efficiency value. For details see text.

| Nuclide | $\epsilon_{G,KCl}$/% | $\epsilon_{G,PbCl_2}$/% | $\epsilon_{G,CO_2}$/% | $\epsilon_{G,CO_2,best}$/% |
|---|---|---|---|---|
| $^{101}$Tc | 63.7±0.2 | 44.3±0.2 | 3.4±0.1 | 11.3±0.1 |
| $^{94}$Y | 46.6±0.4 | 33.7±0.4 | 2.3±0.1 | 8.2±0.1 |
| $^{92}$Sr | 31.0±0.4 | 22.2±0.3 | 1.7±0.1 | 8.9±0.1 |
| $^{101}$Mo | 47.3±0.5 | 40.0±0.6 | 2.6±0.1 | 8.9±0.1 |
| $^{104}$Tc | 45.5±0.4 | 35.3±0.4 | 3.8±0.1 | 11.3±0.1 |
| $^{93}$Sr | 54.4±0.6 | 42.9±0.6 | 3.0±0.2 | 9.4±0.2 |
| Weighted mean | 48.1±4.8 | 36.4±3.6 | 2.8±0.3 | 9.7±0.6 |

Table 6.4: Gas-jet efficiencies calculated by comparing the collection rates $r$ at the target to the ones at the direct catch setup. The efficiencies $\epsilon_{G,KCl}$ for KCl, $\epsilon_{G,PbCl_2}$ for $PbCl_2$, and $\epsilon_{G,CO_2}$ for $CO_2$ as aerosol material are given. For the $CO_2$ gas-jet a higher transport efficiencies were observed at the start of the gas-jet operation. The best values observed under these conditions are listed as $\epsilon_{G,CO_2,best}$. For details see text.

$PbCl_2$ was also tested in the on-line experiments. A higher skimmer efficiency is expected due to a narrower cone for the aerosol particles during the expansion of the gas-jet into the vacuum, since the aerosol particles have a heavier mass [Brü85]. The average gas-jet efficiency observed in the experiments was 36.4±3.6%, which is 25% less than for KCl. The average skimmer efficiency of 21.4±0.4% of the $PbCl_2$ gas-jet is in agreement with the value obtained for KCl within the given uncertainties (see Tab. 6.3). An increase in the skimmer efficiency as in [Brü85] was not observed. This may require an optimization of the distance between capillary and skimmer. The absolute efficiency from the target chamber through the skimmer is only 3.1±0.3%,

due to the fact that the amount of fission products arriving in the skimmer chamber was much lower than for the KCl gas-jet.

The transport efficiency of the $CO_2$ gas-jet has also been studied. It was observed in the first measurements that the transport efficiency in the direct catch measurement was below 1%, despite the successful use of $CO_2$ aerosol particles in other experiments reported in literature (see Tab. 4.1 and [Sil77, Aum79]). In long-term operation the average transport efficiency could be increased to 2.8±0.3% by heating the supply tank with heating bands above the critical temperature of $CO_2$ ($T_c = 31.0°C$) in the range of $T = 33°C$ to 37°C. For these measurements a mixture of $CO_2$ and helium was used. The $CO_2$ flow was kept at 500 ml/min and the helium flow was adjusted from 100 ml/min for measurements in the skimmer chamber to 700 ml/min for the direct catch measurement in order to maintain a pressure of 2.7 bar in the target chamber.

It was observed that the transport efficiency was higher during the first collection procedure of 20 minutes duration after the $CO_2$-bottle was closed for several hours. The best efficiency observed after starting the $CO_2$ gas-jet was 9.7±0.6% with a supply tank and a pressure reducing valve temperature of 33.7°C and 27.5°C, respectively. After 20 minutes the efficiency of the gas-jet had already reduced back to about 2%. This effect has been observed in other experiments as well and was overcome by heating the supply tank above the critical temperature [Sil77]. With the present setup an increase of the transport efficiency up to a supply tank temperature of 37.0°C could not be observed. At first, the efficiency reduction has been assigned to the cooling of the pressure reducing valve by the expanding gas, but no significant increase of the transport efficiency as function of the temperature of the pressure reducing valve was observed. The use of a gas mixture of $CO_2$ with helium or nitrogen in order to decrease the cooling effect in the pressure reducing valve by a smaller $CO_2$ flow was also not successful. It was also tested to use a coagulation volume at room and at dry-ice temperature in order to increase the aerosol particle size, without any impact on the transport efficiency.

A transmission of fission products through the skimmer was only observed for the most intense line in the recorded $\gamma$-spectra, which is the 306.83(3) keV line from the $\beta$-decay of $^{101}$Tc. Using the $^{101}$Tc activity, the skimmer efficiency can be estimated to be 3.2±0.3%, which is one order of magnitude lower than for KCl and $PbCl_2$. This indicates that the $CO_2$ aerosol particles are already almost evaporated when they reach the skimmer chamber. Their mass is not large enough to pass through the skimmer undisturbed by collision with the carrier gas, as it is the case for the KCl or $PbCl_2$ aerosol particles. This may also explain the low efficiency in the direct catch measurements. The $CO_2$ aerosol particles evaporate due to heat transfer from collisions with the carrier gas and are more easily lost due to diffusion as their mass decreases. The high transport efficiency of 25% to 60% in literature [Sil77, Aum79] was achieved with capillaries of 8 mm diameter, and it was also observed that the efficiency decreases with decreasing capillary diameter. A much shorter diffusion path in the capillaries of 0.86 mm and 1 mm that are used in this experiment may be the reason for the low transport efficiency. The use of capillaries with larger diameters is not applicible, because either the pressure for the stopping power in the target chamber cannot be maintained or the gas load in the ECR ion source would

exceed the limit.

The total transport efficiency of the $CO_2$ gas-jet behind the skimmer for $^{101}$Tc is $(6.9\pm0.6)\times10^{-4}$. Thus, the application of the $CO_2$ gas-jet with the present performance is not suitable to study the ionization of fission products in the ion source. The transport of aerosol particles from pure gases is further studied in [Kle12]. If a transport efficiency comparable to the one of KCl can be reached, the contamination of the ion source with solid material could be avoided.

## 6.3 Results of the on-line operation of the ECR ion source

The detection of ionized fission products from the ECR ion source was investigated by implanting the ion beam into an aluminum foil in front of the magnet, where all ions are collected, and behind the magnet, where nuclides with a certain mass number $A$ can be selected. For these measurements the KCl gas-jet has been injected into the ion source. The rate of arriving fission products for one mass number $A$ is in the range of 2000 $s^{-1}$ to 6000 $s^{-1}$ (see Tab. 6.2). This excludes the use of the Faraday cup for the ion detection, since the expected current is below 0.1 pA. The MCP detector could also not be used because the background count rate was higher than the expected signal from the fission products. The background count rate is caused by secondary particles, which are created by ions of the carrier or support gas in the dipole magnet, and could not be further suppressed. Thus, $\gamma$-spectroscopy on collected samples has been applied.

The 1383 keV line of $^{92}$Sr from $\gamma$-spectra recorded from samples collected in front of the magnet are shown in Fig. 6.7. A direct catch measurement is shown as comparison for the detected activity. In order to distinguish activity transported by aerosol particles passing on axis through the ECR plasma on the collection foil, the following measurements were performed: First, the activity was collected by implanting the ion beam with 20 keV energy on the foil. Second, the HV-voltage of the ion source platform was switched off and a positive potential was applied to the extraction electrode to avoid the emission of positive ions from the ion source. Finally, the collection was carried out without plasma in the ECR chamber and no voltage applied to the extraction electrodes. The first and the second measurement yield the same collection rate on the filter, which proves that the detected activity was transported only by aerosol particles and not as ions. The activity of the sample without plasma in the ECR ion source has even a higher yield than the first two measurements. This indicates that the plasma disturbs the propagation of the gas-jet, possibly due to ionization of the aerosol particles in the plasma. The propagation of charged aerosol particles is affected by Coulomb interaction and the electric and magnetic fields in the ion source region. Therefore, the collected activity is lower if the ion source is switched on.

Thus, no significant transport of ionized fission products compared to the aerosol-bound transport was observed in front of the magnet. The collection of fission products behind the dipole magnet was also tested, and no activity was observed for $^{94}$Y ($B$ = 392.5 mT), $^{101}$Mo, and $^{101}$Tc ($B$ = 408.5 mT to 414.5 mT). It was

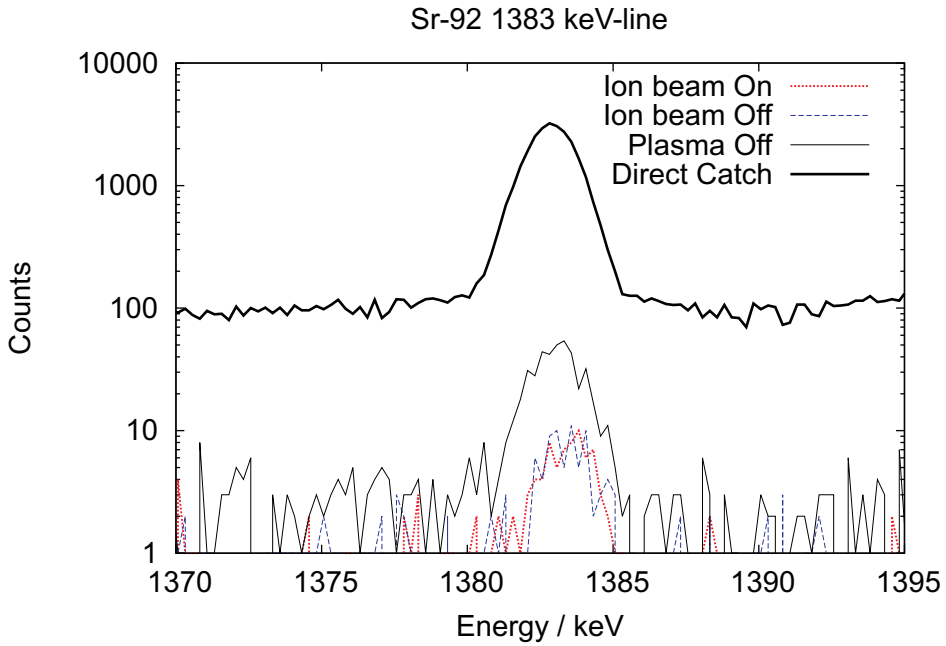


Figure 6.7: Comparison of the activity of $^{92}$Sr collected behind the ECR ion source and a direct catch measurement. For details see text.

also tested, whether short-lived nuclides of krypton, which is transported through the capillary without aerosol particles, can be ionized in the ECR ion source. The short-lived isotopes $^{89}$Kr to $^{93}$Kr were detected by a $\gamma$ detector close to the capillary, but due to the low skimmer transmission of gases, ions of these nuclides could also not be detected.

The lowest collection rate which could have been detected by $\gamma$-spectroscopy was estimated to 10 $s^{-1}$. Thus, this is the upper limit for the yield of ions obtained from the ECR ion source. It was not possible to detect fission products released from the aerosol particles by hot electrons from the ECR plasma, as well as ions from the aerosol particle material. The fission products are not released from the aerosol particles as excepted from the results in Sect. 6.1.

One similar attempt to ionize fission products from a gas-jet in an ECR ion source was made at the SARA on-line separator [Gim92]. In these experiments it was observed that no ionized fission product could be observed if the gas-jet was injected along the main axis of a 2.45 GHz ECR ion source. It was proposed to use a catcher foil for the aerosol particles in the ECR plasma. Fission products could be released from the catcher foil by heating or by sputtering with ions from the ECR plasma. The ECR ion source developed for this purpose has the gas-jet radially injected into the ECR plasma, and a heated catcher foil installed on the opposing side in the ion source. However, no results of on-line tests of this ion source have been reported.

The present ECR ion source was not developed for this purpose. Therefore, the ion source geometry is not suited to install a catcher foil with a good efficiency for the deposition of the aerosol material and the release of the fission products into the ECR plasma. An ECR ion source with a suitable geometry is the MONO 1000 ion source

[Jar02]. The ion source chamber has the diameter of a 2.45 GHz waveguide and four ports provide radial access to the plasma region. The microwave can be injected axially and the gas-jet radially into the ion source or vice versa. Furthermore, the ion source has an ionization efficiency for gases above 90%. Thus, the MONO 1000 ion source provides better conditions for the ionizaton of fission products from a catcher foil compared to the present ion source, which provides no radial access to the ECR plasma due to the permanent magnets around the plasma tube. Further disadvantages of the present source are the ion source chamber with a diameter below the cuf-off wavelength, so that an antenna is required for the microwave injection.

A drawback from using a catcher foil in particular for refractory elements is that the fission products need to be evaporated from the foil. If they are released at all, the release time from the surface by heating or sputtering can be larger than the half-lives of the short-lived nuclides of refractory elements, and it is not clear whether an ECR ion source with catcher foil would perform better than a surface ion source.

Another way to enhance the ionization possibility in the ECR plasma would be to increase the plasma density and the electron temperature in the plasma by choosing an ion source with a higher operating frequency. The ECR ion sources with the highest plasma densities and electron temperatures nowadays available are operating with a frequency of 28 GHz [Hit02]. The critical density for a 28 GHz ion source is $n_{crit} = 9.7{\times}10^{12}$ cm$^{-1}$, and electron temperatures of several 10 keV can be reached in these ion sources [Gel96]. Thus, the plasma density and the electron temperature could be increased by two and three orders of magnitude, respectively, in order to increase the interaction frequency and the energy transfer of the hot electrons to the aerosol particles. However, it is not clear whether these conditions would be sufficient to release atoms from an aerosol particle with a mean diameter of 100 nm.

In conclusion, a 2.45 GHz ECR ion source has been successfully commissioned on a high-voltage platform at TRIGA-SPEC. The ion source was used to commission and specify the dipole magnet. Currents up to 110 $\mu$A of argon were available for off-line tests. The design of ECR ion source was adapted to be operational as a gas-jet coupled ion source on-line. The ionization efficiency of the ECR ion source for aerosol-particle-bound fission products was found to be too low to provide radioactive ion beams for TRIGA-SPEC. The upper limit for the yield of ions is 10 $s^{-1}$. The reason for the low efficiency has been attributed to the lack of capability to release fission products from aerosol particle with hot electrons from the ECR plasma. Future developments of on-line ion sources for TRIGA-SPEC have to alternative approaches for the ionization of fission products. These are discussed in Chap. 8. However, future ion sources will benefit from the installation of the high-voltage platform, the rootspump and skimmer system, that are required for on-line operation of any gas-jet coupled ion source.

# Chapter 7

# Mass and $Q$-value measurement results for neutrino physics

The measurements of atomic masses $M(A, Z)$ and double-beta transition $Q$ values were preformed with the TRIGA-TRAP setup (see Sect. 5.5) using the TOF-ICR technique (see Sect. 3.3). A new estimate of the half-life of the double-electron capture in $^{184}$Os has been performed within this thesis using the experimentally determined $Q$ value with the TRIGA-TRAP mass spectrometer, and the nuclear matrix element (NME) of the transition calculated with state-of-the-art energy density functional (EDF) theory [Rod10a]. The measurement and data evaluation procedure, the measurement results, and their discussion with respect to neutrino physics experiments are presented in this chapter.

## 7.1 Measurement and data evaluation procedure

The atomic masses are determined by measuring the cyclotron-frequency ratio of the ion of interest and a reference ion species, and double-beta transition $Q$ values by the cyclotron-frequency ratio of the mother and daughter nuclides, as discussed in Chap. 4. A detailed description on the measurement and evaluation procedure for TRIGA-TRAP following the example of [Kel03] is found in [Ket10a]. In the following the application of this procedure on the experimental data reported here is described.

The steps of a measurement sequence at TRIGA-TRAP are given in Tab. 7.1. The ions for the measurements were produced using the TRIGA-TRAP laser ablation ion source (see Sect. 5.5). As ablation targets, foils with natural abundances were used for the production of cadmium, palladium and tungsten ions. It was necessary to use a target enriched in $^{184}$Os to 1.5% for the production of $^{184}$Os$^+$ due to its low natural abundance of 0.02%. A pellet with about 30 mg enriched material was pressed with silver as adhesive material as described in Sect. 5.5.

The produced ions are guided to the purification trap, where they are captured by lowering the potential of the endcap electrode at the injection side for 10 $\mu$s. At first, the cyclotron and axial motion is cooled until the ions have accumulated in the center of the trap. As next step, the buffer-gas cooling technique is applied (see Sect. 3.3), consisting of a 10 ms dipolar magnetron excitation to drive all ion

| Measurement step | Location | Duration |
|---|---|---|
| Laser pulse | Ion source | 5 ns |
| Ionization | Ion source | $\approx$ 10 ns |
| Ion transport to the purification trap | Transport section | $\approx$ 50 $\mu$s |
| Ion capture | Purification trap | 10 $\mu$s |
| Axial and cyclotron cooling | Purification trap | 200 ms |
| Dipolar magnetron excitation | Purification trap | 10 ms |
| Quadrupolar cyclotron excitation | Purification trap | 450 ms |
| Radial cooling | Purification trap | 100 ms |
| Ion ejection | Purification trap | 10 $\mu$s |
| Ion transfer to the precision trap | Pumping barrier | $\approx$ 50 $\mu$s |
| Ion capture | Precision trap | 12 $\mu$s |
| Dipolar magnetron excitation | Precision trap | 10 ms |
| First Ramsey excitation pulse | Precision trap | 100 ms / 200 ms |
| Waiting time | Precision trap | 800 ms / 1600 ms |
| Second Ramsey excitation pulse | Precision trap | 100 ms / 200 ms |
| Ion ejection | Precision trap | 10 $\mu$s |
| Ion transfer to the ion detector | TOF-section | $\approx$ 100 $\mu$s |

Table 7.1: An overview of the subsequent steps of a measurement sequence at TRIGA-TRAP with their duration is listed. The approximate numbers are depending on the ion's mass.

species out of the trap center and a quadrupolar excitation of 450 ms at the cyclotron frequency for centering of the desired ion species. The remaining cyclotron motion is cooled away before the ions are ejected from the purification trap. Due to their spatial distribution, only the ions of the desired species pass through the pumping barrier.

Subsequently, the ions are captured in the precision trap, where the cyclotron frequency of the ions is measured with the TOF-ICR technique (see Sect. 3.3). A 10 ms dipolar excitation is used to prepare the ions on a well-defined magnetron orbit. Afterwards, a quadrupolar excitation for the motion conversion is applied using a Ramsey excitation scheme (see Sect. 3.3). Two excitation pulses each of 100 ms duration and a waiting time of 800 ms in between was used as excitation scheme for all nuclides except for the mass and $Q$-value measurements of $^{184}$Os, where two pulses with 200 ms duration and 1600 ms waiting time in between were used to determine the cyclotron frequencies of $^{184}Os^{+}$, $^{184}W^{+}$, and $C_{15}^{+}$. The ions are ejected from the trap and drift slowly through the magnetic field gradient, where the adiabatic conversion of radial into axial motion takes place due to the conservation of the magnetic moment of the ion motion (see Chap. 4.4). Finally, the ions are focused on one of the ion detectors at the end of the beamline, and the time difference between the ejection pulse and the detected signal is recorded with a multi-channel analyzer (Standford Research, SR 430). The measurement cycle is varied around $\nu_c$ and the quadrupolar excitation frequency is changed in each cycle in order to obtain a resonance as shown in Fig. 3.7(f). In total, 41 equidistant frequency steps are performed with a step size of 0.1 and 0.05 Hz for the 100-800-100 ms and 200-1600-

200 ms excitation schemes, respectively. The sequence of these 41 frequency cycles is called one scan. In the measurements reported here, the number of scans for one cyclotron frequency measurement was at least 25, or in case of low ion production rates at least as many scans until about 500 ions in total were detected. The center of the scanned frequency range is the expected value for the cyclotron frequency. The cyclotron frequency is obtained by a least-squares fit of the theoretical line shape [Kre07] to the data points. As an example one cyclotron resonance spectrum of $^{184}Os^{+}$ is shown in Fig. 7.1.

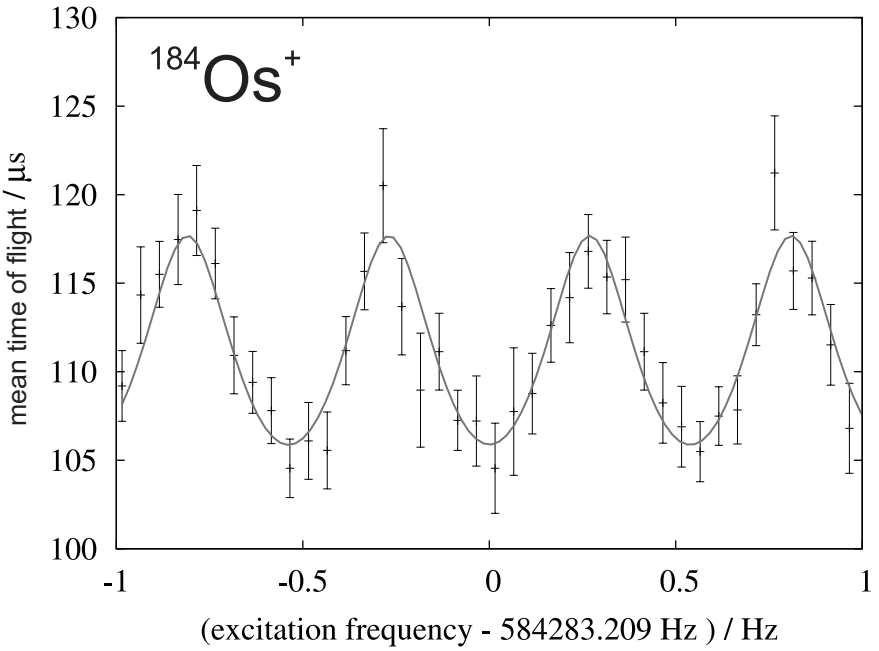


Figure 7.1: Time-of-flight ion-cyclotron resonance of $^{184}Os^{+}$. The mean time of flight is shown as function of the frequency of the quadrupolar excitation signal. The fit curve, which was obtained from a least-squares fit of the theoretical line shape [Kre07] to the data points, is shown as line. In total, about 500 ions were detected for this resonance and a cyclotron frequency of 584283.209(7) Hz was obtained.

The statistical uncertainty of the cyclotron frequency measurement is given by the uncertainty of the center obtained from the fit, which is to a large extent determined by the uncertainty of the time-of-flight data points. The average time-of-flight value is calculated from the time-of-flight distribution for each frequency value [Ero08].

Frequency shifts due to multiple ions in the trap are taken care of in the data evaluation by restricting the ion events used to events where five or less ions were detected. In addition, a count-rate class analysis is performed [Kel03]. For this purpose, the data is divided into at least two different classes in function of the number of detected ions per event, in a way that each class contains a similar number of ions. As result data points for the cyclotron frequency as function of the number of detected ions are obtained, and a linear function is fitted to the data points, as shown in Fig. 7.1, where a count-rate class analysis for a $^{110}Cd$ resonance was performed. The cyclotron frequency is obtained from the fit function at the value

of the detection efficiency of the ion detector (0.35(0.10) for an MCP detector), because this value corresponds to one stored ion in the precision trap assuming 100% transport efficiency in the TOF section.

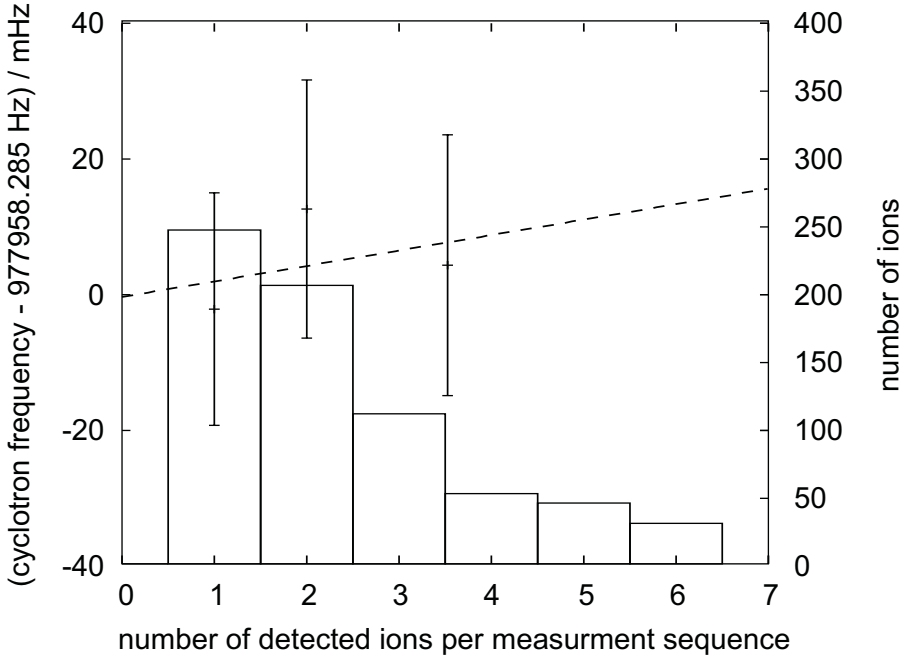


Figure 7.2: Cyclotron frequency values for different count-rate classes are shown for a $^{110}$Cd resonance. The boxes show the total number of ions detected as function of the number of ions detected per measurement sequence. Three count-rate classes with a similar number of ions are used to determine the cyclotron frequency: the single ion, the two ion, and the three to five ion count-rate class. Events with a higher number of detected ions are not considered in the evaluation due to large statistical fluctuations caused by the low statistics of the high ion-number events and a strong impact on the slope of a count-rate class point with large event number. The linear fit function is used to extrapolate the cyclotron frequency value at the position of the detection efficiency of 0.35(0.10). The slope of the fit function is 4(10) mHz per ion number, and thus consistent with zero. For this resonance 977958.285(22) Hz was obtained for the cyclotron frequency.

A count-rate class analysis requires a sufficient number of ions per class, so that the fit function can be applied individually to each count-rate class. In addition, each class should contain a similar total number of ions. In was not possible to perform the count rate analysis for the cyclotron frequency resonances of $^{184}Os^{+}$, because the count rate was so low that mainly single ion events were observed. Thus, it was not possible to divide the data into two classes with equal ion population and the cyclotron frequency of $^{184}Os^{+}$ and the corresponding reference measurements was obtained by restricting the evaluation to one and two ion events without performing a count rate analysis.

The cyclotron-frequency ratios are determined in alternating measurements of the cyclotron frequency of two ion species. Since simultaneous measurements of the cyclotron frequencies of both ion species are not possible, the measurement is

sensitive to temporal fluctuations of the magnetic field. As discussed in Sect. 5.5, the superconducting magnet used at TRIGA-TRAP has active coils to compensate the decrease of the magnetic field strength due to the flux creep effect. The linear magnetic field drift was determined to be $6(2)\times10^{-11}$ min$^{-1}$ [Ket10a], indicating a slight overcompensation. The cyclotron-frequency ratio is obtained by combining three subsequent cyclotron frequency measurements with alternating ion species to one cyclotron-frequency ratio. The cyclotron frequency of the reference ion species recorded in the first and the last of these three measurements is linearly interpolated to the time of the cyclotron frequency measurement of the ion of interest. Thereby, linear magnetic field drifts are accounted for. The statistical uncertainty of the cyclotron-frequency ratio is given by Gaussian error propagation of the uncertainties of the three individual cyclotron frequency measurements. Non-linear magnetic field fluctuations contribute to a systematic uncertainty to the individual cyclotron-frequency ratio measurements with a magnitude of $3.6(1.2)\times10^{-9}$ $\Delta$t / h [Ket10a], where $\Delta$t denotes the time difference between the two reference measurements. In these measurements $\Delta$t was typically kept below two hours in order to limit the systematic uncertainty due to non-linear magnetic-field drifts, except for the $Q$-value measurement of $^{184}$Os. In that case, $\Delta$t was in the range of three to five hours due to the low ion production rate of $^{184}Os^{+}$ with the laser ablation ion source.

A systematic shift of the cyclotron-frequency ratio due to the mass difference between the two ion species needs to be considered as well. The magnitude of this effect was determined by measuring systematically cyclotron-frequency ratios in the mass range of the investigated nuclides $A$ = 84 to 192. The mass range above $m$ = 156 u was investigated in [Ket10a] with carbon clusters ions from $C_{14}^{+}$ to $C_{23}^{+}$, and the systematic shift in this region was determined to be $\epsilon_r/r$ = -2.2(0.2)$\times10^{-9}$ $\Delta m$/u, where $\Delta m$ denotes the mass difference between the two nuclides. If the systematic error is attributed to a misalignment of the trap axis to the magnetic field, it corresponds to a tilt angle of 0.3°. The cyclotron-frequency ratios are corrected for this shift:

$$\delta r_{corr} = r\,(1 + \epsilon_r \Delta m)\,, \tag{7.1}$$

and the uncertainty of the shift is quadrically added to the statistical uncertainty of the measurement. The mass and $Q$-value measurements of cadmium and palladium are performed in the mass range below $m$ = 156 $u$, where the mass-dependent systematic shift was not determined before. Therefore, measurements of the cyclotron-frequency ratios of $C_9^{+}$ to the carbon-cluster ions from $C_7^{+}$ to $C_{11}^{+}$ were performed to quantify this effect in this mass region. The results for the cyclotron-frequency ratios are given in Tab. 7.2 and the deviation of the measurement to the calculated value is shown in Fig. 7.3. $\epsilon_r/r$ = 4.2(6.6)$\times10^{-10}\Delta m$/u is obtained in this mass range. Thus, the mass-dependent shift in these measurements is consistent with zero, and only the uncertainty of the shift is added quadratically to the statistical uncertainty of the frequency ratio. Note, that especially double-beta transition $Q$ values can be determined with high precision, since the contribution of the mass-dependent systematic uncertainty between nuclides with the same mass number $A$ is negligible ($\epsilon_r/r < 10^{-11}$).

Temperature fluctuations in the environment of the superconducting magnet and pressure fluctuations in the liquid gas reservoirs also cause temporal shifts of the cy-

| Ion species | Reference ion | r | $r_{dev}$ / $10^{-9}$ | $ME$ / keV | $\chi^2$ |
|---|---|---|---|---|---|
| $^{12}C_9^+$ | $^{12}C_7^+$ | 1.285716109(37) | -43(37) | -3.4(2.9) | 0.70 |
| $^{12}C_9^+$ | $^{12}C_8^+$ | 1.125000708(11) | -6(11) | -0.6(1.0) | 0.90 |
| $^{12}C_9^+$ | $^{12}C_{10}^+$ | 0.899999575(12) | 3(12) | 3.6(1.4) | 1.27 |
| $^{12}C_9^+$ | $^{12}C_{11}^+$ | 0.818181054(12) | -9(12) | -1.1(1.5) | 1.13 |

Table 7.2: cyclotron-frequency ratios $r$ of carbon-cluster ions, which were used to determine the mass-dependent systematic shift of the cyclotron-frequency ratio in the mass region 84 u $< m <$ 132 u. The deviation to the expected frequency ratio $r_{dev}$, the mass excess $ME$, which is expected to be zero, and the $\chi^2$ of the distribution of the frequency ratio data points in given.

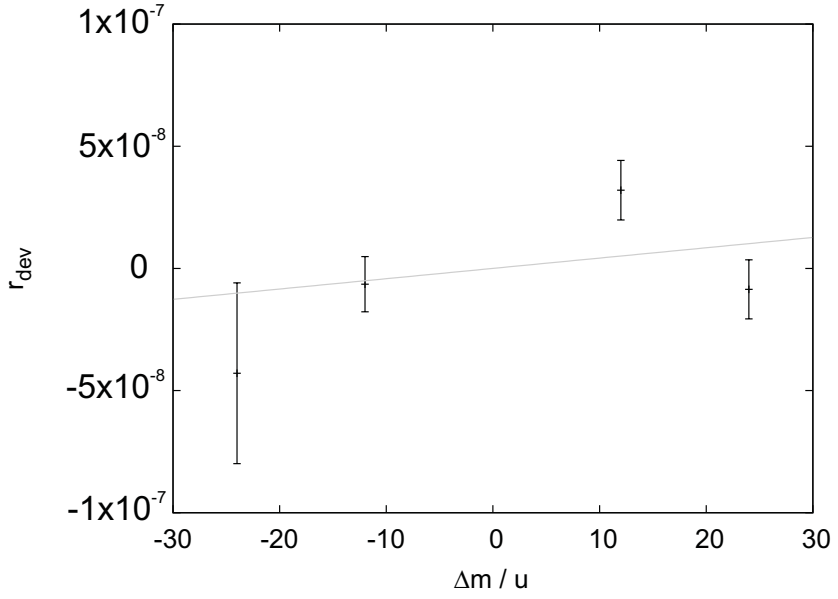


Figure 7.3: Deviation of the cyclotron-frequency ratio from the expected value $r_{dev}$ from Tab. 7.2 as function of the mass difference of the two ion species $\Delta m$. The line shows a linear fit function to the data points with a slope of $\epsilon_r/r = 4.2(6.6)\times10^{-10}\Delta m/\mathrm{u}$.

clotron frequency, which can also manifest in systematic deviations from the true cyclotron-frequency ratio. The magnetic susceptibilities of the materials surrounding the Penning trap, in particular the stainless-steel trap tube, are temperature dependent. Therefore, temperature changes or changes of the boiling point of the liquid helium and nitrogen by pressure changes affect the temporal stability of the magnetic field. The magnitudes of these effects were determined to be about 250 mHz $\Delta T$/K and 3.8 mHz $\Delta p$/mbar for the temperature and pressure changes, respectively. In order to increase the precision of the cyclotron frequency measurement a temperature stabilization of the trap tube, and a pressure stabilization for the liquid helium reservoir have been installed, similar to other Penning-trap mass spectrometers, e.g. SMILETRAP [Ber02, Liu10], ISOLTRAP [Mar08b] or SHIPTRAP [Drö11]. The temperature stabilization is achieved by heating the trap tube up to 30°C by a constant flow of heated air. The heating element consists of four 30 Ω

wire resistors in parallel configuration, which are electrically heated by an adjustable power supply with an average heating power of 120 W and installed close to an axial fan. A PT-100 temperature sensor placed at the injection side of the magnet bore gives a feedback signal to regulate the voltage of the power supply for the temperature stabilization. Fuzzy logic is used as regulation algorithm [Wag12, Mar69] and a maximum deviation from the nominal temperature of less than 0.1°C is reached during one day of operation. The pressure stabilization of the liquid helium reservoir is performed by a commercial regulated valve (MKS 0248A-01000RV), a pressure sensor (MKS Baratron 627B23MBC1B) and PID controller (MKS 250E-1-D), which regulates the helium gas flow out from the liquid helium reservoir. Thereby, the pressure fluctuations during one day of operatio are reduced to less than 0.4 mbar. With these stabilization systems no indication for systematic deviations from the true cyclotron-frequency ratio has been observed in repetitive measurements of the same cyclotron-frequency ratio up to a relative uncertainty of $\delta r/r = 3.4{\times}10^{-9}$.

The values for the corrected cyclotron-frequency ratios given in Tab. 7.3 and Tab. 7.4 are the weighted-mean values of a series of cyclotron-frequency ratio measurements as shown in Fig. 7.4. The uncertainties of the cyclotron frequency values are either the internal error:

$$\delta r_{int} = \sqrt{\frac{1}{\sum_i^N \frac{1}{\delta r_i}}}, \tag{7.2}$$

which is the uncertainty contribution of the uncertainties of the individual data points $\delta r_i$ to the mean value by Gaussian error propagation, if the $\chi^2$ is smaller than one, or the external error:

$$\delta r_{ext} = \delta r_{int}\sqrt{\chi^2}, \tag{7.3}$$

which accounts for the (non-statistical) fluctuations of the data points around the mean value, if the $\chi^2$ is larger than one.

## 7.2 Results of the mass and $Q$-value measurements with TRIGA-TRAP

The $Q$ values of four different double-beta transitions and the atomic masses of the involved nuclides have been determined. The results of the $Q$-value measurements are presented in Tab. 7.3. The individual cyclotron-frequency ratio measurements for the determination of the $Q$-value are shown in Fig. 7.4. A list of the cyclotron-frequency ratios of the investigated nuclides to carbon cluster ions is found in Tab. 7.4, as well as the mass excesses $ME$ derived from these measurements. These values are compared to the AME 2003 values for the mass excesses in Fig. 7.5. The uncertainties obtained for the measured values are comparable or smaller than the AME 2003 values. Therefore, the mass measurements reported here will enter the next Atomic-Mass Evaluation.

The $Q$ values can also be calculated by taking the mass differences $m_M$-$m_D$ of the mother (M) and daughter (D) ions from the mass measurements. These values are also shown in Tab. 7.3 as mass-measurement $Q$ values, although their uncertainty is higher due to a lower number of recorded frequency ratios. These values serve

Table 7.3: The average cyclotron-frequency ratios $r$ of the mother nuclides to the daughter nuclides of the investigated double-electron capture transitions are listed. The $Q$ values for these transitions are given as well. The direct measurement $Q$-value is obtained via $r$ by using equation (3.19), and the mass measurement $Q$-value from the mass difference of the individual masses given in Table 7.4. The result of the latest Penning-trap $Q$-value measurement, and the one from the atomic-mass evaluation (AME) 2003 [Aud03] are given as comparision.

| Transition | Cyclotron frequency ratio | Direct measurement $Q$-value / keV | Mass measurement $Q$-value / keV | Latest Penning trap $Q$-value / keV | AME 2003 [Aud03] $Q$-value / keV |
|---|---|---|---|---|---|
| $^{106}$Cd-$^{106}$Pd | 0.999971870 5(57) | 2775.01(0.56) | 2775.8(2.5) | 2775.39(0.10)[Gon11] | 2770(7) |
| $^{108}$Cd-$^{108}$Pd | 0.999997293 4(55) | 272.04(0.55) | 271.4(1.9) | – | 272(6) |
| $^{110}$Pd-$^{110}$Cd | 0.999980290 3(114) | 2017.8(1.2) | 2017.3(2.5) | 2017.85(0.64)[Fin12] | 2004(11) |
| $^{184}$Os-$^{184}$W | 0.999991516 3(34) | 1453.68(0.58) | 1453.9(1.5) | – | 1451.2(1.6) |

Table 7.4: The corrected cyclotron-frequency ratios $r_{corr}$ of the ions of interest to the carbon-cluster reference ions obtained in the direct mass measurements are given. The relative uncertainties of the measurement $\delta r/r$, the mass excesses $ME$ calculated from each cyclotron-frequency ratio, the average mass excesses $ME_{\mathrm{avg}}$, and the mass excesses $ME_{\mathrm{lit}}$ listed in the AME 2003 [Aud03] are also presented.

| Ion species | Reference ion | $r_{corr}$ | $\delta r/r$ | $ME$ / keV | $ME_{\mathrm{avg}}$ / keV | $ME_{\mathrm{lit}}$ / keV |
|---|---|---|---|---|---|---|
| $^{106}Cd^{+}$ | $^{12}C_9^+$ | 0.980615266(16) | $1.6 \times 10^{-8}$ | -87132.6(1.6) | -87133.5 (1.9) | -87132 (6) |
| | $^{12}C_8^+$ | 1.103192822(35) | $3.2 \times 10^{-8}$ | -87137.2(3.1) | | |
| $^{106}Pd^{+}$ | $^{12}C_9^+$ | 0.980587670(18) | $1.9 \times 10^{-8}$ | -89908.8(1.8) | -89909.3 (1.7) | -89902 (4) |
| | $^{12}C_8^+$ | 1.103161788(49) | $4.4 \times 10^{-8}$ | -89912.4(4.4) | | |
| $^{108}Cd^{+}$ | $^{12}C_9^+$ | 0.999112789(16) | $1.6 \times 10^{-8}$ | -89254.2(1.6) | -89254.0 (1.5) | -89252 (6) |
| | $^{12}C_{10}^+$ | 0.899201063(40) | $4.4 \times 10^{-8}$ | -89253.1(4.5) | | |
| $^{108}Pd^{+}$ | $^{12}C_9^+$ | 0.999110092(12) | $1.2 \times 10^{-8}$ | -89525.5(1.2) | -89525.4 (1.2) | -89524 (3) |
| | $^{12}C_{10}^+$ | 0.899198638(39) | $4.3 \times 10^{-8}$ | -89524.2(4.4) | | |
| $^{110}Cd^{+}$ | $^{12}C_9^+$ | 1.017620488(14) | $1.4 \times 10^{-8}$ | -90352.1(1.4) | -90350.8 (2.1) | -90353.0 (2.7) |
| | $^{12}C_{10}^+$ | 0.915858014(20) | $2.1 \times 10^{-8}$ | -90347.6(2.2) | | |
| $^{110}Pd^{+}$ | $^{12}C_9^+$ | 1.017640557(16) | $1.6 \times 10^{-8}$ | -88333.2(1.7) | -88333.5 (1.4) | -88349 (11) |
| | $^{12}C_{10}^+$ | 0.915876025(25) | $2.7 \times 10^{-8}$ | -88334.4(2.8) | | |
| $^{184}Os^{+}$ | $^{12}C_{15}^+$ | 1.021958367 4(67) | $6.6 \times 10^{-9}$ | -44251.47(1.13) | -44251.47(1.13) | -44256.60 (1.34) |
| $^{184}W^{+}$ | $^{12}C_{15}^+$ | 1.021949696 0(55) | $5.4 \times 10^{-9}$ | -45705.40(0.94) | -45705.40(0.94) | -45707.54 (0.87) |
| $^{12}C_{16}^+$ | $^{12}C_{15}^+$ | 1.066666865 9(70) | $7.0 \times 10^{-9}$ | -0.62(1.25) | -0.62(1.25) | 0 (0) |

only as a consistency check, because it is advantageous to measure directly the cyclotron-frequency ratio of the mother and daughter nuclides for a precise $Q$ value, since in measurements of mass doublets mass-dependent uncertainties are generally negligible and only one cyclotron-frequency ratio has to be determined for the $Q$-value measurement. The results of the individual measurements are discussed below.

## Results for the $^{106}$Cd $\xrightarrow{\epsilon\epsilon}$ $^{106}$Pd (+ 2 $\nu_e$) transition

The isotope $^{106}$Cd is an interesting candidate for double-$\beta^+$ decay and double-electron capture experiments due to the large $Q$-value 2770(7) keV [Aud03] and its comparably high natural abundance 1.25(6)% [Ber11]. The $Q$ value in the AME 2003 was determined by individual mass measurements of $^{106}$Cd and $^{106}$Pd, which are based on measurements with a double-focussing magnet spectrometer [Dam63], and neutron-capture reactions [Fir07]. A $Q$ value of 2775.01(0.56) keV was obtained in a direct measurement of the mass difference of the two nuclides using the TRIGA-TRAP mass spectrometer [Smo12a]. The individual cyclotron-frequency ratios of this measurement are shown in Fig. 7.4(a).

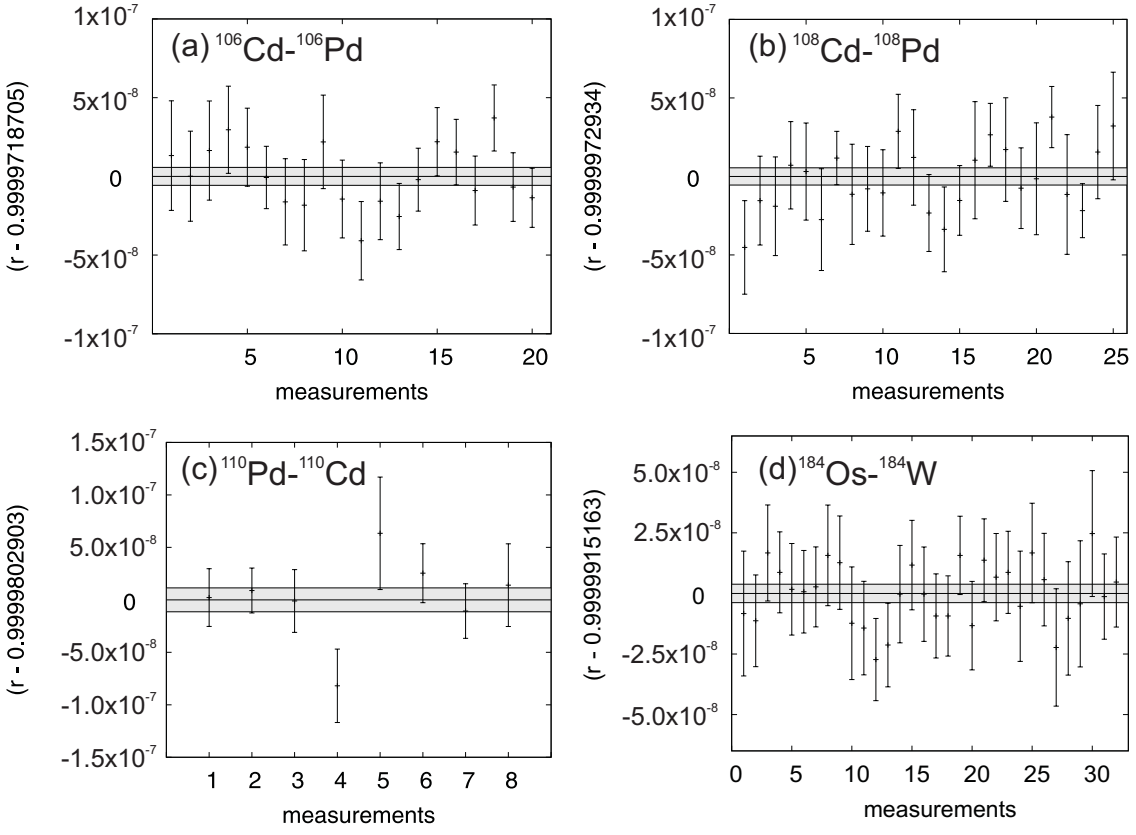


Figure 7.4: Individual cyclotron-frequency ratios $r$ measured for the $Q$-value determination for (a) $^{106}$Cd-$^{106}$Pd, (b) $^{108}$Cd-$^{108}$Pd, (c) $^{110}$Pd-$^{110}$Cd, and (d) $^{184}$Os-$^{184}$W. The central lines show the average cyclotron-frequency ratios, the grey bands are their 1-$\sigma$ uncertainties.

The atomic-mass values of $^{106}$Cd and $^{106}$Pd were determined as well, and values with improved uncertainty by a factor of 3.2 and 2.4, respectively, compared to the

previous literature values were obtained. The atomic-mass values are compared via the mass excess (see equation (2.26)) in Tab. 7.4. The value for $^{106}$Cd is in agreement with the previous measurements, whereas the value for $^{106}$Pd shows a slight discrepancy of 7.3 keV (1.8 $\sigma$). The $Q$ value calculated from the difference of the two mass values is in agreement with the one obtained from directly measuring the cyclotron-frequency ratio of the mother and daughter nuclides. Furthermore, there was a recent measurement with SHIPTRAP [Gon11], where a $Q$-value of 2775.39(0.10) keV was obtained, which is also in agreement with the TRIGA-TRAP values. The lower uncertainty of the SHIPTRAP measurement is due to a shorter delay between the reference measurements and due to a longer Ramsey excitation of 100-1800-100 ms.

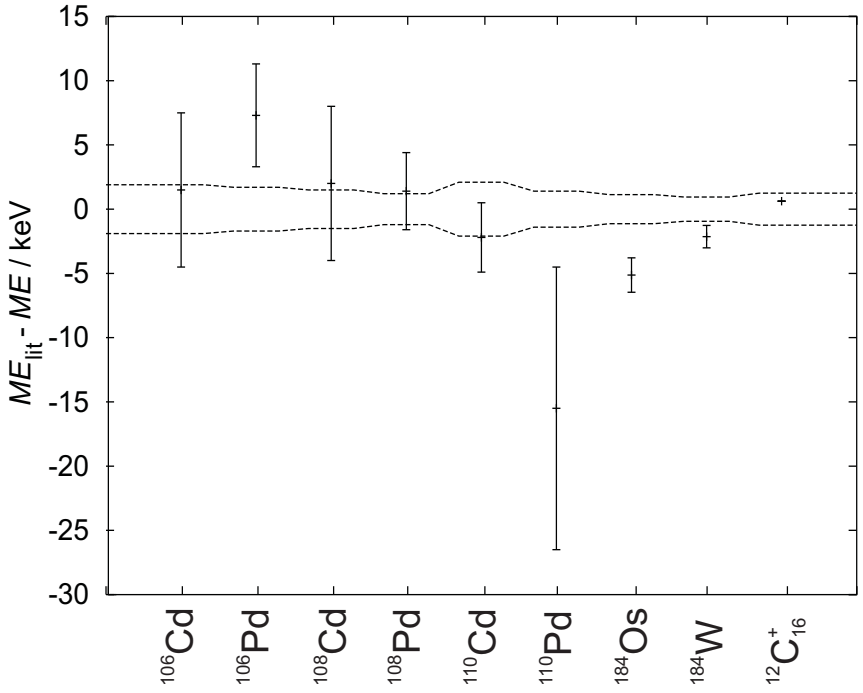


Figure 7.5: Comparison of the atomic masses measured at TRIGA-TRAP and the AME2003 mass values. The differences of the mass excesses from the AME 2003 values to the results listed in Tab. 7.4 are shown for all investigated nuclides with the uncertainty of the AME 2003. The solid lines mark the 1-$\sigma$ uncertainties of the AME 2003 values. For details see text.

$^{106}$Cd is investigated by several experiments searching for the double-electron capture transitions [Blo07, Bel11, Ruk11]. Recently, the lower limits on the half-lives of the double-electron capture processes have been investigated for transitions going to the ground-state of $^{106}$Pd, as well as resonant transitions to excited states in $^{106}$Pd [Bel11, Ruk11]. The lower limit for the two-neutrino accompanied transition to the ground state in the order of $10^{19}$ to $10^{20}$ y, and for the following resonant transitions the limits for the half-lives have been found [Bel11]:

$$T_{1/2}^{0\nu KK} > 3.8 \times 10^{20}\text{y} \;\; (E_\gamma = 2717.59(21)\ \text{keV}, J^\pi = \text{unknown})\,, \tag{7.4}$$

$$T_{1/2}^{0\nu KL} > 9.6 \times 10^{20}\text{y} \;\; \left(E_\gamma = 2741.0(5)\ \text{keV}, J^\pi = 4^+\right). \tag{7.5}$$

These values are the best restrictions on the half-life of resonantly enhanced double-electron capture in $^{106}$Cd available. Note, that the spin and parity of these excited state are unfavorable due to the small nuclear matrix element, which has its largest value for a $0^+ \rightarrow 0^+$ transition. The excited state at 2717.59(21) keV has unknown spin and parity, but it decays to 100% into the excited $3^+$ state at 1557.59 keV, which excludes a spin of 0 or 1 for this state [Kri11]. Using the AME 2003 $Q$ value the excess energies of these two excited states were 3.0(6.0) keV and 1.5(6.0) keV, respectively, and therefore they were consistent with zero. Considering the new $Q$-value measurements a strong resonant enhancement to these excited states can be excluded. The excess energies to these excited states become 8.3(0.2) keV and 6.9(0.5) keV, respectively. An energy degeneracy to another excited state in $^{106}$Pd with $E_\gamma$ = 2748.2(4) keV, $J^\pi = 2,3^-$ for a double-electron capture from the $KL_3$ shells was reported with an excess energy of 330(410) eV [Gon11], which is also consistent with zero. The uncertainty of this value is now limited by the uncertainty of the excitation energy of the nuclear state. Due to the different parity of the ground state of the mother and the excited nuclear state of the daughter nuclide and the low probability of electron capture from the $L_3$-atomic orbital, a favorable half-life for this transition can be excluded as well. $^{106}$Pd has another excited state at 2737(1) keV, where spin and parity have not been assigned so far. This transition might be of interest in case of $J_f^\pi = 0^+$ [Kri11]. The excess energy $\Delta$ to this excited state for the capture from the K and $L_1$ shell is 10.2(1.0) keV, which is limited by the uncertainty of the excitation energy $E_\gamma$. Thus, further studies concerning the excitation energy, spin, and parity of this state are required to conclude whether the decay to this excited state is favorable for neutrino experiments.

## Results for the $^{108}$Cd $\xrightarrow{\epsilon\epsilon}$ $^{108}$Pd (+ 2 $\nu_e$) transition

The $Q$-value of double-electron capture in $^{108}$Cd was determined to be 272.04(0.55) keV in the first direct measurement of this transition [Smo12a]. The individual cyclotron-frequency ratios of this measurement are shown in Fig. 7.4(b). Thereby, the AME 2003 value was confirmed and the precision improved by more than an order of magnitude. The measured mass values of $^{108}$Cd and $^{108}$Pd as listed in Table 7.4 agree within one standard deviation with the previous measurements [Dam63, Fir07, Cas80, Tak80, Kuh75]. In addition, the uncertainties of the $^{108}$Cd and $^{108}$Pd mass values were improved by a factor of 4 and 2.5, respectively. The $Q$ value calculated from the mass differences is 271.4(1.9) keV, which is in agreement with the value obtained from the direct cyclotron-frequency ratio measurement and the AME 2003 value.

The resonance condition of the double-electron capture is not fulfilled in $^{108}$Cd. The excess energy to the ground state in $^{108}$Pd is 222.56(0.55) keV for the capture of two K-shell electrons. The first excited state in $^{108}$Pd is the $J^\pi = 2^+$ state with an excitation energy of 433.938(5) keV [Bla00]. The energy difference to this state is larger than 161.94(0.55) keV depending on which electrons would be hypothetically captured.

$^{108}$Cd is contained in the sources used in the experiments searching for double-electron capture in $^{106}$Cd, but a detection of the decay signature of $^{108}$Cd is hindered

due to the small $Q$-value of the decay by a beta-decay background at low $\gamma$-energies [Blo07, Bel11].

## Results for the $^{110}$Pd $\xrightarrow{\beta\beta}$ $^{110}$Cd + 2 e$^-$ (+ 2 $\overline{\nu}_e$) transition

The double-beta decay $Q$-value of $^{110}$Pd has been also determined. $^{110}$Pd is one of the eleven nuclides with a $Q_{\beta\beta}$-value above 2 MeV that are considered as suitable candidates for the search of neutrinoless double-beta decay. Nevertheless, the $Q_{\beta\beta}$ value of $^{110}$Pd in the AME 2003 was only known with an uncertainty of 11 keV due to the uncertainty of the $^{110}$Pd mass. The mass values of the two nuclides were obtained via neutron capture reactions [Fir07], beta decay [Dan63, Mor67], other nuclear reactions [Kuh75, Coh84, Tak80], and by mass measurements with a magnet spectrometer [Dam63]. Two direct $Q$-value measurements with Penning traps have been recently performed. A measurement was performed at ISOLTRAP [Fin10, Fin12], which obtained a $Q$-value of 2017.85(0.64) keV and showed a discrepancy of 14 keV from the AME 2003 value. The other measurement, which is reported here, resulted in a $Q$-value of 2017.8(1.2) keV [Smo12a], which confirms the measurement at ISOLTRAP. The individual cyclotron-frequency ratios are shown in Fig. 7.4(c). The discrepancy is due to the mass value of $^{110}$Pd, which is off by 16 keV, whereas the mass of $^{110}$Cd is in agreement with the AME 2003 value (see Tab. 7.4). The new $Q$-value measurements predict a larger phase-space for the decay, and therefore a shorter half-life of the transition. The half-life for the $0\nu\beta^-\beta^-$ was reevaluated in [Fin12] to be $6.8\times10^{23}$ eV$^2$/$|\langle m_\nu\rangle|^2$ years.

Despite the large $Q_{\beta\beta}$ value and the large natural abundance of $^{110}$Pd, the experimental data on the double-beta decay is scarce, even the $2\nu\beta^-\beta^-$ transition to the ground state in $^{110}$Cd with a predicted half-life in the range from $1.2\times10^{19}$ to $2.9\times10^{21}$ has not been observed yet [Leh11]. Upper limits of the double-beta decay into excited states in $^{110}$Cd have been recently determined [Leh11].

## Results for the $^{184}$Os $\xrightarrow{\epsilon\epsilon}$ $^{184}$W (+ 2 $\nu_e$) transition

The double-electron capture in $^{184}$Os to the excited $0^+$ state with 1322.152(22) keV energy in $^{184}$W has been marked in [Kri11] as interesting transition, even though a full resonant enhancement of the transition was not expected considering the AME 2003 $Q$ value. The low spin of the nuclear excited state, the capture of two K-shell electrons, and the large nuclear radius lead to a reasonably short half-life. Using an empirical value for the nuclear matrix element (NME) of $M^{0\nu}(0^+) = 6$ and $\langle m_{\nu_e}\rangle\, c^2 = 1$ eV, a half-life in the range of 0.6 to $2.0\times10^{27}$ years has been reported [Kri11]. Depending on the strength of the resonant enhancement a much shorter half-life compared to other double-electron capture transitions may result.

The excess energy $\Delta$ (see equation (2.46)) is -11.3(1.6) keV, using an excitation energy of the two K-shell electron-hole state of 140.370 keV from [Kri11], and the $Q$ value from the AME 2003 of 1451.2(1.6) keV, which is based on the mass values derived via neutron-capture reactions [Gre74, Bus75, Bru87, Fir07]. Within this thesis, the $Q$-value of this transition was determined with the TRIGA-TRAP mass spectrometer by recording 32 cyclotron-frequency ratios, which are shown in

Fig. 7.4(d). For these measurements a Ramsey excitation scheme with two pulses of 200 ms separated by a 1600 ms waiting time has been used. The $Q$ value derived from the cyclotron-frequency ratio via equation (3.19) is 1453.68(0.58) keV (see Tab. 7.3), which shows a slight deviation of 1.5 $\sigma$ compared to the AME 2003.

The mass values of $^{184}Os^{+}$ and $^{184}W^{+}$ obtained by cyclotron-frequency ratio measurements of $^{184}Os^{+}$ and $^{184}W^{+}$ to $^{12}C_{15}^{+}$ (see Tab. 7.4) show a deviation of 5.13 keV (3.8 $\sigma$) and 2.14 keV (2.3 $\sigma$) from the AME 2003 values, respectively. Unlike the AME 2003 mass values, which are linked via several nuclear reactions to the atomic-mass standard carbon, the measurements presented here provide a direct link. The difference of the atomic masses obtained in these measurements is also in agreement with the direct $Q$-value measurement (see Tab. 7.3). In addition, a cross-reference of the cyclotron-frequency of $^{12}C_{15}^{+}$ to $^{12}C_{16}^{+}$ has been performed to ensure the accuracy of the measurement (see Tab. 7.4).

In order to obtain a new value for $\Delta$, $B_{2h}$ was calculated by V.M. Shabaev *et al.* using the Dirac-Fock method [Bra77] including frequency-dependent Breit interaction, quantum electrodynamics (QED) and correlation corrections. The calculations were performed for the Fermi model of the nuclear charge distribution with $r_{\mathrm{RMS}}$=5.3670 fm for $^{184}W$ [Ang04], resulting in $B_{2h}$= 140.418(0.012) keV. The nuclear excitation energy $E_\gamma$ was taken from [Bag10]. Using the $Q$ value measured here, $\Delta$ is slightly reduced to -8.89(0.58) keV, suggesting the half-life to be shorter than previously assumed.

## Comparison of the resonance factors

The half-life for the $0\nu\epsilon\epsilon$ process was given in equations (2.45), using the excess energy in (2.44), and the transition potential in (2.47). The transition potential contains the NME $M^{0\nu}(J_f^\pi)$ and the electron capture probability, which have to be calculated. In order to compare the experimental results, the resonance factor $R$ is extracted from the equation for the half-life, which depends on the excess energy $\Delta$, i.e. the measured $Q_{\epsilon\epsilon}$ value:

$$R = \frac{\Gamma_{2h}}{\Delta^2 + \Gamma_{2h}^2/4} = \frac{\Gamma_{2h}}{(Q_{\epsilon\epsilon} - B_{2h} - E_\gamma)^2 + \Gamma_{2h}^2/4}. \tag{7.6}$$

The maximum value of the resonance factor for $\Delta = 0$ is:

$$R_{\mathrm{Max}} = \frac{4}{\Gamma_{2h}}. \tag{7.7}$$

The relative resonance factors $R/R_{\mathrm{Max}}$ of the most promising $0^+ \rightarrow 0^+$ transitions listed in [Kri11], and all transitions between ground states with a $Q_{\epsilon\epsilon}$-value below 1 MeV are shown in Fig. 7.6. Transitions to final states with higher spins have been excluded, because a much smaller value for the NME is expected. The $Q_{\epsilon\epsilon}$ values were either taken from the AME 2003 [Aud03] or from the latest measurements [Eli11d, Gon11, Kol11, Eli11b, Eli11a, Eli11c, Drö12]. The corresponding values for $B_{2h}$, $\Gamma_{2h}$ and $E_\gamma$ were either taken from these references or from [Lar77, DeF08, DeF96, Kri11]. In case, no value for $\Gamma_{2h}$ was available the width of the two-electron holes-state was taken as twice the width of the one K-level hole, which was interpolated from the data tabulated in [Cam01].

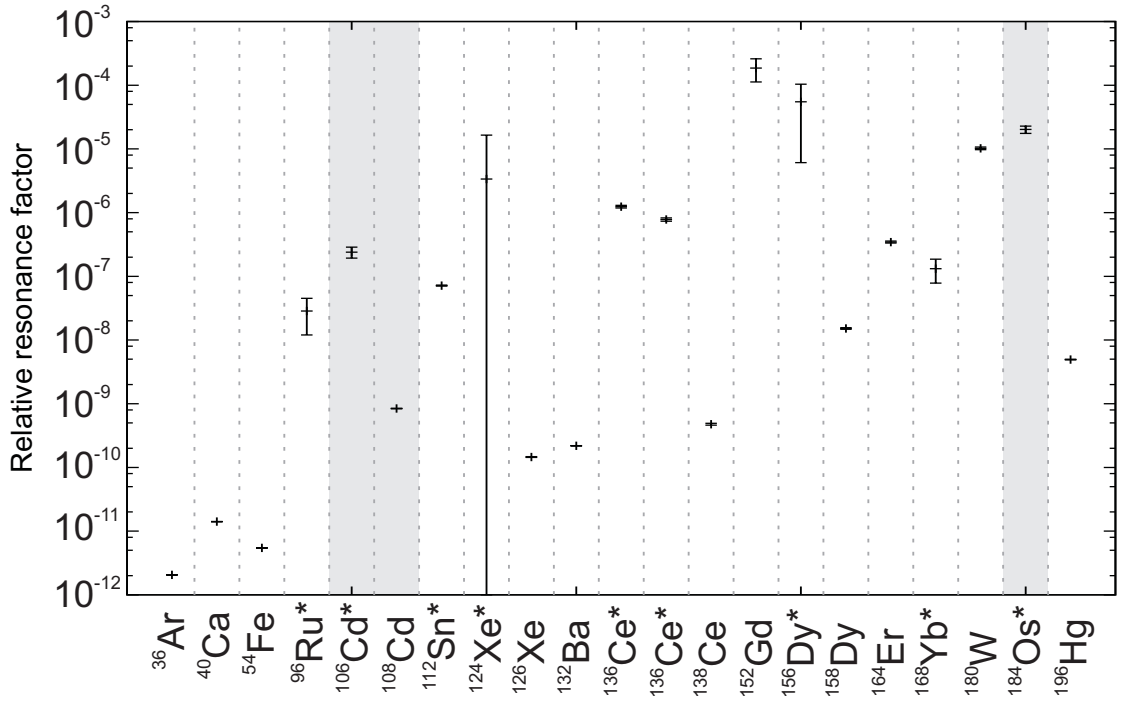


Figure 7.6: Comparison of relative resonance factors $R/R_{\mathrm{Max}}$ of double-electron capture transitions to final states with $J_f^\pi = 0^+$. The transitions to excited nuclear states are marked with the symbol *. The corresponding excitation energies are: 2742(1) keV for $^{96}$Ru, 2737(1) keV for $^{106}$Cd, 1871.00(19) keV for $^{112}$Sn, 2853.2(0.6) keV for $^{124}$Xe, 2315.32(0.07) and 2349.5(0.5) keV for $^{136}$Ce, 1988.5(0.2) keV for $^{156}$Dy, 1422.10(0.03) keV for $^{168}$Yb, and 1322.152(0.022) keV for $^{184}$Os. The transitions studied within this thesis are marked with a gray background. The large uncertainty of the resonance factor in case of $^{124}$Xe is due to the lack of a high-precision $Q$-value measurement. For details see text.

The relative resonance factors range from $10^{-12}$ to $2{\times}10^{-4}$ with $^{152}$Gd having the highest value. Depending on the excess energy, a relative increase of the decay rate due to the resonant enhancement by seven orders of magnitude between double-electron capture transistions has been observed so far. However, it is still four orders of magnitude lower than it could be expected for a full energy degeneracy. For $^{152}$Gd half-lives in the range from $4{\times}10^{28}$-$6.2{\times}10^{29}$ years have been reported depending on the calculation method for the NME [Eli11b, Rod12, Fan12] and assuming an effective electron neutrino mass of 50 meV.

For the candidates studied within this thesis, a longer half-life can be expected from the resonance factors. In absolute terms, the resonance factor $R$ is only 0.3 % of the one for $^{152}$Gd in case of the transition of $^{106}$Cd into the 2737(1) keV state in the daughter nucleus. As discussed above, a resonant enhancement for $^{108}$Cd was not expected due to the large excess energy of the transition. This results in $R$ being more than five orders of magnitude lower compared to $^{152}$Gd.

$^{184}$Os is placed as third best candidate according to the resonance factor among the $0^+ \rightarrow 0^+$ transitions investigated so far, following $^{152}$Gd, and $^{156}$Dy. Compared to $^{152}$Gd, the resonance factor $R$ of $^{184}$Os has a relative magnitude of 3.4% due to

the difference in $\Gamma_{2h}$. In order to compare the half-life of double-electron capture in $^{184}$Os, it is necessary to include the NME and the electron wave functions and excitation energies. The values were recalculated, and the results are discussed in the following section.

## 7.3 A newly evaluated half-life of the neutrinoless double-electron capture in $^{184}$Os

The value reported for the half-life of neutrinoless double-electron capture in $^{184}$Os of $0.7\times10^{27}$ y and $2.0\times10^{27}$ y [Kri11] is normalized to an effective neutrino mass of 1 eV/$c^2$ and an empirical value for the NME of $M^{0\nu} \approx 6$. The latter value is typically obtained for nuclides in the region of $^{184}$Os with the quasiparticle random-phase approximation (QRPA) method [Sim09] assuming a spherical configuration of the initial and final states. However, it is a well-established fact that nuclides in this region are deformed [Nat08]. The calculations reported here were performed by Tomás Rodríguez *et al.* using state-of-the-art energy density functional (EDF) calculations, which have been successfully applied for calculations of NMEs of neutrinoless double-beta transitions [Rod10a, Rod12]. Fig. 7.7(a) shows the result of the NME calculations as function of the quadrupole deformation $\beta$ and $\beta'$ of the initial and final state, respectively. Two different parametrizations of the Gogny functional, D1S [Ber84] and D1M [Gor09], have been used to describe the underlying nucleon-nucleon interactions. Using this method, the quadrupole deformation of the initial and final states is consistently described.

The probability distribution of having a certain deformation for the wave functions of the ground state in $^{184}$Os ($0^+_1$) and the three lowest lying $0^+$ states in $^{184}$W ($0^+_1$ to $0^+_3$) is shown in Fig. 7.7(b) using the Gogny D1S functional. Large ground-state deformations are predicted for these two nuclides, which has been also observed experimentally [Nat08]. The $0^+_2$ state is predicted to have a slightly smaller $\beta'$ value, whereas the $0^+_3$ state, which is likely the resonant final state in $^{184}$W, has a larger $\beta'$ value compared to the other states.

The NME is obtained by folding the Gamow-Teller and Fermi matrix elements with these deformation-dependent wave functions. The results of the NME calculations are shown in Tab. 7.5. Both components show a similar behavior in function of the quadrupole deformation [Rod10a, Rod12]. As example the Fermi component using the D1S Gogny functional is shown in Fig. 7.7(a) as function of $\beta$ and $\beta'$. The calculations show that the hypothetical transitions between spherical states yield the highest value for the NME, which resembles the empirical value used in [Kri11] quite well. If the deformation of the nuclides is considered, the NME is reduced by about one order of magnitude. In Fig. 7.7(a) two trends can be observed: First, for similar deformations of the initial and final state ($\beta \approx \beta'$), the NME decreases with increasing deformation. Second, for a given value of $\beta$ a reduction of the NME is found, which increases with the difference between the two deformation parameters $|\beta' - \beta|$.

Thus, the NME for the transition between the two ground-states is significantly reduced compared to the hypothetical spherical case due to the large predicted values

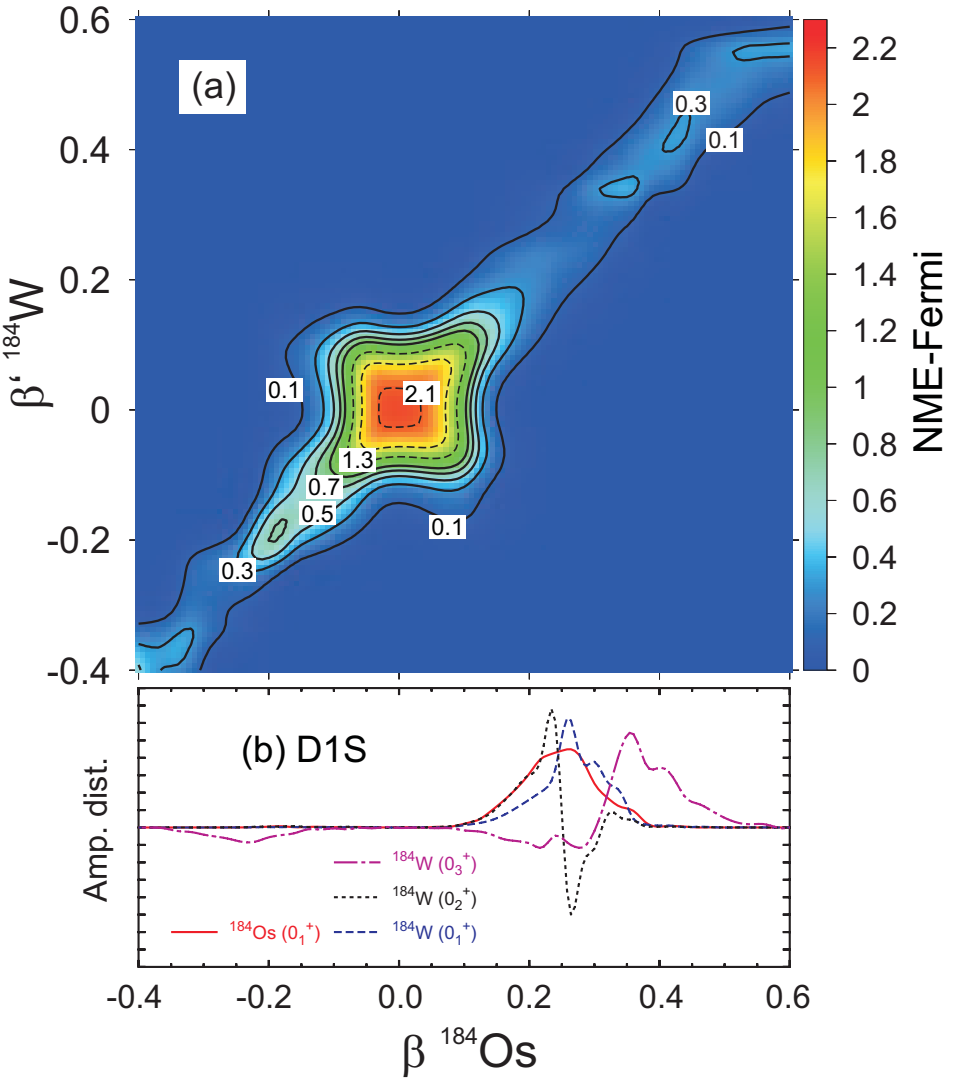


Figure 7.7: The intensity of the Fermi component of the NME for the neutrinoless double-electron capture in $^{184}$Os is shown in (a) as a function of the quadrupole deformation $\beta$ and $\beta'$ of the $^{184}$Os and $^{184}$W nuclei, respectively [Rod10a, Rod12]. The Gamow-Teller component represents similar behavior and is omitted. Amplitude distributions of having a given deformation for the ground state of $^{184}$Os and the three lowest lying $0^+$ states of $^{184}$W is shown in (b) using the Gogny D1S functional. The sum of the squares is normalized to one. Similar results are obtained with the Gogny D1M functional.

for $\beta$ and $\beta'$ of about 0.25. For the excited states, an even smaller NME is obtained. This is due to the fact that the wave function of the $0_2^+$ state has to be orthogonal to the ground state, which leads to cancellations when calculating the NME. The $0_3^+$ state has a significantly larger value for $\beta'$ compared to the one for $\beta$ of the initial states. Hence, due to the trends observed in Fig. 7.7(a), the NME is further reduced.

Note, that the EDF calculations predict a much higher excitation energy for the likely resonant $0_3^+$ state. As consequence the quadrupole deformation of the $0_3^+$ state used for the NME calculation may be incorrect. In that case, the NME

Table 7.5: Excitation energies $E(0_n)^+$, $n$ = 1,2,3, the Fermi component $M^{0\nu}_{\epsilon\epsilon,F}$, the Gamow-Teller component $M^{0\nu}_{\epsilon\epsilon,GT}$, and the total value for the neutrinoless double-electron capture NMEs $M^{0\nu}_{\epsilon\epsilon}$ are listed for the hypothetical spherical configuration and for the first three $0^+$ states in $^{184}$W calculated by the Gogny D1S and D1M functionals including shape mixing. The experimental excitation energies are compared to the theoretical ones. For details see text.

| Quantity | Gogny D1S | Gogny D1M | Experiment |
|---|---|---|---|
| $E(0_1^+)$ | 0 | 0 | 0 |
| $E(0_2^+)$ | 1459 keV | 1135 keV | 1002.49(4) keV |
| $E(0_3^+)$ | 3508 keV | 3169 keV | 1322.152(22) keV |
| $M^{0\nu}_{\epsilon\epsilon,\mathrm{F}}$(sph.) | 2.138 | 2.150 | - |
| $M^{0\nu}_{\epsilon\epsilon,\mathrm{GT}}$(sph.) | 6.079 | 6.027 | - |
| $M^{0\nu}_{\epsilon\epsilon}$(sph.) | 8.217 | 8.177 | - |
| $M^{0\nu}_{\epsilon\epsilon,\mathrm{F}}(0_1^+)$ | 0.252 | 0.167 | - |
| $M^{0\nu}_{\epsilon\epsilon,\mathrm{GT}}(0_1^+)$ | 0.712 | 0.463 | - |
| $M^{0\nu}_{\epsilon\epsilon}(0_1^+)$ | 0.964 | 0.631 | - |
| $M^{0\nu}_{\epsilon\epsilon,\mathrm{F}}(0_2^+)$ | 0.151 | 0.133 | - |
| $M^{0\nu}_{\epsilon\epsilon,\mathrm{GT}}(0_2^+)$ | 0.426 | 0.371 | - |
| $M^{0\nu}_{\epsilon\epsilon}(0_2^+)$ | 0.577 | 0.504 | - |
| $M^{0\nu}_{\epsilon\epsilon,\mathrm{F}}(0_3^+)$ | 0.055 | 0.042 | - |
| $M^{0\nu}_{\epsilon\epsilon,\mathrm{GT}}(0_3^+)$ | 0.157 | 0.121 | - |
| $M^{0\nu}_{\epsilon\epsilon}(0_3^+)$ | 0.212 | 0.163 | - |

of the transition to the ground state can be interpreted as an upper limit for the NME, because either $|\beta' - \beta|$ has a larger value for the transition to the $0_3^+$ state, or cancellations in the NME caused by the orthogonality to the two lower $0^+$ states reduce the NME.

The leptonic factors in the equation for the half-life (see Eq. (2.47)) were calculated using the one-configuration method for an extended nucleus [Bra77]. As result

$$P_{\epsilon\epsilon} = |A_{\alpha\beta}|^2 = |\Psi_\alpha|^2 \, |\Psi_\beta|^2 = 1.19617 \times 10^{33} \text{ eV}^6 \tag{7.8}$$

was obtained in natural units. For the nuclear charge radius of $^{184}$W, the value of 5.382 fm from [Ang04] has been used. Finally, the half-life for resonant neutrinoless double-electron capture transitions in $^{184}$Os to the three lowest $0^+$ states in $^{184}$W can be obtained using the average values for the NMEs given in Tab. 7.5:

$$T_{1/2}\left(^{184}\text{Os } 0_1^+ \rightarrow \ ^{184}\text{W } 0_1^+\right) = 1.9 \times 10^{33} \frac{1 \text{ eV}^2}{\langle m_{\epsilon\epsilon} \rangle^2} \text{ y}, \tag{7.9}$$

$$T_{1/2}\left(^{184}\text{Os } 0_1^+ \rightarrow \ ^{184}\text{W } 0_2^+\right) = 2.3 \times 10^{32} \frac{1 \text{ eV}^2}{\langle m_{\epsilon\epsilon} \rangle^2} \text{ y}, \tag{7.10}$$

$$T_{1/2}\left(^{184}\text{Os } 0_1^+ \rightarrow \ ^{184}\text{W } 0_3^+\right) = 1.6 \times 10^{30} \frac{1 \text{ eV}^2}{\langle m_{\epsilon\epsilon} \rangle^2} \text{ y}. \tag{7.11}$$

Although the squares of the NMEs $|M^{0\nu}_{\epsilon\epsilon}|^2$ for the transition to the $0_1^+$ and $0_2^+$ state are more than an order of magnitude larger, the transitions are suppressed by four

and three orders of magnitude, respectively, compared to the transition to the $0_3^+$ state due to the large excess energy. Thus, the shortest half-life of $1.6 \times 10^{30}$ years is obtained for the transition to the $0_3^+$ state. In case of an incorrect prediction of the quadrupole deformation by the EDF calculations, the lower limit for the half-life for this transition is

$$T_{1/2}\left(^{184}\text{Os } 0_1^+ \rightarrow \ ^{184}\text{W } 0_3^+\right) \geq 8.8 \times 10^{28} \frac{1 \text{ eV}^2}{\langle m_{\epsilon\epsilon} \rangle^2} \text{ y}, \tag{7.12}$$

assuming the value for the ground state transition as an upper limit of the NME.

The half-life of neutrinoless double-electron capture in $^{152}$Gd, which is the transition with the strongest enhancement, was predicted with two methods for the calculation of the NME. $^{152}$Gd and the daughter nuclide $^{152}$Sm are also significantly deformed similar as in the case $^{184}$Os, so that the deformation of the nuclides has to be considered in the calculations. The deformed QRPA method has been applied to this transition and a half-life in the range of $4.7{\times}10^{28}$ to $4.8{\times}10^{29}$ years assuming and effective electron neutrino mass $\langle m_{\nu_e} \rangle$ of 50 meV [Fan12] has been predicted. It was also found that the NME reduces by a factor 2 to 3, if the deformation of the nuclides is considered. The application of the same EDF calculations as for the NME values presented here to the case of $^{152}$Gd yields a half-life of $4.2{\times}10^{29}$ to $6.2{\times}10^{29}$ years also assuming $\langle m_{\nu_e} \rangle = 50$ meV [Rod12]. Although the results show discrepancies, a significant increase of the half-life is found by both methods, if the quadrupole-deformation degree of freedom is included.

In comparison to $^{152}$Gd, the half-life of neutrinoless double-electron capture in $^{184}$Os of $6.4 \times 10^{32}$ for $\langle m_{\nu_e} \rangle = 50$ meV is three orders of magnitude larger, if the NMEs obtained by the same EDF calculations are used. Therefore, $^{184}$Os is not a suitable candidate for an experiment searching for the $0\nu\epsilon\epsilon$-process. However, if the current experimental limits for the detection of the neutrinoless double-electron capture are considered, which are in the order of $10^{19}$ to $10^{21}$ years [Bel11], the observation of neutrinoless double-electron capture remains a great challenge, even for the best candidate found so far.

Transitions to excited states with higher spin were not included in Fig. 7.6. The most energy-degenerate excited states with higher spins have been found for the $0\nu\epsilon\epsilon$ process in $^{156}$Dy [Eli11a] into the excited $2^+$ state at 2003.749(5) keV energy ($\Delta =$ 0.04(0.1) keV) and $^{106}$Cd [Gon11] into the excited state at 2748.2(4) keV energy with $J_f^\pi = 2^-$ or $3^-$. However, the decay rates of these transitions are suppressed to due the small leptonic factor $P_{\epsilon\epsilon}$ and the negative parity of the state [Gon11], respectively.

The resonance conditions of a few interesting transitions proposed in [Kri11] have not been studied yet. The $0\nu\epsilon\epsilon$ process in $^{124}$Xe to the excited $0^+$ state in $^{124}$Te at 2853.2(6) keV energy ($\Delta \geq 1.2(2.3)$ keV) could result in a shorter half-life. $^{130}$Ba could be a promising candidate considering the transition to two excited states with energies of 2608.426(19) keV and 2622.32(9) keV. However, the spin and parity of these excited states is not known. In case of a spin-parity $0^+$ can be assigned to these states, these transitions might be of interest for neutrino experiments. In $^{190}$Pt a resonant enhancement could take place for a transition to an excited state with 1382.4(2) keV and $J_f^\pi = (1, 2, 3)^+$. The excess energy to this excited state ranges

from $\Delta = 0.8(5.9)$ keV to 15.6(5.9) keV, depending on which electrons are captured. The $Q$ values of $^{124}$Xe and $^{130}$Ba have been recently investigated at SHIPTRAP and the results will be published soon [Eli12]. The $Q$ value of $^{190}$Pt was not yet studied due to the low natural abundance of the isotope (0.014%). For a $Q$-value measurement at TRIGA-TRAP, an enriched sample would be required.

# Chapter 8

# Conclusions and Outlook

The resonance conditions of three neutrinoless double-electron capture transitions have been investigated within this work. As an important contribution, the $Q$ values have been measured using the Penning-trap mass spectrometer TRIGA-TRAP. The uncertainties of the $Q$ values were improved up to a factor of ten compared to the literature values from the AME 2003 [Aud03]. Using the new results of the $Q$-value measurements, it was found that neutrinoless double-electron capture transitions in $^{106}$Cd, $^{108}$Cd and $^{184}$Os is not suited for neutrino experiments due to their long half-life. In $^{106}$Cd the excess energy to an excited state with $E_\gamma = 2748.2(4)$ keV energy and $J_f^\pi = 2^-$,$3^-$ was found to be 330(410) eV, thus consistent with zero. However, the large value of the resonance factor is compensated by a small nuclear matrix element due to the high spin and different parity of the excited state and a low double-electron capture probability from the $KL_3$ shells [Gon11]. $^{108}$Cd was excluded from the list of suitable candidates for the search for neutrinoless double-electron capture due to the large excess energy of the transition. For the neutrinoless double-electron capture in $^{184}$Os, the partial resonant enhancement reported in [Kri11] has been confirmed with an improved $Q$-value measurement. An excess energy of -8.89(0.58) keV to the excited $0^+$ state with 1322.152(22) keV energy in the daughter nuclide has been measured. The half-life of this transition was reevaluated by using values for the nuclear matrix element (NME) obtained by state-of-the-art energy density functional (EDF) calculations performed by T.R. Rodríguez *et al.* [Rod10a, Rod12] and calculations of the electronic properties and wave functions with the Dirac-Fock method [Bra77] performed by V.M. Shabaev *et al.* The EDF calculations showed that the quadrupole deformation of the initial and final state are important parameters for the nuclear matrix element. A reduction of the NME of one order of magnitude was found if shape mixing of the initial and final state was included, compared to the hypothetical transition between spherical nuclides. The half-life for the transition to the excited state with 1322.152(22) keV energy was found to be $1.6\times10^{30}$ eV$^2/\langle m_{\nu_e}c^2\rangle^2$ years. Even in case the deformation of the final excited state predicted by the EDF calculations is not correct, a lower limit of the half-life for this transition of $8.8\times10^{28}$ eV$^2/\langle m_{\nu_e}c^2\rangle^2$ years has been obtained. The half-life of this transition is about three orders of magnitude longer compared to the best candidate found so far, which is $^{152}$Gd [Eli11b]. Therefore, $^{184}$Os is also not suited for the search of neutrinoless double-electron capture.

The $Q$ value of the double-beta decay in $^{110}$Pd has been also determined in this work. A measurement with the ISOLTRAP mass-spectrometer, which reported a discrepancy to the AME 2003 $Q$ value [Fin12], was confirmed. The half-life of the neutrinoless double-beta decay in $^{110}$Pd is $6.8{\times}10^{23}$ eV$^2/\langle m_{\nu_e}c^2\rangle^2$ [Fin12] using the new $Q$ value.

The atomic masses of the eight nuclides involved in the studied double-beta transitions have been directly linked to carbon by a cyclotron-frequency ratio measurement to a carbon cluster ion. The atomic masses were determined with higher precision than reported in the AME 2003, except for $^{184}$W, which has an uncertainty of 940 eV compared to 870 eV in literature. The high-precision mass values determined in this thesis will be considered in the next Atomic-Mass Evaluation.

The experimental setup for the operation of a gas-jet coupled on-line ion source for TRIGA-SPEC has been commissioned and tested within this thesis. This included the installation of a 30 kV high-voltage platform, a skimmer system and a rootspump system for the differential pumping, and the modification of a 2.45 GHz ECR ion source for the on-line operation with gas-jet injection. The ECR ion source has been successfully operated as off-line ion source. Ion beams of gaseous species up to 110 $\mu$A could be reliably provided. The dipole magnet mass separator was commissioned and characterized using this ion source. The ionization yields of fission products in on-line operation are not sufficient to use the ECR ion source for the on-line coupling. This is due to the fact that fission products are injected into the ion source with aerosol particles as carrier particles, and the bond between the fission products and the aerosol particles cannot be destroyed in the ECR plasma.

The neutron-rich fission products for the experiments at TRIGA-SPEC have to be provided with a different ionization method. As a first step, the gas-jet coupled ion source of the HELIOS on-line mass separator has been rebuilt and will be used for the first on-line mass measurements with TRIGA-TRAP [Ren14]. The HELIOS ion source can be operated in two modes, the high-temperature mode, where ions are produced in a hot tungsten tube by surface ionization, and the plasma mode, where in addition a plasma discharge is present in the region between the skimmer and the surface ionizer. Overall efficiencies, including gas-jet, ionization and ion beam transport efficiency through a dipole mass separator, were determined in [Maz81, Brü85]. The surface ionization mode reached overall efficiencies of 1-4 % at 2800 K for Ba, Ce, Pr, and Nd [Brü85]. A larger variety of elements could be ionized with the plasma mode, but a lower overall efficiency was archieved. Ionization effcencies in the order of $10^{-3}$ to $10^{-4}$ were reported for Sr, Y, Sn, Sb, Te, Ba, La, Ce, Pr and Nd [Brü85]. Sn, Sb and Te could be only obtained by operating the ion source in the plasma mode. The on-line coupling of TRIGA-SPEC will be completed with this ion source by performing first experiments on short-lived nuclides. Recently, the first mass-separated ion beam of radioactive rubidium ions has been detected behind the dipole magnet [Ren14]. However, new developements are still required in order to make full use of all elements producted and extracted from the TRIGA reactor.

A new approach for the ionization of aerosol-bound fission products with lasers will be tested at TRIGA-SPEC [Sch15]. Mass spectrometers for the analysis of aerosol particles use in flight laser ablation of aerosol particles to study the compo-

sition of the single aerosol particles [Tho97b, Mor98, Zel99]. It was demonstrated that pulsed infra-red and UV-lasers can ablate and ionize large fragments of the aerosol particle and a representative sample of ions from the aerosol particle can be obtained. This method will be applied in the HELIOS ion source at TRIGA-SPEC to destroy the aerosol particles that passed through the skimmer. In addition, resonant laser ionization of a certain element can be performed in order to selectively enhance its ionization efficiency. The development of this gas-jet coupled (resonant) laser ion source will be reported in [Sch15].

The mass measurements on the neutron-rich fission products can be used to test and improve the predictive power of nuclear mass models far away from the valley of stability [Ket08]. The production rates of the neutron-rich radionuclides beyond the maximum yield are rapidly decreasing with the neutron number $N$. In order to cope with the low production rates of these exotic nuclides, it is helpful to use a more ion economic cyclotron-frequency measurement method than the TOF-ICR technique, which requires typically at least a few hundred ions for a cyclotron resonance. One method to increase the access to nuclides with low production rates is the use of a non-destructive ion-cyclotron-resonance detection method, which can use the same ion for several measurement cycles. This requires a half-life of the ion of one second or longer for a mass measurement. The implementation of such a detection system is ongoing at TRIGA-TRAP. Non-destructive ion detection can be performed in a Penning trap by detecting the image current in the trap electrodes induced by the confined charged particles. The cyclotron frequency is obtained by Fourier transformation of the detected image current and is therefore called Fourier-transformation ion-cyclotron-resonance (FT-ICR) technique. The induced current of a singly-charged ion with $A = 100$ is only in the order of 10-100 fA. The detection system for this tiny current uses a superconducting tank circuit with a resonance frequency close to the expected cyclotron frequency of the ions of interest and low-noise amplifiers to convert the signal into a measurable voltage drop. In addition, the Penning traps and the detection electronics are operated at cryogenic temperatures, 77 K and 4.2 K, respectively, to reduce the thermal noise. This detection system is expected to be able to perform a mass measurement with a single ion with a half-life of one second or longer. The detection electronics have been developed and specified. The developed FT-ICR detection system is sensitive to single ions [Ket10b]. In the near future, the detection of the first ion signal will be demonstrated and mass measurements on radionuclides with half-lives longer than one second will be performed [Eib13]. In addition, a broad-band FT-ICR detection system to analyze the content of the purification is planned. Details of the development of the FT-ICR detection systems for TRIGA-TRAP can be found in [Ket06, Rep08, Knu09, Ket10b, Eib13].

The FT-ICR detection system provides excellent conditions to perform mass measurements on nuclides with extremely low production rates but rather long half-lives. Thus, it is well suited to perform mass measurements for example on super-heavy elements. The TRIGA-TRAP Penning traps are exchangeable with the Penning-trap system used at SHIPTRAP, so that the FT-ICR detection system can be used to study super-heavy elements behind the velocity filter SHIP. So far, mass measurements on nobelium and lawrencium have been performed [Dwo10], and the FT-ICR

detection system will allow to access nuclides with higher proton numbers $Z$ and even lower production rates.

Ultimately, the TRIGA-TRAP setup will migrate to the future FAIR facility at GSI as part of the MATS (Measurements with Advanced Trapping Systems) experiment [Rod10b]. The Super Fragment Separator (Super-FRS) at FAIR provides radionuclides produced by in-flight reactions with higher yields compared to other existing radioactive ion beam facilities today. Therefore, the radioactive ion beams from this facility will be used to extend the experimental data on atomic masses even further in direction of the r-process and the neutron drip line.

# Bibliography


[Ahm02] Q.R. Ahmad *et al.*, "Direct evidence for neutrino flavor transformation from neutral-current interactions in the Sudbury Neutrino Observatory", Phys. Rev. Lett. **89**, 011301 (2002).

[Ahm04] S.N. Ahmed *et al.* "Measurement of the total active $^{8}$B solar neutrino flux at the Sudbury Neutrino Observatory with enhanced neutral current sensitivity", Phys. Rev. Lett. **92**, 181301 (2004).

[Alt86] G.D. Alton, "Semi-empirical mathematical relationships for electropositive adsorbate induced work function changes", Surf. Sci. **175**, 226-240 (1986).

[Alt93] G.D. Alton, "Ion sources for accelerators in materials research", Nucl. Instr. Meth. B **73**, 221-288 (1993).

[And62] P.W. Anderson, "Theory of flux creep in hard superconductors", Phys. Rev. Lett. **9**, 309-311 (1962).

[Ang04] I. Angeli, "A consistent set of nuclear RMS charge radii: properties of the radius surface $R(N, Z)$", At. Data Nucl. Data Tab. **87**, 185-206 (2004).

[Ärj86] J. Ärje *et al.*, "The ion guide isotope separator on-line, IGISOL", Nucl. Instr. Meth. A **247**, 431-437 (1986).

[Äst73] J. Äystö *et al.*, "Transport efficiency of the helium-jet recoil-transport method with pure helium", Nucl. Instr. Meth. **111**, 531-537 (1973).

[Aud03] G. Audi *et al.*, "The AME 2003 atomic mass evaluation: (II). Tables, graphs and references", Nucl. Phys. A **729**, 337-676 (2003).

[Aum79] D.C. Aumann *et al.*, "Studies of the formation mechanism of aerosols in a gas-jet recoil-transport system using pure gases as carrier", Nucl. Instr. Meth. **165**, 35-46 (1979).

[Bag10] , C.M. Baglin, "Nuclear Data Sheets for A = 184", Nucl. Data Sheets **111**, 275-523 (2010).

[Bau67] E. Baust, "Die Anlagerung von radioaktiven Atomen und Ionen an Aerosolteilchen", Z. Phys. A **199**, 187-206 (1967).

[Bel11] P. Belli *et al.*, "Search for double beta decay processes in $^{106}$Cd with the help of $^{106}CdWO_4$ crystal scintillator", arXiv:1110.3690 [nucl-ex] (2011).

[Ber83] J. Bernabeu *et al.*, "Neutrinoless double electron capture as a tool to measure the electron neutrino mass", Nucl. Phys. B **223**, 15-28 (1983).

[Ber84] J.F. Berger *et al.*, "Microscopic Analysis of Collective Dynamics in low-energy fission", Nucl. Phys. A **428** 25-36 (1984).

[Ber02] I. Bergstroem *et al.*, "SMILETRAP: A Penning trap facility for precision mass measurements using highly charged ions", Nucl. Instr. Meth. A **487**, 618-651 (2002).

[Ber11] M. Berglund *et al.*, "Isotopic compositions of elements 2009 (IUPAC Technical report)", Pure App. Chem. **83**, 397-410 (2011).

[Bet33] H. Bethe *et al.*, "Experimental nuclear physics", Wiley, New York, 1933.

[Bet36] H.A. Bethe *et al.*, "Nuclear Physics A. Stationary States of Nuclei", Rev. Mod. Phys. **8**, 139 (1936).

[Bet08] K. Bethge *et al.*, "Kernphysik", Springer-Verlag, Berlin Heidelberg, third edition (2008).

[Bey13] T. Beyer, PhD thesis, *in preparation*, Ruprecht-Karls-Universität Heidelberg (2013).

[Bil06] S.M. Bilenky, "Neutrino Majorana", Ann. Fond. Louis de Broglie **31**, 139-154 (2006).

[Bla00] J. Blachot, "Nuclear Data Sheets for A = 108", Nucl. Data Sheets **91**, 135-296 (2000).

[Bla02] K. Blaum *et al.*, "Carbon clusters for absolute mass measurements at ISOLTRAP", Eur. Phys. J. A **15**, 245-248 (2002).

[Bla03a] K. Blaum *et al.*, "Recent developments at ISOLTRAP: towards a relative mass accuracy of exotic nuclei below $10^{-8}$", J. Phys. B **36** 921 (2003).

[Bla03b] K. Blaum *et al.*, "A novel scheme for a highly selective laser ion source", Nucl. Instr. Meth. B **204**, 331-335 (2003).

[Bla04] K. Blaum *et al.*, "Population inversion of nuclear states by a Penning trap mass spectrometer", Eur. Phys. Lett. **67**, 586 (2004).

[Bla06] K. Blaum, "High-accuracy mass spectrometry with stored ions", Phys. Rep. **425**, 1-78 (2006).

[Bla10] K. Blaum *et al.*, "Penning traps as a versatile tool for precise experiments in fundamental physics", Contemp. Phys. **51**, 149-175 (2010).

[Blo05] M. Block *et al.*, "The ion-trap facility SHIPTRAP", Eur. Phys. J. A **25**, 49-50 (2005).

[Blo07] T. Bloxham *et al.*, "First results on double beta-decay modes of Cd, Te, and Zn Isotopes", Phys. Rev. C **76**, 025501 (2007).

[Blo10] M. Block *et al.*, "Direct mass measurements above uranium bridge the gap to the island of stability", Nature **463**, 785-788 (2010).

[Boh39] N. Bohr *et al.*, "The mechanism of nuclear fission", Phys. Rev. **56**, 426 (1939).

[Böh92] F. Böhm *et al.*, "Physics of Massive Neutrinos", Cambridge University Press, Cambridge, second edition (1992).

[Böh09] C. Böhm, Diploma thesis: "Setup of a carbon-cluster laser ion source and the application of the invariance theorem at ISOLTRAP", Johannes Gutenberg-Universität Mainz (2009).

[Bol90] G. Bollen *et al.*, "The accuracy of heavy-ion mass measurements using time of flight-ion cyclotron resonance in a Penning trap", J. Appl. Phys. **68**, 4355-4374 (1990).

[Bol92] G. Bollen *et al.*, "Resolution of nuclear ground and isomeric states by a Penning trap mass spectrometer", Phys. Rev. C **46**, 2140-2143 (1992).

[Bol96] G. Bollen *et al.*, "ISOLTRAP: a tandem Penning trap system for accurate on-line mass determination of short-lived isotopes", Nucl. Instr. Meth. A **368**, 675-697 (1996).

[Bra77] V. Bratsev *et al.*, Bull. Acad. Sci. USSR, Phys. Ser. **41**, 173 (1977).

[Bre08] M. Breitenfeldt *et al.*, "The elliptical Penning trap: Experimental investigations and simulations", Int. J. Mass Spectr. **275**, 34-44 ( 2008).

[Bro86] L.S. Brown *et al.*, "Geonium theory: Physics of a single electron or ion in a Penning trap", Rev. Mod. Phys. **58**, 233-311 (1986).

[Bro89] D.A. Bromley, "Treatise on Heavy-Ion Science: Volume 8, Nuclides Far From Stability", Plenum Publishing Corporation, New York (1989).

[Bro04] I.G. Brown, "The physics and Technology of Ion Sources", Wiley-VCH Verlag, Weinheim (2004).

[Brü79] M. Brügger, Diploma thesis: "Ankopplung eines Gasjettransportsystems an einen Massenseparator und Abtrennung neutronenreicher Nuklide aus dem Spaltproduktgemisch", Johannes Gutenberg-Universität Mainz (1979).

[Brü83] M. Brügger, PhD thesis: "Entwicklung einer Hochtemperatur-oberflächenionenquelle für den Heliumjet Massenseparator HELIOS und Zerfallsstudien an massengetrennten, neutronenreichen Praseodymisotopen", Johannes Gutenberg-Universität Mainz (1983).

[Brü85] M. Brügger *et al.*, "Operation of a high temperature ion source at the helium-jet on-line isotope separator facility HELIOS", Nucl. Instr. Meth. A **234**, 218-223 (1985).

[Bru87] A.M. Bruce *et al.* "Average resonance capture studies of $^{185,187}$W: The Nilsson model and the SU(3) Bose-Fermi symmetry scheme", Nucl. Phys. A **465**, 221-239 (1987).

[Bus75] D.L. Bushnell *et al.*, "States in $^{184}$W via neutron capture and beta-decay excitations", Phys. Rev. C **11**, 1401-1421 (1975).

[Cal95] G. Callies *et al.*, "Time-resolved observation of gas-dynamic discontinuities arising during excimer laser ablation and their interpretation", J. Phys. D **28**, 794 (1995).

[Cam84] R. Campargue, "Progress in overexpanded supersonic jets and skimmed molecular beams in free-jet zones of silence", J. Phys. Chem. **88**, 4466-4474 (1984).

[Cam01] J.L. Campbell *et al.*, "Width of the atomic K-$N_7$ levels", At. Data Nucl. Data Tab. **77**, 1-56 (2001).

[Car70] T.A. Carlson *et al.*, "Calculated ionization potentials for multiply charged ions", At. Data Nucl. Data Tab. **2**, 63-99 (1970).

[Cas80] R.F. Casten *et al.*, "$^{109}$Pd: Difficulties in particle-rotor models for unique-parity states and revision of spectroscopic factors", Phys. Rev. C **21**, 65-97 (1980).

[Cha07] A. Chaudhuri *et al.*, "Carbon-cluster mass calibration at SHIPTRAP", Eur. Phys. J. D **45**, 47-53 (2007).

[Coh84] M.D. Cohler *et al.*, "Measurement of the mass of $^{110}$Pd and $^{114}$Pd using the ($^{14}$C,$^{16}$O) reaction", Z. Phys. A **319**, 107-109 (1984).

[Com74] M.B. Comisarow *et al.*, "Fourier-transform ion-cyclotron-resonance spectroscopy", Chem. Phys. Lett. **25**, 282-283 (1974).

[Dah00] D.A. Dahl, "SIMION for the personal computer in reflection", Int. J. Mass Spectr. **200**, 3-25 (2000).

[Dam63] R.A. Damerow *et al.*, "Atomic Masses from Ruthenium to Xenon", Phys. Rev. **132**, 1673-1681 (1963).

[Dan63] H. Daniel *et al.*, "Zerfallsschema und Matrixelemente für den Beta-Übergang $^{110m}$Ag-$^{110}$Cd", Z. Phys. A **172**, 202-209 (1963).

[DeF96] D. De Frenne *et al.*, "Nuclear Data Sheets for A = 112", Nucl. Data Sheets **79**, 943-1102 (1996).

[DeF08] D. De Frenne *et al.*, "Nuclear Data Sheets for A = 106", Nucl. Data Sheets **109**, 943-1102 (2008).

[Dem08] W. Demtröder, "Experimentalphysik 1, Mechanik und Wärme", Springer-Verlag, Berlin Heidelberg, fifth edition (2008).

[Dil00] J. Dilling *et al.*, "The SHIPTRAP project: A capture and storage facility at GSI for heavy radionuclides from SHIP", Hyp. Int. **127**, 491-496 (2000).

[Doi85] M. Doi *et al.*, "Double-beta decay and Majorana neutrino", Prog. Theor. Phys. Supp. **83**, 1-175 (1985).

[Doi93] M. Doi *et al.*, "Neutrinoless modes of double beta decay", Prog. Theor. Phys. **89**, 139-159 (1993).

[Dom00] M. Dombsky *et al.*, "Commissioning and initial operation of a radioactive beam ion source at ISAC", Rev. Sci. Instr. **71**, 978-980 (2000).

[Drö11] C. Dröse *et al.*, "Investigation of the magnetic field fluctuation and implementation of a temperature and pressure stabilization at SHIPTRAP", Nucl. Instr. Meth. A **632**, 157-163 (2011).

[Drö12] C. Dröse *et al.*, "Probing the nuclide $^{180}$W for neutrinoless double-electron capture exploration", Nucl. Phys. A **875**, 1-7 (2012).

[Dwo10] M. Dworschak *et al.*, "Penning trap mass measurements on nobelium isotopes", Phys. Rev. C **81**, 064312 (2010).

[Ebe00] K. Eberhardt *et al.*, "The research reactor TRIGA Mainz - a neutron source for versatile applications in research and education", Kerntechnik **65**, 5-6 (2000).

[Egu03] K. Eguchi *et al.*, "First results from KAMLAND: Evidence for reactor antineutrino disappearance", Phys. Rev. Lett. **90**, 021802 (2003).

[Eib09] M. Eibach, Diploma thesis: "Characterization of a carbon aerosol generator in a helium gas-jet for the extraction of fission products from the research reactor TRIGA Mainz", Johannes Gutenberg Universität Mainz (2009).

[Eib10] M. Eibach *et al.*, "Transport of fission products with a helium gas-jet at TRIGA-SPEC", Nucl. Instr. Meth. A **613**, 226-231 (2010).

[Eib13] Martin Eibach, PhD thesis: "Setup of a non-destructive ion detection at TRIGA-TRAP", Johannes Gutenberg Universität Mainz (2013).

[Eit09] G. Eitel *et al.*, "Position-sensitive ion detection in precision Penning-trap mass spectrometry", Nucl. Instr. Meth. A **606**, 475-483 (2009).

[Eld72] O. Eldridge, "Electron cyclotron heating as resonant diffusion", Phys. Fluids **15**, 676-682 (1972).

[Eli11a] S. Eliseev *et al.*, "Multiple-resonance phenomenon in neutrinoless double-electron capture", Phys. Rev. C **84**, 012501 (2011).

[Eli11b] S. Eliseev *et al.*, "Resonant enhancement of neutrinoless double-electron capture in $^{152}$Gd", Phys. Rev. Lett. **106**, 052504 (2011).

[Eli11c] S. Eliseev *et al.*, "Octupolar-Excitation Penning-Trap Mass Spectrometry for $Q$-Value Measurement of Double-Electron Capture in $^{164}$Er", Phys. Rev. Lett. **107**, 152501 (2011).

[Eli11d] S. Eliseev *et al.*, "$Q$ values for neutrinoless double-electron capture in $^{96}$Ru, $^{162}$Er, and $^{168}$Yb", Phys. Rev. C **83**, 038501 (2011).

[Eli12] S. Eliseev *et al.*, "$Q$ values for neutrinoless double-electron capture in $^{124}$Xe and $^{130}$Ba", to be pusblished (2012).

[Eng94] T.R. England *et al.*, "Evaluation and compilation of fission product yields", Los Alamos National Laboratory Report LA-UR-94-3106, 1-173 (1994).

[Ero08] T. Eronen, PhD thesis: "High precision $Q_{EC}$ value measurements of superallowed $0^+ \rightarrow 0^+$ beta decays with JYFLTRAP", University of Jyväskylä" (2008).

[Fab86] N. Fabricius *et al.*, "Observation of superheating during picosecond laser melting", Sol. State Comm. **58**, 239-242 (1986).

[Fan12] D.L. Fang *et al.*, "Evaluation of the resonance enhancement effect in neutrinoless double-electron capture in $^{152}$Gd, $^{164}$Er, and $^{180}$W atoms", Phys. Rev. C **85**, 035503 (2012).

[Fed08] V.N. Fedosseev *et al.*, "ISOLDE RILIS: New beams, new facilities", Nucl. Instr. Meth. B **266**, 4378-4382 (2008).

[Fin51] B. Finkle *et al.*, "Radiochemical Studies: The Fission products", McGraw-Hill Book Company, Inc. (1951).

[Fin10] D. Fink, Diploma thesis: "The ISOLTRAP Laser-Ablation Ion Source and Q-Value Determination of the $^{110}$Pd Double Beta Decay", Johannes Gutenberg-Universität Mainz (2010).

[Fin12] D. Fink *et al.*, "$Q$ Value and Half-Lives for the Double-beta-Decay Nuclide $^{110}$Pd", Phys. Rev. Lett. **108**, 062502 (2012).

[Fir07] R.B. Firestone *et al.*, "Database of Prompt Gamma Rays from Slow Neutron Capture for Elemental Analysis", International Atomic Energy Agency, Vienna (2007).

[Gab09] G. Gabrielse, "Why is sideband mass spectrometry possible with ions in a Penning trap?", Phys. Rev. Lett. **102**, 172501 (2009).

[Gäg91] H.W. Gäggeler *et al.*, "OLGA II, an on-line gas chemistry apparatus for applications in heavy element research", Nucl. Instr. Meth. A **309**, 201-208 (1991).

[Gel79] M. Gell-Mann *et al.*, "Proceedings of the Supergravity Workshop at Stony Brook", North-Holland, Amsterdam, 1979.

[Geo05] S. George, Diploma thesis: "Application of the Ramsey method in high-precision Penning trap mass spectrometry", Universität Münster (2005).

[Geo07a] S. George *et al.*, "The Ramsey method in high-precision mass spectrometry with Penning traps: Experimental results", Int. J. Mass Spectr. **264**, 110-121 (2007).

[Geo07b] S. George *et al.*, "Ramsey method of separated oscillatory fields for high-precision Penning trap mass spectrometry", Phys. Rev. Lett. **98**, 162501 (2007).

[Geo11] S. George *et al.*, "Damping effects in Penning trap mass spectrometry", Int. J. Mass Spectr. **299**, 102-112 (2011). Phys. Rev. C **84**, 028501 (2011).

[Gel96] R. Geller, "Electron cyclotron resonance ion sources and ECR plasmas", Institute of Physics Publishing, Bristol (1996).

[Gim92] G. Gimond *et al.*, "Present status of singly charged ion ECR sources at the SARA on-line separator", Nucl. Instr. Meth. B **70**, 118-124 (1992).

[Gir04] A. Girard *et al.*, "Electron cyclotron resonance plasmas and electron cyclotron resonance ion sources: Physics and technology (invited)", Rev. Sci. Instr. **75**, 1381-1388 (2004).

[Gon11] M. Goncharov *et al.*, "Probing the nuclides $^{102}$Pd, $^{106}$Cd, and $^{144}$Sm for resonant neutrinoless double-electron capture",

[Gor09] , S. Goriely *et al.*, "First Gogny-Hartree-Fock-Bogoliubov Nuclear Mass Model", Phys. Rev. Lett. **102**, 242501 (2009).

[Grä80] G. Gräff *et al.*, "A direct determination of the proton electron mass ratio", Z. Phys. A **297**, 35-39 (1980).

[Gre74] R.C. Greenwood *et al.* "Level structure of $^{184}$W from the $^{183}$W(n, $\gamma$) reaction", Nucl. Phys. A **223**, 66-102 (1974).

[Gün93] R. Günther, Diploma thesis: "Charakterisierung der Eigenschaften der KCl-Aerosolpartikel eines He-Gasjets", Johannes Gutenberg-Universität Mainz (1993).

[Gün97] R. Günther, PhD thesis: "Optimierung eines He(KCl)-Gasjet-Transportsystems und Untersuchung der Elemente 104, 105, und 106", Johannes Gutenberg-Universität Mainz (1997).

[Ham06] G. Hampel *et al.*, "The research reactor TRIGA Mainz", ATW **51**, 328-330 (2006).

[Hax84] W.C. Haxton, "Double beta decay", Prog. Nucl. Part. Phys. **12**, 409-479 (1984).

[Her01] F. Herfurth *et al.*, "A linear radiofrequency ion trap for accumulation, bunching, and emittance improvement of radioactive ion beams", Nucl. Instr. Meth. A **469**, 254-275 (2001).

[Hin08] F. Hinterberger, "Physik der Teilchenbeschleuniger und Ionenoptik", Springer-Verlag, Berlin-Heidelberg, second edition (2008).

[Hir94] M. Hirsch *et al.*, "Nuclear structure calculation of $\beta^+/\beta^+$, $\beta^+$/EC and EC/EC decay matrix elements", Z. Phys. A **347**, 151-160 (1994).

[Hit02] , D. Hitz *et al.*, "Results and interpretation of high frequency experiments at 28 GHz in ECR ion sources, future prospects", Rev. Sci. Instr. **73**, 509-512 (2002).

[Hof07] S. Hofmann *et al.*, "The reaction $^{48}$Ca + $^{238}$U $\rightarrow$ $^{286}$112 studied at the GSI-SHIP", Eur. Phys. J. A **32**, 251-260 (2007).

[Huy92] M. Huyse *et al.*, "Status report of the Leuven Isotope Separator On-Line (LISOL)", Nucl. Instr. Meth. B **70**, 50-55 (1992).

[Iak85] I.T. Iakubov *et al.*, "The Coulomb explosion of charged drops", Sol. State Comm. **53**, 427-430 (1985).

[Ich02] S. Ichikawa *et al.*, "Performance of the multiple target He/$PbI_2$ aerosol jet system for mass separation of neutron-deficient actinide isotopes", Nucl. Instr. Meth. B **187**, 548-554 (2002).

[Jac88] B. Jacquot *et al.*, "Source d' ions lourds Caprice 10 GHz 2 $\omega_{ce}$", Nucl. Instr. Meth. **269**, 1-6 (1988).

[Jar02] P. Jardin *et al.*, "Mono 1000: A simple and efficient 2.45 GHz electron cyclotron resonance ion source using a new magnetic structure concept", Rev. Sci. Instr. **73**, 789-791 (2002).

[Jar10] P. Jardin *et al.*, "Latest developments at GANIL for stable and radioactive ion beam production", Rev. Sci. Instr. **81**, 02A909 (2010).

[Kar82] T. Karlewski, Diploma thesis: "Optimierung einer Plasmaionenquelle für die on-line Massentrennung von leichten Spaltprodukten mit dem HELIOS-System", Johannes Gutenberg-Universität Mainz (1982).

[Kaw90] H. Kawano *et al.*, "Temperature dependence of the positive ionization effciency of sodium chloride molecules incident upon a polycrystalline tungsten surface heated in a high vacuum", Int. J. Mass Spectr. **97**, 131-141 (1990).

[Kel99] R. Kelly *et al.*, "Contribution of vaporization and boiling to thermal-spike sputtering by ions or laser pulses", Phys. Rev. E **60**, 2616-2625 (1999).

[Kel03] A. Kellerbauer *et al.*, "From direct to absolute mass measurements: A study of the accuracy of ISOLTRAP", Eur. Phys. J. D **22**, 53-64 (2003).

[Ket06] J. Ketelaer, Diploma thesis: "Development of a non-destructive Fourier transform-ion cyclotron resonance detection system for singly charged ions in a cryogenic Penning trap", Johannes Gutenberg-Universität Mainz (2006).

[Ket08] J. Ketelaer *et al.*, "TRIGA-SPEC: A setup for mass spectrometry and laser spectroscopy at the research reactor TRIGA Mainz", Nucl. Instr. Meth. A **594**, 162-177 (2008).

[Ket09a] J. Ketelaer *et al.*, "Recent developments in ion detection techniques for Penning trap mass spectrometry at TRIGA-TRAP", Eur. Phys. J. A **42** 311-317 (2009).

[Ket09b] J. Ketter, Diploma thesis: "Verbesserung der Ionennachweissysteme des Präzisions-Penningfallen-Massenspektrometers TRIGA-TRAP", Johannes Gutenberg- Universität (2009).

[Ket10a] J. Ketelaer *et al.*, "Accuracy studies with carbon clusters at the Penning trap mass spectrometer TRIGA-TRAP", Eur. Phys. J. D **58**, 47-52 (2010).

[Ket10b] J. Ketelaer, PhD thesis: "The construction of TRIGA-TRAP and direct high-precision Penning trap mass measurements on rare-earth elements and americium", Johannes Gutenberg-Universität Mainz (2010).

[Ket11] J. Ketelaer *et al.*, "Mass measurements on stable nuclides in the rare-earth region with the Penning-trap mass spectrometer TRIGA-TRAP", Phys. Rev. C **84**, 014311 (2011).

[Kir86] T. Kirsten, "Nuclear Beta Decay and Neutrino", Proc. Int. Symp. on Nuclear Beta Decays and Neutrinos (1986).

[Kir90] R. Kirchner, "On the thermoionization in hot cavities", Nucl. Instr. Meth. A **292**, 203-208 (1990).

[Kla01] H.V. Klapdor-Kleingrothaus *et al.*, "Latest results from the Heidelberg-Moscow double beta decay experiment", Eur. Phys. J. A **12**, 147-154 (2001).

[Kla04] H.V. Klapdor-Kleingrothaus *et al.*, "Search for neutrinoless double beta decay with enriched $^{76}$Ge in Gran Sasso 1990-2003", Phys. Lett. B **586**, 198-212 (2004).

[Kle12] S. Klein, Diploma thesis: "Effizienzbestimmung des aerosolgebundenen Transports von Spaltprodukten mit dem $CO_2$-Gasjet", Johannes Gutenberg-Universität Mainz (2012).

[Klu03] H.-J. Kluge *et al.*, "Lasers for nuclear physics", Spectr. Acta B **58**, 1031-1045 (2003).

[Knu09] K. Knuth, Diploma thesis: "Aufbau eines breitbandigen FT-ICR-Nachweissystems für TRIGA-TRAP", Johannes Gutenberg-Universität (2009).

[Kog02] M. Koga *et al.*, "Measurement of ion temperature in ECR $Ar/N_2$ plasma", Surf. Coat. Techn. **171**, 216-221 (2002).

[Koh04] V.S. Kolhinen *et al.*, "JYFLTRAP: a cylindrical Penning trap for isobaric beam purification at IGISOL", Nucl. Instr. Meth. A **528**, 776-787 (2004).

[Koh08] V.S. Kolhinen *et al.*, "MLLTRAP: A Penning trap facility for high-accuracy mass measurements", Nucl. Instr. Meth. B **266**, 4547-4550 (2008).

[Kol11] V.S. Kolhinen *et al.*, "On the resonant neutrinoless double-electron-capture decay of $^{136}$Ce", Phys. Lett. B **697**, 116-120 (2011).

[Kön95] M. König *et al.*, "Quadrupole excitation of stored ion motion at the true cyclotron frequency", Int. J. Mass Spectr. **142**, 95-116 (1995).

[Krä10] J. Krämer, PhD thesis: "Construction and Commissioning of a Collinear Laser Spectroscopy Setup at TRIGA Mainz and Laser Spectroscopy of Magnesium Isotopes at ISOLDE (CERN)", Johannes Gutenberg Universität Mainz (2010).

[Kre92a] M. Kretzschmar, "Single particle motion in a Penning trap: description in the classical canonical formalism", Phys. Scr. **46**, 544 (1992).

[Kre92b] M. Kretzschmar, "Excitation of particle motions in a Penning trap: description in the classical canonical formalism", Phys. Scr. **46**, 555 (1992).

[Kre07] M. Kretzschmar, "The ramsey method in high-precision mass spectrometry with penning traps: Theoretical foundations", Int. J. Mass Spectr. **264**, 122-145 (2007).

[Kre08] M. Kretzschmar, "Theory of the elliptical Penning trap", Int. J. Mass Spectr. **275**, 21-33 (2008).

[Kri11] M.I. Krivoruchenko *et al.*, "Resonance enhancement of neutrinoless double electron capture", Nucl. Phys. A **859**, 140-171 (2011).

[Kud09] Yu. Kudryavtsev *et al.*, "Dual chamber laser ion source at LISOL", Nucl. Instr. Meth. B **267**, 2908-2917 (2009).

[Kug00] E. Kugler, "The ISOLDE facility", Hyp. Int. **129**, 23-42 (2000).

[Kuh75] A.W. Kuhfeld *et al.*, "A study of the nucleus $^{107}$Ag in the core-excitation model with the (p, t) and (t, d) reactions", Nucl. Phys. A **247**, 152-186 (1975).

[Kul11] P. Kulkarni *et al.*, "Aerosol Measurement", John Wiley and Sons, Inc., Hoboken, New Jersey, third edition (2011).

[Lan25] I. Langmuir *et al.*, "Thermionic effects caused by vapours of akali metals", Proc. Roy. Soc. London A **107**, 61 (1925).

[Lar77] F.P. Larkins, "Semiempirical Auger-electron energies for elements $10 \leq Z \leq 100$", At. Data and Nucl. Data Tables **20**, 311-387 (1977).

[Leh11] B. Lehnert *et al.*, "A first search of excited states double beta and double electron capture decays of $^{110}$Pd and $^{102}$Pd", Phys. Lett. B **705** 47-51 (2011).

[Let87] V.S. Lethokov, "Laser Photoionization Spectroscopy", Academic Press, Orlando, 1987.

[Lie92] M. Liehr *et al.*, "A low power 2.45 GHz ECR ion source for multiply charged ions", Rev. Sci. Instr. **63**, 2541-2543 (1992).

[Liu10] Y. Liu *et al.*, "Improved temperature regulation of Penning trap mass spectrometers", Int. J. Mass Spectr. **294**, 28-32 (2010).

[Lor03] P. Lorazo *et al.*, "Short-pulse laser ablation of solids: From phase explosion to fragmentation", Phys. Rev. Lett. **91**, 225502 (2003).

[Lor06] P. Lorazo *et al.*, "Thermodynamic pathways to melting, ablation, and solidification in absorbing solids under pulsed laser irradiation", Phys. Rev. B **73**, 134108 (2006).

[Lot67] W. Lotz, "An empirical formula for the electron-impact ionization cross-section", Z. Phys. A, **206**, 205-211 (1967).

[Lun09] D. Lunney *et al.*, "COLETTE: A linear Paul-trap beam cooler for the online mass spectrometer MISTRAL", Nucl. Instr. Meth. A, **598**, 379-387 (2009).

[Mac69] R.D. MacFarlane *et al.*, "The helium-jet recoil transport method", Nucl. Instr. Meth. **73**, 285-291 (1969).

[Maj04] F.G. Major *et al.*, "Charged particle traps: physics and techniques of charged particle field confinement", Springer Verlag, Berlin Heidelberg (2004).

[Mar69] P.N. Marinos, "Fuzzy logic and its application to switching systems", IEEE Trans. Comp. C **18**, 343 (1969).

[Mar08a] M. Marie-Jeanne *et al.*, "Towards a magnetic field stabilization at ISOLTRAP for high-accuracy mass measurements on exotic nuclides", Nucl. Instr. Meth. A **587**, 464-473 (2008).

[Mar08b] M. Marie-Jeanne *et al.*, "Charge breeding ions for nuclear physics with the PHOENIX ECRIS", Nucl. Instr. Meth. B **266**, 4387-4390 (2008).

[Mau04] J. Maul, PhD thesis: "Ortsaufgelöster Nachweis von Elementspuren mittels Laserablation und Resonanzionisations-Massenspektrometrie und Untersuchungen zur Laserablations-Dynamik", Johannes Gutenberg-Universität Mainz (2004).

[Maz80] A.K. Mazumdar *et al.*, "The on-line isotope separation facility HELIOS at the Mainz reactor", Nucl. Instr. Meth. **174**, 183-188 (1980).

[Maz81] A.K. Mazumdar *et al.*, "Performance of the on-line isotope separation facility HELIOS at the Mainz reactor", Nucl. Instr. Meth. **186**, 131-134 (1981).

[Moo10] I.D. Moore *et al.*, "A study of on-line gas cell processes at IGISOL.", Nucl. Instr. Meth. B **268**, 657-670 (2010).

[Mor67] J.A. Moragues *et al.*, "Decay of $^{110m}$Ag to $^{110}$Cd", Nucl. Phys. A **99**, 652-668 (1967).

[Mor98] B.D. Morrical *et al.*, "'Coupling Two-Step Laser Desorption/Ionization with Aerosol Time-of-Flight Mass Spectrometry for the Analysis of Individual Organic Particles", J. Am. Soc. Mass Spectr. **9**, 1068-1073 (1998).

[Mou10] B.J. Mount *et al.*, "Double-$\beta$-decay $Q$ values of $^{74}$Se and $^{76}$Ge", Phys. Rev. C **81**, 032501 (2010).

[Mül80] A. Müller *et al.*, "Absolute ionisation cross sections for electrons incident on $O^+$ , $Ne^+$, $Xe^+$ and $Ar^{i+}$ (i=1,...,5) ions", J. Phys. B **13**, 1877 (1980).

[Mün79] G. Münzenberg *et al.*, "The velocity filter SHIP, a separator of unslowed heavy ion fusion products", Nucl. Instr. Meth. **161**, 65-82 (1979).

[Mut88] K. Muto *et al.*, "Neutrinos", Springer-Verlag, Berlin (1988).

[Nak10] T. Nakagawa *et al.*, "First results from the new RIKEN superconducting electron cyclotron resonance ion source (invited)", Rev. Sci. Instr. **81**, 02A320 (2010).

[Nat08] National Nuclear Data Center, Information extracted from the NuDat2 database, "http://www.nndc.bnl.gov/nudat2/" (2008).

[Nei08] D. Neidherr *et al.*, "Measurement and simulation of the pressure ratio between the two traps of double Penning trap mass spectrometers", Nucl. Instr. Meth. B **266**, 4556-4559 (2008).

[Nie01] A. Nieminen *et al.*, "Beam cooler for low-energy radioactive ions", Nucl. Instr. Meth. A **469**, 244-253 (2001).

[Nie02] A. Nieminen *et al.*, "On-line ion cooling and bunching for collinear laser spectroscopy", Phys. Rev. Lett. **88**, 094801 (2002).

[Nie12] B. Niessen, Diploma thesis: "Entwicklung einer Plasma-Ionenquelle für radioaktive Isotope und Implementierung und Inbetriebnahme einer offline Ionenquelle am TRIGA-Reaktor", Johannes Gutenberg-Universität Mainz (2012).

[Nix72] J.R. Nix, "Calculation of fission barriers for heavy and superheavy nuclei", Ann. Rev. Nucl. Sci. **22**, 65-120 (1972).

[Nör09] W. Nörtershäuser *et al.*, "Nuclear charge radii of $^{7,9,10}$Be and the one-neutron halo nucleus $^{11}$Be", Phys. Rev. Lett. **102**, 062503 (2009).

[Ott08] E.W. Otten *et al.*, "Neutrino mass limit from tritium beta decay", Rep. Prog. Phys. **71**, 086201 (2008).

[Oza00] A. Ozawa *et al.*, "New magic number, $N = 16$, near the neutron drip line", Phys. Rev. Lett. **84**, 5493-5495 (2000).

[Pau77] W. Pauli, "Fünf Arbeiten zum Ausschliessungspronzip und zum Neutrino", Wissenschaftliche Buchgesellschaft, Darmstadt (1977).

[Per02] D. Perez *et al.*, "Ablation of solids under femtosecond laser pulses", Phys. Rev. Lett. **89**, 255504 (2002).

[Per03] D. Perez *et al.*, "Molecular-dynamics study of ablation of solids under femtosecond laser pulses", Phys. Rev. B **67**, 184102 (2003).

[Pie54] J.R. Pierce, "Theory and Design of Electron Beams", Van Nostrand, New York, (1954).

[Pop91] O.A. Popov, "Effects of magnetic field and microwave power on electron cyclotron resonance-type plasma characteristics", J. Vac. Sci. Techn. A **9**, 711-716 (1991).

[Pov09] K. Povh *et al.*, "Teilchen und Kerne", Springer-Verlag, Berlin Heidelberg, eighth edition (2009).

[Rai04] S. Rainville *et al.*, "An ion balance for ultra-high-precision atomic mass measurements", Science **303**, 334-338 (2004).

[Rei56] F. Reines *et al.*, "The neutrino", Nature **178**, 446-449 (1956).

[Ren09] D. Renisch, Report: "Herstellung von Gd-targets für TRIGA-TRAP", Institut für Kernchemie, Johannes Gutenberg-Universität (2009).

[Ren12] D. Renisch *et al.*, "Targets on superhydrophobic surfaces for laser ablation ion sources", Nucl. Inst. Meth. A, **676**, 84-89 (2012).

[Ren14] D. Renisch, PhD thesis: "Aufbau einer online-Ionenquelle am TRIGA Mainz Forschungsreaktor", Johannes Gutenberg-Universität (2014).

[Red09] M. Redshaw *et al.*, "Improved atomic masses of $^{84,86}$Kr and $^{129,132}$Xe", Phys. Rev. A **79**, 012506 (2009).

[Rep08] J. Repp, Diploma thesis: "Setup of a non-destructive ion detection system and magnetic field investigations for precision mass measurements at TRIGA-TRAP", Johannes Gutenberg-Universität Mainz (2008).

[Rod03a] V. A. Rodin *et al.*, "Uncertainty in the $0\nu\beta\beta$ decay nuclear matrix elements", Phys. Rev. C **68**, 044302 (2003).

[Rod03b] D. Rodriguez, PhD thesis: "A radiofrequency quadrupole buncher for accumulation and cooling of heavy radionuclides at SHIPTRAP and high precision mass measurements on unstable krypton nuclides at ISOLTRAP", Universidad de Valencia (2003).

[Rod10a] T.R. Rodríguez *et al.*, "Energy density functional study of nuclear matrix elements for neutrinoless beta beta decay", Phys. Rev. Lett. **105**, 252503 (2010).

[Rod10b] D. Rodriguez *et al.*, "MATS and LaSpec: High-precision experiments using ion traps and lasers at FAIR", Eur. Phys. J. **183**, 1-123 (2010).

[Rod11] T.R. Rodríguez *et al.*, "Neutrinoless double beta decay studied with configuration mixing methods", Prog. Part. Nucl. Phys. **66**, 436-440 (2011).

[Rod12] T.R. Rodríguez *et al.*, "Calculation of nuclear matrix elements in neutrinoless double electron capture", Phys. Rev. C **85**, 044310 (2012).

[Ruk11] N.I. Rukhadze *et al.*, "New limits on double-beta decay of $^{106}$Cd", Nucl. Phys. A **852**, 197-206 (2011).

[Rus02] R.E. Russo *et al.*, "Peer reviewed: The physics of laser ablation in microchemical analysis", Anal. Chem. **74**, 70-77 (2002).

[Sav91] G. Savard *et al.*, "A new cooling technique for heavy ions in a Penning trap", Phys. Lett. A **158**, 247-252 (1991).

[Sav08] G. Savard *et al.*, "Radioactive beams from gas catchers: The CARIBU facility", Nucl. Instr. Meth. B **266**, 4086-4091 (2008).

[Sch76] H. Schmeing *et al.*, "The Chalk river helium jet and skimmer system", Nucl. Instr. Meth. **139**, 335-342 (1976).

[Sch87] H. Schmeing *et al.*, "The Chalk river helium-jet ion source", Nucl. Instr. Meth. B **26** 321-327 (1987).

[Sch91] L. Schweikhard, "Theory of quadrupole detection Fourier-transform ion cyclotron resonance", Int. J. Mass Spectr. **107**, 281-292 (1991).

[Sch97] N. Schmitz, "Neutrinophysik", Teubner Verlag, Stuttgart (1997).

[Sch05] S. Schoenert *et al.*, "The germanium detector array (GERDA) for the search of neutrinoless beta decays of $^{76}$Ge at LNGS", Nucl. Phys. B **145**, 242-245 (2005).

[Sch10] F. Schwellnus *et al.*, "The laser ion source trap for highest isobaric selectivity in online exotic isotope production", Rev. Sci. Instr. **81**, 02A515 (2010).

[Sch15] F. Schneider, PhD thesis: "Development of a gas-jet coupled laser ion source for TRIGA-SPEC", Johannes Gutenberg-Universität (2015).

[Sco88] G. Scoles, "Atomic and Molecular Beam Methods: Volume 1", Oxford University Press, New York (1988).

[Sil77] R.J. Silva *et al.*, "A gas-jet recoil-transport system for fission products and its application to a continuous chemical separation procedure in the gas phase", Nucl. Instr. Meth. **147** 371-378 (1977).

[Sim08] F. Śimkovic *et al.*, "Anatomy of the $0\nu\beta\beta$ nuclear matrix elements", Phys. Rev. C **77**, 045503 (2008).

[Sim09] F. Śimkovic *et al.*, "$0\nu\beta\beta$-decay nuclear matrix elements with self-consistent short-range correlations", Phys. Rev. C **79**, 055501 (2009).

[Smi08] M. Smith *et al.*, "First Penning-trap mass measurement of the exotic halo nucleus $^{11}$Li", Phys. Rev. Lett. **101**, 202501 (2008).

[Sol08] A. Solders *et al.*, "Determination of the proton mass from a measurement of the cyclotron frequencies of $D^+$ and $H_2^+$ in a Penning trap", Phys. Rev. A **78**, 012514 (2008).

[Smo08a] C. Smorra, Diploma thesis: "Setup of a carbon-cluster laser ion source for high-precision mass spectrometry", Johannes Gutenberg-Universität (2008).

[Smo08b] C. Smorra, Report: "Studies of a laser ablation ion source extraction system", Institut für Kernchemie, Johannes Gutenberg-Universität (2008).

[Smo09] C. Smorra *et al.*, "A carbon-cluster laser ion source for TRIGA-TRAP", J. Phys. B **42**, 154028 (2009).

[Smo12a] C. Smorra *et al.*, "Direct mass measurements of cadmium and palladium isotopes and their double-beta transition $Q$ values", Phys. Rev. C **85**, 027601 (2012).

[Smo12b] C. Smorra *et al.*, "$Q$-value and half-life of double-electron capture in $^{184}$Os", to be published (2012).

[Spi05] H. Spieler, "Semiconductor detector systems", Oxford University Press (2005).

[Sti92] T.H. Stix, "Waves in Plasmas", Springer-Verlag Berlin / Heidelberg (1992).

[Str67] V.M. Strutinsky, "Shell effects in nuclear masses and deformation energies", Nucl. Phys. A **95**, 420-442 (1967).

[Suc98] K. Suchy, "Polarizations of magnetohydrodynamic waves in a cold multi-species plasma", Contr. Plas. Phys. **38**, 615-622 (1998).

[Suj04] Z. Sujkowski *et al.*, "Neutrinoless double electron capture: A tool to search for Majorana neutrinos", Phys. Rev. C **70**, 052501 (2004).

[Tak80] E.M. Takagui *et al.*, "$^{111}$In-$^{109}$In mass difference", Phys. Rev. C **21**, 1667-1669 (1980).

[Tan85] I. Tanihata *et al.*, "Measurements of interaction cross sections and nuclear radii in the light p-shell region", Phys. Rev. Lett. **55**, 2676-2679 (1985).

[Tan08] I. Tanihata, "Radioactive beam science, past, present and future", Nucl. Instr. Meth. B **266**, 4067-4073 (2008).

[Tay33] J.B. Taylor, "The Evaporation of Atoms, Ions and Electrons from Caesium Films on Tungsten", Phys. Rev. **44**, 432 (1933).

[Thi75] C. Thibault *et al.*, "Direct measurement of the masses of $^{11}$Li and $^{26-32}$Na with an on-line mass spectrometer", Phys. Rev. C **12**, 644-657 (1975).

[Tho97a] J.J. Thomson, "Cathode rays", Phil. Mag. **5**, 293-316 (1897).

[Tho97b] D.S. Thomson *et al.*, "Thresholds for Laser-Induced Ion Formation from Aerosols in a Vacuum Using Ultraviolet and Vacuum-Ultraviolet Laser Wavelengths", Aerosol Sci. Tech. **26**, 544-559 (1997).

[Tur91] A.L. Turkevich *et al.*, "Double-beta decay of $^{238}$U", Phys. Rev. Lett. **67**, 3211-3214 (1991).

[Vol82] M.B. Voloshin *et al.*, "Conversion of an atomic electron into a positron and double $\beta^+$ decay", JETP Lett. **35**, 656-659 (1982).

[Wag12] A. Wagner, PhD thesis: "Measurement of the g-factor of Li-like silicium", Ruprecht-Karls Universität Heidelberg (2012).

[Web04] C. Weber, PhD thesis: "Konzeption eines kryogenen Penningfallenaufbaus für SHIPTRAP und Massenbestimmungen von Radionukliden um den Z = 82 - Schalenabschluss an ISOLTRAP", Ruprecht-Karls Universität Heidelberg (2004).

[Wei35] C. Weizsäcker, "Zur Theorie der Kernmassen", Z. Phys. A **96**, 431 (1935).

[Wen00] K. Wendt *et al.*, "Resonant laser ionization mass spectrometry: An alternative to AMS?", Nucl. Instr. Meth. B **172**, 162-169 (2000).

[Wol76] H. Wollnik, "Principles behind a He-jet system and its application for isotope separation", Nucl. Instr. Meth. **139**, 311-318 (1976).

[Wol95] B. Wolf, "Handbook of Ion Sources", CRC Press, Boca Raton, Florida (1995).

[Wri92] D. Wright, "Beamwidths of a diffracted laser using four proposed methods", Opt. Quant. Electr. **24**, 1129-1135 (1992).

[Yad04] V. Yadav *et al.*, "Electron cyclotron resonance heating in a short cylindrical plasma system", Pramana **63**, 563-577 (2004).

[Yan80] T. Yanagida, "Horizontal symmetry and masses of neutrinos", Prog. Theor. Phys. **64**, 1103-1105 (1980).

[Yav09] M. Yavor, Private communications (2009).

[Zde02] Yu. Zdesenko *et al.*, "Has neutrinoless double $\beta$ decay of $^{76}$Ge been really observed?", Phys. Lett. B **546**, 206-215 (2002).

[Zel99] A. Zelenyuk *et al.*, "Mass Spectrometry of Liquid Aniline Aerosol Particles by IR/UV Laser Irradiation", Anal. Chem. **71**, 1802-1808 (1999).

[Zel04] A. Zelenaka *et al.*, "Emittance studies of the 2.45 GHz permanent magnet ECR ion source", Rev. Sci. Instr. **75**, 1653-1655 (2004).

[Zha99] H. Zhang, "Ion Sources", Springer-Verlag, Berlin-Heidelberg (1999).

[Zub98] K. Zuber, "On the physics of massive neutrinos", Phys. Rep. **305**, 295-364 (1998).

[Zub01] K. Zuber, "COBRA: double beta decay searches using CdTe detectors", Phys. Lett. B **519**, 1-7 (2001).

[Zub04a] K. Zuber, "Double beta decay", Contemp. Phys. **45**, 491-502 (2004).

[Zub04b] K. Zuber, "Neutrino Physics", Institute of Physics Publishing, Bristol, first edition (2004).

[Zud86] F. Zude, Diploma thesis: "Transportverhalten von Spaltprodukten in Gasjetsystemen", Johannes Gutenberg-Universität (1986).

# Acknowlegements

During my PhD time at the TRIGA-TRAP experiment I have received many support from my supervisors, collaborators, colleagues, friends, and my family, and I would like to thank all of them.

At first, I would like to thank my supervisor Klaus Blaum, who made it possible to do the research for my thesis at the TRIGA-TRAP experiment and for his continuous support during the whole time. Klaus inspired me with interest in Penning trap physics in his lectures at the Johannes Gutenberg-Universität Mainz in 2005 and 2006, and I have enjoyed working in this research field since then.

I received a lot of help from quite many co-workers, which were working in the lab during my PhD time. These are Szilard Nagy, Rafael Ferrer, Jens Ketelaer, Sebastian George, Dennis Neidherr, Jochen Ketter, Julia Repp, Martin Eibach, Konstantin Knuth, Thomas Beyer, Dennis Renisch, Sebastian Klein, and Fabian Schneider. I would like to thank all members of the TRIGA-SPEC collaboration for their advice and helpful discussions, in particular Wilfried Nörtershäuser, Christopher Geppert, Jörg Krämer, Andreas Krieger, Michael Hammen, Nadja Frömmgen, and Benjamin Niessen from the TRIGA-Laser group, Christoph E. Düllmann, Klaus Eberhardt, Jörg Runke, Norbert Trautmann, and Norbert Wiehl from the Nuclear Chemistry Department, Michael Block and Frank Herfurth from GSI.

I am indebted to Alfred Müller from the Institut für Atom- und Molekülphysik at the Justus-Liebig-Universität in Gießen, who borrowed the ECR ion source to TRIGA-SPEC, which was tested as on-line ion source in this thesis. Furthermore, I acknowledge the scientific advise about ECR ion sources from Pierre Delahaye, who also allowed me to participate in an on-line run of the PHOENIX charge-breeder at ISOLDE in 2008, which was very instructive for me. Furthermore, I would like to thank Antonio Villari from Pantechnik for helpful discussions about ECR ion sources.

For the design of the ion optics of the common beamline and the pulsed drift tube, I acknowledge the discussions with Mikhail Yavor in 2009 at the Max -Planck-Institut für Kernphysik.

My work included the mechanical construction of the high-voltage platform of the on-line ion source and the beamline up to the switchyard, therefore the help of several mechanical workshops was essential for completing this thesis. I would like to thank the mechanical workshop of the Insititut für Physik, in particular Sigbert Felzer for their support. The mechanical workshop of the Institut für Kernchemie always provided help in a fast and uncomplicated way and I like to thank Gerhard Lehr, Ullrich Krille, and Atilla Peil their patience and their support. The construction department and the mechanical workshop at the MPI-K, as well as the mechanical

workshop at the Max-Planck-Institut for Chemistry in Mainz manufactured vacuum chambers and parts of the on-line ion source. In particular, I would like to thank the MPI-K workshop for making the antennas of the ECR ion source, which proved to be quite a challenge.

For the design of the high-voltage cage, we received help from the RISIKO experiment from group of Klaus Wendt, in particular from Fabio Schwellnus. The mechanical construction of the high-voltage cage was supported by Ralph Zilly from the MPI-K. For the installation of the electronic parts of the high-voltage I received a lot of help from Vitali Janzen and the electronics workshop in the Institut für Kernchemie.

The Penning trap experiments concerning the neutrinoless double-electron capture $Q$-values were performed in collaboration with Sergey Eliseev from MPI-K, and the SHIPTRAP group at GSI. The theoretical calculations of the nuclear matrix elements and the leptonic factors for the half-life of $^{184}$Os were performed by Tomás Rodríguez, Gabriel Martínez-Pinedo, and Karl-Heinz Langanke from GSI, and Vladimir Shabaev, Ilya Tupitsyn and Natalia Zubova from the Department of Physics of the St. Petersburg State University, respectively. I would like to thank them for their cooperation. I would also like to thank Daniel Fink for the discussions about the masses of $^{110}$Pd and $^{110}$Cd. Furthermore, I acknowledge the help of Anke Wagner with the temperature stabilization system and its control software.

I was able to participate in the internship program at RIKEN in Japan for three month during my PhD time. I would like to thank Michiharu Wada for his kind support and hospitality during that time. I was able to join the first successful tests of the multi-reflection time-of-flight mass spectrometer, which has been developed for SLOWRI at the RIKEN RIBF facility. I would also like thank his group members, Tetsu Sonoda, Peter Schury, and Yuta Ito for the pleasant stay. I was also able to visit the superconducting ECR ion source at the RIBF facility, and I acknowledge helpful discussions about the on-line coupling with Takahide Nakagawa.

I enjoyed to be part of the Penning trap group of Klaus Blaum, and I would like to thank all other colleagues in Mainz and in Heidelberg for their cooperation and for the good working atmosphere. I also enjoyed the common events like the MATS days, and the Run for Children in Mainz with all of you.

I would also like to thank all of you who accompanied me in good and rough times in the last four years, and everyone who made my life in Mainz pleasant. In particular, I would like to thank my family for continuously encouraging me and for the good family unity, which is very precious to me.

# Erklärung

Hiermit erkläre ich, dass ich die vorliegende Arbeit selbst verfasst habe und keine weiteren außer den angegebenen Quellen und Hilfsmittel verwendet habe.

Heidelberg, den 15.05.2012

Christian Smorra